EFFECTS OF LOCAL DEFORMATIONS ON LATERAL RESPONE OF BRIDGE FRAMES

Silvia Mazzoni, Gregory L. Fenves, Jamison B. Smith

University of California, Berkeley

Final Report to California Department of Transportation

Contract No. 59A0201

April 2004

Acknowledgments

The authors would like to aknowledge the active participation and support of Craig Whitten and Tariq Nasroor, of the California Department of Transportation. Their contributions were valuable from the inception to the completion of this research project. Financial support from the California Department of Transportation was made possible through Contract number 59A0201.

In addition, this work was supported in part by the Pacific Earthquake Engineering Research Center through the Earthquake Engineering Research Centers Program of the National Science Foundation under Award number EEC-9701568.

Contents

Table of Figures

Chapter 1. Introduction

Since reinforced-concrete bridges are designed to have plastic hinges forming at the ends of columns, joint flexibility can be expected. The flexibility of the beam-column joint produces structural deformations that may be of significant magnitude under certain conditions. In addition to the contribution to structural displacements, joint deformations reduce the bond strength of the anchorage of the longitudinal reinforcement in the columns. The loss of anchorage strength results in a rotation of the column due to the relative elongation and slip of the column longitudinal reinforcement. Although the general effects of these deformation modes may be known, there is currently no simplified model available to designers for including these local deformations in either capacity or demand analyses. Researchers have proposed numerous models that capture the bond slip behavior of bars anchored in beam-column joints and have considered the problem of joint shear, but the formulations can be complicated and are not easily implemented into a design procedure.

The structural system considered in this study is a two-column plane frame, representative of a transverse bridge bent, as illustrated in Figure 1-1. The two modes of local deformations in the transverse bridge bent are shown graphically in Figure 1-2 and Figure 1-3. Because the deformations due to bar elongation are a result of the formation of the column plastic hinge, they are herein referred to as hinge deformations and flexibilities. In modeling the nonlinear inelastic response of the hinge deformations, a number of cases considering various distributions of bond stress along the anchorage length were considered. The variation in bond stress results in a variation of flexibility of the rotational element. In modeling the beam-column

joint as a nonlinear inelastic element, a number of cases considering various maximum joint shear strengths and post-yield stiffnesses were considered.

The objective of this report is to investigate these two sources of local deformations, joint shear and rotation due to bar elongation, quantify their behavior, and develop simple models with appropriate parameters to be used in the design and analysis of bridge structures subjected to earthquake ground motion. To this aim, a series of parameter studies are performed to determine the effects of the local deformations on the global behavior of the lateral bridge bent; both nonlinear static capacity and time-history demand analyses were performed. Both types of analyses are performed on the structural systems with and without local-deformation. The results of the study are used to develop simplified models to be used within the framework of performance-based design and evaluation.

1.1. Review of Previous Research

Several research programs, experimental and computational, have studied the response of beam-column subassemblages subjected to cyclic loading. The earliest studies have focused mainly on experimental tests of building-frame subassemblages, although more recent studies have also focused on bridge frames. The principal difference between these two structural systems is that building-frame components are designed to localize inelastic deformations in the beam elements, while they are designed to localize in the column elements of bridge frames. Reinforced-concrete bridge frames have been studied more extensively and are the focus of the computational study presented herein.

The response of the anchorage of member longitudinal reinforcement has been studied at the local level, leading to a number of bond-stress-distribution models. The effects of the bar

elongation and slip on the global response of structures, however, have typically been addressed only in the calculation of lateral deformation capacities.

1.1.1. Joint Shear Deformations

Joint ACI-ASCE Committee 352 has published design recommendations for beam-column joints in buildings, most recently in 1991. [ACI-ASCE 352, 1991] Building joints are separated into two types: Type 1 for joints designed only for strength, and Type 2 for those required to retain strength under deformation reversals into the inelastic range. They are then classified as interior, exterior, or corner joints, on the basis of the number and size of beams framing into the joint. The report gives extensive detailing requirements that outline the amount and arrangement of transverse reinforcement that should be placed in the joint to provide adequate strength and nominal ductility for joints subjected to large deformation reversals. It is assumed that if a joint is properly classified and the reinforcement requirements are met, the joint will be able to withstand a certain level of joint shear. This nominal joint shear strength is calculated as

$$V_n = 0.083\gamma\sqrt{f_c'}\cdot b_j \cdot h \tag{1-1}$$

Where γ is a parameter ranging from 12 for Type 2 corner joints (the worse case) to 24 for Type 1 interior joints (best case), b_j and h are the dimensions of the joint core, and f_c' is measured in MPa. The committee also recommends that the designer proportion column and beam strength for type 2 joints so that the sum of the nominal moment strengths of the columns be 1.4 times the sum of the nominal beam moment strengths in the loading direction. This recommendation is intended to force plastic hinging into the beams rather than the columns. The development of member longitudinal reinforcement is addressed through equations for the development length of both hooked and straight bars anchoring into the joint. Also, for longitudinal bars passing

through the joint, it is recommended that the bars be selected so that the joint dimension parallel to the bar is at least twenty times the bar diameter. An extensive bibliography and appendices with design examples and suggestions for future research are included.

A thorough review of the development of the theory of joint design and behavior for both buildings and bridges is given in [Mazzoni, 1997]. Two competing joint design philosophies are discussed: in the first, force transfer mechanisms such as the diagonal compression strut mechanism and the truss mechanism are responsible for carrying member end forces across the joint. In the second, a joint is assumed to have a nominal shear capacity based on its geometry if a set of prescriptive detailing requirements is followed. (The ACI-ASCE Committee 352 report follows the latter philosophy.) The effects of bar anchorage, quantity of column longitudinal reinforcement, and column axial load on the response of the beam-column joint are also discussed.

The aim in capacity design of buildings for earthquake loading is to detail the beams and adjacent columns so that inelastic behavior is concentrated in the beams. It is expected that the columns at the lowest level will develop plastic hinges at their bases, but it is desirable to prevent hinging from occurring at the top of these first-story columns as well, therefore avoiding the formation of a single-story collapse mechanism. Proper strength proportioning of the beams and columns in a building allows for greater overall displacement ductility and energy dissipation capacity because yielding is spread throughout the structure and not concentrated at the lowest level. However, the lack of redundancy of bridge structures and the desire to introduce as little damage as possible to the superstructure require that the column be allowed to yield adjacent to the beam-column joint and the cap beam remain nominally elastic when subjected to earthquake excitation. So-called ‘plastic hinging’ may also be expected at the pier base and is dependent on the detailing of the pier-footing connection. Because of this difference in design strategies it is

expected that the behavior of beam-column joints in bridges will not be the same as those in buildings. Also, the detailing requirements, expected shear strength, and the effect of the numerous design variables developed in the study of building-frame structures are not necessarily directly applicable to bridge structures.

Following extensive damage to bridges in the 1989 Loma Prieta earthquake, the California Department of Transportation (Caltrans) initiated several studies to determine best repair and retrofit practices for existing bridges. Later testing focused on developing recommendations for new construction so that the joint failures seen in Loma Prieta could be avoided in future bridge design projects. The standard design practice for cap beam-pier joints until very recently included a nominal amount of joint transverse reinforcement, either hoops or a spiral, in addition to the column and beam longitudinal reinforcement. Two series of tests, one with round columns and the other with rectangular columns, at the University of California, San Diego investigated the response of knee joints with this simple detailing and with different improved detailing strategies. [Ingham, June 1994; Oct. 1994] The first test in each series was conducted on a specimen designed to be similar to joints that saw heavy damage in the Loma Prieta earthquake. These as-built specimens exhibited brittle response with low ductility and low strength. Three more tests were performed in each series: a repair of the original specimen, a retrofit applied to duplicates of the original specimens, and new designs based on the authors' research into alternative joint force transfer mechanisms. The repair, retrofit, and new-design specimens performed better than the original specimens. Also, the alternative joint force transfer mechanism, whereby a portion of the joint compression strut was anchored by reinforcement placed in the cap beam immediately adjacent to the joint, was determined to improve the response of the joint. Tests on three tee-joint specimens at the University of California, Berkeley sought to develop retrofit strategies for older tee joints. A prestressed cap beam retrofit provided

the best joint behavior resulting in very little damage to the joint and little loss of load transfer capacity at large displacements. [Lowes, 1995]

Retrofit strategies for outrigger knee joints were investigated in tests performed at UC Berkeley [Stojadinovic, 1995]. Two initial tests of specimens similar to then-current designs, one with a long outrigger beam and the other with a short outrigger, exhibited brittle failure of the joint when the column longitudinal bars on the outside face of the knee joint split away from the joint core. The joint in the long outrigger specimen was repaired by replacing the core concrete and placing additional transverse reinforcement. This repair provided increased joint strength and prevented the bond split failure, resulting in transfer of damage to the beam while the column remained essentially elastic. Five other specimens tested two proposed upgrade strategies. The first was a “ductile” upgrade which allowed plastic hinging to occur in both the column and the beam and the second, a “strong” upgrade, concentrated yielding into a single plastic hinge in the column adjacent to the beam-column joint. Both upgrades improved upon the as-built specimen response by protecting the joint and allowing the joint to sustain greater deformations. The “strong” upgrade encased the column plastic hinge region, joint region, and the outrigger beam in steel plate and was chosen as the preferred upgrade strategy for its stability and predictability; the ductile upgrade, while successful, relied on a beam torsion mechanism that was not well understood. The tests showed that while the joints in the failed as-built specimens were still able to transfer gravity loads in their damaged state, their ability to transfer lateral forces was contingent upon preserving the integrity of the knee joint.

While the new design recommendations developed in these tests performed well, they often required large amounts of transverse reinforcement in the joint core. Prestressing of the cap beam and the use of headed reinforcement were recognized as possible ways to ease the congestion of reinforcement in the joint while still providing adequate strength and ductility. The

retrofit specimen in [Ingham, June 1994] and the new design in [Ingham, Oct. 1994] utilized post-tensioning to increase the strength and confinement of the joint with good results. In particular, shear deformation in the new design (specimen 8 in the report) was deemed insignificant by the authors and the joint was determined to have behaved elastically.

Testing on a half-scale multi-column bent investigated the resistance of a precast, prestressed cap beam and joint to brittle failure due to large principal stresses developed in the joint core [Sritharan, 1997]. The joint utilized less mild transverse reinforcement than other, similar tests but performed just as well with limited joint damage, despite joint principal compression stresses that exceeded recommended limits. Another test by researchers at UC San Diego replaced the transverse reinforcement in the joint core with headed reinforcement [Ingham, 1996; SEQAD, 1995]. Column longitudinal reinforcement was terminated with heads as well. The specimen was designed similar to test unit 7 of the earlier knee joint tests by Ingham for comparison purposes. Behavior was better than that expected by the researchers and actually exhibited less strength reduction at peak displacement cycles than the specimen detailed with standard transverse reinforcement. However, the lack of joint hoops and spirals allowed penetration of column longitudinal bar strains into the joint core, which would have resulted in anchorage failure had the bars not been terminated with heads. The authors concluded that headed reinforcement is a viable alternative to the use of hooked bars for column and beam longitudinal reinforcement but that headed bars should only be used in addition to joint hoops or spiral reinforcement that effectively confine the joint core.

A recent project at the University of California, Berkeley further investigated the performance of joints designed with headed reinforcement, this time with a combination of both conventional (spirals and hoops) and headed (used for additional vertical and horizontal joint transverse reinforcement) reinforcement [Naito, 1998; 2001]. Also, column longitudinal

reinforcement utilized headed bars instead of hooks or straight development. Performance of the new designs as compared to baseline specimens tested in the same project was deemed acceptable by the authors and the force-displacement and joint shear response envelopes of the headed specimens closely resembled those of the conventionally reinforced specimens.

Interest in the performance of the beam-column joint in double-deck bridge structures was motivated by the collapse of the Cypress Street Viaduct during the Loma Prieta earthquake. Caltrans soon initiated a study into retrofit strategies and new design recommendations for these structures. One set of tests at UC Berkeley investigated retrofits for exterior joints typical to San Francisco double-deck viaducts with columns framing into both the top and bottom of the joint [Moehle, 1993]. The first test unit, an as-built specimen, developed the expected joint shear strength of 0.42pfc' (MPa) with no signs of shear distress during the test. This specimen was repaired and strengthened with the addition of post-tensioning rods running the length of the beam and attached to the backside of the joint. The third test was a retrofit strategy consisting of a steel jacket around the joint and the column adjacent to the joint in addition to exterior post-tensioning rods as in the repaired specimen. Both specimens improved upon the behavior of the as-built specimen; the repaired unit developed larger shear strength (1.0pfc' (MPa)) but at the expense of low post-yield toughness, and the steel-jacketed retrofit developed similar maximum joint shear strength as the repaired specimen but with greater ductility and much less post-yield strength degradation.

Another series of tests on the lower-level beam-column joint of a double-deck viaduct concluded that ACI-ASCE 352 recommendations were adequate to reach the target joint shear stress levels outlined in that committee report [Mazzoni, 1997]. However, anchorage of the

column longitudinal reinforcement through the joint was an important limiting factor on the strength of the beam-column joint when subjected to larger demands than recommended by Committee 352. A joint force transfer model that explicitly accounted for the anchorage of the column longitudinal reinforcement in the joint core was developed and used to accurately model the response of the specimen.

1.1.2. Bar Elongation and Slip

Bar elongation and slip are primarily affected by the bond available between the reinforcing bar and the concrete into which it is embedded. This transfer of force is a combination of mechanisms collectively referred to as bond stress. Researchers over the years have sought to accurately determine the various mechanisms and their contributions to the aggregate bond stress quantity. The state-of-the-art report by ACI Committee 408 summarizes the research on bond under cyclic loading and discusses the bond mechanisms; the factors that affect bond strength under cyclic loads, and bond behavior under both high-cycle and low-cycle (e.g., earthquake ground motion) loading [ACI 408, 1992]. The primary bond mechanisms are chemical adhesion between steel and concrete, mechanical bearing developed between the bar deformations and concrete, and friction developed along the bar surface. Of these, bearing is the primary source of bond stress at near-ultimate loading. Bond failure occurs in one of two ways: pullout failure where the concrete between bar deformations shears away from the concrete mass and the bar slips out of the block resisted only by friction, and splitting failure of the surrounding concrete caused by tensile radial stresses caused by lug bearing forces. Splitting failure occurs when there is insufficient confinement on the concrete mass. Numerous factors affect the bond stress developed under cyclic loads, among them concrete compressive strength, cover (both on the side and end of the bar), bar size and spacing, available anchorage length, geometry of the bar deformations, steel yield strength, amount and distribution of

transverse steel (provides confinement that resists splitting failure and increases the strength of the concrete), strain range, number and amplitude of cycles, and surface condition of the bar (e.g., epoxy coatings). High- and low-cycle fatigue loading are discussed at length and the anchorage requirements of several international codes are reviewed; for bars anchored into or passing through beam-column joints subjected to low-cycle loading, the requirements of ACI-ASCE 352 are recommended.

The response of bars anchored in a confined concrete mass is of particular interest in this study because the beam-column joints of modern bridge bents are detailed with the intent of producing a well-confined joint core. Early studies sought to quantify the local bond stress-slip relationship of deformed bars embedded along a short length into confined concrete blocks [e.g., Morita, 1973; Viwathanatepa, 1979]. An extensive study by Eligehausen expanded on these works with a series of over one hundred push and pull-out specimens with the goal of determining a general relationship for the local bond stress-slip behavior of embedded reinforcing bars [Eligehausen, 1983]. The authors were particularly interested in the post-yield bond stress response and the effects of confining reinforcement, bar diameter, concrete strength, bar spacing, transverse pressure, and loading rate on the full range of bar stresses were assessed. A backbone curve that describes bar stress at all levels of slip was developed along with relationships that account for the reduction in bond stress with cyclic loading. In these and most other reports, slip is actually the combination of both bar elongation and rigid-body bar slip (displacement of the bar relative to the surrounding concrete) since it is rather difficult to separate the two modes.

These local bond stress-slip models were used extensively by later researchers to develop increasingly sophisticated analytical models of the reinforcing bar-concrete system in an attempt to accurately model the variation of bond stress along the length of a bar, the slip

occurring at the free surface of the concrete block, and the additional rotation of a column or beam adjacent to the joint due to elongation and slip of the bar. One such model uses an average pre-yield bond stress and determines post-yield bond stress based on available development length and the known bar stress [Morita, 1984]. By dividing the bar into discrete segments along its development length within the joint and solving the bond stress boundary value problem, a reasonable prediction of the distribution of bond stress along the bar can be made [Filippou, 1985]. Yankelevsky took models of each of the discrete components of bond stress and combined them with a cyclic deterioration relationship based on Eligehausen's work to predict both the monotonic pullout and cyclic response of embedded bars [Yankelevsky, 1992]. A more complicated finite element model using the flexibility method of structural analysis also gives good results and, according to the author, is computationally efficient when compared to the usual stiffness method [Monti, 1993]. Other models based on finite element analysis and fracture mechanics are available but they are more complicated than the simple model developed in this report. Also, they are not easily integrated into structural analysis programs or design procedures already in use by bridge designers.

1.2. Beam-Column Joint Tests Database

Several of the experimental test programs discussed in this chapter were cataloged thoroughly in a *Beam-Column Joint Database* included in this report as the appendix. The objective of this compilation was to collate the data from tests on bridge beam-column joints into a compact form useful to the goals of this report. To that end, only reports that included plots of joint shear stress versus shear strain were included in the database. Other tests that did not meet this requirement were previously discussed in Chapter 1.1. Each record in the database includes figures of the geometry and reinforcement detailing of the specimen. A text summary of important geometric and reinforcement quantities is also provided. Important joint shear

response quantities such as maximum joint shear stress, principal stresses, strains, and contribution of the joint deformation to overall specimen deformation are tabulated. A wide range of values for each of these quantities is observed and is discussed in detail in Chapter 2. Finally, the joint shear stress-strain hysteresis, a narrative on the test progression and results, and a description of the failure mode are presented.

A number of conclusions can be developed from a review of the database records. As expected, ductile behavior of the bridge structure depends in large part on maintaining the integrity and post-yield strength of the beam-column joint. Capacity design will fail and will not give the desired performance if inelastic deformation accumulates in the joint. Also, poor joint shear response can have a significant contribution on the displacement of the system, ranging from less than 2% (nominally elastic response) in the best cases to as much as 40% for the worst case. Note, however, that the latter value is for a joint subjected to displacements well beyond what it would be expected to sustain in many seismic event. Another expected result is that, in general, the greater the amount of reinforcement in the joint region, the better the joint response both in terms of maximum joint shear stress capacity and joint integrity at specimen failure. For specimens with well-detailed joints, failure due to buckling and subsequent fracturing of the column longitudinal reinforcement was the most common failure mode. This occurred because plastic hinging was forced into the column, as desired. In general, bridge tee and knee joints are significantly weaker than interior joints in framed structures, as the framing members provide additional confinement to the joint core.

Prestressing of the cap beam and joint shows promise as a way to reduce the amount of reinforcement in the joint and also as a method for strengthening the joint, both for retrofit and new construction. However, attention must be paid to the principal compression stresses developed in the joint so that the joint force transfer mechanism is not undermined by excessive

compression force. Use of headed reinforcement in tandem with joint hoop or spiral reinforcement results in behavior similar to joints using standard reinforcement. Also, use of headed reinforcement can be used to replace hooked bars anchoring into the joint core. Both uses of headed bars can help to reduce congestion in the joint as hooks become unnecessary.

1.3. Organization of Report

With a statement of the objectives of the research to develop simplified models for joint and hinge flexibilities, a review of the relevant literature, and a collection and interpretation of experimental data, this report is organized as follows:

- Chapter 2 presents the behavior and modeling of beam-column joints. The deformation mechanisms are presented and the model is developed. The observations and trends of the beam-column joint database are also presented.
- Chapter 3 presents the behavior and modeling of bar elongation and slip. The deformation mechanisms are presented and the model is developed.
- Chapter 4 provides a validation of models for the joint and hinges. The proposed models are compared to measured response of experimental test data. The validation is performed at both the local level and at the global level.
- Chapter 5 presents the results of the lateral-frame analysis. The effects of joint and hinge flexibilities on the static and dynamic behavior of a representative bridge bent, hence on the capacities and demands, are presented.
- Chapter 6 introduces a consistent linearization procedure recommended for seismic design of bridge frames. The development and implementation of the procedure are presented in this chapter.
- Chapter 7 is a summary of finding and recommendations for design. The summary presents the results of the research presented in the report. Recommendations for modeling within simplified design and analysis procedures are also given in the chapter.

1.4. Figures

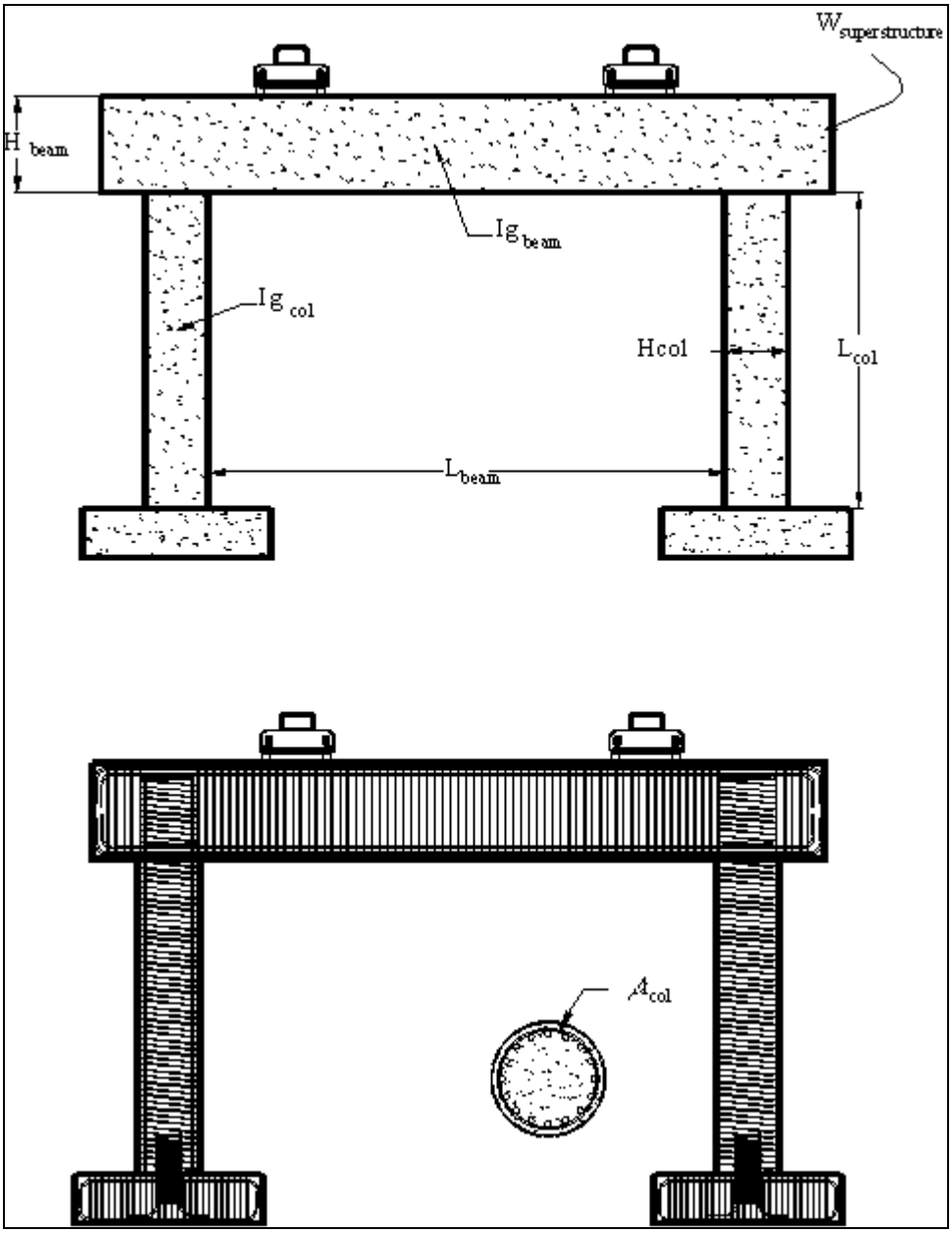

Figure 1-1: Representative Reinforced-Concrete Two-Column Bridge Bent

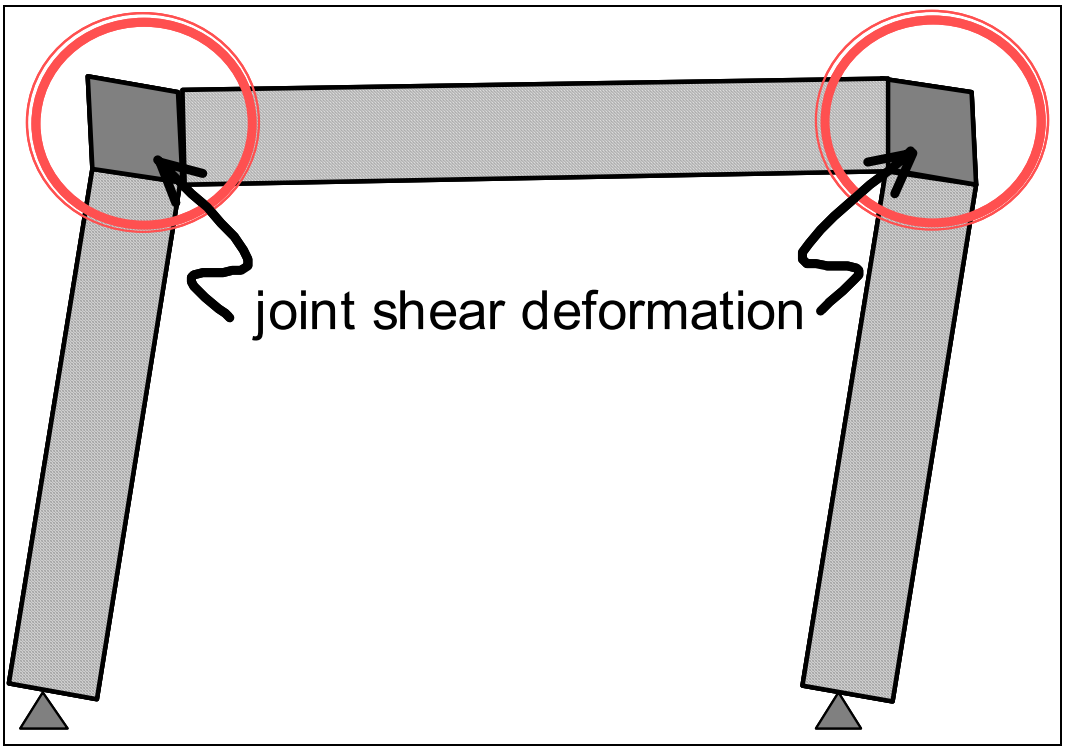

Figure 1-2: Effects of Local Joint Shear Deformation on System Lateral Deformation

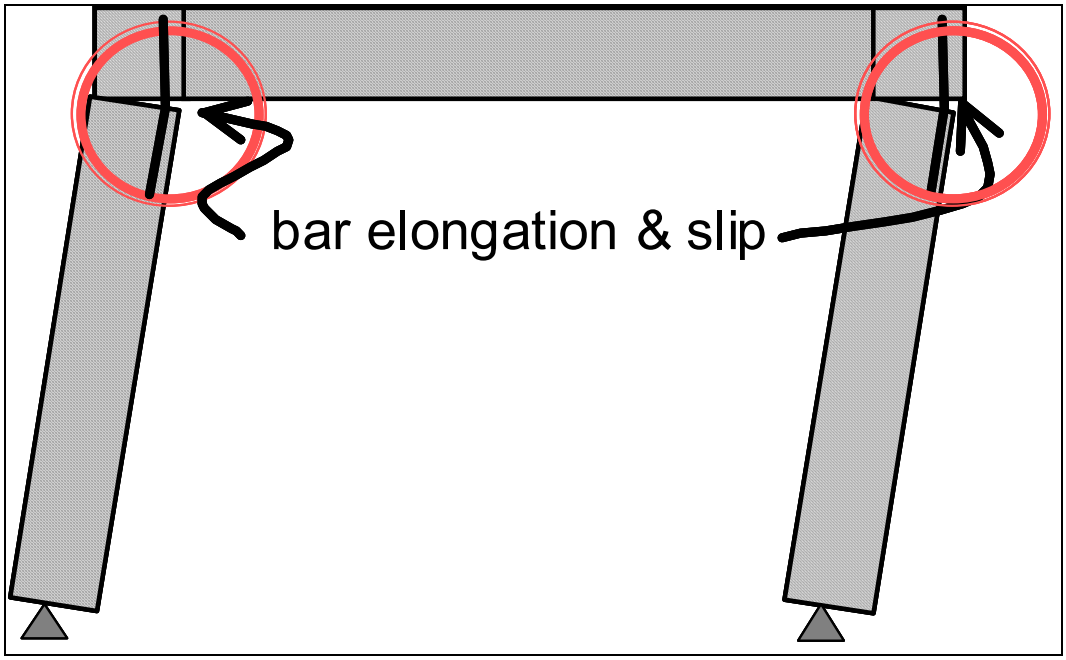

Figure 1-3: Effects of Local Elongation and Slip of Column Longitudinal Reinforcement on System Lateral Deformation

Chapter 2. Behavior and Modeling of Beam-Column Joints

In spite of the different joint configurations in new and existing bridge structures, current design and analysis methods assume rigidity and infinite strength in the beam-column connections. Beam-column joints of both building and bridge structures, however, have been studied extensively in recent years and their strength and flexibility characteristics have been documented for varied geometries, detailing, and applied forces. To sort through the data on bridge-specific tests, a database of these results was compiled with relevant details of the design objectives, response quantities, and results cataloged. From the database, trends were noted and parameters for the envelope of a nonlinear relationship for joint shear stress versus shear strain were developed. From this shear stress-strain relationship, a moment-rotation model was developed for a zero-length spring element used to represent the beam-column joint in a finite-element analysis.

2.1. Beam-Column Joint Database for Bridge Structures

While the volume of test data on beam-column joints in bridge frames is significantly smaller than that for building frames, it is still substantial enough to gain an understanding of beam-column joint behavior. To facilitate the navigation of the available test data, a database of the results of pertinent tests was compiled and is included as Appendix A. The database was used primarily for the development of the joint shear deformation model presented in this chapter, hence only those tests which provide joint shear stress and shear strain data are included. The more recent specimens were designed according to capacity design principles

where yielding and inelastic deformation are expected to concentrate in the column adjacent to the joint-column interface. The included retrofit and repair specimens were detailed to overcome original design deficiencies that prevented them from developing and sustaining a plastic hinge in the column.

Table 2-1 lists the ten records found in the database, their geometry, column type, and literature reference. The Knee-Ing series of tests were performed at UC San Diego following the Loma Prieta earthquake to examine the behavior of non-ductile joint designs prevalent in existing bridges, recommended repair and retrofit schemes for these joints, and new designs intended to improve on the as-built behavior. Knee-Ing-RCT-7 was a 1/3-scale new design specimen with two interlocking circular spirals in the rectangular column. Knee-Ing-RND-4 was a repaired specimen and Knee-Ing-RND-6 was a retrofit; both had circular, spirally reinforced columns. The DD-Maz series of tests at UC Berkeley were 1/3-scale models of the lower-level beam-column joint of a double-deck bridge. The specimens were detailed to develop and sustain joint shear stresses similar in magnitude to exterior joints found in buildings.

The Tee-Nai series investigated the use of headed reinforcement in tee joints. Headed bars replaced the additional horizontal and vertical reinforcement now used in joint designs. Also, to ease congestion of reinforcement in the joint, the column longitudinal bars were terminated with headed rather than hooks. The columns in these 3/8-scale specimens were circular and spirally reinforced. The next record, Tee-Sri-RND-IC1 was one of a series of three tests on tee joints performed at UC San Diego to evaluate new designs. The specimens in this series were 1/3-scale with circular, spirally reinforced columns and were designed so that a portion of the tension couple developed in the joint could anchor outside the joint, relieving the demand on reinforcement in the joint interior. This external joint force-transfer mechanism allowed the specimen to use straight bar anchorage for the column longitudinal reinforcement

(rather than hooks) by improving tensile anchorage conditions. Knee-Sri-Rnd-1 and Tee-Sri-Rnd-2 are the knee and tee joint, respectively, of a 1/2-scale multi-column bridge bent specimen tested at UC San Diego. The specimen was designed to further test the external joint force-transfer mechanism as in the previous specimen (IC1). To further relieve congestion in the specimen and improve beam bar anchorage, mechanical couplers were used to splice beam longitudinal reinforcement.

The records in the database include information on the geometry, design, detailing, and response of each specimen. Figures and text summaries support the quantitative data. The fields of the database are summarized in Table 2-2. The reader is directed to the literature review and appendix introduction for further information about the database and a description of other bridge beam-column joint tests that were not included. While the database was compiled with the goal of developing a shear deformation model, it should also be a useful reference for future researchers interested in determining what aspects of bridge beam-column joint behavior have already been studied and what the findings of those studies were.

2.2. Database Observations and Trends

2.2.1. Joint Classification by Strength

The shear stress-strain response envelope for all the tests in the database is shown in Figure 2-1. The individual curves can be found in the Appendix. A cursory inspection of the envelopes in the included database suggests that there is no single joint shear stress-strain envelope that can represent the behavior of all bridge beam-column joints. However, Priestley developed a model of joint shear behavior that can serve as a starting point (Figure 2-2)[Priestley, 1993]. Priestley's model relates joint principal tension stress to joint rotation (or, equivalently, joint shear strain) for an unreinforced joint. The model is based on tests on

outrigger-bent knee joints conducted at the University of California, San Diego (Knee-Ing-RCT-1 in the Appendix). The model consists of three points, the first of which corresponds to a principal tension stress of 0.29pfc' MPa (3.5pfc' psi) with an initial slope taken as the shear Modulus of concrete, G_c, based on the standard mechanics equations:

$$G_c = \frac{E_c}{2(1+\nu)} \tag{2-1}$$

Where Poisson's ratio ν equals 0.2, and E_c is the elastic Modulus of concrete given in ACI Building Code §8.5.1[ACI 318, 1999]:

$$E_c = 4733\sqrt{f_c'}(MPa) = 57{,}000\sqrt{f_c'}(psi) \tag{2-2}$$

The second slope, $G_{cracked}$, is derived from the ratio of cracked to uncracked stiffness of the joint that, according to Priestley, "can be related to the relative stiffness of the column rebar to the uncracked concrete shear stiffness:"

$$G_{cracked} = \rho_{col} E_s \tag{2-3}$$

Where ρ_{col} is the column longitudinal steel ratio and E_s is the elastic Modulus of the column longitudinal reinforcement. The result is a second slope equal to 0.3*Gc that terminates at a joint principal tension stress of 0.42pfc' MPa (5pfc' psi). The final segment is a linear descent to an ultimate shear strain of 0.01 at zero principal tension stress.

The initial cracking strength of the joint, the transition from the initial stiffness to the second, is limited primarily by the tensile strength of the concrete. When principal tensile stresses in the joint become larger than the tensile strength of the concrete, cracks form and the stiffness of the joint is reduced as shown in the second slope of the Priestley curve. In an

unreinforced joint, steel is not available to take up this additional tensile force and the eventual result is a brittle failure mode. However, for a confined joint, joint reinforcement limits the size of cracks, takes up the additional tensile force, and allows the joint to continue to deform and carry additional shear force until the steel fractures or another portion of the structure fails. The model developed in this chapter assumes a confined joint and so the latter behavior can be expected.

Though it is generally accepted that principal stresses govern the behavior of the joint and portray its behavior more accurately, it is more common in the literature to report shear stress values. Looking at Figure 2-1, three distinct groupings of joint shear stress-strain envelopes are noted and therefore three classes of behavior will be represented: the 'weak' joint, the 'intermediate' joint, and the 'strong' joint, all in reference to the relative strengths of the joints in shear. This grouping is based solely on the measured shear stress-strain response, and is not representative of design characteristics of the joint specimens. Figure 2-3 shows the envelopes and the defining points along the shear stress-strain relationships of the three models. Two other classes of non-yielding joints are also considered in the report but not shown in the figure: the elastic joint and the rigid joint. The elastic joint is a linear model defined by a single stiffness value and the rigid joint has infinite shear stiffness, transmitting forces with no associated deformation. Both classes have infinite strength and are considered as baselines for the comparison of joint behavior.

The weak joint model has low ultimate shear strength (0.42pfc' MPa) and representative specimens have moderate ductility compared to the rest of the data. The slope of the first segment of all three models is taken as G_c as in Priestley's envelope. The second segment begins at a shear stress of 0.29pfc' MPa and proceeds to the ultimate strength of 0.42pfc' MPa

on a slope of 0.1*Gc. Figure 2-4 shows the envelopes for the joint specimens classified as weak plotted with the weak model envelope. The two joints in this category were designed using the exterior joint force transfer mechanism described earlier and thus have a reduced amount of transverse reinforcement in the joint interior and straight anchorage of the column longitudinal reinforcement.

The intermediate joint model has moderate ultimate strength (0.62pfc' MPa). This model represents both tee and knee joints with moderate amounts of transverse reinforcement in the joint and favorable column longitudinal bar anchorage conditions. Like the weak model, the first segment of the intermediate model extends to 0.29pfc' MPa. The second segment has a slope of 0.1*Gc to the ultimate joint shear strength of 0.62pfc' MPa (Figure 2-5). The strong joint model exhibits the expected strength of a building exterior joint condition as determined by ACI 352 ($1.52pf_c$' MPa), about twice that of the intermediate model (Figure 2-6). The strong model represents all of the double-deck joint specimens, and one knee joint with a large quantity of joint transverse reinforcement. The first segment is defined by the same slope Gc as the others and its second segment begins at a joint shear strength of 0.62pfc' MPa. The second segment extends from this yield point to the ultimate point at 1.52pfc' MPa. The second slope value of 0.25*Gc is a compromise between the double-deck specimens which have a relatively stiff second slope and the knee joint specimens which are much less stiff post-yield. All three models are shown in the figures with a positive third slope equal to Gc/500 but other values could be

chosen to model different joint behavior after reaching the ultimate joint shear strength (e.g., a negative slope would represent strength degradation). Table 2-3 sorts the specimens contained in the database into the three strength categories. Again, it is important to note that these values are not intended to mirror the exact response of any one test but instead seek to represent the general strength characteristics of the range of joint behaviors seen in the database.

2.2.2. Comparison of Design Quantities and Joint Shear Strength

In the previous section, joints were grouped on the basis of their measured ultimate shear strength. While useful for analysis of structures for which joint shear stress-strain data is available or for comparative studies, this grouping provides no information as to what type of joints would be able to develop a particular strength. Therefore, it is useful to study the design parameters that contribute to joint shear strength in an attempt to give the designer insight into the probable behavior of the beam-column joint in a new or existing design. With this information, a more accurate analysis of the structure can be made by using the simplified methods developed in this report without having to resort to physical testing.

Several combinations of transverse and longitudinal steel contained in the joint were chosen as the design quantities to be compared to the joint strength categories for each database specimen. Knee joints and transverse-direction tests of the double-deck specimens are separated into opening and closing actions due to the expected differences in strength between the two directions. These differences are due to the variation in axial load and the strength characteristics of the closing and opening force transfer mechanisms. The first design quantity is the volumetric ratio of joint transverse reinforcement, consisting of hoops or spiral reinforcement and any additional vertical or horizontal reinforcement (e.g., hairpins or vertical stirrups). Figure 2-7 shows the relationship between this volumetric ratio and the joint shear strength category for the tests contained in the database.

The second design quantity is the volumetric ratio of transverse and column longitudinal reinforcement in the joint. This ratio is computed as:

$$\rho_t + \frac{A_{sCol}}{A_{jH}} \tag{2-4}$$

Where ρ_t is the volume ratio of transverse reinforcement, A_{sCol} is the area of column longitudinal reinforcement, and A_{jH} is the horizontal area of the joint. The second term, though calculated as an area ratio, is equivalent to a volume ratio when multiplied by the length of the column reinforcement and divided by the height of the joint, assumed for simplicity to be equivalent, thus canceling out of the equation. In all the specimens in the database, this is approximately true. Also for simplicity, hooks in the column longitudinal reinforcement are ignored. Figure 2-8 plots this second design quantity against the joint shear strength category.

Figure 2-9 shows the relationship between the third design quantity, the nominal volumetric ratio of all steel contained in the joint (transverse, column and beam longitudinal reinforcement), and the joint strength category. This volumetric ratio is computed similarly to Equation 2.3 with the same assumptions made about beam longitudinal reinforcement as for column longitudinal reinforcement:

$$\rho_t + \frac{A_{sCol}}{A_{jH}} + \frac{A_{sBeam}}{A_{jV}} \tag{2-5}$$

Where A_{jV} is the vertical area of the joint.

The data show that with an increase in the amount amounts of transverse and longitudinal reinforcement there is a corresponding increase in joint shear strength. Greater amounts of transverse steel increase the available confining stress on the joint (up to a limiting point), and a larger area of longitudinal steel, especially that in the column, induces greater maximum stresses attainable in the joint. Also, joints in double-deck structures are generally

stronger in all loading directions than knee joints or tee joints. This is due primarily to geometry; the existence of a framing member on all but one face of the joint significantly increases the confinement of the joint core, allowing the joint to withstand greater shear stresses before deteriorating. The large amount of beam longitudinal reinforcement passing through the joint might also provide some additional shear resistance to the joint.

An unexpected result was the comparative strength of tee joints to knee joints. Under both closing and opening action, the knee joints in this study are usually stronger than tee joints with similar amounts of reinforcement. There are one or two outliers, but the trends seem to hold. The single rectangular column in the study is a knee joint specimen and displays markedly different joint shear behavior than the other knee joint specimens. It has by far the largest ductility of the entire group (truncated in Figure 2-1, but extends to a shear strain as high as 0.02 for joint opening) and is stronger than all of the other knee joints. However, without comparison to other joints with similar geometry (rectangular column, interlocking spiral or hoop reinforcement in the column and joint core), it is difficult to draw conclusions or separate knee joints with rectangular columns out from those with round columns. Besides joint shear strength, the plots give no information as to the ductility of the joints. However, in some cases, this information is not available or complete due to the limited actuator excursion available in several of the test setups, or failure of other components in the test specimens before significant deformation of the joint.

2.3. Modeling of Joint Shear Behavior

Given the joint shear stress-strain envelopes, a simple model suitable for inclusion in a structural analysis program is needed. Modeling the shear flexibility as a single zero-length rotational spring, shown in Figure 2-10, is appropriate and adds only one degree of freedom to

the system for each modeled joint. The spring model is defined by characteristic points in a moment-rotation relationship corresponding to characteristic points in the joint shear stress-strain relationship. This method models only the pure shear deformation of the joint panel and ignores other modes of joint deformation such as dilation and bending. A discussion of joint deformation modes is found in the literature [Ingham, June 1994].

The shear stresses on the joint panel can be converted to bending moments, as shown in Figure 2-11. The horizontal and vertical joint shear forces (V_{jh} and V_{jv}, respectively) are equal to the joint shear stress, τ, times the joint shear area parallel to the shear force:

$$\begin{aligned} V_{jh} &= \tau\, t_j b_j \\ V_{jv} &= \tau\, t_j h_j \end{aligned} \tag{2-6}$$

Where b_j, h_j, and t_j are the joint width, height, and out-of-plane depth, respectively. The bending moments at the panel boundary are equal to the couples resulting from the joint shear forces:

$$M_j = V_{jh} h_j = V_{jv} b_j \tag{2-7}$$

As expected the two moments equilibrate each other. Hence, spring moment corresponding to a certain joint shear stress is obtained from the expression:

$$M_j = \tau(h_j b_j t_j) \tag{2-8}$$

The above expression indicates that the bending moment is equal to the joint shear stress times the volume of the joint. To simplify the model, the joint dimensions will be taken equal to the minimum dimensions of the members framing into it. For pure shear deformations, the rotation of the spring element, Θj, is equal to the joint shear strain, γ:

$$\Theta_j = \gamma \tag{2-9}$$

Thus a series of moment-rotation envelopes corresponding to the various joint-response types is obtained, as shown in Figure 2-12.

2.4. Tables

Table 5-1. Records in Beam-Column Joint Database

Designation	Geometry	Column	Reference
Knee-Ing-RCT-7	Knee	Rectangular	[Ingham, Jun 1994]
Knee-Ing-RND-4	Knee	Circular	[Ingham, Oct 1994]
Knee-Ing-RCT-6	Knee	Circular	[Ingham, Oct 1994]
DD-Maz-1	Double-Deck	Circular	[Mazzoni, 1997]
DD-Maz-2	Double-Deck	Circular	[Mazzoni, 1997]
Tee-Nai-RND-A1	Tee	Circular	[Naito, 1999, 2001]
Tee-Nai-RND-A2	Tee	Circular	[Naito, 1999, 2001]
Tee-Sri-RND-IC1	Tee	Circular	[Sritharan, 1994]
Knee-Sri-RND-1	Knee (in multi-column bent)	Circular	[Sritharan, 1997]
Tee-Sri-RND-2	Tee (in multi-column bent)	Circular	[Sritharan, 1997]

Table 5-2. Data Fields in the Beam-Column Joint Database

Field Name	Description
Geometry Figures	Joint geometry, test setup, cross sections
General	
Reference	Designation in this report (e.g., Knee-Sri-RND-1), brief bibliographic reference
Type	Knee, Tee, or Double-deck
Retrofit?	Is the joint a retrofit or not?
Column	Column geometry (rectangular, circular)
Joint	Brief description of joint
Scale	Scale of test specimen as compared to prototype
Test Objective	Performance goals for the test specimen
Test Scope	Loading protocol, test parameters
Design Philosophy	Design assumptions and goals
Specimen Details	
f_c'	Compressive strength of concrete in column, beam, and joint
Column	Size, length, reinforcement details, axial load
Beam(s)	Size, length, reinforcement details
Joint	Transverse reinforcement, additional horizontal and vertical joint reinforcement
Quantified response	Numerical response quantities (max joint shear stress, strain, max. principal stresses, percent deformation due to joint deformation)
Failure Mode	Brief description of specimen failure mode
Hysteresis Description	Plot of joint shear stress-strain (t-g) response, text description of test progression and results
Results/Conclusions	Assessment of joint behavior, importance of joint shear deformations

Table 5-3. Strength Categorization of Joint Specimens

Strength Category	Joint Specimen
(1) Weak	Knee-Sri-RND-1 (open) Tee-Sri-RND-IC1
(2) Intermediate	Knee-Sri-RND-1 (close) Knee-Ing-RND-6 (open, close)* Tee-Nai-RND-A1 Tee-Nai-RND-A2 Tee-Sri-RND-2
(3) Strong	Knee-Ing-RCT-7 (open, close) Knee-Ing-RND-4 (open, close)* DD-Maz-1 (open & close Transverse, Longitudinal) DD-Maz-2 (open & close Transverse, Longitudinal)

Table 5-4. Envelopes for Joint Strength Models

Joint Model Envelopes	Weak	Intermediate	Strong
First (Yield) Point	0.29	0.29	0.62
Second Point	0.42	0.62	1.25
First Slope	Gc	Gc	Gc
Second Slope	Gc / 10	Gc / 10	Gc / 4

Table 5-5. Categorization by Volume Ratio of All Joint Transverse Reinforcement

All Transverse Steel	Weak	Intermediate	Strong
Tee	< 1.25%	> 1.25%	?
Knee - Open	# 1%	1% - 1.5%	> 2.5% (?)
Knee - Close	?	# 1.5%	> 1.5%?
DD Transverse - Open	?	?	T
DD Transverse - Close			
DD Longitudinal			

Table 5-6. Categorization by Volume Ratio of Joint Transverse & Column Longitudinal Reinforcement

Transverse & Column Longitudinal Steel	Weak	Intermediate	Strong
Tee	< 2.5%	> 2.5%	?
Knee - Open	(outlier)	2.5% - 3%	> 3%
Knee - Close	?	2.5% - 3%	> 3%
DD Transverse - Open	?	?	T
DD Transverse - Close			
DD Longitudinal			

Table 5-7. Categorization by Volume Ratio of All Steel in Joint (excluding hooks on longitudinal bars)

All Transverse and Longitudinal Steel	Weak	Intermediate	Strong
Tee	< 4%	> 4%	?
Knee - Open	(outlier)	< 4%	> 4%
Knee - Close	?	< 4% (+ outlier)	> 4%
DD Transverse - Open	?	?	T
DD Transverse - Close			
DD Longitudinal			

2.5. Figures

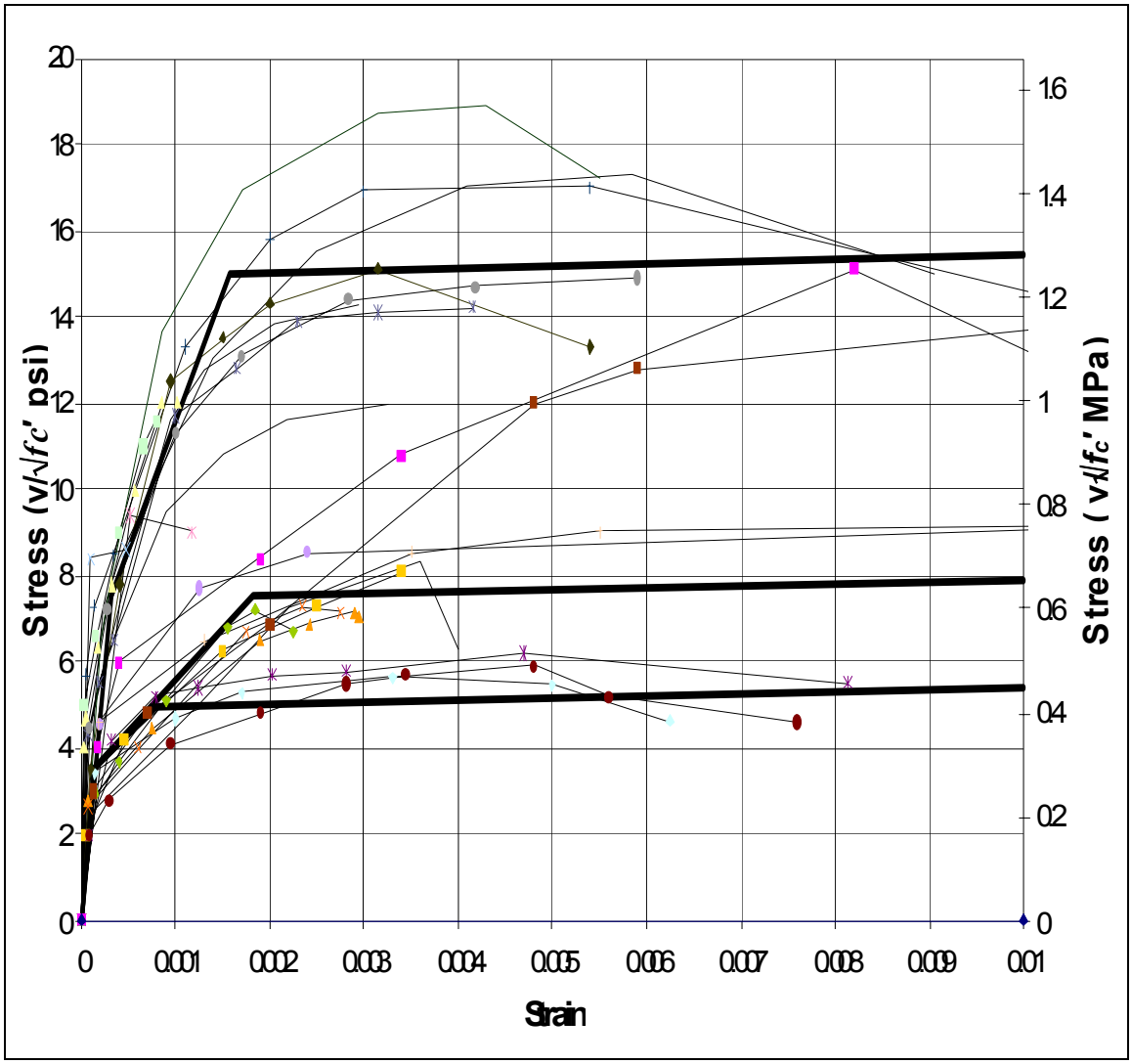

Figure 2-1: Shear Stress-Strain Envelopes for All Joint Database Specimens

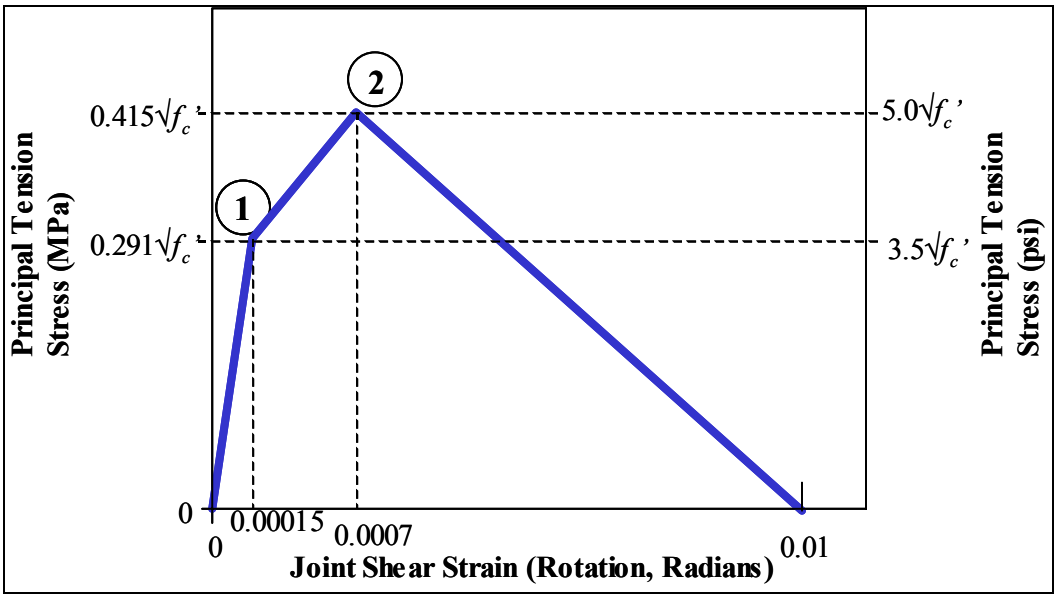

Figure 2-2: Response envelope for unconfined Joint [Priestley, 1993]

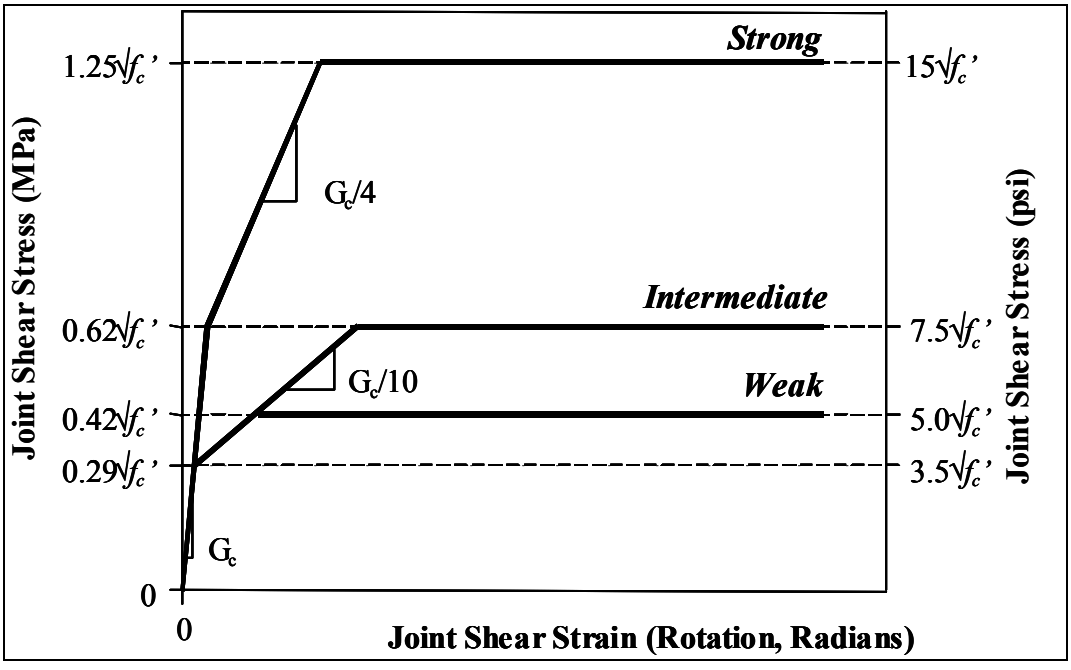

Figure 2-3: Envelopes for Categories of Joint Behavior

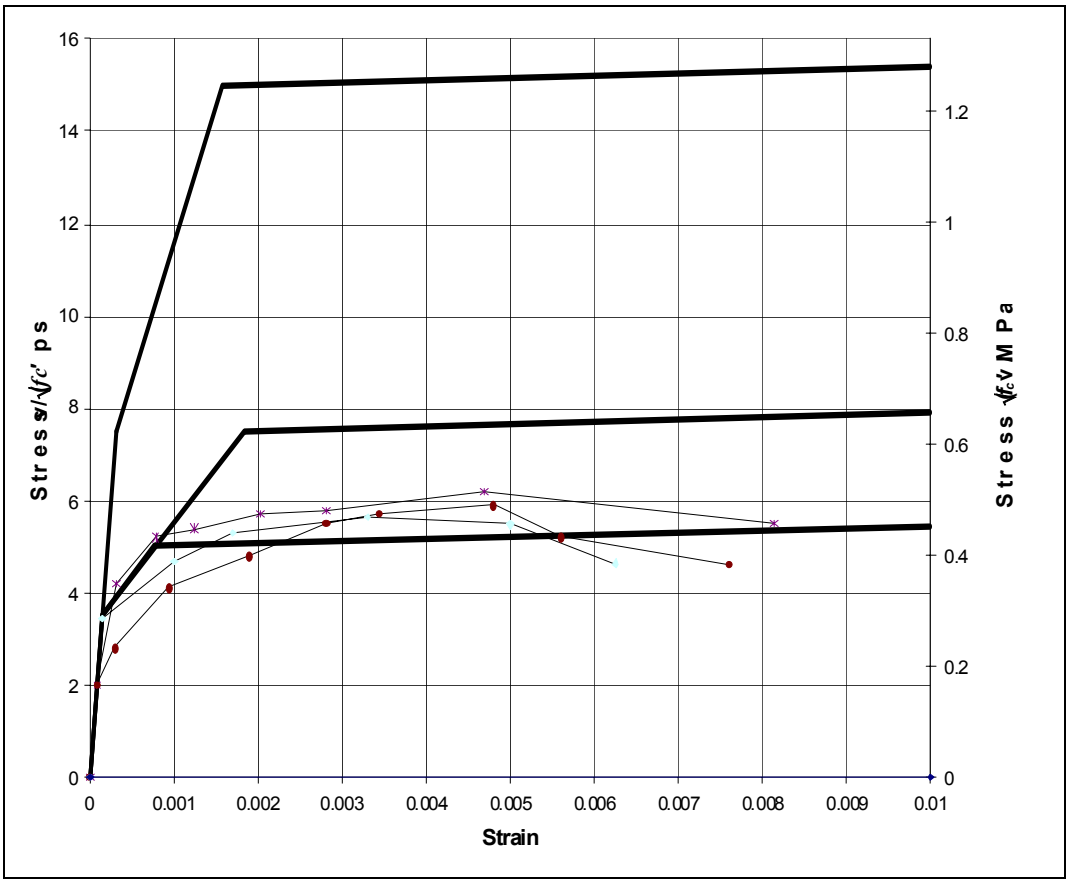

Figure 2-4: Weak Joint Shear Stress-Strain Model and Data

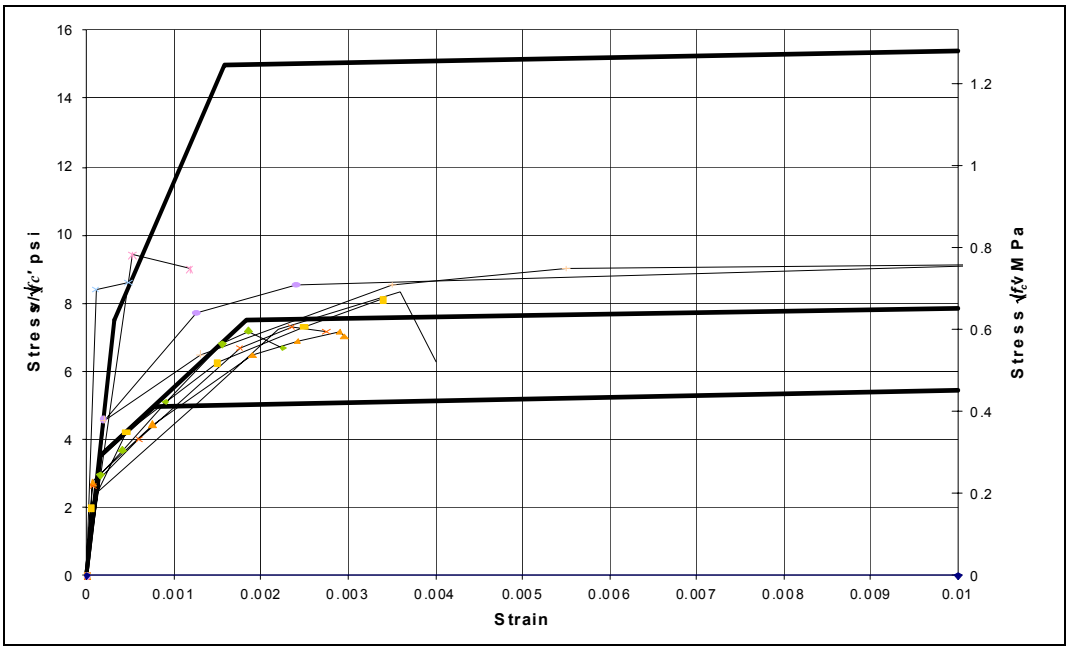

Figure 2-5: Strong Joint Shear Stress-Strain Model and Data

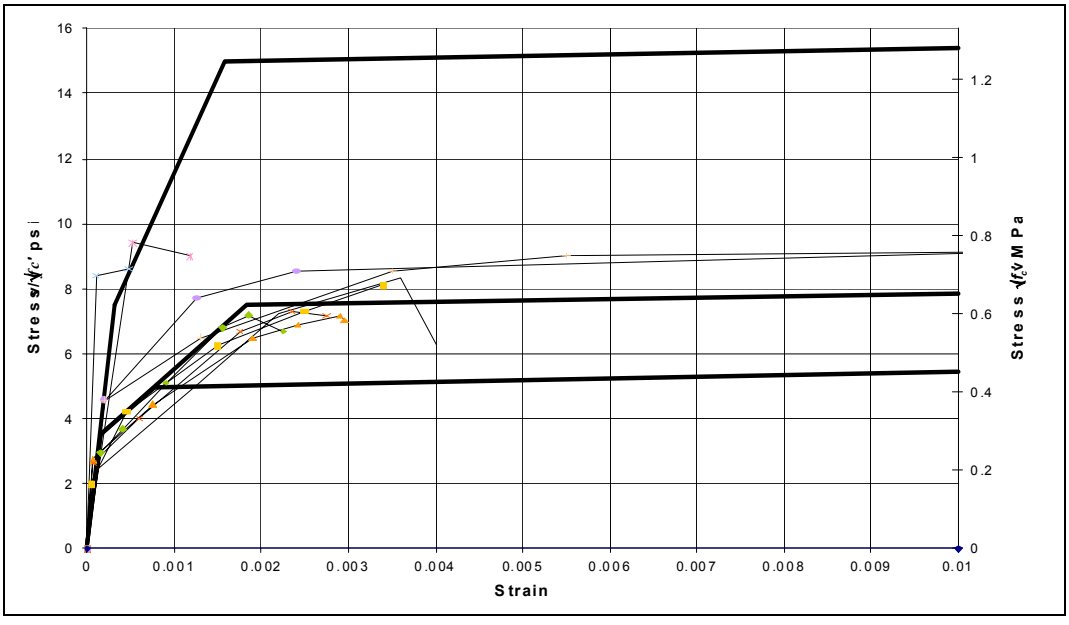

Figure 2-6: Intermediate Joint Shear Stress-Strain Model and Data

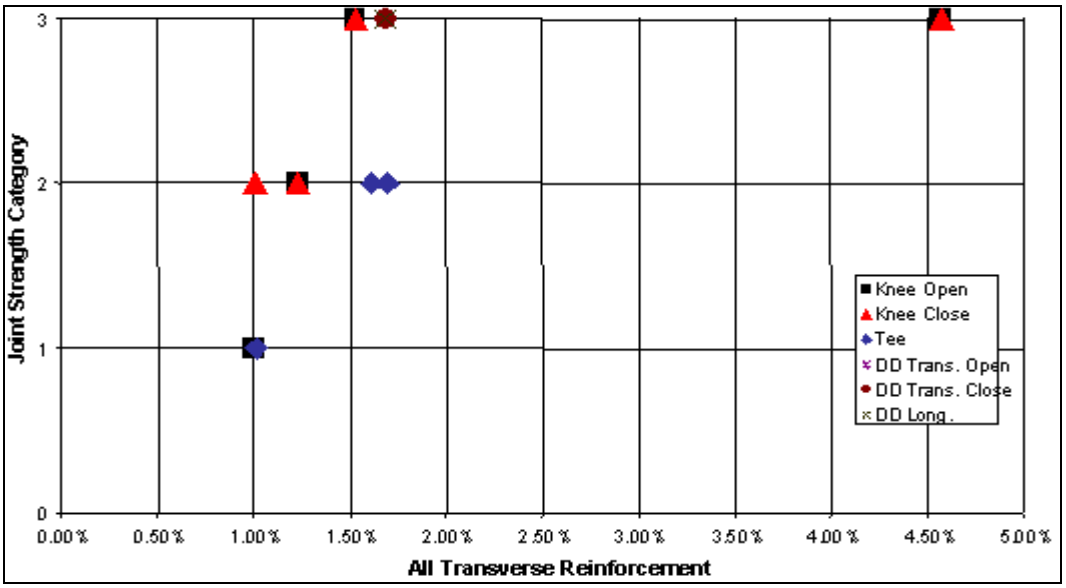

Figure 2-7: Volume Ratio of Transverse Reinforcement versus Joint Strength Category

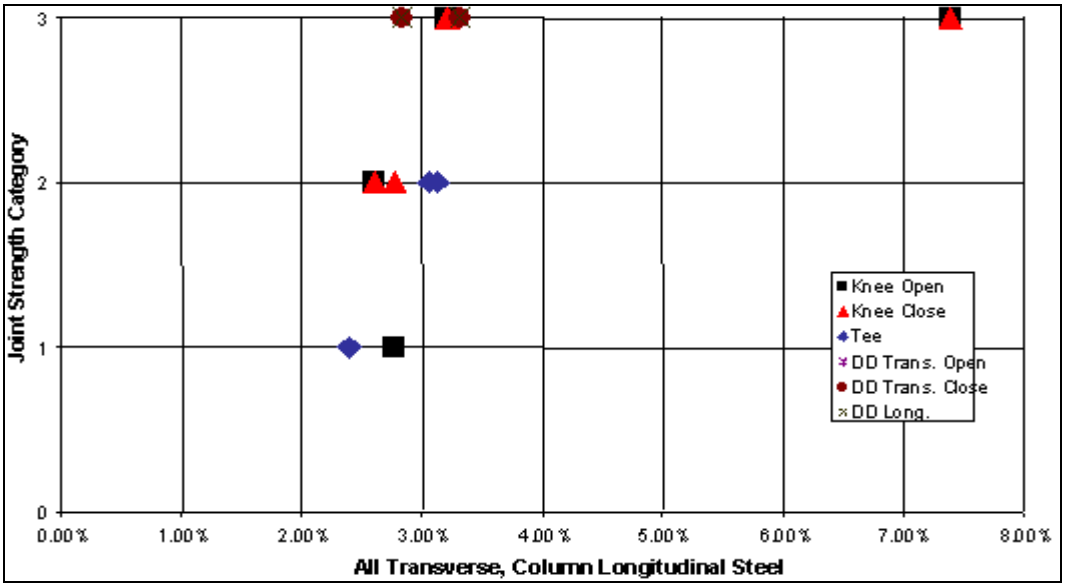

Figure 2-8: Volume Ratio of Transverse and Column Longitudinal Reinforcement versus Joint Strength Category

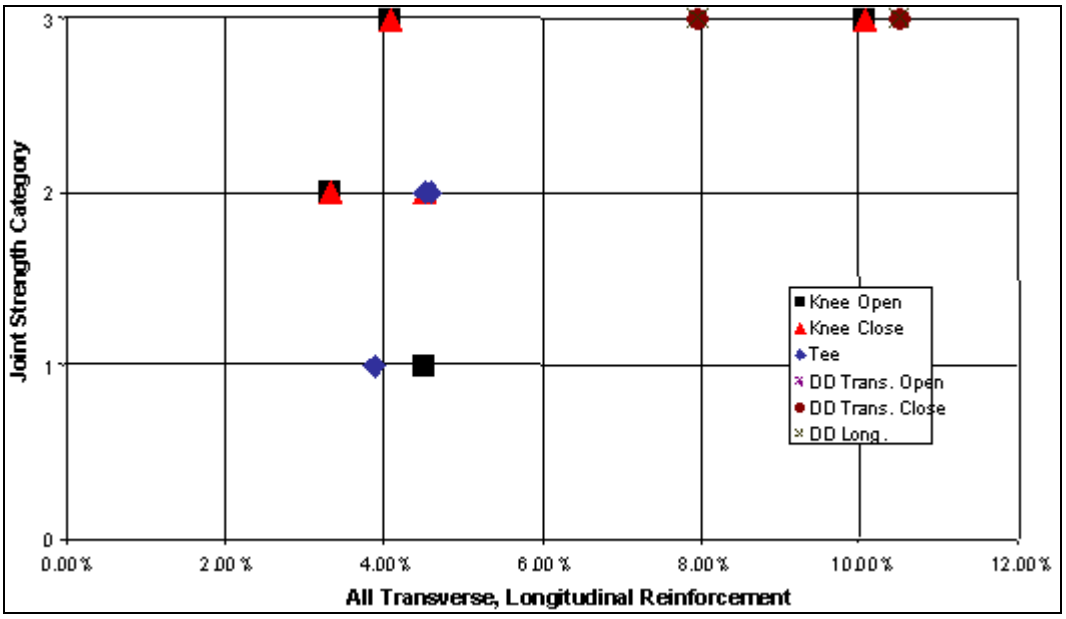

Figure 2-9: Volume Ratio of All Transverse and Longitudinal Reinforcement versus Joint Strength Category

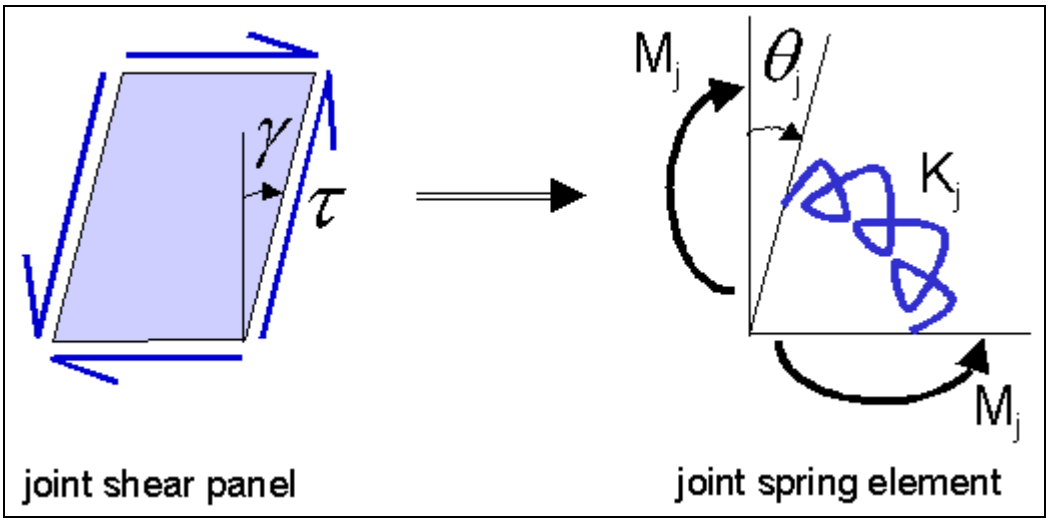

Figure 2-10: Joint Shear Deformation Model

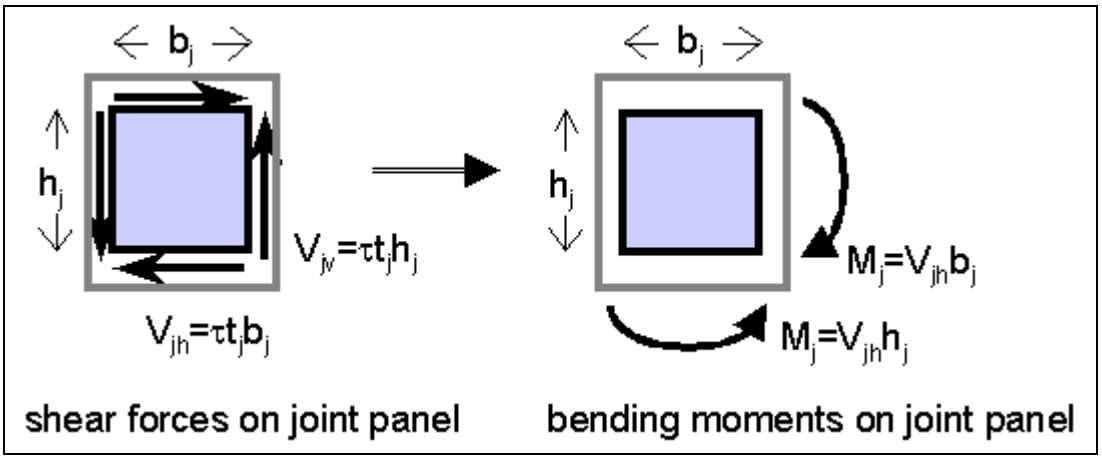

Figure 2-11: Joint panel boundary shear forces and bending moments

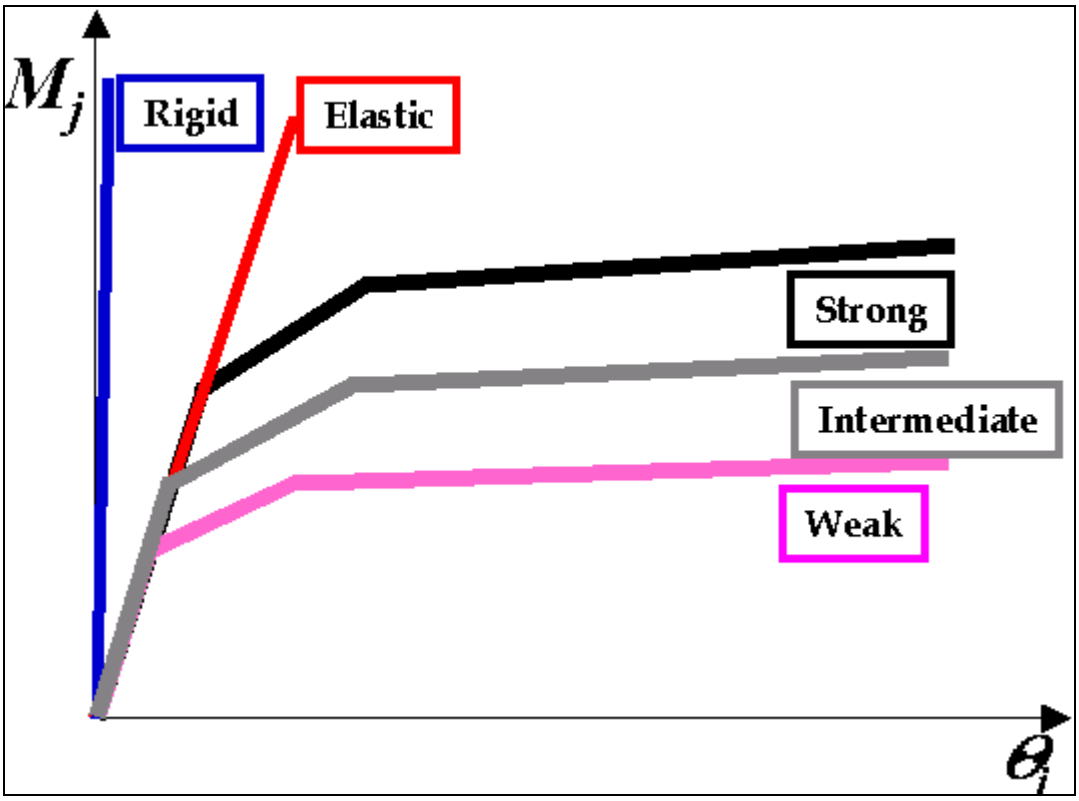

Figure 2-12: Series of moment-rotation envelopes for joint-panel spring model

Chapter 3. Behavior and Modeling of Bar Elongation and Slip

The second source of local deformations is typically referred to as "bar slip," in reality a combination of two types of deformation with common elements of resistance and a similar impact on global deformations. Bar slip is properly defined as rigid-body translation of a reinforcing bar relative to the surrounding concrete and is resisted by friction developed within the concrete. Bar elongation is the second constituent of the lump quantity "bar slip" and is defined as the total extension of a reinforcing bar at a particular point relative to the concrete. Bar elongation is often referred to as "yield penetration" since its effects are most significant once the bar yields and damages the surrounding concrete. It is due to the cumulative axial strain from the point of zero stress to the reference point. The point of reference in this study is the theoretical point of maximum tensile bar strain under flexural loading, corresponding to the extreme tension bar of the section of maximum bending moment at the column-joint interface. In bridge structures, where plastic hinges are designed to occur in the columns, the effect of both bar slip and bar elongation is a rigid-body rotation of the column section immediately adjacent to the beam-column joint, as shown in Figure 3-1. In this investigation, bar elongation is considered as the primary mode of deformation and is presented herein. The bond slip is assumed to be relatively small due to the improved anchorage conditions provided in current Caltrans detailing practice. For the case of poor anchorage conditions, the bar-elongation model can be made more flexible to account for the possible presence of bar slip.

The principal mechanism of both bar elongation and slip is the condition of bond stress: the interface between the concrete and the reinforcing bar has a finite capacity for force transfer.

Since a perfectly rigid embedment condition is not possible, especially during repeated cyclic loading into the inelastic range, whether by bar elongation or bar slip, some deformation will occur. A very brief discussion of bond stress is offered here as the topic has been studied and reviewed extensively in the literature. It is generally agreed in the literature that the development of bond stress between a reinforcing bar and concrete is the aggregate of several different mechanisms, primarily chemical adhesion between steel and concrete, friction between the steel bar and surrounding concrete, and mechanical interlock of the bar deformations with the surrounding concrete. Of the three, mechanical interlock is the most significant but the other two play important roles in both low-stress conditions (where the chemical adhesion is not yet overcome) and high-stress, high-cycle fatigue conditions (where friction is the only component still able to contribute).

Several factors influence the development of bond stress. For static loads, the standard ACI development and splice length equations (ACI 318, Chapter 12) account for concrete strength (included as pf_c'), steel yield strength f_y, bar diameter, position of the bar within the element (especially when near member surfaces), and use of epoxy coatings. When considering dynamic excitation, additional factors considered are the stress level of the bar beyond yield, the number of cycles preceding the current state, the strain level reached during these cycles, and the rate at which cycles were induced. The static factors are fairly easily accounted for. However, the interplay of the various dynamic factors is especially complex and when combined with large stresses (and the resulting large strains) common in seismic applications, approximations and generalizations of the behavior of the anchored bar are common. In that vein, a simplified model of the bond stress problem that captures a reasonable approximation of the envelope of behavior of an anchored reinforcing bar is the goal of this chapter.

3.1. Modeling Bar Elongation

The tension in the longitudinal reinforcement causing the bar elongation is the result of flexural loading at the column-joint interface. The mechanism of rotation leads the column-joint interface to behave like a hinge. Thus, together with a moment-curvature model at the column-section level, an additional moment-rotation model will be developed in this chapter. The amount of bar elongation is the result of the cumulative axial strain in the bar at the column-joint interface, where the bar stress and strain are at maximum. Based on the material stress-strain relationship, the axial strain is dependent on the distribution of stress along the anchorage length – from the point of zero stress to the point of maximum stress at the interface (Figure 3-2). This stress distribution is dictated by the bond-stress distribution and strength along the anchorage length. Rather than model each of the individual components of bond stress (adhesion, friction, and mechanical interlock), an approximation of average bond stresses is assumed and, when combined with a model of the reinforcing steel stress-strain behavior, a relationship between bar stress (or strain) and total bar elongation can be derived.

Three different bond stress distributions will be presented and developed in this section and their behavior and suitability evaluated in later sections. These three bond-stress distributions are shown in Figure 3-3. The simplest bond-stress distribution is that of a single average value of bond stress u constant along the entire bar development length. For applications where steel strains are below yield levels, this distribution is fairly reasonable and is the basis for the ACI development-length equations. However, for reinforcing bars subjected to inelastic strains, it does not account for reduced bond strength due to damage of the surrounding concrete. The second distribution, an “elastic-plastic” distribution, addresses this problem. Two constant bond-stress values are chosen, one for the portion of the bar where stresses remain below yield, u_e, and a second, lower value, u_p, for the portion of the bar that

experiences stresses above the yield level. Lastly, a linear distribution is a further refinement of the elastic-plastic distribution, taking into account the increasing damage that occurs with greater steel strains beyond yielding. The trapezoidal distribution establishes a constant bond stress value u_e along the elastic portion of the bar, then deceases it linearly to zero from the bar yield point to the point of maximum stress, at the joint-column interface.

The bar-elongation models used for all three of the bond stress distribution models depend heavily on the steel stress-strain relationship used in their derivation. It is possible to use a complex multilinear steel model like that suggested in the Caltrans Bridge Design Specification (BDS) however, for this study, a simpler linear model was desired. After an evaluation of different types of curve, a trilinear steel stress-strain relationship (Figure 3-4) was found to be ideal for the development of the hinge moment-rotation relationship. The three points that define the curve are the yield point (ε_y, f_y), initiation of strain hardening (ε_p, f_p), and ultimate (ε_u, f_u). The intermediate point (ε_{p2}, f_{p2}) lies on the line between the plastic and ultimate points and is used later in the development of the bar elongation moment-rotation model. Each of the stresses is later represented in terms of f_y and the strains, with the exception of ε_y, are given in terms of ε_u as shown in the figure.

Since the constant bond stress model is a special case of the elastic-plastic model, it will not be derived separately. In the derivation, the distribution of bar axial stress is determined from the assumed bond-stress distribution. The material properties are then used to determine the axial-strain distribution, which is then integrated along the entire development length to calculate the total bar elongation. The simplest case is that of a bar subjected to a force that causes the bar to develop a maximum stress equal to or less than f_y, the specified yield strength of steel. Because the bond stress is assumed constant along the entire length, the axial stress distribution is triangular up to the yield point (Figure 3-5) and is described by the equation:

$$f_s(x) = f_y\left(1 - \frac{x}{l_d}\right) \tag{3-1}$$

Where the origin lies at the point of maximum stress and l_d is the development length of the bar, it is derived by equilibrating the bar axial stress change and the bond stress acting on the surface of the bar along the entire development length:

$$f_y \cdot \left(\pi \cdot \frac{d_b^{\,2}}{4}\right) = l_d \cdot (\pi \cdot d_b) \cdot u_e \tag{3-2}$$

Where d_b is the nominal bar diameter. Solving for the development length:

$$l_d = \frac{d_b f_y}{4u_e} \tag{3-3}$$

In the elastic range, the triangular axial-strain distribution is obtained by dividing the bar stress by the elastic modulus, E_s:

$$\varepsilon_s(x) = \varepsilon_y\left(1 - \frac{x}{l_d}\right) \tag{3-4}$$

Taking the integral of bar strain over the development length gives total bar elongation:

$$\delta(x) = \int_0^{l_d} \varepsilon_s(x) \cdot dx \tag{3-5}$$

Substituting for l_d and working out the integral yields the final equation for δ_y, the elongation of a bar subjected to a maximum tensile stress of f_y:

$$\delta_y = \frac{1}{8} \cdot \varepsilon_y \cdot d_b \cdot \frac{f_y}{u_e} \tag{3-6}$$

The result of the local deformation mode of bar elongation is a rigid-body rotation of the member section adjacent to the beam-column joint. Therefore, it is necessary to correlate local bar elongation to its global effect, column section rotation. To simplify the problem, it is assumed that the section rotates about its mid-depth so that, given a column width of H_c, the section rotation is:

$$\theta_y = \frac{\delta_y}{H_c / 2} \tag{3-7}$$

Substituting for δ_y gives:

$$\theta_y = \frac{\varepsilon_y d_b f_y}{4 H_c u_e} \tag{3-8}$$

Figure 3-2 shows graphically the change in bar stress and the resulting bar strain and elongation as the stress in the bar increases to ultimate. The next step is to extend the relationship between bar stress and section rotation to strain levels between yield and ultimate. Instead of using continuous equations to describe this relationship, bar elongations were calculated at the defining points on the steel stress-strain curve. This procedure results in a linearized section rotation model (Figure 3-6). The post-yield rotation equations are derived similar to the yield rotation above. The resulting set of section rotation equations for the elastic-plastic steel model is (EP superscript):

$$\begin{aligned}
\theta_y^{EP} &= \frac{1}{4} \cdot \frac{d_b}{H_c} \varepsilon_y \frac{f_y}{u_e} \\
\theta_p^{EP} &= \theta_y^{EP} + \frac{1}{4} \cdot \frac{d_b}{H_c} \cdot \left(\varepsilon_y + \gamma_1 \cdot \varepsilon_u\right) \cdot \left(\alpha_1 - 1\right) \cdot \frac{f_y}{u_p} \\
\theta_{p2}^{EP} &= \theta_y^{EP} + \frac{1}{4} \cdot \frac{d_b}{H_c} \cdot \left[\left(\varepsilon_y + \gamma_1 \cdot \varepsilon_u\right) \cdot \left(\alpha_1 - 1\right) + \varepsilon_u \cdot \left(\gamma_1 + \gamma_2\right) \cdot \left(\alpha_2 - \alpha_1\right)\right] \frac{f_y}{u_p} \\
\theta_u^{EP} &= \theta_y^{EP} + \frac{1}{4} \cdot \frac{d_b}{H_c} \cdot \left[\left(\varepsilon_y + \gamma_1 \cdot \varepsilon_u\right) \cdot \left(\alpha_1 - 1\right) + \varepsilon_u \cdot \left(1 + \gamma_1\right) \cdot \left(\alpha_3 - \alpha_1\right)\right] \frac{f_y}{u_p}
\end{aligned} \tag{3-9}$$

Equations for the constant bond stress moment-rotation model are easily derived from the elastic-plastic model by replacing u_p and u_e with a single value of bond stress u and solving for the new rotation values.

The derivation for the Linear bond stress model proceeds in a similar fashion to the elastic-plastic model (L superscript):

$$\theta_y^L = \frac{1}{4}\cdot\frac{d_b}{H_c}\cdot\varepsilon_y\cdot\frac{f_y}{u_e}$$

$$\theta_p^L = \theta_y^L + \frac{1}{3}\cdot\frac{d_b}{H_c}\cdot(\alpha_1 - 1)\cdot(\varepsilon_y + 2\cdot\gamma_1\cdot\varepsilon_u)\cdot\frac{f_y}{u_e}$$

$$\theta_{p2}^L = \theta_y^L + \frac{d_b}{H_c}\cdot\left[\gamma_1\cdot\varepsilon_u\cdot(\alpha_2 - 1) - (\gamma_1\cdot\varepsilon_u - \varepsilon_y)\cdot\frac{1}{3}\cdot\frac{(\alpha_1 - 1)^2}{\alpha_2 - 1}\right. \tag{3-10}$$

$$\left. + \varepsilon_u\cdot(1 - \gamma_1)\cdot\left(\frac{(\alpha_2 - \alpha_1)^2}{\alpha_3 - \alpha_1} - \frac{1}{3}\cdot\frac{(\alpha_2 - \alpha_1)^3}{(\alpha_3 - \alpha_1)\cdot(\alpha_2 - 1)}\right)\right]\cdot\frac{f_y}{u_e}$$

$$\theta_u^L = \cdot\theta_y^L + \frac{d_b}{H_c}\cdot\left[\gamma_1\cdot\varepsilon_u\cdot(\alpha_1 - 1) - (\gamma_1\cdot\varepsilon_u - \varepsilon_y)\cdot\frac{1}{3}\cdot\frac{(\alpha_1 - 1)^2}{\alpha_3 - 1} + \varepsilon_u\cdot(\alpha_3 - \alpha_1)\right.$$

$$\left. + \varepsilon_u\cdot(\gamma_1 - 1)\cdot\frac{1}{3}\cdot\frac{(\alpha_3 - \alpha_1)^2}{\alpha_3 - 1}\right]$$

We now have an expression for the section rotation θ in terms of various stress, strain, and geometric quantities. A moment-curvature analysis of the column section at the joint interface not only yields a relationship between section moment and section curvature and also the strain state of the outermost compressive and tensile fibers. Thus, we can link the section rotation to the section moment through the steel stress-strain model. To further simplify the process, a linearized form of the moment-curvature relationship is used with three characteristic points: yield, nominal, and ultimate (Figure 3-7). The yield point (ϕ_y, M_y) is reached when the outermost column longitudinal bar yields in tension. The nominal point (ϕ_n, M_n) is defined at the nominal moment capacity of the section as defined in ACI 318 and is reached when the outermost concrete compressive fiber reaches a strain of ε_c=0.003. The ultimate condition (ϕ_u, M_u) is defined as the point at which the outermost fiber of the confined concrete core reaches a limiting compressive strain ε_{cu}. The Mander model for confined concrete used in this study defines this limiting strain as the minimum of two values,

$$\theta_y^L = \frac{1}{4}\cdot\frac{d_b}{H_c}\cdot\varepsilon_y\cdot\frac{f_y}{u_e}$$

$$\theta_p^L = \theta_y^L + \frac{1}{3}\cdot\frac{d_b}{H_c}\cdot\left(\alpha_1 - 1\right)\cdot\left(\varepsilon_y + 2\cdot\gamma_1\cdot\varepsilon_u\right)\cdot\frac{f_y}{u_e}$$

$$\theta_{p2}^L = \theta_y^L + \frac{d_b}{H_c}\cdot\left[\gamma_1\cdot\varepsilon_u\cdot\left(\alpha_2 - 1\right) - \left(\gamma_1\cdot\varepsilon_u - \varepsilon_y\right)\cdot\frac{1}{3}\cdot\frac{\left(\alpha_1 - 1\right)^2}{\alpha_2 - 1}\right. \tag{3-11}$$

$$\left. + \varepsilon_u\cdot\left(1 - \gamma_1\right)\cdot\left(\frac{\left(\alpha_2 - \alpha_1\right)^2}{\alpha_3 - \alpha_1} - \frac{1}{3}\cdot\frac{\left(\alpha_2 - \alpha_1\right)^3}{\left(\alpha_3 - \alpha_1\right)\cdot\left(\alpha_2 - 1\right)}\right)\right]\cdot\frac{f_y}{u_e}$$

$$\theta_u^L = \cdot\theta_y^L + \frac{d_b}{H_c}\cdot\left[\gamma_1\cdot\varepsilon_u\cdot\left(\alpha_1 - 1\right) - \left(\gamma_1\cdot\varepsilon_u - \varepsilon_y\right)\cdot\frac{1}{3}\cdot\frac{\left(\alpha_1 - 1\right)^2}{\alpha_3 - 1} + \varepsilon_u\cdot\left(\alpha_3 - \alpha_1\right)\right.$$

$$\left. + \varepsilon_u\cdot\left(\gamma_1 - 1\right)\cdot\frac{1}{3}\cdot\frac{\left(\alpha_3 - \alpha_1\right)^2}{\alpha_3 - 1}\right]$$

Where f_{sy} is the steel yield strength, ε_{su} is the steel ultimate strain, ρ_s is the volumetric steel ratio of transverse reinforcement, and F_{co} is the compressive strength of concrete [Mander, 1988].

Given the moment-curvature relationship, the outermost column longitudinal bar in tension is taken as the reference point for elongation calculations. The section is assumed to remain planar and therefore the rigid-body rotation of the entire section can be determined from two values, the elongation of the outermost bar and the rotation arm (half the column depth as previously stated). The steel stress at each of the three points is determined and the rotation values θ_y, θ_n, and θ_u are calculated by linear interpolation between the points in the bar stress-section rotation relationship derived above. Note again that two analyses are required: the first defines a generic bar stress-section rotation model based solely on an assumed bond stress distribution and bar stress-strain relationship. The second is an analysis of a particular concrete member section for moment-curvature. Combining the two yields a section moment-rotation relationship corresponding to the effects of bar elongation.

A summary of the procedure is given as follows:

1) Develop bar stress-section rotation model by calculating section rotations in terms of bar stress at the defining points (e.g., f_y, f_p) of the linearized bar stress-strain curve.

2) Calculate the column section moments-curvature relationship.

3) With the moment-curvature relationship, determine the outermost reinforcing bar strain at yield, nominal, and ultimate section curvatures, assuming a linear strain distribution across the member section.

4) Given bar strains at yield, nominal and ultimate section curvatures, calculate outermost bar stress from steel stress-strain relationship.

5) Interpolate on general bar stress-rotation curve (from step 1 above) to determine section rotation at yield, nominal, and ultimate moments: these values of section moment and rotation define the final linearized moment-rotation model for the specific column section under consideration.

Note that θ_{xy} in the bar stress-rotation relationship is equivalent to the final value θ_y in the moment- rotation relationship because both are defined by the yield point of the reinforcing steel. However, θ_{xu} (ultimate rotation from the bar stress-section rotation model, defined by yield of the steel reinforcing bar; "x"-superscript denotes the steel model type, "L" for linear, "EP" for elastic-plastic) is NOT equivalent to θ_u in the final moment-rotation model. θ_u is defined by the limiting value of concrete strain in the column section (per the Mander model) and will generally be less than θ_{xu}, the maximum possible section rotation caused when the outermost bar reaches the fracture point as defined in the steel stress-strain curve.

3.2. Comparison and Verification of Moment-Rotation Models

The numerical models were compared to physical measurements to evaluate the performance of the model and to compare the effect of different steel and bond stress models on the final moment-rotation model. Two experimental tests were used in the evaluation. One test was on the lower-level beam-column connection of a double-deck bridge structures [Mazzoni, 1997]. The second test was on a cantilever bridge column [Lehman, 1998]. The two tests represent different types of longitudinal-reinforcement anchorage: the column longitudinal

reinforcement of the first test set is continuous through the beam-column joint; the longitudinal reinforcement of the cantilever column is anchored with standard hooks into the footing, which is not loaded. The test specimen characteristics are summarized in Table 3-1 and Figure 3-8.

In physical tests it is often difficult to separate the flexure deformation and the bar-slip rotation at the column-joint interface, thus the measurements are combined. To separate the deformation modes, the numerical moment-curvature was validated using the flexural-deformation measurements taken at a section away from the interface. Once the validity of this model was verified, the measured and numerical combined flexure and bar-elongation measurements were compared for the section at the interface. The physical tests done by Mazzoni and by Lehman were selected since they presented the data necessary for the comparison. Tests that were otherwise attractive could not be used because moment- rotation data was not included in the final report (e.g., [Sritharan, 1996], [Sritharan, 1997], [Naito, 2000]).

Several options for components of the moment-rotation model have been presented in earlier sections, specifically the steel model (bilinear vs. trilinear stress-strain relationship) and the choice of three different bond-stress models, constant bond stress, elastic-plastic, and trapezoidal. All moment-curvature calculations use a Mander confined concrete model for the core concrete, a Todeschini unconfined concrete model for cover concrete, and one of the two linearized steel models using generic stress and strain properties as noted in Table 3.2. Following is a comparison of the results of using the different steel models, then a comparison of bond models, and finally an evaluation of the full moment-rotation relationship.

3.2.1. Comparison of Steel Models

Specimens M1a and L415 were used to compare the effect of the steel model on the moment- curvature response and moment-rotation due to bar elongation. A set of figures (Figure

3-10, Figure 3-9, Figure 3-12, Figure 3-11) shows the hysteresis curves as presented in the test reports overlaid with the results of moment-curvature analysis and moment-rotation analysis by the proposed procedure. Table 3-8 lists the geometric parameters used for the analysis. The last column specifies two non-dimensional parameters α_e and α_p, which are multiplied by the square root of the nominal concrete strength to yield the bond-stress value used. These multipliers, α_e and α_p, represent the bond stress in the elastic region and the post-yield region, respectively, as shown in Figure 3-3. For the "M" series, a weak bond stress model was selected since the column longitudinal reinforcement is subjected to tension on one side of the joint and compression on the other, while the joint was subjected to shear deformations well into the inelastic region. The with bond stress values of α_e=1.25 and α_p=0.5 (where the nominal concrete strength was given in MPa) were, therefore, chosen for these tests.

Similarly, for the "L" series a strong bond stress model is specified with values of α_e=2.5 and α_p=1.25. These larger values were chosen to reflect the higher quality anchorage available due to the use of hooked column longitudinal bars and the non-loaded footing. Tests by Eligehausen suggested that bond stress values as high as 2.5 pfc' (MPa) are attainable for bars cast in well-confined concrete blocks. For the weak model, the quantity 1.25 pf_c' (MPa) yields acceptable results, as presented later in this chapter. The value u_p=0.5 pf_c' (MPa) is roughly the same as that used in the ACI development length and splice equations and seems reasonable for a bar cast in poorly confined or damaged concrete.

The elastic-plastic bond model was used for this comparison but similar results would be found for the trapezoidal or constant bond stress models. It is first noted that there is very little

difference for either specimen between the moment-curvature or moment-rotation envelopes resulting from use of the trilinear or bilinear steel model. As expected, the bilinear model is more flexible post-yield since, for all stresses beyond yield, the bilinear model yields a larger strain and therefore a larger bar elongation and corresponding section rotation. The stiffer post-yield result of the trilinear model is more in keeping with the trend of the data and, because there is little added difficulty in using it, the trilinear steel model is chosen over the bilinear steel model for this study.

3.2.2. Comparison of Constant Bond Stress and Elastic-Plastic Bond Models

The elastic-plastic bond stress model as used in the previous section already shows promising results. It yields a fair representation of the initial branch of both the moment-curvature and moment-rotation curves and, while slightly underestimating the curvature and rotation for specimen L415, the slope of the three segments have a general trend at the correct stiffness. The constant bond stress model is a theoretically weaker model because it accounts for damage to the bond mechanism through gross averaging. To properly account for damage in the post-yield region where most of the bar elongation takes place, the constant bond stress value u would have to be chosen very close to the post-yield value used in the elastic-plastic model. While the overall trend would be reasonable, the pre-yield elongation will be overestimated. This error might not be very large or even significant but, similar to the comparison of using a bilinear or trilinear steel model, the added complexity of deriving equations for the elastic-plastic model is minimal and appears to yield better results. The elastic-plastic model still uses averaging to account for damage and the variability in bond stress along the length of the bar but is somewhat more refined in that it considers the two different areas separately. Figure 3-13 shows a comparison of moment-rotation using the constant bond stress model and the elastic-plastic model for specimen M1a using a constant bond stress value of 1.25 pf_c' (MPa) and the same

values as earlier for the elastic-plastic model. Moment-curvature is not presented because the bond model does not effect the calculation of curvature.

3.2.3. Comparison of Elastic-Plastic and Trapezoidal Bond Models

The theoretical advantage of the trapezoidal model over the elastic-plastic model is that it more closely approximates the actual bond stress distribution found in a reinforcing bar anchored in a confined concrete block. However, this comes at the expense of a more complicated derivation and longer equations. Comparisons will show little difference in the range of stresses encountered by the reference bar in the specimens reviewed here. Figure 3-14 compares the bar elongation (normalized to the bar diameter d_b) vs. bar strain behavior of the two models and shows that, for strains less than the plastic strain ε_p, the models have very similar results and are identical until yield. After reaching ε_p, they diverge more significantly and for all values of strain greater than ε_p, the trapezoidal model yields an increasingly larger bar elongation as the strain approaches ε_u.

Using a different pair of specimens, Figure 3-16 and Figure 3-18 show this expected behavior: a less rigid moment-rotation response for strains beyond yield for the trapezoidal model. (Figure 3-15 and Figure 3-17 show the Moment-Curvature data with the envelope calculated for this study) The models yield similar results; for the bond stress values chosen here, the trapezoidal model will always have larger rotations, but in this case not significantly greater. A significant advantage of the elastic-plastic model is that it allows more flexibility to customize the two regions of the bar whereas, with the trapezoidal model, the choice of ue defines the entire model. Based on the specimen comparison, the somewhat simpler equations, and the advantage of more closely controlling the model through choice of appropriate bond stresses, the elastic-plastic model is preferred for this study. A set of figures (Figure 3-19, Figure 3-20, Figure 3-21, Figure 3-22, Figure 3-23, Figure 3-24) give moment-curvature and moment-

rotation comparisons using the trilinear steel model and elastic-plastic bond model for the specimens not already presented. (L430, M1b, M2b) The results are not perfect but for such general models of steel and bond they are promising. The moment- rotation curve follows the envelope of the test data in all cases and represents the stiffness of the data in the strain-hardening range reasonably well. The results could be tailored for each individual test by looking more closely at the bond conditions and more accurately representing the steel model but such effort would betray the goal of this study which is to produce a simplified model that performs reasonably well for a range of cases.

3.2.4. Discussion of Development Length

We have so far ignored discussion of the development lengths generated by the proposed models as compared to that actually available in the comparison specimens. While the approximate methods used here will almost never yield an accurate development length, it seems important that development lengths are not grossly over- or under-estimated; otherwise, and lacking strong evidence to the contrary, the model would not make sense. The equations for development length are derived by equating the total bond stress along the length of the bar and the total bar force and then solving for the development length, l_d. For the elastic-plastic bond model, l_d is for stresses greater than yield, where f_{smax} is the stress in the steel bar at ultimate section curvature. For the seven specimens considered in this chapter, Table 3-3 compares the development lengths obtained from the above formulas with the lengths physically available for bar development. Unfortunately, the anchorage for both series of tests is not straight as assumed in the proposed model. The “M” series longitudinal bars are part of a double-deck structure and are therefore subjected to push-pull loading and must develop both in compression and tension through the joint depth. Therefore, effectively half of the joint depth is available for development of each column’s bars and thus, the proposed model predicts much larger

development lengths than are available. However, the model is intended to be simple and is only an average of the aggregate behavior at the joint interface. The model assumes that the full rotation occurs due to elongation of the bar developing in the joint whereas in reality, the column is subjected to inelastic deformations at the joint interface and this region outside the joint could very well contribute to the rigid-body rotation.

The “L” series predicts much smaller development lengths than are physically available in the joint. The specimen’s bars are anchored with hooks and therefore offer much better anchorage than with a straight-bar development. The bond stress parameters were chosen based on this expected condition and result in a reasonable approximation of the moment-rotation behavior. However, they do not adequately predict the development conditions. Given these two sets of results, it is concluded that more investigation and comparison to tests with straight bar development are needed to adequately evaluate the problem of development length. However, the proposed model behaves well given its limitations.

3.3. Conclusions

Figure 3-25 compares two moment-rotation envelopes; one consisting only of flexural deformations and one that adds the contribution of bar elongation, to the data from specimen M1a. From this plot it can be seen how significant the contribution of bar elongation can be to the overall stiffness characteristics and deformation behavior of a structure. An analysis could easily underestimate the demands and capacities of a structure by ignoring these contributions.

The model recommended in this chapter consists of a trilinear steel stress-strain relationship and a linearized moment-rotation model based on a two-parameter “elastic-plastic” bond stress distribution. Equations were also developed for a single parameter “trapezoidal”

bond stress distribution and a bilinear steel stress-strain relationship. The proposed model is easily implemented and yields promising results.

3.4. Tables

Table 5-1. Parameters of Tests Used in Verification of Moment-Rotation Model

Specimen Mark	**H_c** (cm)	**P_{dl}/A** (%)	ρ_R (%)	ρ_s (%)	**Bar Size**	**f_c' (MPa)**	α_e / α_p **(MPa)**
M1a	55.9	5.73	1.3	0.91	# 5	35.2	1.25 / 0.5
M1b	55.9	5.31	1.3	0.91	# 5	37.9	1.25 / 0.5
M2a	55.9	5.98	1.85	0.91	# 6	37.9	1.25 / 0.5
M2b	55.9	5.30	1.85	0.91	# 6	42.7	1.25 / 0.5
L407	61	7.56	0.75	0.67	# 5	29.6	2.5 / 1.25
L415	61	7.39	1.5	0.67	# 5	30.3	2.5 / 1.25
L430	61	7.06	3.0	0.67	# 5	31.7	2.5 / 1.25

"M" series: [Mazzoni, 1997]; "L" series: [Lehman, 1998]

H_c: column depth

P_{dl}/A: Axial load to cross-sectional area ratio

ρ_R: longitudinal-steel ratio

ρ_s: transverse-steel ratio

f_c': concrete compressive strength

Table 5-2. Steel Model Parameters

Point	**Stress**	**Value**		**Strain**	**Value**
Yield (ε_y, f_y)	f_y	483 MPa (70 ksi)		ε_y	f_y / E_s
Plastic (ε_p, f_p)	$\alpha_1 \cdot f_y$	$\alpha_1 = 1.25$		$\gamma_1 \cdot \varepsilon_u$	$\gamma_1 = 1/3$
Intermediate Plastic (ε_{p2}, f_{p2})	$\alpha_2 \cdot f_y$ $\alpha_3 \cdot f_y$	interpolated		$\gamma_2 \cdot \varepsilon_u$	$\gamma_2 = 2/3$
Ultimate (ε_u, f_u)		$\alpha_3 = 1.5$		ε_u	0.1

Table 5-3. Summary of Development Length Results

Specimen	Elastic-Plastic	Trapezoidal	Available	ε_{smax}	f_{smax}
M1a	50.1 cm (19.7 in)	45.3 cm (17.8 in)	66 cm /2 * (26 in / 2)	0.066	662 MPa (96.1 ksi)
M1b	47.8 cm (18.8 in)	43.3 cm (17.0 in)	66 cm /2 (26 in / 2)	0.064	659 MPa (95.8 ksi)
M2a	54.6 cm (21.6 in)	49.7 cm (19.6 in)	66 cm /2 (26 in / 2)	0.054	642 MPa (93.0 ksi)
M2b	51.1 cm (20.1 in)	46.5 cm (18.3 in)	66 cm /2 (26 in / 2)	0.053	639 MPa (92.7 ksi)
L407	24.1 cm (9.5 in)	24.1 cm (9.5 in)	~59cm + hook** (~22" + hook)	0.061	653 MPa (94.8 ksi)
L415	17.7 cm (8.9 in)	17.7 cm (8.9 in)	~59cm + hook (~22" + hook)	0.048	630 MPa (91.4 ksi)
L430	20.7 cm (8.1 in)	20.7 cm (8.1 in)	~59cm + hook (~22" + hook)	0.035	607 MPa (88.0 ksi)

Notes:

* - The notation “66cm /2" indicates that the bar was subjected to push-pull loading and that, while the joint depth is 66cm, only ½ that amount is available for development from either side of the joint.

** - The “L”-series column longitudinal bars are hooked with a straight development portion of roughly 59 cm (22 in).

3.5. Figures

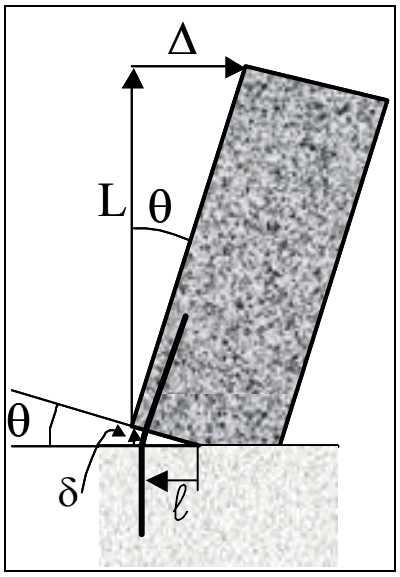

Figure 3-1: Column Rotation due to Bar Elongation

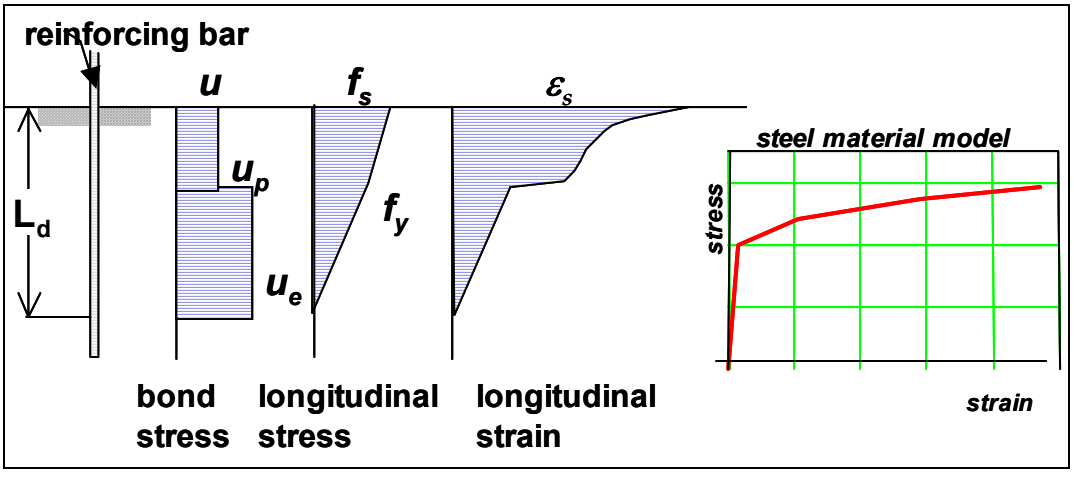

Figure 3-2: Bar anchorage-zone characteristics

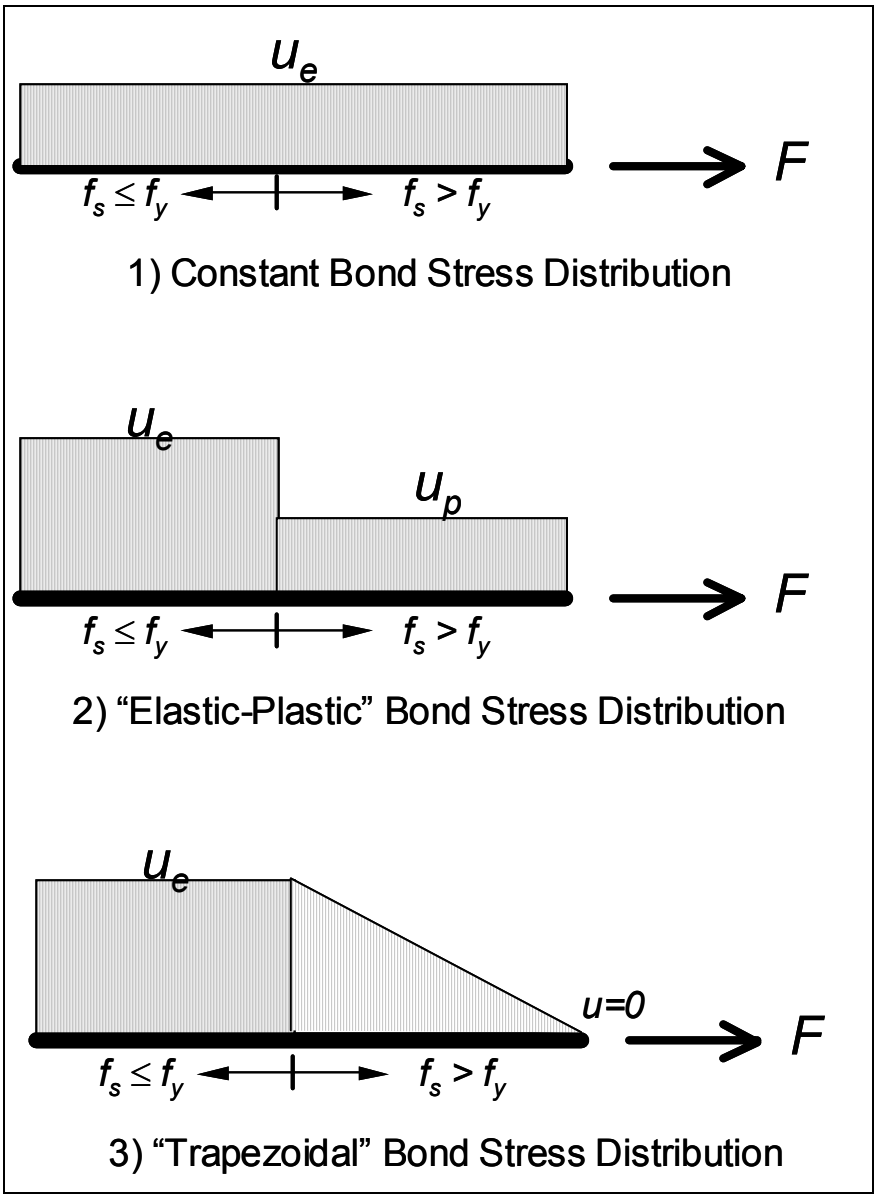

Figure 3-3: Bond-stress distributions

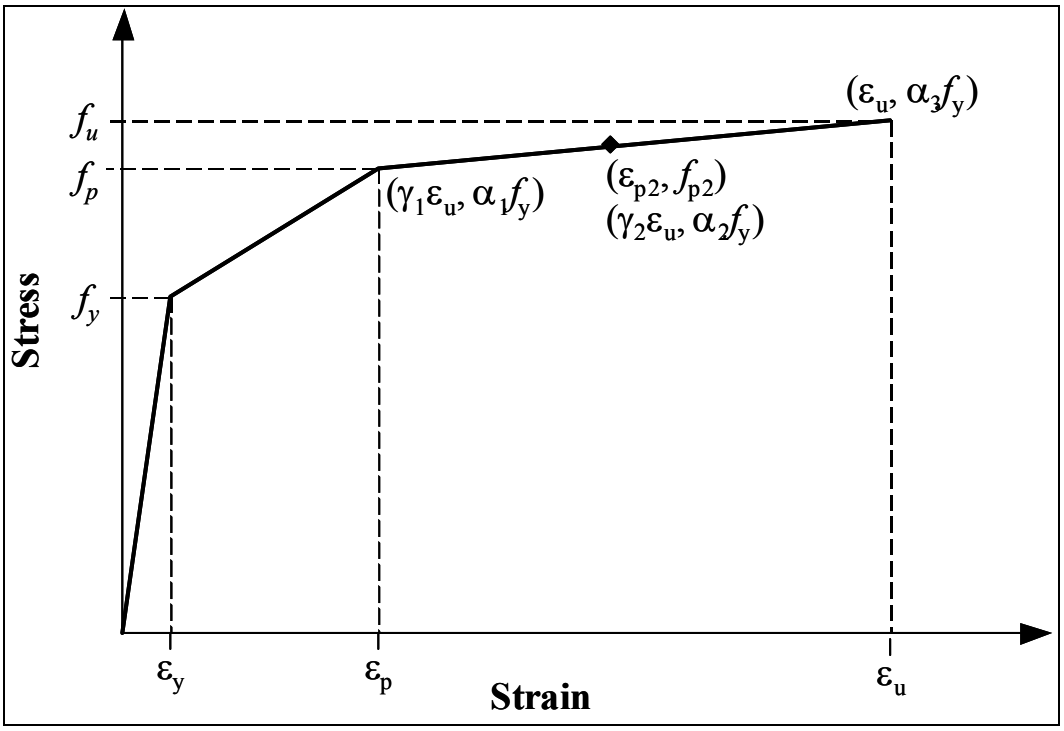

Figure 3-4: Steel Material Stress-Strain Relationship

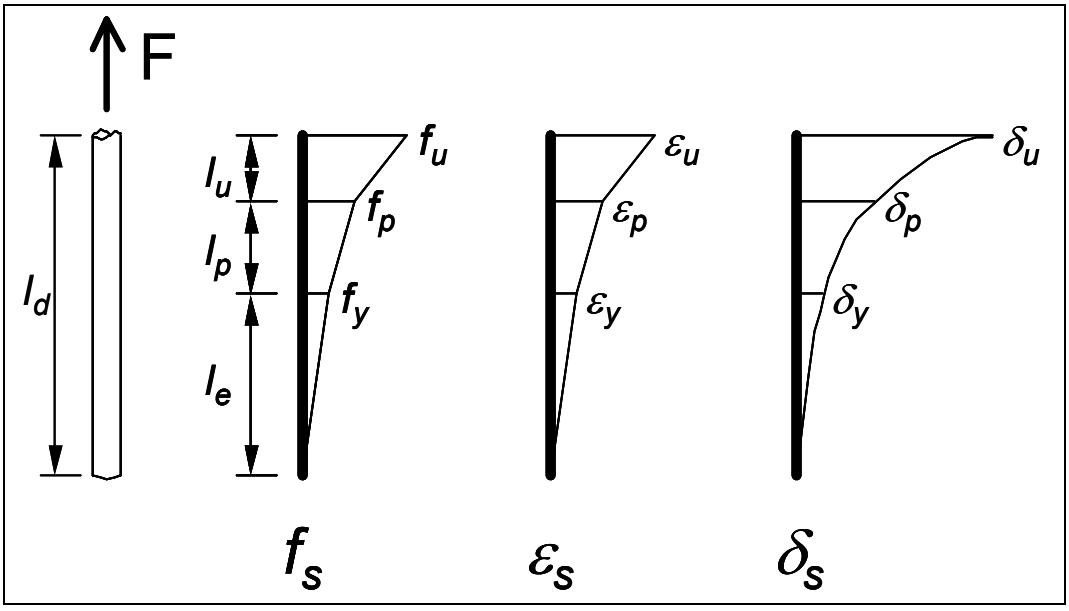

Figure 3-5: Graphical Representation of Bar Stress, Strain, and Elongation

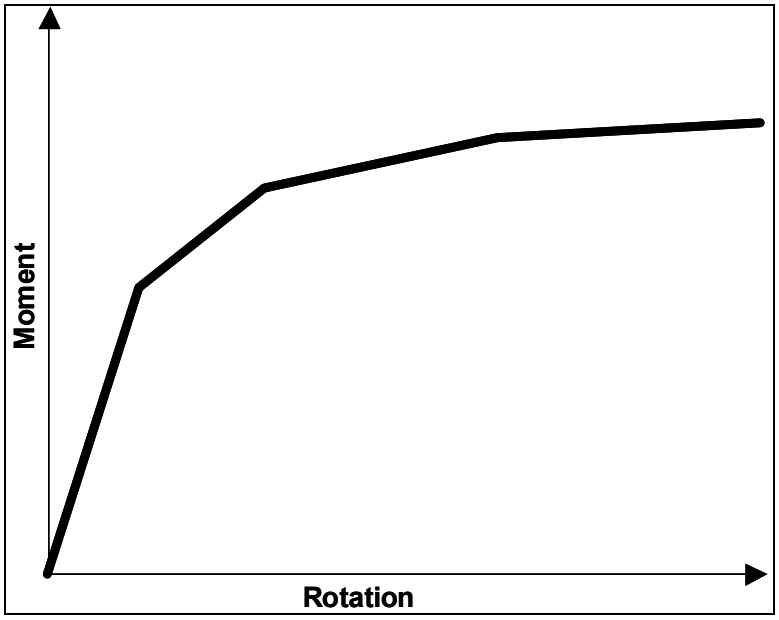

Figure 3-6: Linearized Section Rotation Model

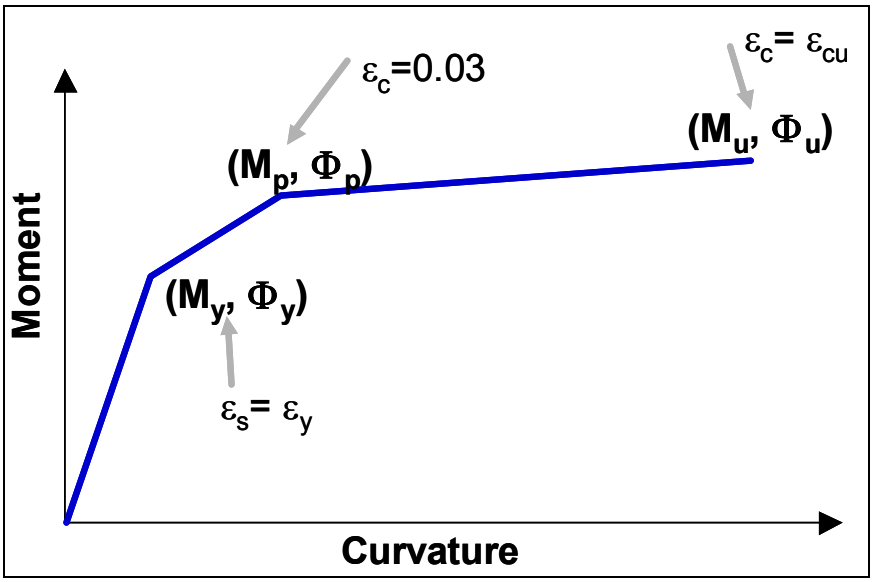

Figure 3-7: Reference Points in the Moment-Curvature Relationship

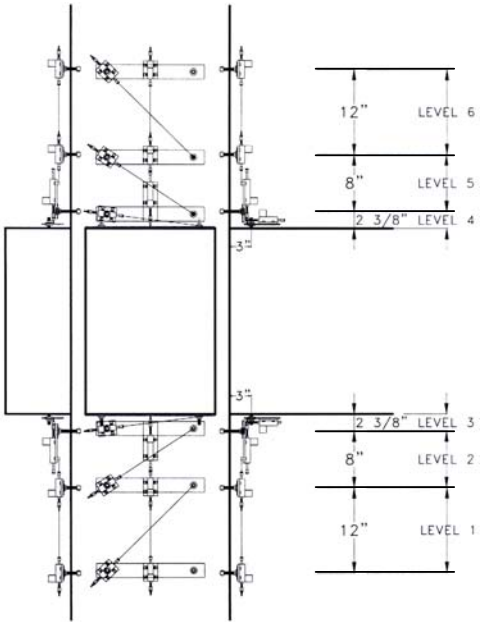

From [Mazzoni, 1997] ("M" series)

Double-Deck Subassembly

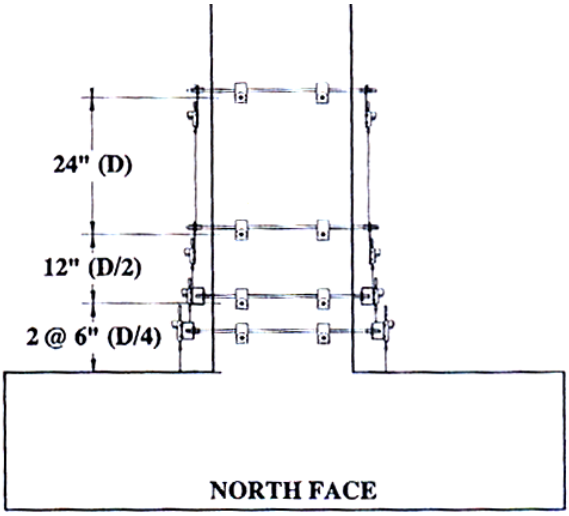

From [Lehman, 1998] ("L" series)

Tee-Joint Subassembly

Figure 3-8: Geometry of Comparison Specimens

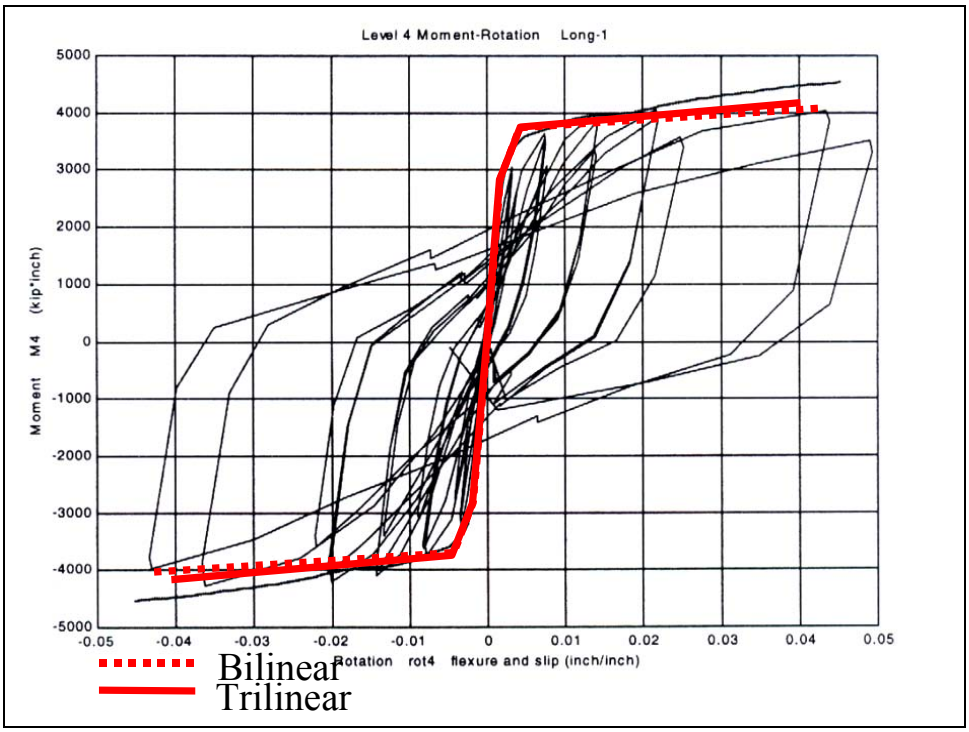

Figure 3-9: M1a - Moment-Rotation with Elastic-Plastic Bond Model

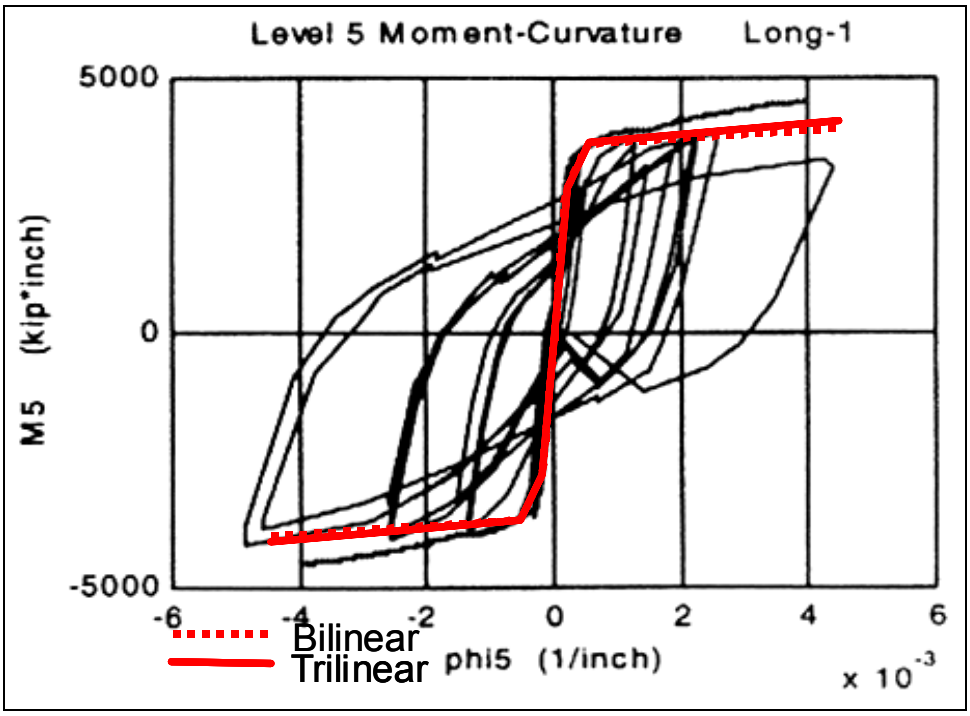

Figure 3-10: M1a - Moment-Curvature with Elastic-Plastic Bond Model

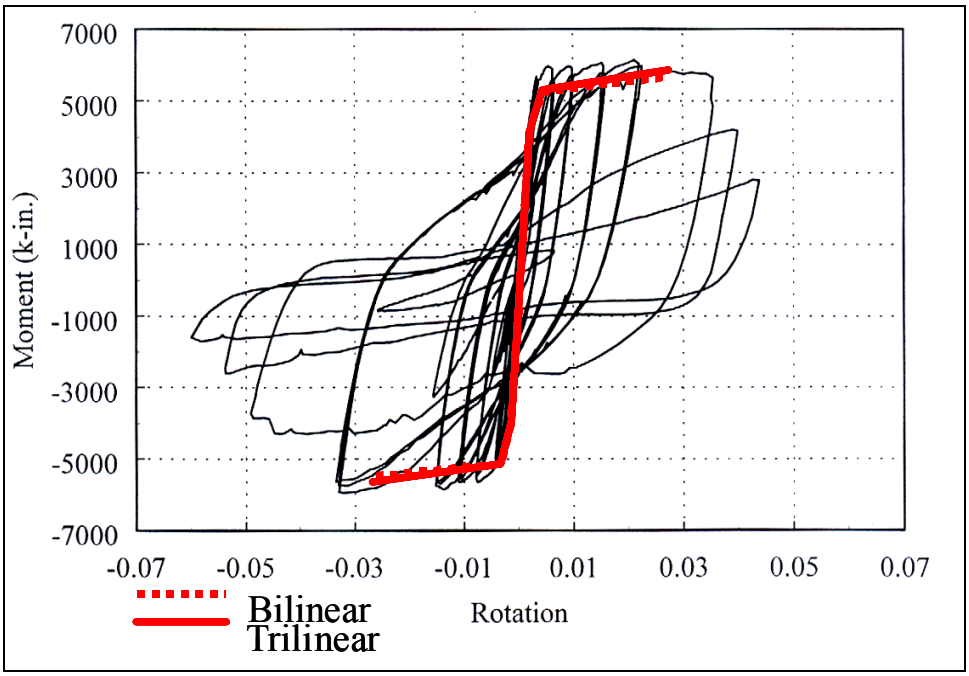

Figure 3-11: L415 - Moment-Rotation with Elastic-Plastic Bond Mode

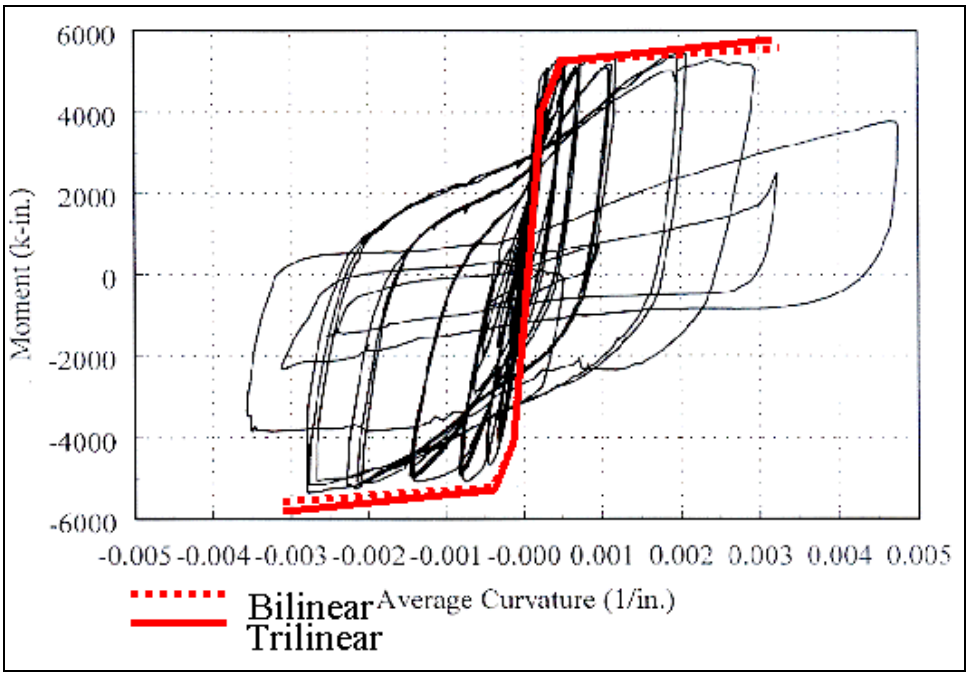

Figure 3-12: L415 - Moment-Curvature with Elastic-Plastic Bond Model

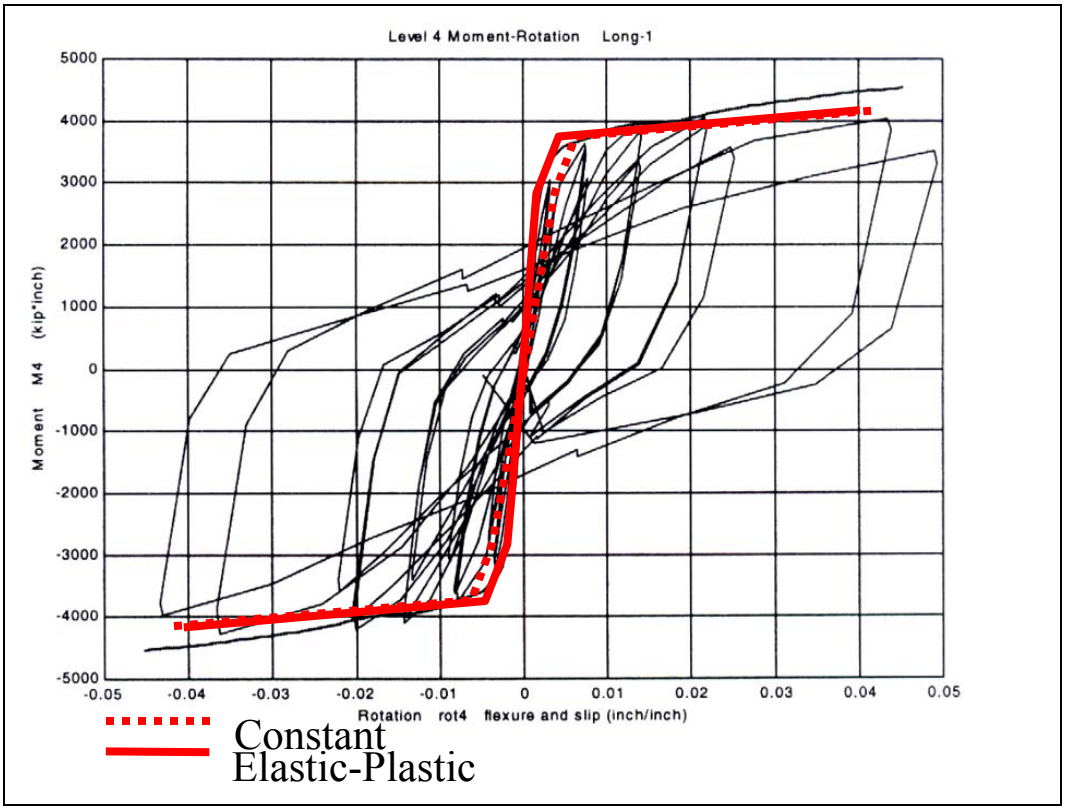

Figure 3-13: M1a - Moment-Rotation with Elastic-Plastic Bond Model

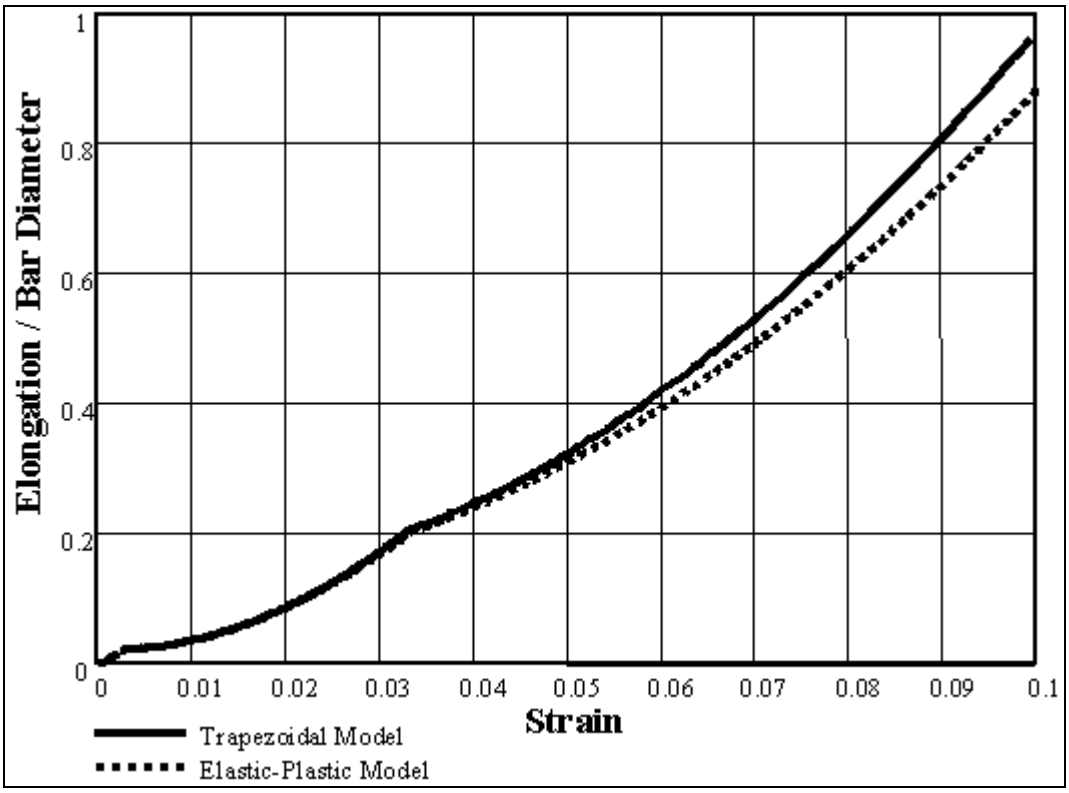

Figure 3-14: Comparison of Elastic-Plastic and Trapezoidal Models

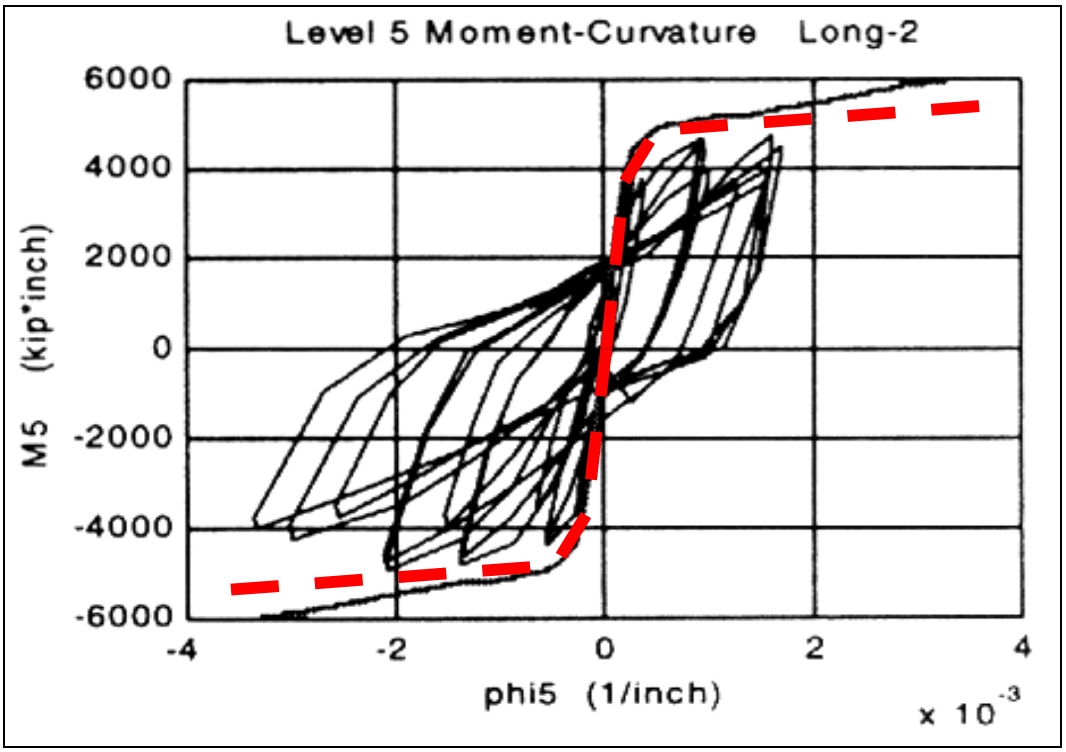

Figure 3-15: M2a - Moment-Curvature with Trilinear Steel Model

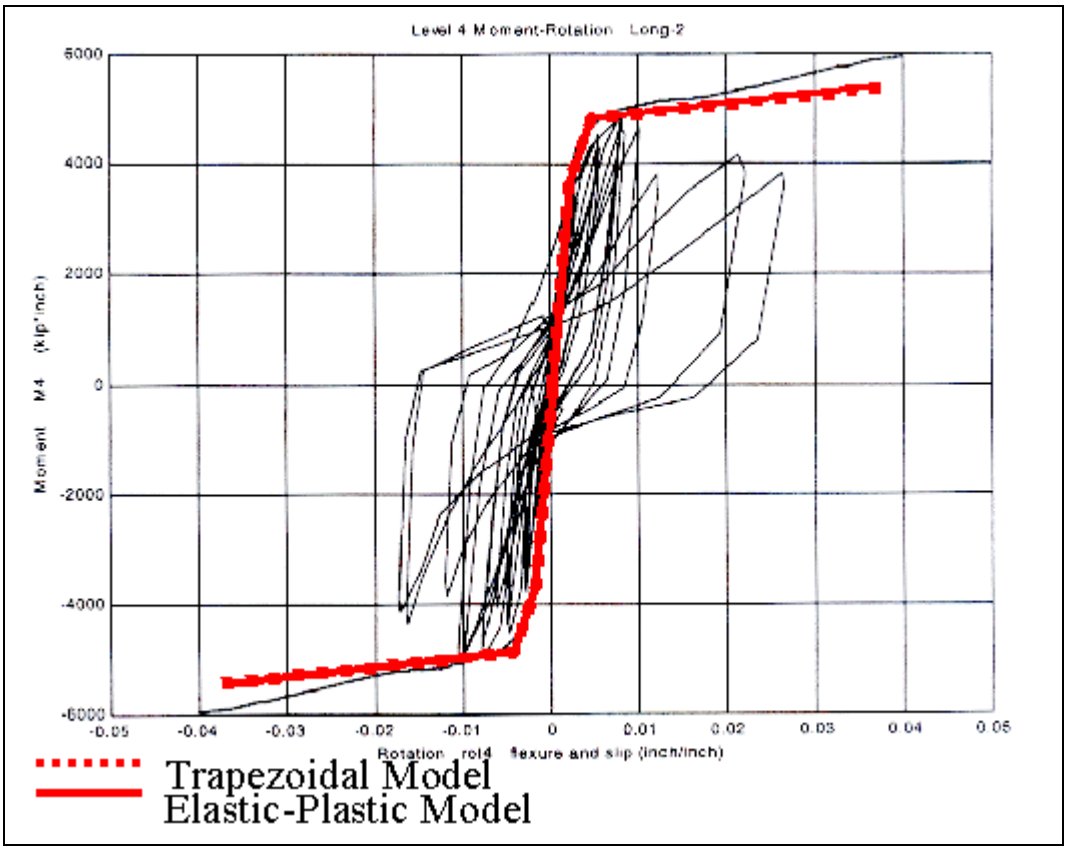

Figure 3-16: M2a - Moment-Rotation with Trilinear Steel Model

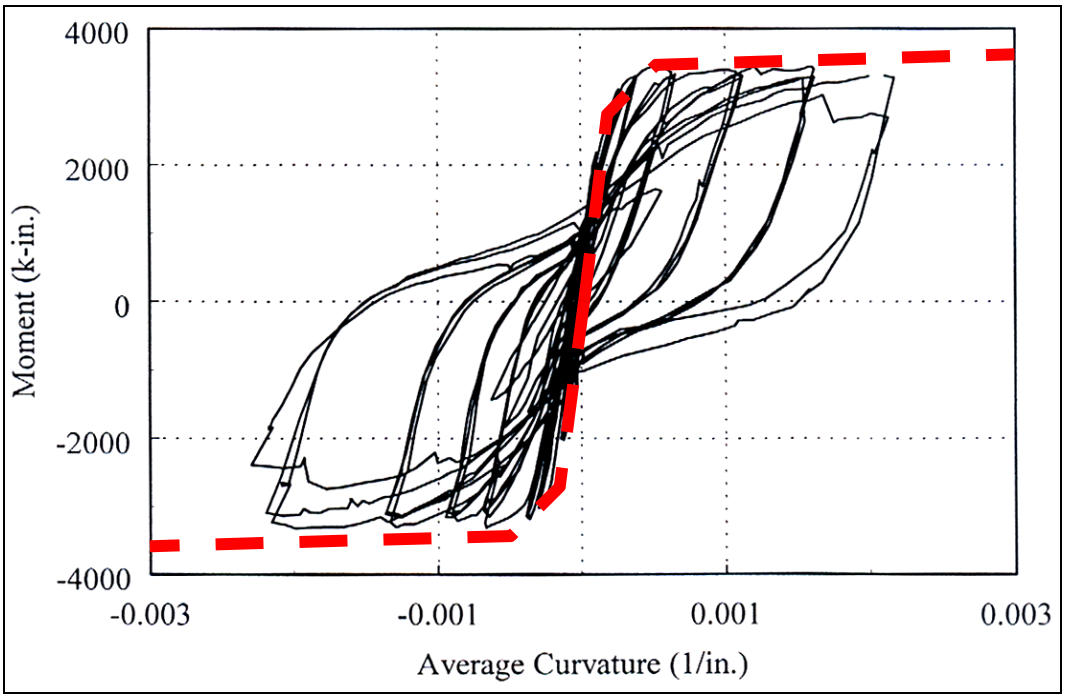

Figure 3-17: L407 - Moment-Curvature with Trilinear Steel Model

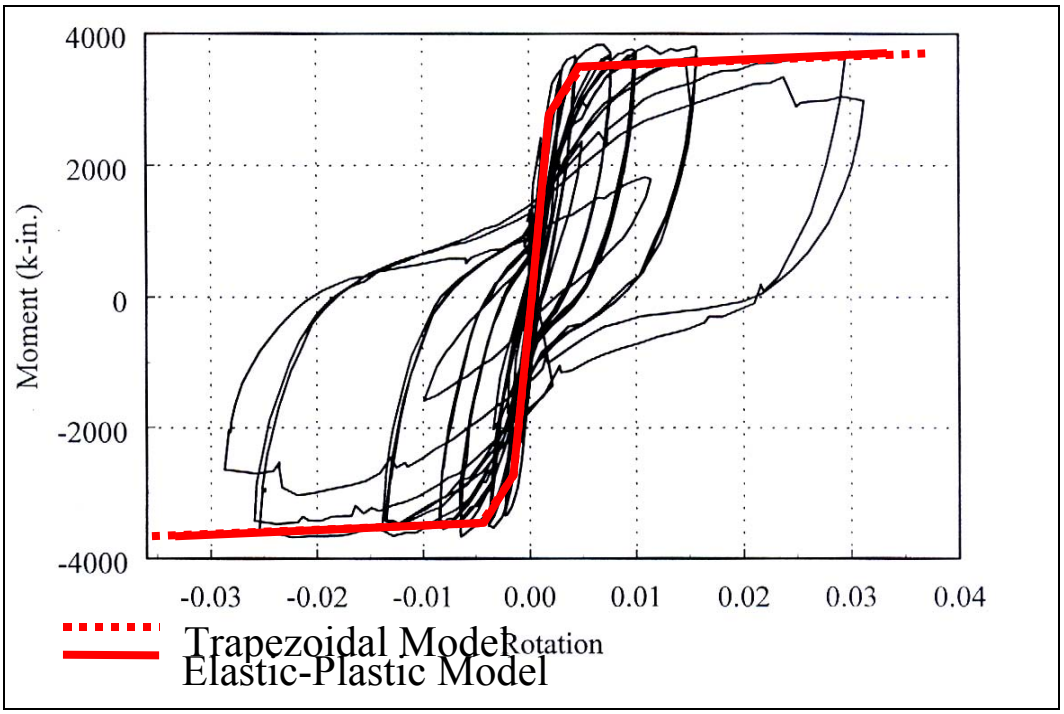

Figure 3-18: L407 - Moment-Rotation with Trilinear Steel Model

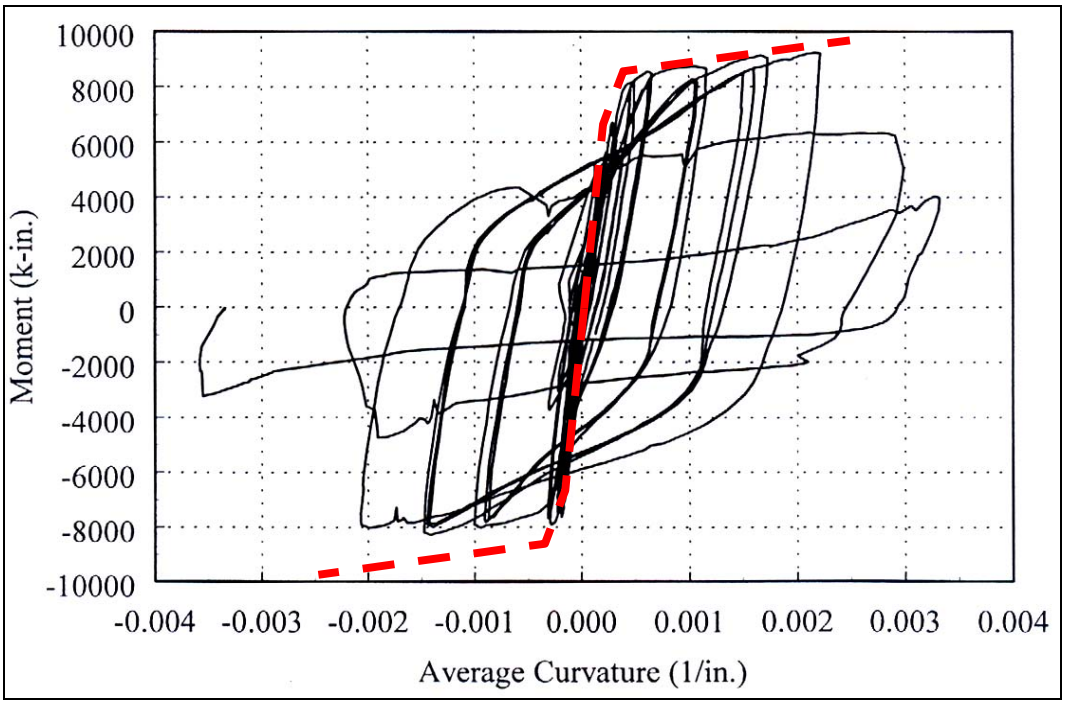

Figure 3-19: L430 - Moment-Curvature for Trilinear Steel, Elastic-Plastic Bond Models

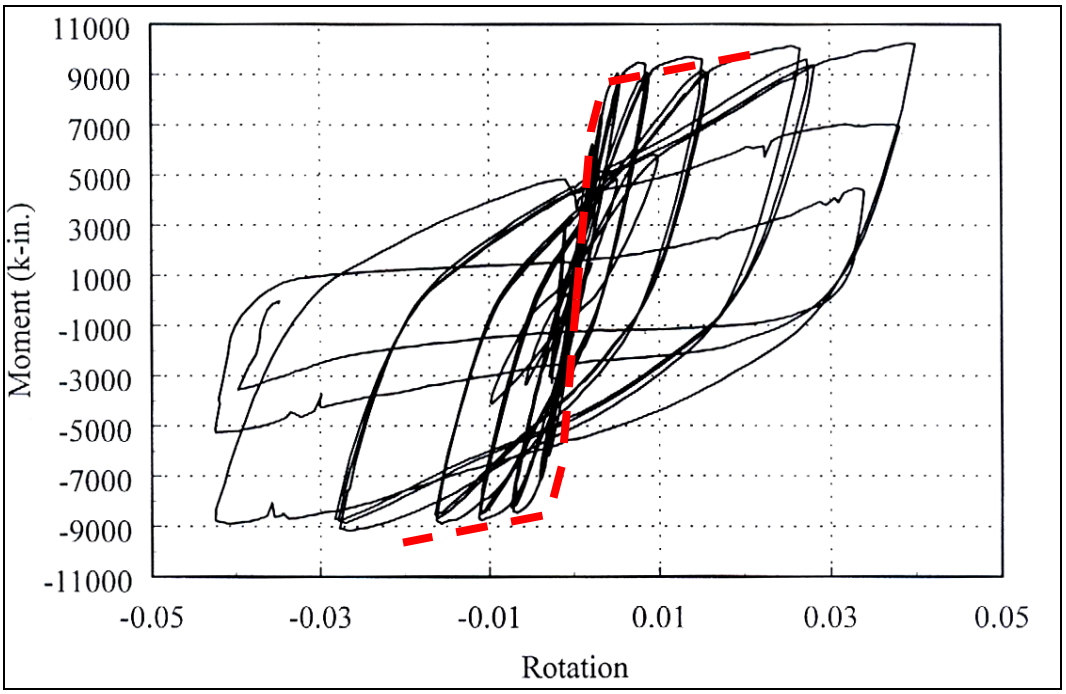

Figure 3-20: L430 - Moment-Rotation for Trilinear Steel, Elastic-Plastic Bond Models

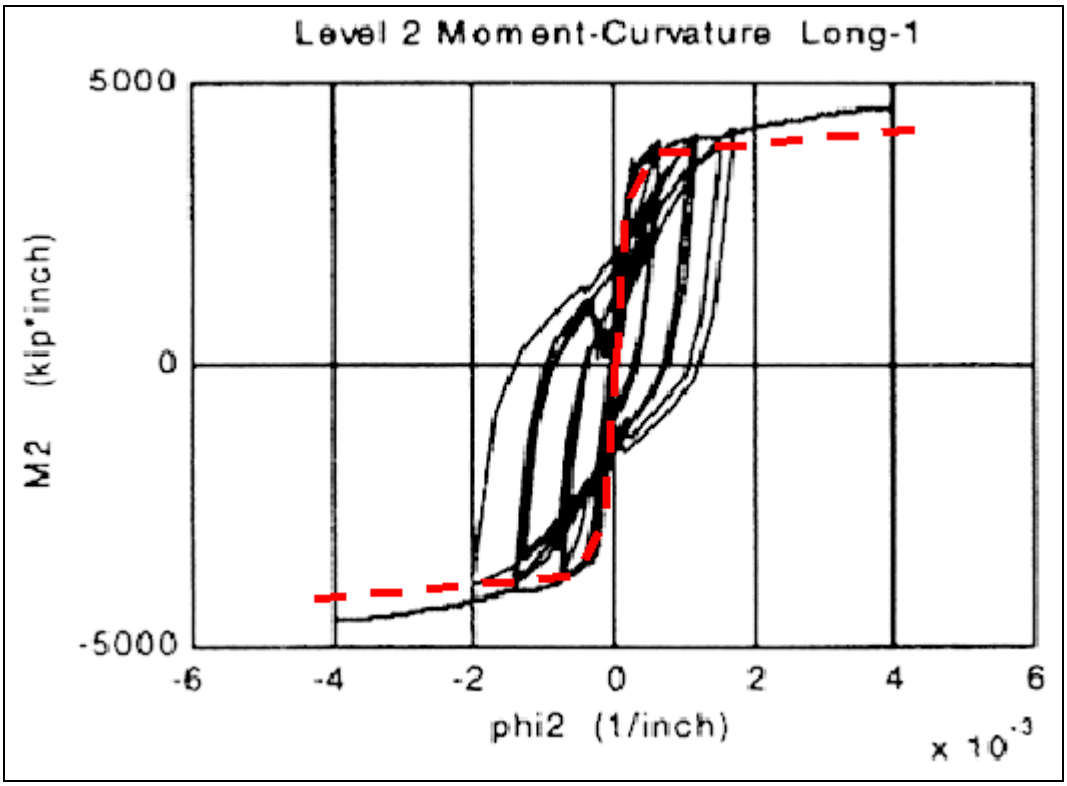

Figure 3-21: M1b - Moment-Curvature for Trilinear Steel, Elastic-Plastic Models

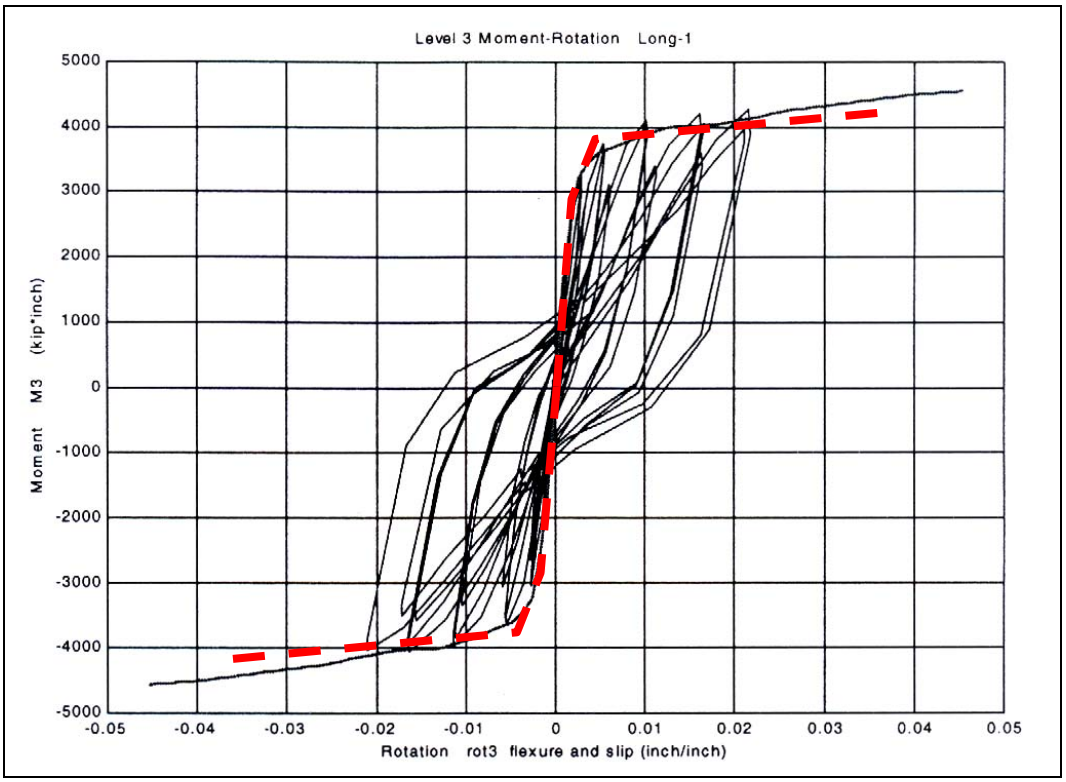

Figure 3-22: M1b - Moment-Rotation for Trilinear Steel, Elastic-Plastic Models

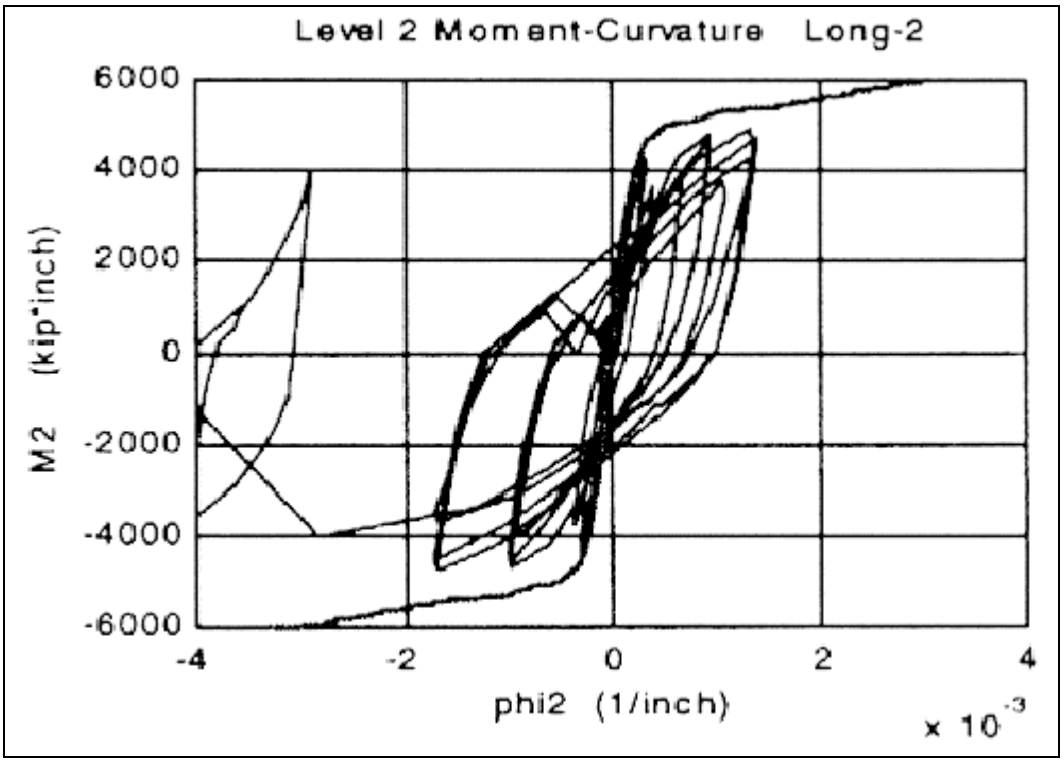

Figure 3-23: M2b - Moment-Curvature for Trilinear Steel, Elastic-Plastic Models

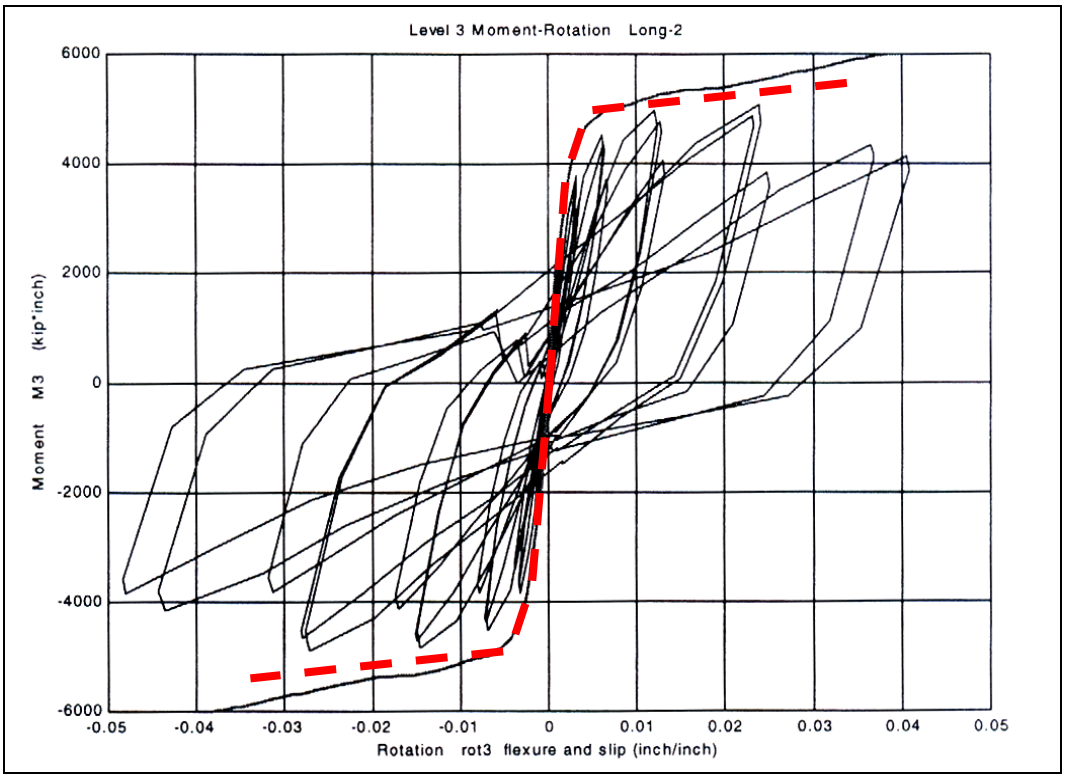

Figure 3-24: M2b - Moment-Rotation for Trilinear Steel, Elastic-Plastic Models

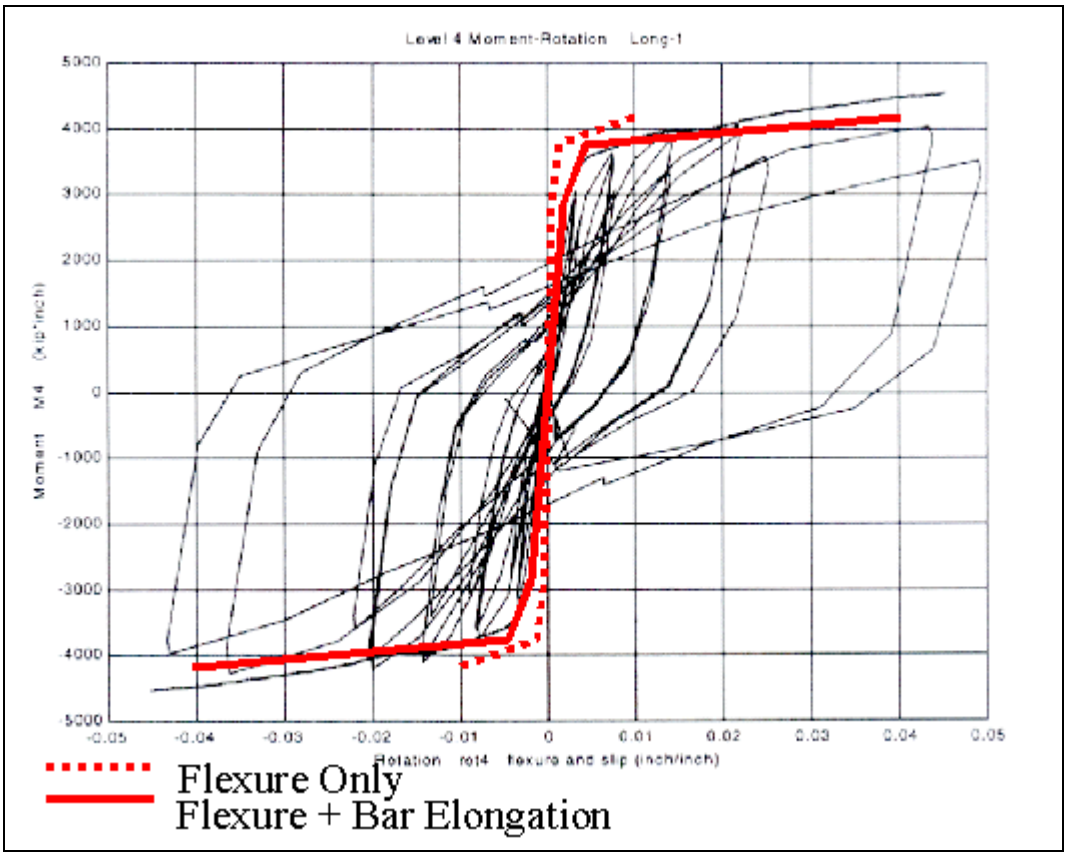

Figure 3-25: M1a - Significance of Bar Elongation to Moment-Rotation Response

Chapter 4. Validation of Models for Joints and Hinges

The objective of this chapter is to demonstrate the validity of these models by comparison to experimental testing. The measured response of the beam-column subassemblages tested by Mazzoni was used to validate the implementation of the simplified joint and hinge numerical models in a structural system [Mazzoni, 1997]. The experimental subassemblage shown in Figure 4-1 consisted of a beam-column connection with beams framing into three vertical faces and columns framing above and below the beams. The geometry and material properties are given in Table 5-4 . The finite element model included inelastic beams and columns and spring elements for the beam-column joints and the bar elongation and slip (Figure 4-2). The spring element representing the beam-column joint was developed in Chapter 2 and will be referred to herein as the “joint model.” The bar-elongation spring model developed in Chapter 3 is the “hinge model” because it is a characteristic of the plastic-hinge zone of the piers. Both spring models consist of nonlinear-inelastic zero-length rotational-spring elements. To validate the numerical model of the subassemblage, the response of a static pushover analysis of the numerical model was compared to the envelope of the response curve of the experimental system subjected to cyclic loading of increasing displacement amplitude. The response of the model with different hinge elements (from flexible to rigid) and joint elements (from weak to rigid) was used in the comparison.

The model validation is a two-step process. In the first step, the response is compared at the local level. Moment-curvature and rotation responses are evaluated for the hinge models, and shear stress-strain responses are evaluated for the joint models. The second step of the

validation consists of using the hinge and joint model that best represented the experimental response in evaluating the global force-deformation relationship.

4.1. Validation of Hinge Model

The local response of the column-hinge elements has been presented in Chapter 3 with the objective of selecting the material properties; particularly steel stress-strain relationship and bond-stress distribution model. A trilinear relationship for the steel model was selected, and the elasto-plastic model was selected for the bond-stress distribution.

The primary characteristics of the hinge model are the bond stresses in the elastic and inelastic region of the anchorage of the column longitudinal reinforcement. The value of the bond-stress affects the resulting flexibility of the hinge without affecting the strength of the hinge. Better anchorage conditions, such as bar hooks, are associated with higher bond-stress values and lesser bar elongation, resulting in a stiffer hinge model. A straight anchorage may result in lower bond-stress values, leading to a more flexible hinge. A range of bond-stress values was used in the evaluation (weak, intermediate, and strong) as well as a rigid hinge. The rigid case was used in the evaluation as the reference case of no hinge effects. The bond-stress values and the corresponding hinge moment-rotation characteristics are represented in Figure 4-3. The actual strength of the hinge is dictated by the strength of the column section in flexure, as presented in Chapter 3, in which the yield, nominal and ultimate moments are determined from a moment-curvature analysis (Figure 3-6).

In a bridge frame, bar yield and elongation occur at the column-joint interface. Although the model separates the flexural and the bar-elongation response, it is difficult to take separate measurements of these deformation mechanisms at the interface. Curvature measurements, however, were also made at column sections away from the interface, as shown in the Figure

3-8. Because bar-elongation is not expected to occur in this region, the flexural component of the numerical model was compared for this location. Once the flexural model was validated, comparing the moment-rotation response of the combined mechanisms at the column-joint interface validated the bar-elongation model.

The validation results for the flexural model are shown in Figure 4-4 and Figure 4-5. The moment-curvature response of Specimen-1 shows a very good correlation between the model and experimental data. Specimen-2 was unable to reach its design strength because the insufficient development length in the joint depth did not develop the bars in tension on both sides of the joint. The model, however, is still able to capture the initial stiffness in flexure and identify the point where inelastic behavior initiates.

The moment-rotation response measured at the column-joint interface was compared to the numerical model of the combined mechanisms of flexure and bar-elongation, as shown in Figure 4-6 and Figure 4-7. The comparison show that the rigid hinge model, which does not take into account the bar-elongation mechanism, is able to estimate the strength of the section, although it significantly underestimates the deformation. The comparison shows that a weak hinge model, with significantly low bond-stress values best represents the experimental data. This phenomenon is attributed to the fact that the column longitudinal reinforcement is continuous through the joint (Figure 4-8).

To further validate the model for the hinge, it was compared with the data for the Lehman test series (Figure 4-9) [Lehman, 1998]. The strong-hinge model provides a better representation of the experimental data because the column longitudinal reinforcement is anchored into the footing using standard hooks (Figure 4-10).

4.2. Validation of Joint Model

A series of joint springs corresponding to joints with a range of shear strengths was used in the evaluation (weak, intermediate, and strong) of the joint model, as well as a rigid joint. As with the hinge model comparison, the rigid case is a reference point representing no joint effects. The shear stress-strain characteristics of the beam-column joints used in the analysis are shown in Figure 4-11. These models were described in Chapter 3. The measured joint shear stresses and strains measured for the Mazzoni tests were used in the validation.

The comparison is shown in Figure 4-12. The different joint models are plotted on the same graph to determine which model is most representative of the experimental data. The “strong” joint model appears to be the most accurate for both test specimens. These results indicate that the maximum shear measured in the test was limited by the column flexural strength, as per the design. The shear strength of joint of Specimen-2, in contrast, limited the maximum shear in the joint.

An evaluation of the local response of both hinge and joint models and mechanisms indicates that the strength of Specimen-1 was limited by the flexural strength of the column, while that of Specimen-2 was limited by the shear strength of the beam-column connection. A comparison of the models with the experimental data at the global force and deformation level will confirm these results in the next section.

4.3. Validation of Substructure Model

The weak-hinge model and the strong-joint model were incorporated into the finite-element model shown in Figure 4-2. The beam and bottom-column supports were modeled as pin connections to represent the boundary conditions of the experimental setup shown in Figure

4-1. The subassemblage was subjected to a series of quasi-static displacement-controlled unidirectional and bidirectional displacement cycles of increasing amplitude imposed at the top of the specimen. The numerical model was subjected to a monotonic lateral displacement of the top of the specimen in the longitudinal direction. Both models were subjected to a constant axial load on the columns representative of gravity loading.

The lateral deflection and applied load measured at the top of the physical model during the unidirectional cycles in the longitudinal direction were plotted against the calculated base shear and top-node lateral deflection of the numerical model for both specimens, as shown in Figure 4-13. The experimental data are compared to two numerical models: (a) a model including only the flexural deformations of the beams and columns (rigid hinges and joints) and (b) a model including flexural response and the hinge and joint flexibilities corresponding to those selected from the validation at the local level.

The comparison indicates that both numerical models are able to estimate the lateral strength of the bridge substructure. The flexure-only model, however, grossly underestimates the lateral-deformation capacity of the subassemblage. In simplified design, this is compensated by including a yield-penetration factor in the calculation of the plastic-hinge length that accounts for the hinge flexibility.

4.4. Summary

In summary, this chapter has presented the joint and hinge models incorporated into a model of a bridge subassemblage. Experimental data were used to validate the behavior of these models at both the local and global levels. The validation has shown that the range of values chosen to represent the bond-stress distribution and the joint shear strength yield results that are consistent with physical measurements. The comparison of the hinge model to

experimental setups where both strong and weak anchorage conditions exist has shown that bond-stress values need to be selected carefully. The validation of the joint model has shown that joint shear strength can be a limiting factor in the overall behavior of the structural system.

4.5. Tables

Table 5-4. Numerical Model Parameters for Mazzoni Tests [Mazzoni, 1997]

Model Parameters	Mazzoni 1 -Below	Mazzoni 1 -Above	Mazzoni 2 -Below	Mazzoni 2 -Above
Geometry:				
Column Diameter (Hcol)	22"	22"	22"	22"
Column Length (Lcol)	4'-11"	5'-10"	4'-11"	5'-10"
Longitudinal reinforcing ratio (ρ_l)	1.30%	1.30%	1.85%	1.85%
Transverse reinforcing ratio (ρ_s)	0.91%	0.91%	0.90%	0.90%
Material:				
Steel yield stress (f_y)	70 ksi	70 ksi	70 ksi	70 ksi
Steel ultimate stress (f_u)	108 ksi	108 ksi	116	116
Steel ultimate strain (ε_u)	0.125	0.125	0.1	0.1
Transverse steel yield stress (f_{yh})	70 ksi	70 ksi	70 ksi	70 ksi
Concrete compressive strength (f_c')	5480 psi	5140 psi	6160 psi	5530 psi
Confined concrete compressive strength	7370 psi	7020 psi	8070 psi	7420 psi
Confined concrete ultimate strain (ε_{cu})	0.016	0.017	0.015	0.16

Some steel parameters were estimated from graphs

Confined concrete parameters were calculated from Mander's model of confined concrete.

4.6. Figures

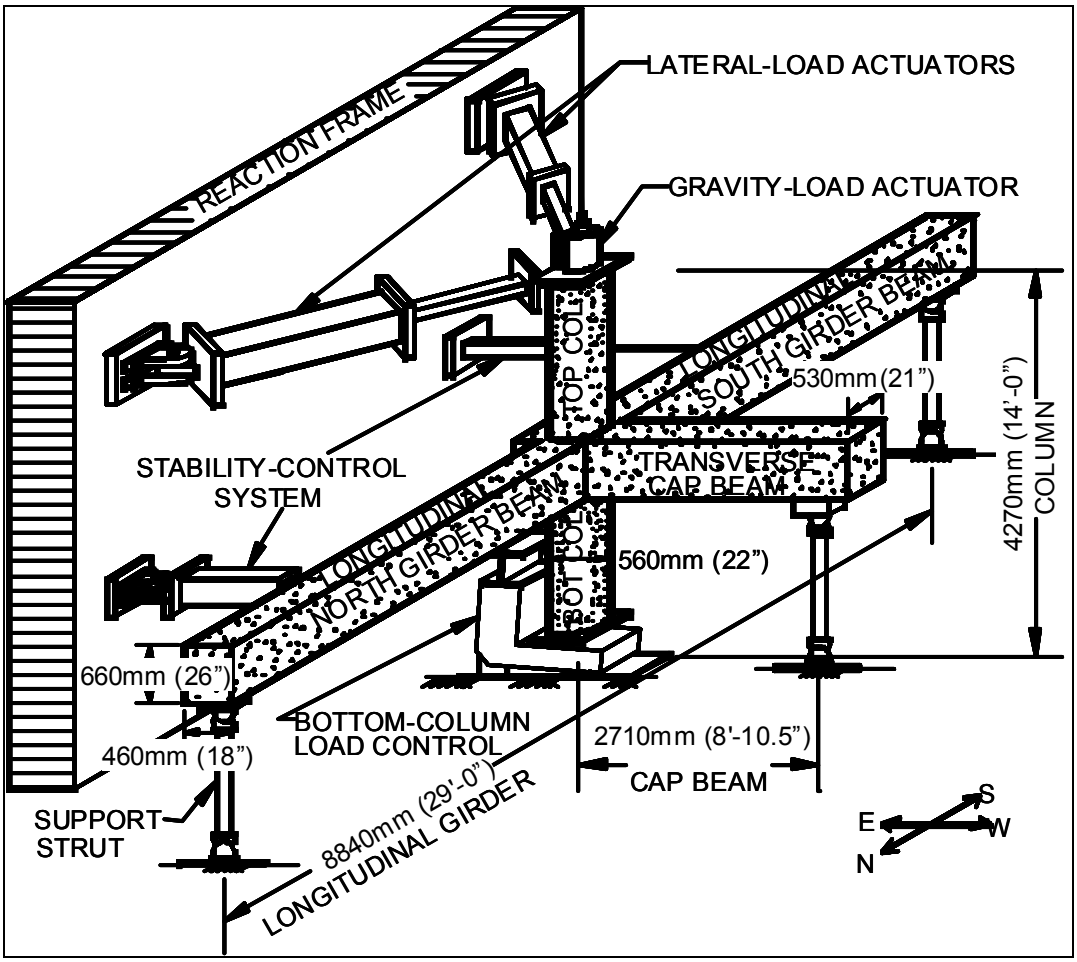

Figure 4-1: Laboratory Test-Specimen Setup for lower-level beam-column connection [Mazzoni, 1997]

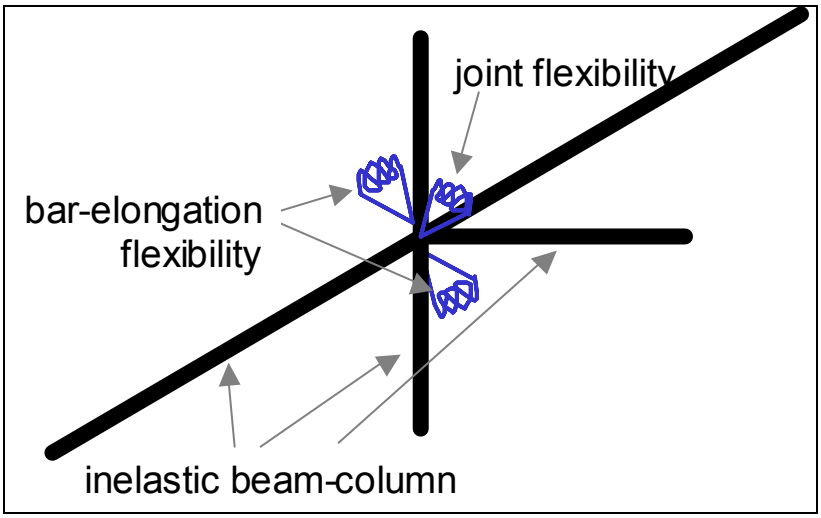

Figure 4-2: Finite Element Model of Beam Column Joint Subassemblage -- Elements

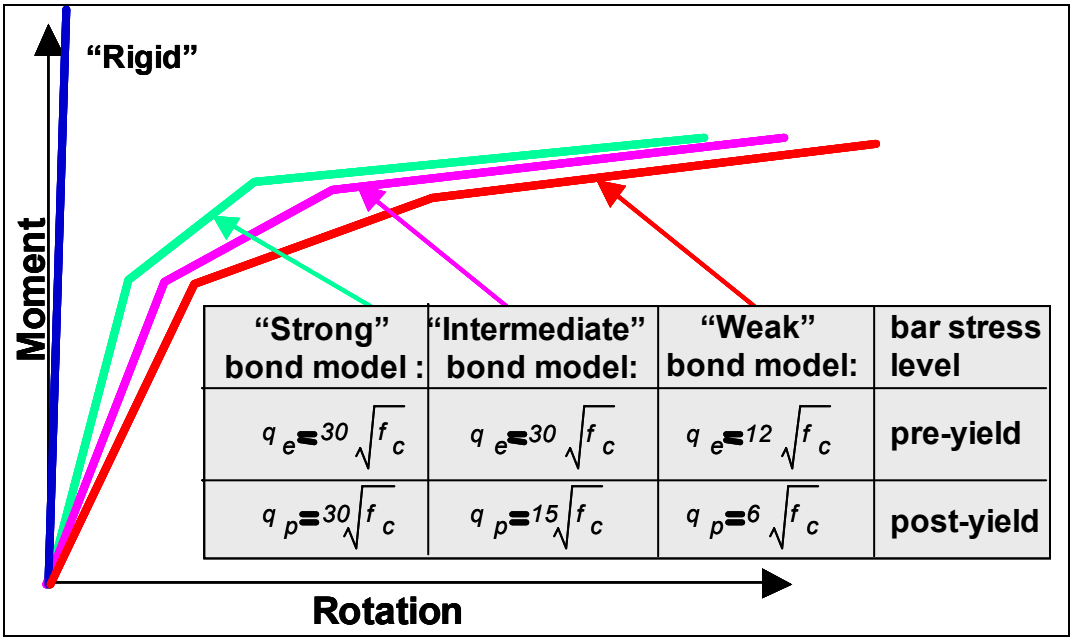

Figure 4-3: Moment-Rotation Response of Hinge based on Bond Strength of Anchorage

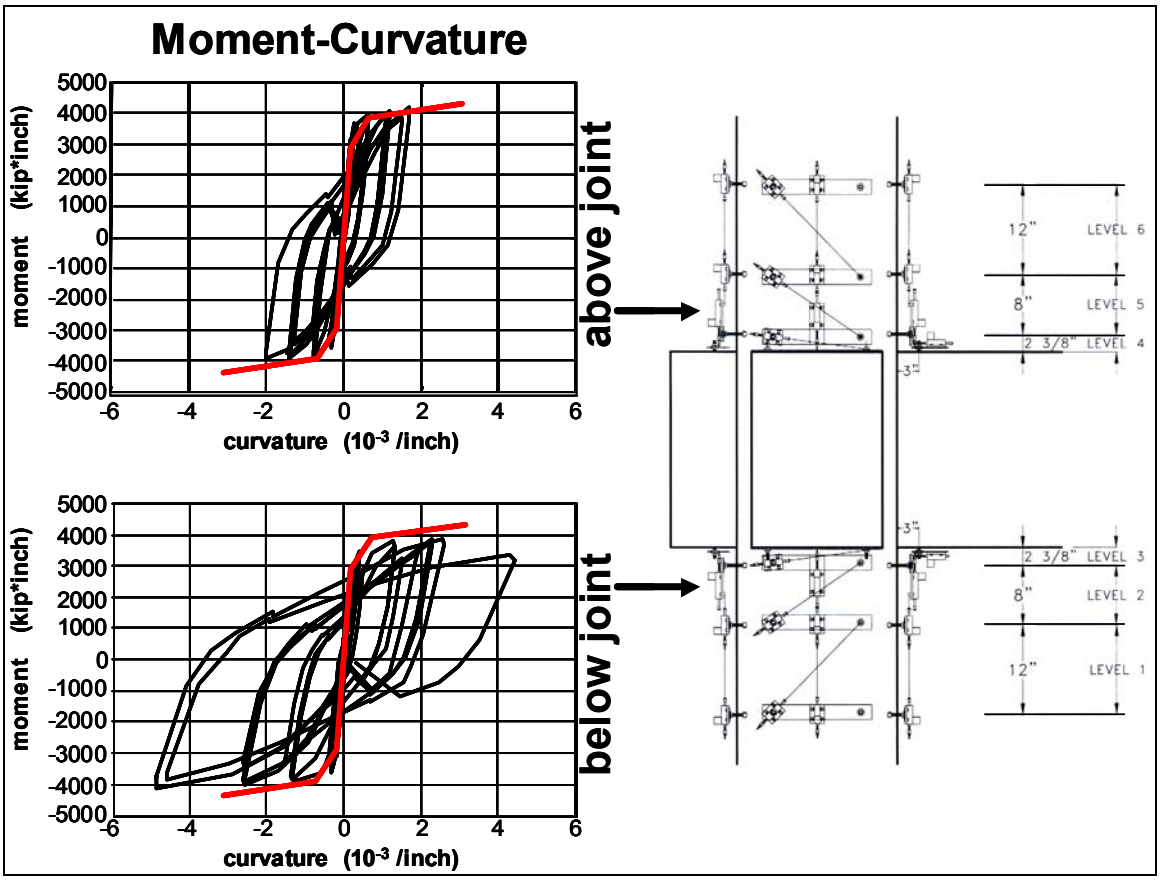

Figure 4-4: Moment-Curvature Response, Mazzoni Specimen 1

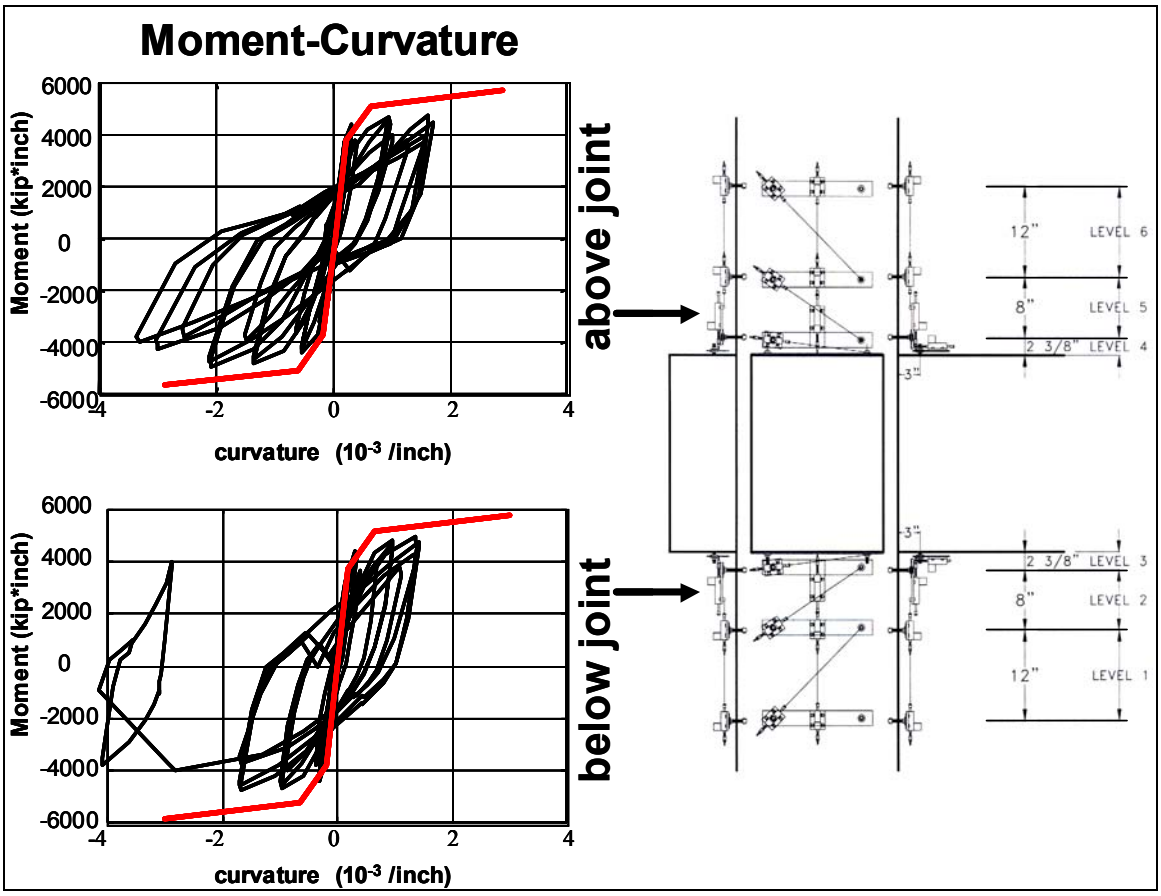

Figure 4-5 Moment-Curvature Response, Mazzoni Specimen 2

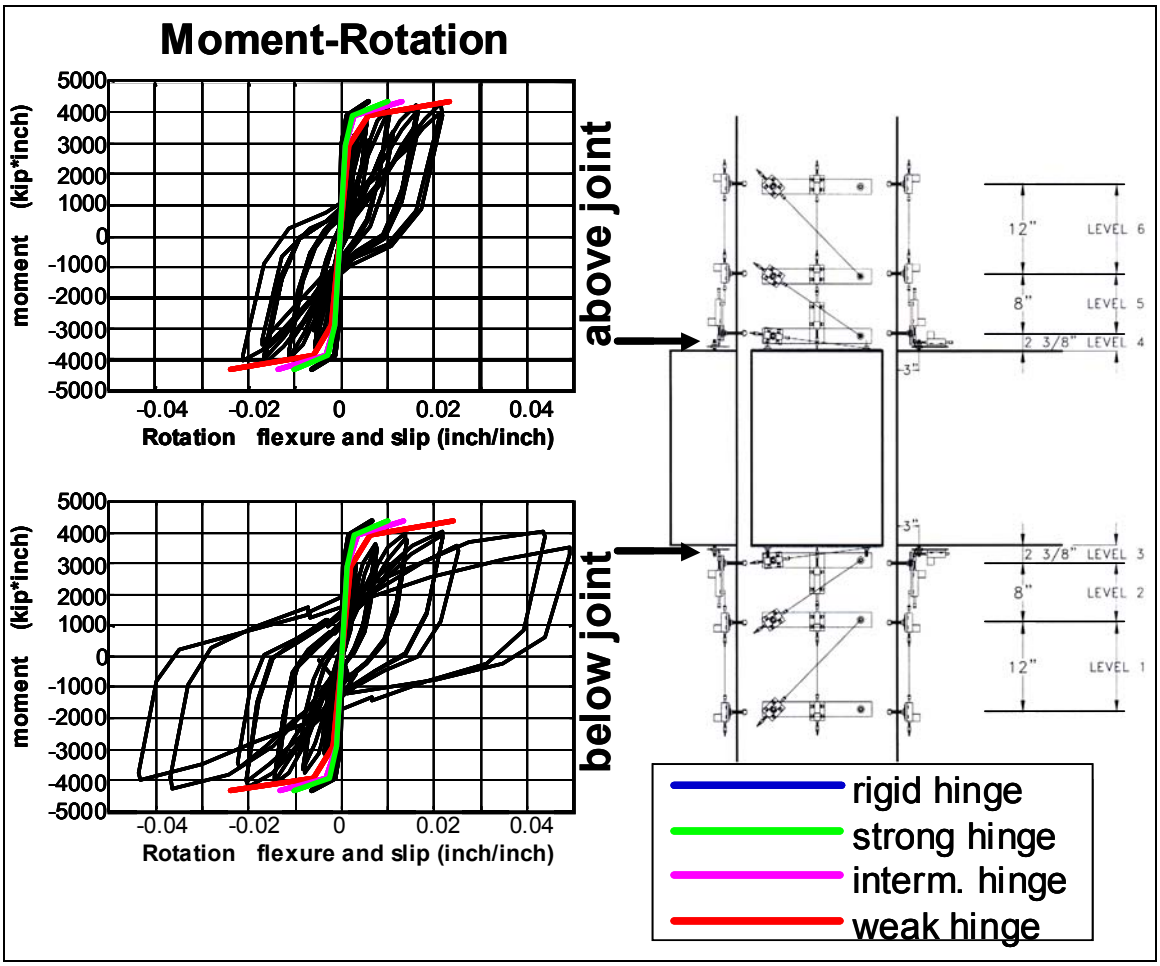

Figure 4-6: Moment-Rotation Response, Mazzoni Specimen 1

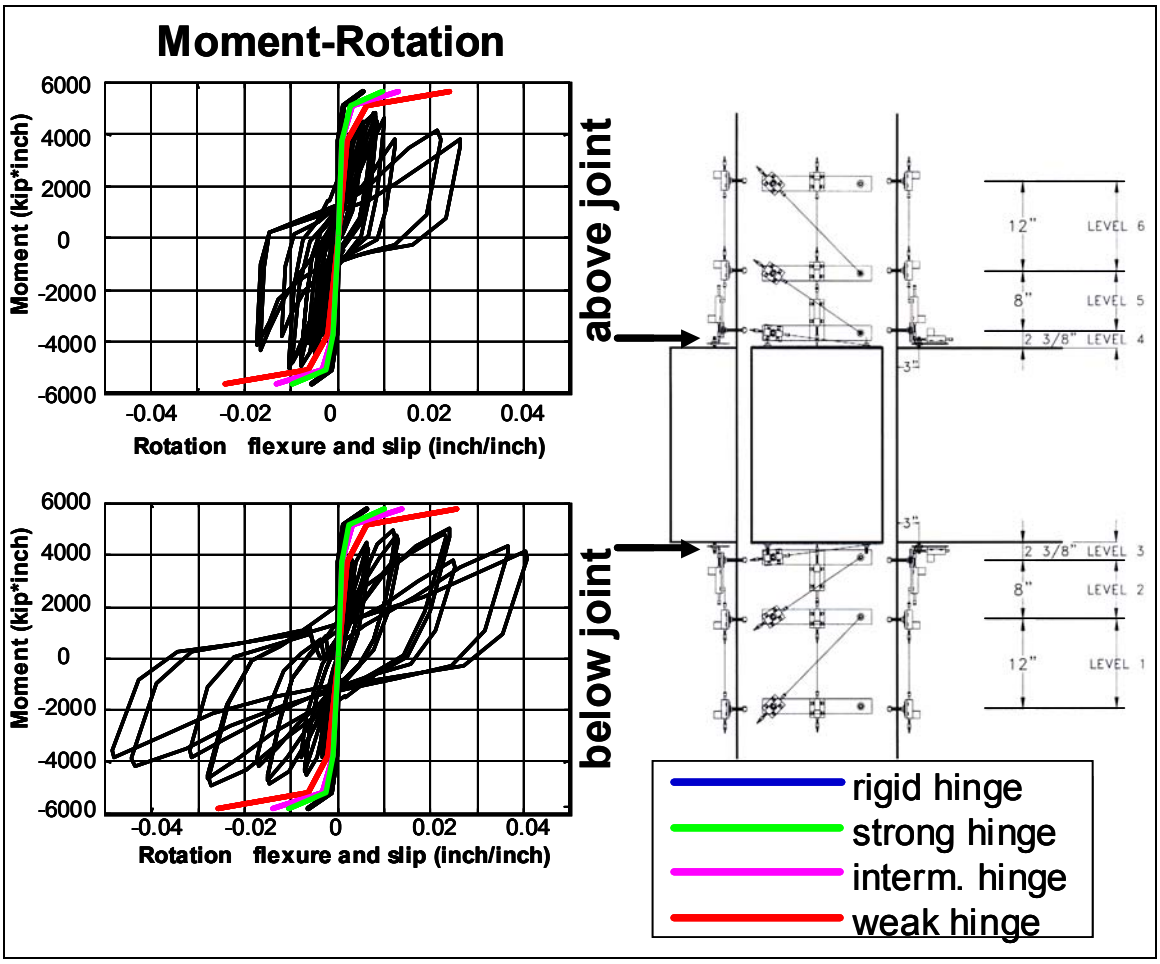

Figure 4-7: Moment-Rotation Response, Mazzoni Specimen 2

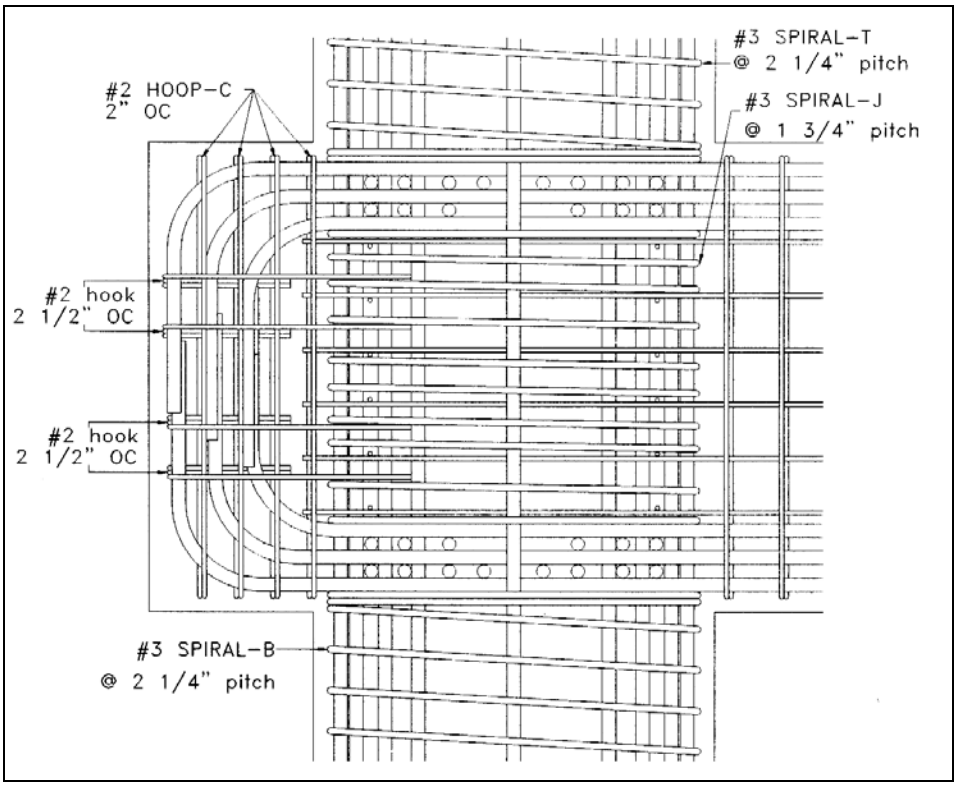

Figure 4-8: Reinforcement-Anchorage Detail, Mazzoni

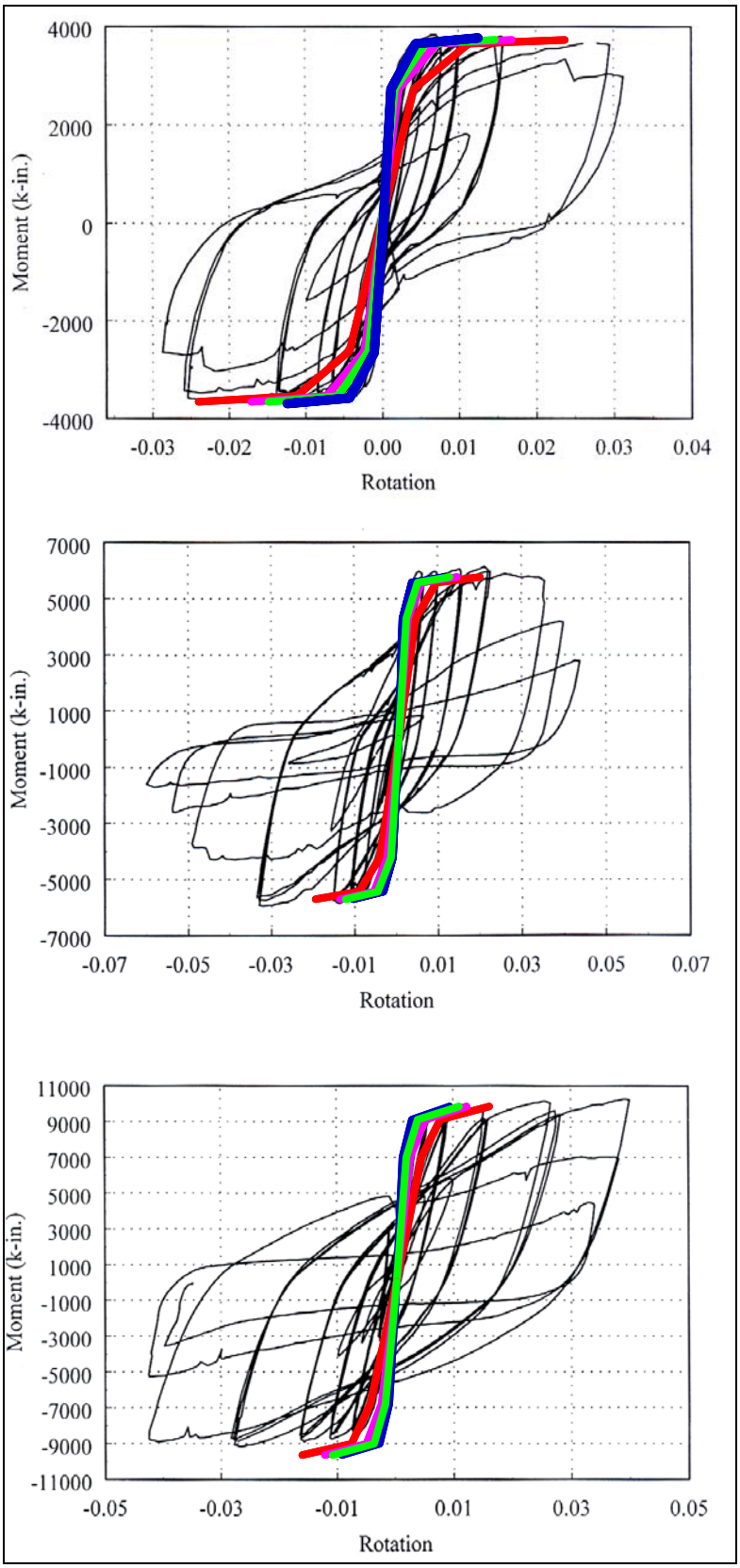

Figure 4-9: Moment-Rotation Response, Lehman

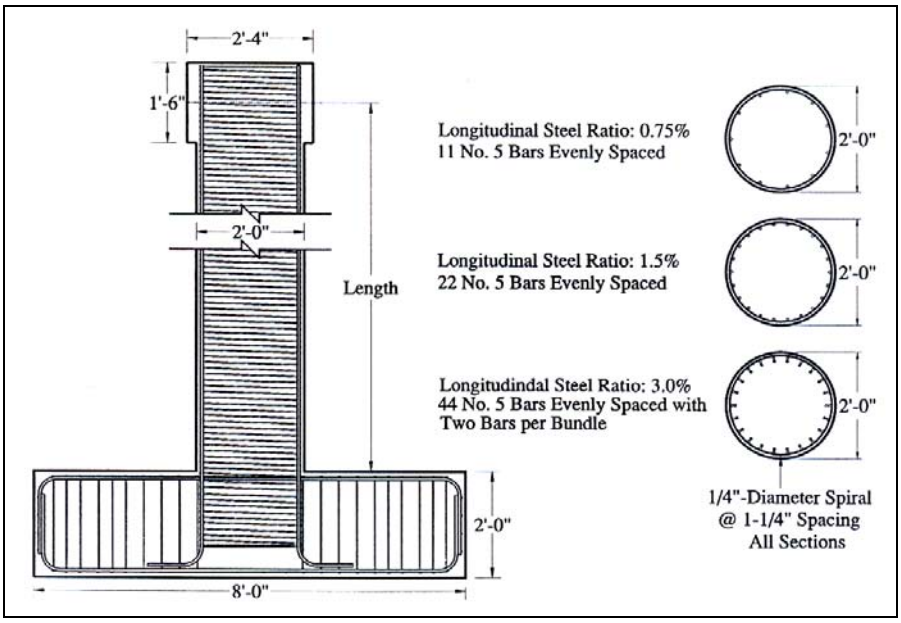

Figure 4-10: Reinforcement-Anchorage Detail, Lehman

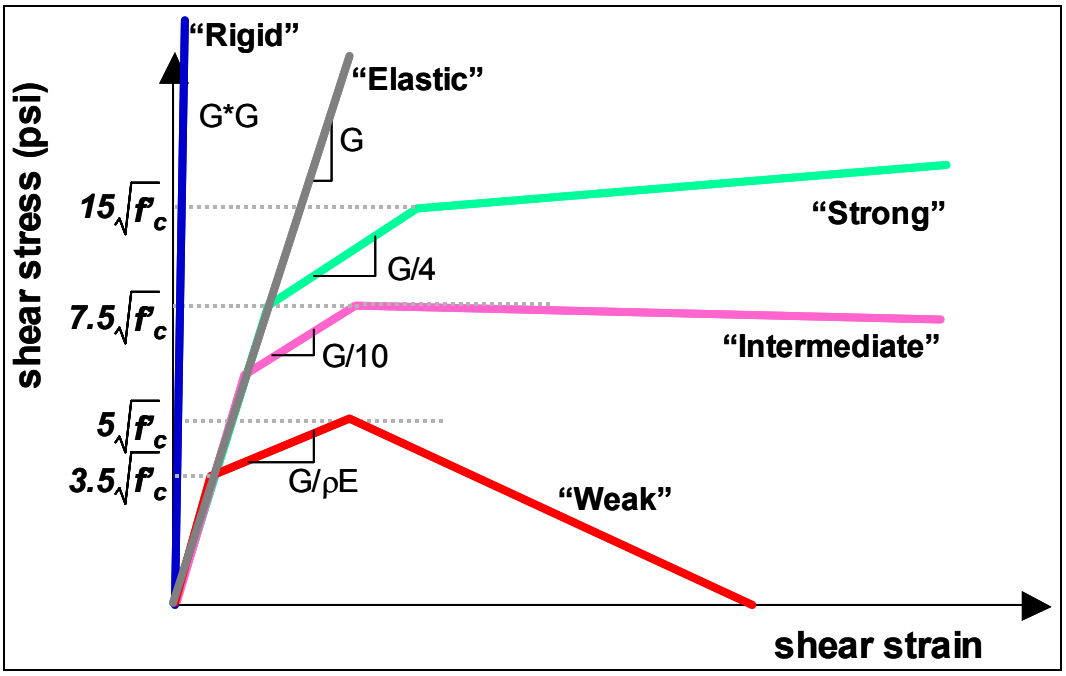

Figure 4-11: Models of Joint Shear Strength

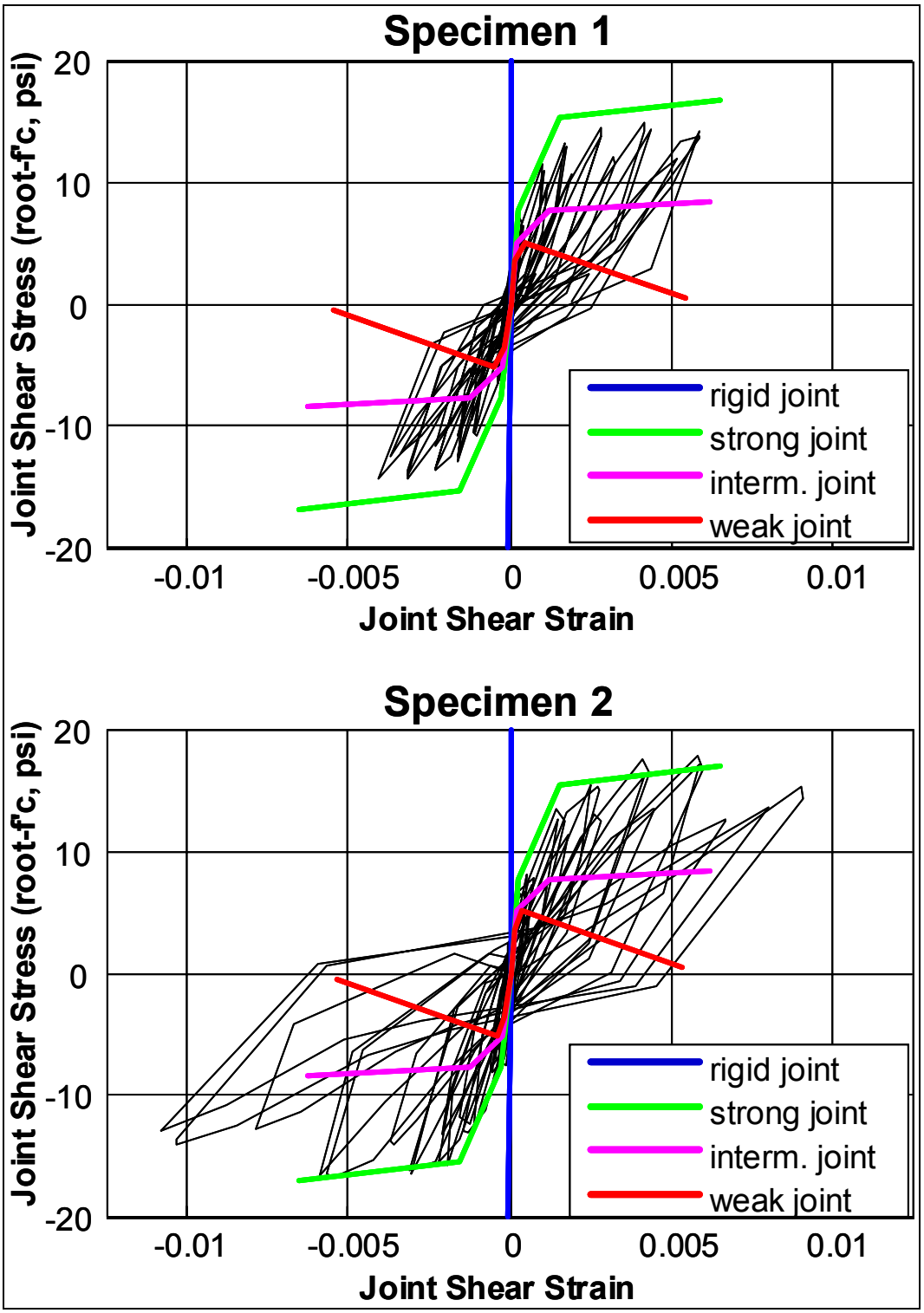

Figure 4-12: Joint Shear Response, Mazzoni

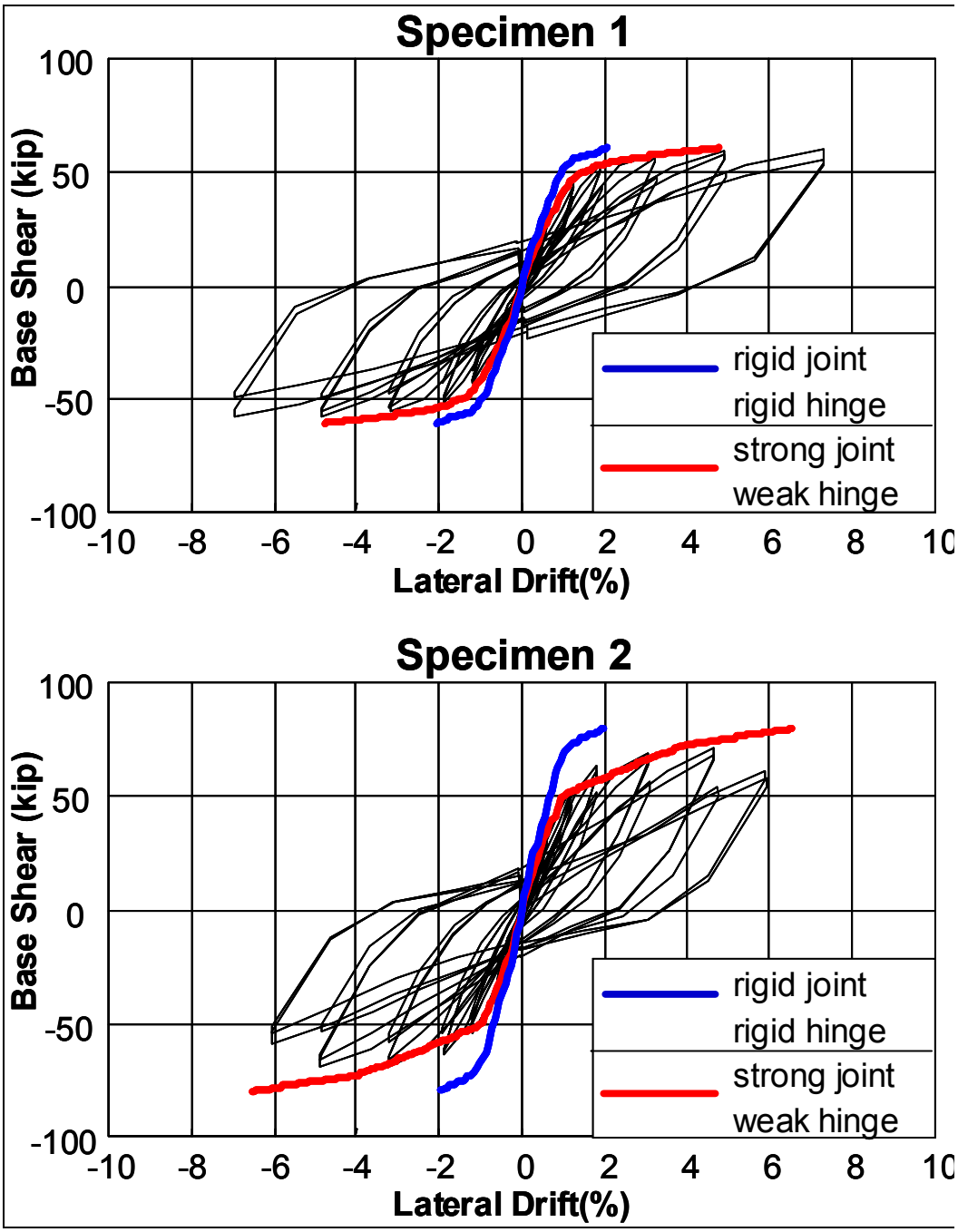

Figure 4-13: Force-Deformation Response of Test Specimens

Chapter 5. Lateral-Frame Analysis

The effects of local deformations on the global response of a bridge system were studied by performing static and dynamic analyses on a finite-element model of a representative bridge bent, shown in the Figure 1-1. The bridge bent consisted of inelastic circular piers connected to an elastic prismatic beam. A set of four frames with varying strength and stiffness characteristics was used in the study. These characteristics were varied by varying the size of the structural elements and the amounts of longitudinal reinforcement, without changing the overall characteristics of the frames. The range of characteristics used is representative of the range of design parameters typical of existing Caltrans bridge bents. The critical design parameters of these frames are shown in the table (see Table 5-1).

In the both types of analyses the structure was subjected to lateral loads as well as gravity loads. The gravity loads represented the dead-load weight of the superstructure uniformly distributed along the beam member. The mass used for the inertial loads in the dynamic analysis was obtained from the super-structure weight. Only translational inertia was considered.

The static loading consisted of an imposed lateral translation of the deck in the plane of the frame to the prescribed limit state. This limit state was defined by either the maximum column curvature limited by concrete crushing, hinge failure, or joint failure. The dynamic loading consisted of a set of acceleration ground-motion records imposed at the supports. The ground-

motion records are given in the tables (Table 5-2, Table 5-3, Table 5-4, Table 5-5). These ground motions were sorted into four bins of twenty ground motions each:

- small magnitude, small distance
- small magnitude, large distance
- large magnitude, small distance
- large magnitude, large distance

All of the ground motions were scaled by a factor of 1.5 to ensure nonlinear response in the structure.

5.1. Finite-Element Model of Bridge Bent

As the beams are designed to remain elastic when the structure is subjected to the design loads, it was represented in the finite-element model by using an elastic beam-column element where only the cross-sectional area, moments of inertia and material elastic stiffness are prescribed. Nonlinear beam-column elements, which consider the spread of plasticity along the element length, were used to represent the columns. The non-linear element properties were prescribed by defining a cross-section with fibers representing the reinforcement, core and cover concrete core independently. The supports at the column bases were modeled as pin supports, where all degrees-of-freedom are restrained, except for rotation in the plane of the frame.

The columns and beams were connected using zero-length elements that represented the rotational flexibility resulting from the elongation of the column longitudinal reinforcement (hinge model) and the beam-column joint (joint model), independently, as shown in the figure (Figure 5-1). A zero-length element connects two nodes that are defined at the same location, using a multi-linear force-deformation relationship. The moment-rotation relationship for the

hinge and joint were developed in the previous chapters. A set of five hinge models with varying bond-strength, and resulting rotation flexibility, as well as a set of seven joint models with varying joint shear strength, and resulting moment strength, were studied in both the static and dynamic analyses (Figure 5-2).

5.2. Nonlinear Static Analysis

In the nonlinear static analysis, the frames were subjected to simultaneous gravity and lateral loads. The lateral loads were applied by imposing a lateral displacement of the deck level of monotonically increasing amplitude. The maximum lateral deflection was determined when one of the following was reached:

- concrete crushing in the column members (flexural strength of columns)
- maximum-moment capacity of hinge
- maximum shear strength of beam-column joint (before strength degradation).

In the static analysis the effects of hinge and joint flexibility were considered separately by varying the characteristics of one type of element while keeping the other rigid.

The lateral force-deformation response of the four test frames where only flexural deformations are considered is shown in the figure (Figure 5-3), this is the case where both hinge and joint are rigid. This response was used as the baseline response in the evaluation of local-deformation effects. The key differences between these frames are the column size and the amount of column longitudinal reinforcement. In the lateral-load response, the change in column size results in a change of lateral stiffness of the structure. The change in amount of column longitudinal reinforcement results in a change in lateral-load strength. These parameter-

variations were selected as strength and flexibility are the important two characteristics in the hinge and joint response.

5.2.1. Effects of Hinge Flexibility on Capacity Curve

The effects of the hinge flexibility on the capacity curve of each frame are shown in the figure (Figure 5-4). The data indicate that while the hinge flexibility does not affect the total base shear coefficient for the frames studied, it does affect the maximum lateral-drift capacity of each frame. The effects of hinge flexibility on the lateral drift and displacement-ductility capacity of each frame are shown in the subsequent figures (Figure 5-5 and Figure 5-6). These data indicate that the hinge flexibility does affect both capacities. The increase in lateral-drift capacity of the frames is a direct result of the increase in hinge flexibility. The ductility capacity is increased when an elastic hinge is used rather than a rigid one. The ductility capacity of the frames with the strong and intermediate hinges increases with respect to that of the frames with elastic hinges. These effects are actually due to the change in yield and maximum displacements. On the other hand, the effects of the weak hinge are not predictable. When weak-bond conditions exist in a structure, a detailed analysis such as the one presented in this report needs to be performed and the hinge behavior be monitored.

The moment-rotation response of the hinges in the tension and compression columns of each frame is shown in the figure (Figure 5-7). The effects of axial force on hinge response are consistent with those on flexural columns. The data indicate that since the elastic strength of the hinge is the same as the elastic strength of the column, bar elongation and pullout contribute inelastic deformations once the column critical section yields. This phenomenon cannot be prevented and is often taken into account in design using yield-penetration models. What these results indicate, however, is that the stability of the hinge needs to be maintained throughout the column inelastic response. In design, providing confinement to the hinge zone prevents hinge-

strength loss. Proper anchorage of the column longitudinal reinforcement, however, must also be provided in the design by improving the bond conditions in the anchorage zone. This is achieved by providing one of the following:

- Bar-termination in standard hook or T-head
- Sufficient beam depth for development length
- Transverse reinforcement in the joint region to maintain the integrity of the concrete in the anchorage zone and to provide a force-transfer mechanism.

5.2.2. Effects of Joint Flexibility on Capacity Curve

The effects of the joint flexibility on the capacity curve of each frame are shown in Figure 5-8. The data show that joint flexibility does not affect the response of a bridge frame, but joint strength does. This is evident when the effect is observed on the lateral drift and displacement-ductility capacity of the frames (Figure 5-9 and Figure 5-10). Joint effects come into play when the joint shear demands are sufficiently high, as shown in the response of the joints in the tension and compression sides of each frame (Figure 5-11). When joint demands are sufficiently high and joint shear strength is comparatively low, joint flexibility can lead to a significant reduction in strength, as well as possible premature structural collapse, as shown in the response of Frame 4. The apparent increase in lateral-deformation capacity of the Type4 joint in Frame 4 should not be relied on, because this type of joint is not expected to sustain such large deformations.

In design, it is recommended to limit the joint response in the elastic range. This can be achieved by strengthening the joint in one of the following manners:

- Provide transverse reinforcement in the joint region
- Increase the joint size by increasing the beam depth.

Improved joint response can also be achieved by decreasing the demands on the joint by limiting column strength by limiting size and amount of longitudinal reinforcement.

In the evaluation of existing structures, it is important that the strength of and demands on the beam column connection be estimated properly. This estimation should be based on the size of the members framing into it, the amount of member longitudinal and transverse reinforcement and the geometric configuration of the connection. The post-yield strength of the joint should be evaluated to determine whether the joint is expected to lose strength or not, as this determines whether the joint response is acceptable or not. This evaluation should be based on the amount and distribution of the longitudinal and transverse reinforcement in the joint region, as well as the geometric configuration of the connection. When a beam-column joint is not expected to remain elastic, a detailed analysis such as the one presented in this report should be performed and the joint response be monitored.

5.3. Nonlinear Dynamic Analysis

The finite-element model was subjected to simultaneous vertical gravity load in the superstructure and a seismic input motion at the supports. The effects of the local flexibilities on the nonlinear dynamic response were studied independently. The same variation of hinge and joint flexibilities as in the nonlinear static analysis were used. In the figures, each graph represents the response of an individual frame to various ground motions. The response parameter of interest is shown in the vertical axis, while the hinge or joint type is shown in the horizontal axis.

The effect of hinge flexibility on the maximum lateral-drift demand on each frame subjected to near-field and far-field ground motions is shown in the figures (Figure 5-12 and Figure 5-13). The data indicate that while the maximum lateral drift is affected by the hinge flexibility, the effect is negligible, and is due in the slight variation in shift in natural period of the structure. No significant difference in response is noted between near-field and far-field ground motions. The effect of joint flexibility on the dynamic response of the structure indicates that the only measurable effect is the shift in natural frequency between the case of a rigid joint and the elastic one (Figure 5-14 and Figure 5-15).

The effect of the collapse of the weak joint in Frame 4 is noted when the ratio maximum-displacement demand to lateral-deformation capacity is plotted (Figure 5-16 and Figure 5-17). While the displacement demand may seem to not be affected by joint flexibility, the reduced displacement capacity needs to be taken into account. The same data plotted for the effects of hinge flexibility indicate a reduction in demand/capacity ratio (Figure 5-18 and Figure 5-19). This reduction is due to the increase in lateral-deformation capacity resulting from the added flexibility.

5.4. Tables

Table 5-1. Design Parameters of Test Frames

Frame ID	1	2	3	4
Column Diameter (ft)	5.5	5.5	6.5	6.5
Col. Long. Steel Ratio	1.25%	1.75%	1.25%	1.75%
Column Length (ft)	36	36	36	36
Beam Width	5.5	5.5	6.5	6.5
Beam Depth (ft)	8	8	8	8
Beam Length (ft)	36	36	36	36
Column Axial Load/$A_g f_c'$	9.64%	9.64%	5.71%	5.71%
Superstructure Weight (kip)	3000	3000	3000	3000
Elastic Period (sec)	0.64	0.64	0.393	0.393
Ground-Motion Factor	1.5	1.5	1.5	1.5

Table 5-2. Ground-Motion Data Set: small magnitude, small distance

Record ID	Event	Year	Magnitude	R (km)	PGA (g)	PGV (cm/s)
IV79cal	Imperial Valley	1979	6.5	23.8	0.078	13.3
IV79chi	Imperial Valley	1979	6.5	28.7	0.27	24.9
IV79e01	Imperial Valley	1979	6.5	15.5	0.139	16
IV79e12	Imperial Valley	1979	6.5	18.2	0.116	21.8
IV79e13	Imperial Valley	1979	6.5	21.9	0.139	13
IV79qkp	Imperial Valley	1979	6.5	23.6	0.309	36.3
IV79wsm	Imperial Valley	1979	6.5	15.1	0.11	21.9
LV80kod	Livermore	1980	5.8	21.7	0.04	4
LV80srm	Livermore	1980	5.8	17.6	0.076	6.1
MH84agw	Morgan Hill	1984	6.2	29.4	0.032	5.5
MH84g02	Morgan Hill	1984	6.2	15.1	0.069	2.9
MH84g03	Morgan Hill	1984	6.2	14.6	0.194	11.2
MH84gmr	Morgan Hill	1984	6.2	14	0.113	6
PM73phn	Point Mugu	1973	5.8	25	0.112	14.8
PS86psa	N. Palm Springs	1986	6	16.6	0.187	12.2
WN87cas	Whittier Narrows	1987	6	16.9	0.332	27.1
WN87cat	Whittier Narrows	1987	6	28.1	0.042	3.8
WN87flo	Whittier Narrows	1987	6	17.9	0.115	7.1
WN87w70	Whittier Narrows	1987	6	16.3	0.151	8.7
WN87wat	Whittier Narrows	1987	6	24.5	0.104	9

Table 5-3. Ground-Motion Data Set: small magnitude, large distance

Record ID	Event	Year	Magnitude	R (km)	PGA (g)	PGV (cm/s)
BO42elc	Borrego	1942	6.5	49	0.068	3.9
CO83c05	Coalinga	1983	6.4	47.3	0.131	10
CO83c08	Coalinga	1983	6.4	50.7	0.098	8.6
IV79cc4	Imperial Valley	1979	6.5	49.3	0.128	15.6
IV79cmp	Imperial Valley	1979	6.5	32.6	0.186	13.9
IV79dlt	Imperial Valley	1979	6.5	43.6	0.238	26
IV79nil	Imperial Valley	1979	6.5	35.9	0.109	11.9
IV79pls	Imperial Valley	1979	6.5	31.7	0.057	5.4
IV79vct	Imperial Valley	1979	6.5	54.1	0.167	8.3
LV80stp	Livermore	1980	5.8	37.3	0.073	7.6
MH84cap	Morgan Hill	1984	6.2	38.1	0.099	4.9
MH84hch	Morgan Hill	1984	6.2	32.5	0.071	7.4
MH84sjb	Morgan Hill	1984	6.2	30.3	0.036	4.4
PS86h06	N. Palm Springs	1986	6	39.6	0.063	4.4
PS86ino	N. Palm Springs	1986	6	39.6	0.064	6.6
WN87bir	Whittier Narrows	1987	6	56.8	0.299	37.8
WN87cts	Whittier Narrows	1987	6	31.3	0.051	3.5
WN87har	Whittier Narrows	1987	6	34.2	0.071	7.3
WN87sse	Whittier Narrows	1987	6	35.7	0.042	3.9
WN87stc	Whittier Narrows	1987	6	39.8	0.118	5.1

Table 5-4. Ground-Motion Data Set: large magnitude, small distance

Record ID	Event	Year	Magnitude	R (km)	PGA (g)	PGV (cm/s)
IV40elc	Imperial Valley	1940	7	12	0.215	30.2
LD92yer	Landers	1992	7.3	24.9	0.245	51.5
LP89agw	Loma Prieta	1989	6.9	28.2	0.172	26
LP89cap	Loma Prieta	1989	6.9	14.5	0.443	29.3
LP89g03	Loma Prieta	1989	6.9	14.4	0.367	44.7
LP89g04	Loma Prieta	1989	6.9	16.1	0.212	37.9
LP89gmr	Loma Prieta	1989	6.9	24.2	0.226	16.4
LP89hch	Loma Prieta	1989	6.9	28.2	0.247	38.5
LP89hda	Loma Prieta	1989	6.9	25.8	0.279	35.6
LP89svl	Loma Prieta	1989	6.9	28.8	0.207	37.3
NR94cnp	Northridge	1994	6.7	15.8	0.42	60.8
NR94far	Northridge	1994	6.7	23.9	0.273	15.8
NR94fle	Northridge	1994	6.7	29.5	0.24	26.2
NR94glp	Northridge	1994	6.7	25.4	0.206	7.4
NR94hol	Northridge	1994	6.7	25.5	0.231	18.3
NR94stc	Northridge	1994	6.7	13.3	0.368	28.9
SF71pel	San Fernando	1971	6.6	21.2	0.174	14.9
SH87bra	Superstition Hills	1987	6.7	18.2	0.156	13.9
SH87icc	Superstition Hills	1987	6.7	13.9	0.358	46.4
SH87wsm	Superstition Hills	1987	6.7	13.3	0.172	23.5

Table 5-5. Ground-Motion Data Set: large magnitude, large distance

Record ID	Event	Year	Magnitude	R (km)	PGA (g)	PGV (cm/s)
BM68elc	Borrego Mountain	1968	6.8	46	0.057	13.2
LD92ind	Landers	1992	7.3	55.7	0.109	15.2
LD92psa	Landers	1992	7.3	37.5	0.089	13.8
LP89a2e	Loma Prieta	1989	6.9	57.4	0.171	13.7
LP89fms	Loma Prieta	1989	6.9	42.4	0.141	12.9
LP89hvr	Loma Prieta	1989	6.9	31.6	0.134	15.4
LP89sjw	Loma Prieta	1989	6.9	32.6	0.112	15.7
LP89slc	Loma Prieta	1989	6.9	36.3	0.194	37.5
NR94bad	Northridge	1994	6.7	56.1	0.1	5.8
NR94cas	Northridge	1994	6.7	49.6	0.136	7.1
NR94cen	Northridge	1994	6.7	30.9	0.322	22.9
NR94jab	Northridge	1994	6.7	46.6	0.068	7.6
NR94lh1	Northridge	1994	6.7	36.3	0.087	9.4
NR94loa	Northridge	1994	6.7	42.4	0.152	8
NR94lv2	Northridge	1994	6.7	37.7	0.063	7.2
NR94php	Northridge	1994	6.7	43.6	0.067	16.9
NR94pic	Northridge	1994	6.7	32.7	0.186	14.3
NR94sor	Northridge	1994	6.7	54.1	0.063	5.9
NR94sse	Northridge	1994	6.7	60	0.194	12.1
NR94ver	Northridge	1994	6.7	39.3	0.153	10.1

5.5. Figures

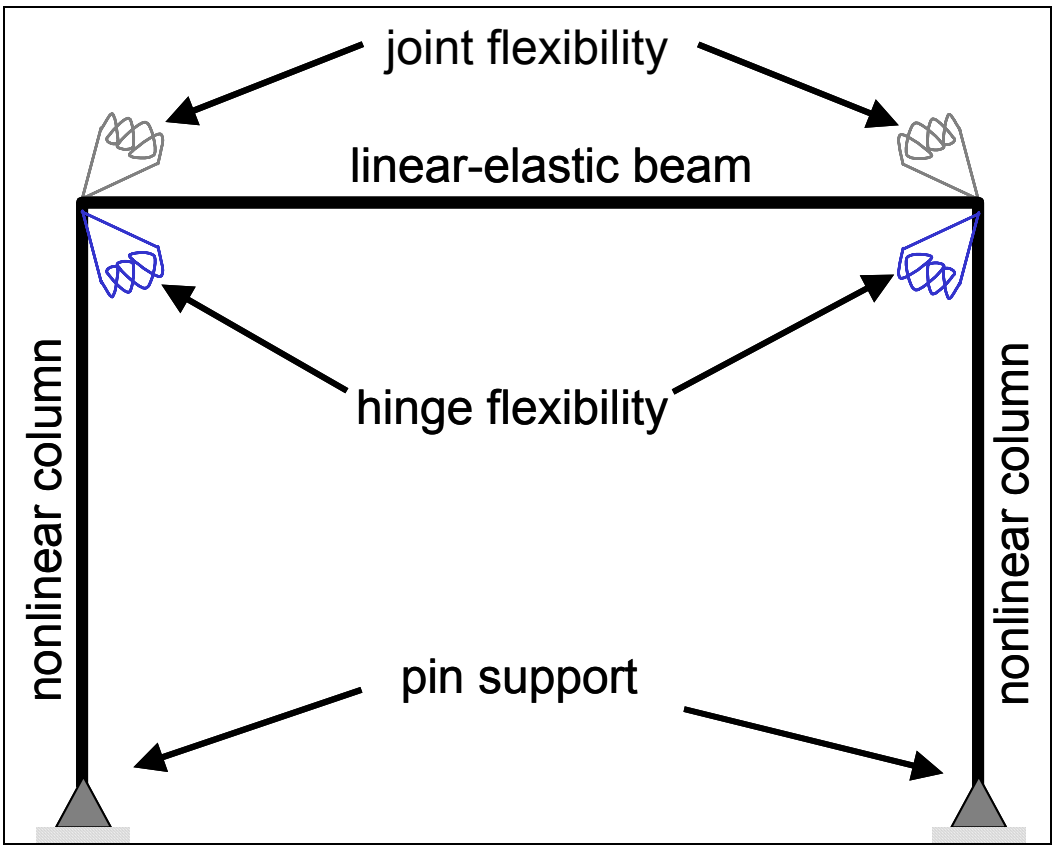

Figure 5-1: Graphical Representation of Finite-Element Model

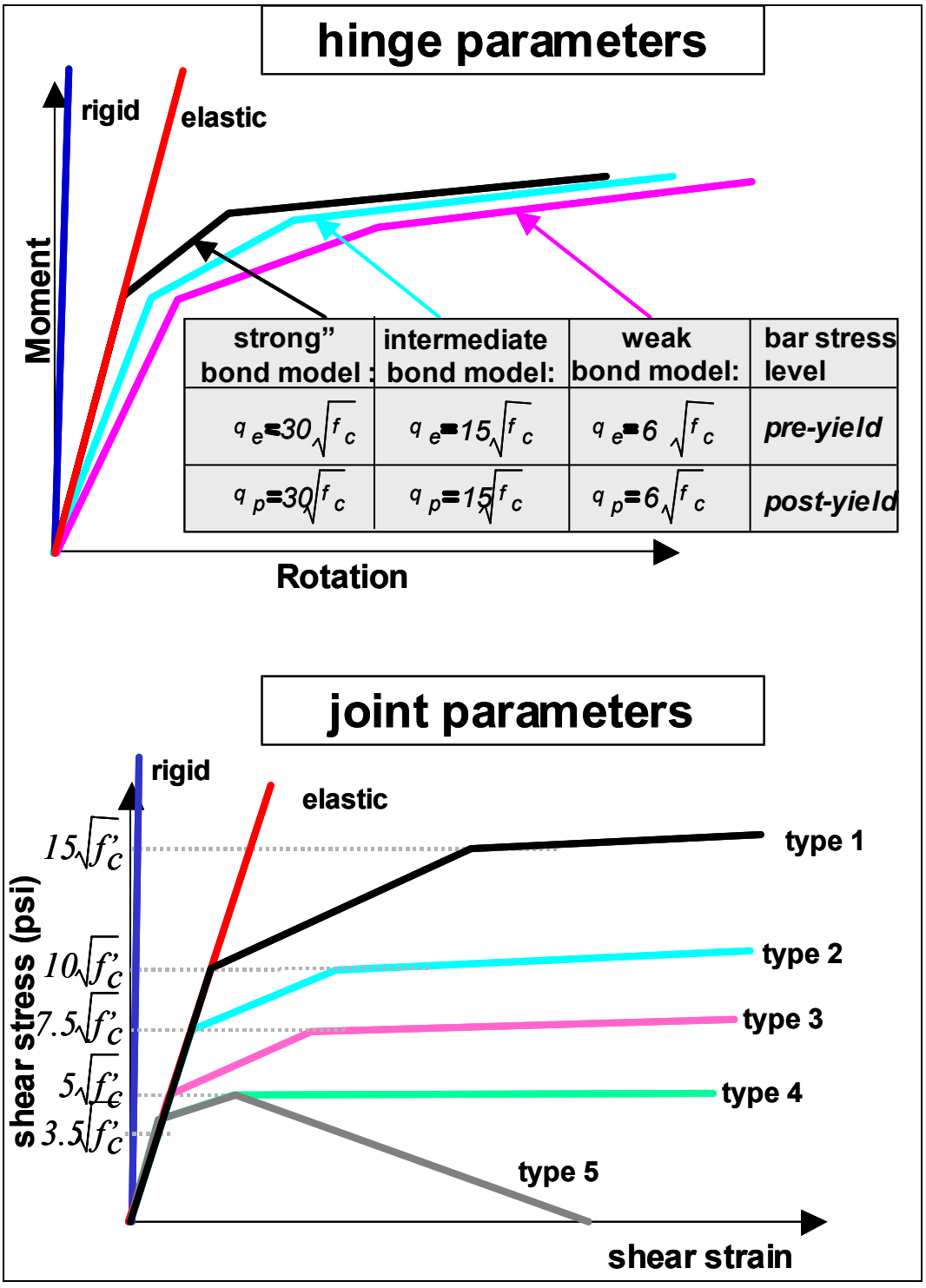

Figure 5-2: Hinge and Joint Parameters

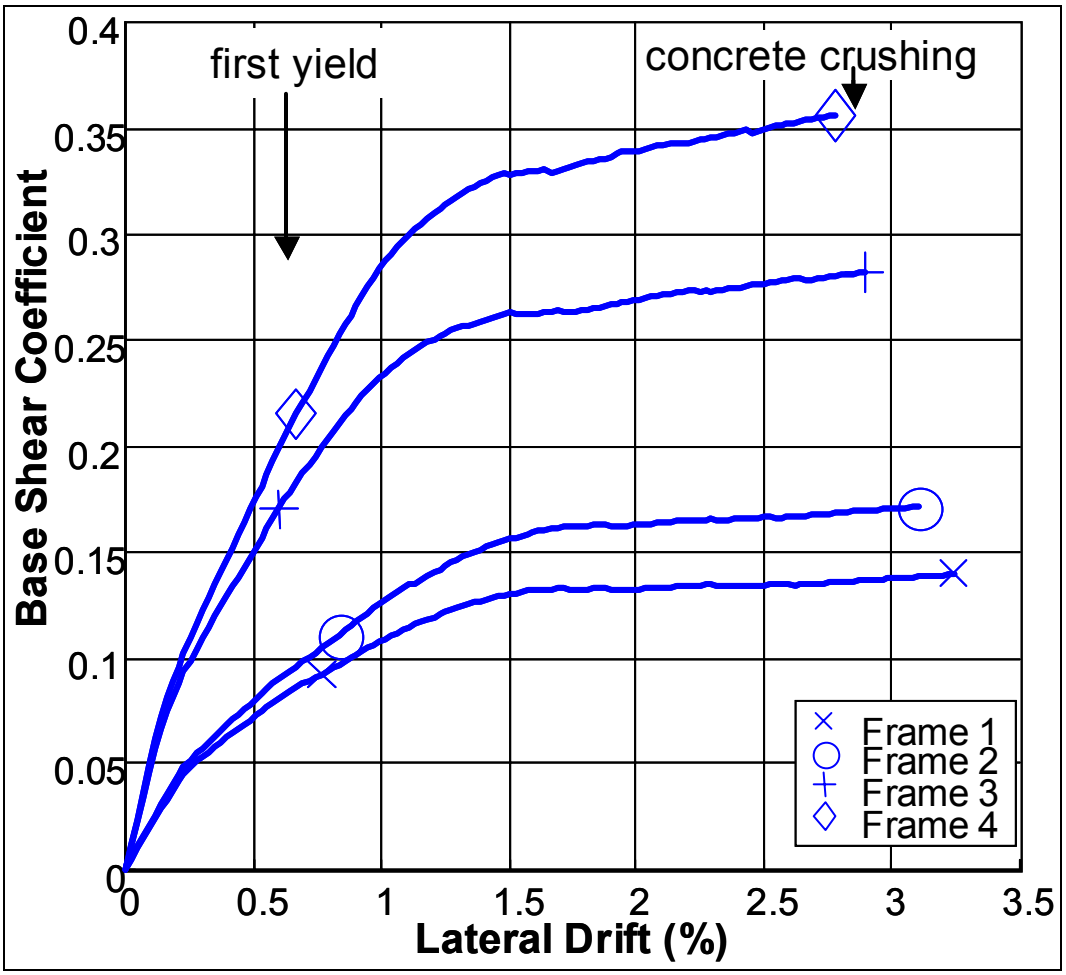

Figure 5-3: Lateral-Load Response of Frames -- Flexure Only

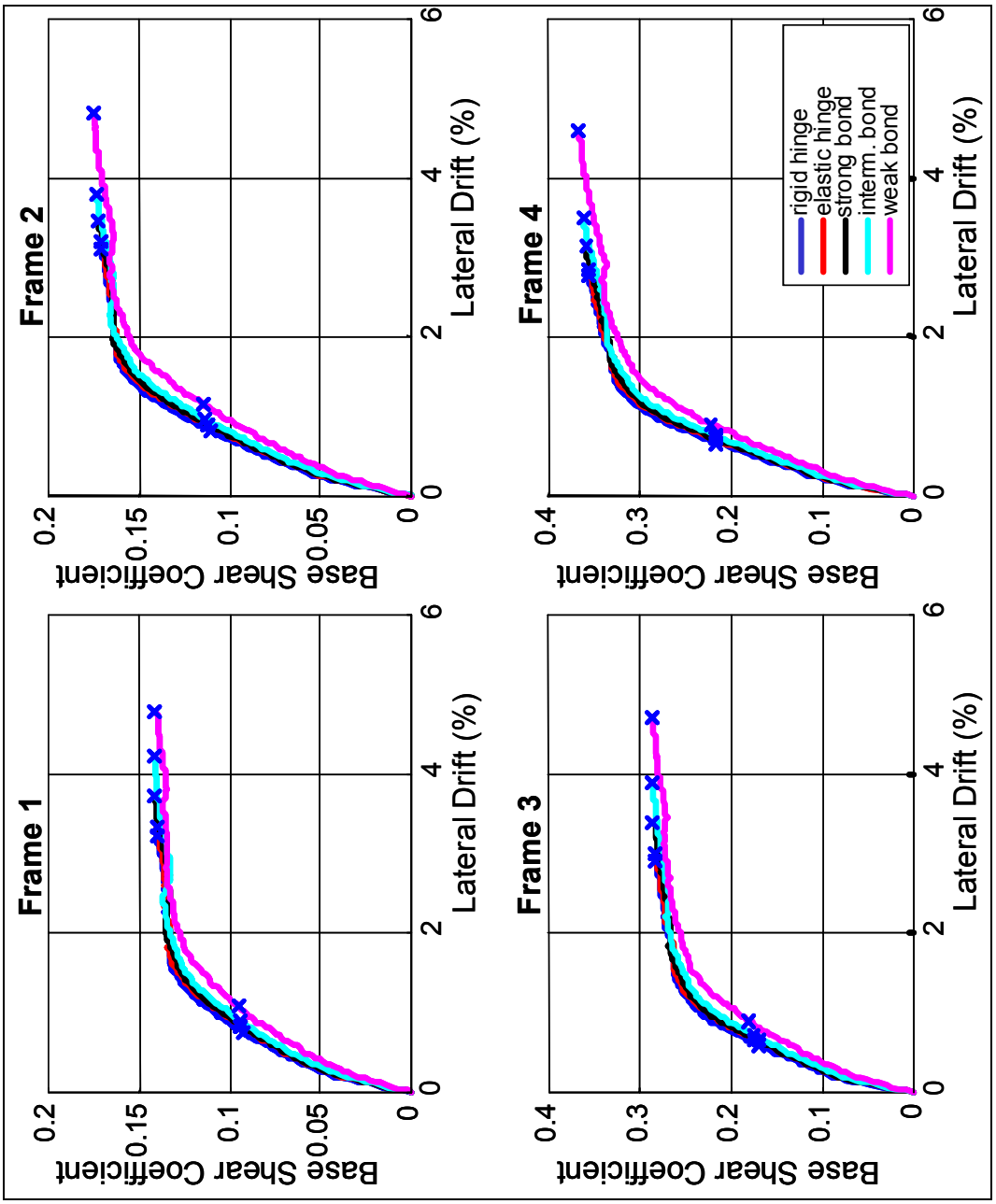

Figure 5-4: Effect of Hinge Flexibility on Capacity Curve (rigid joints)

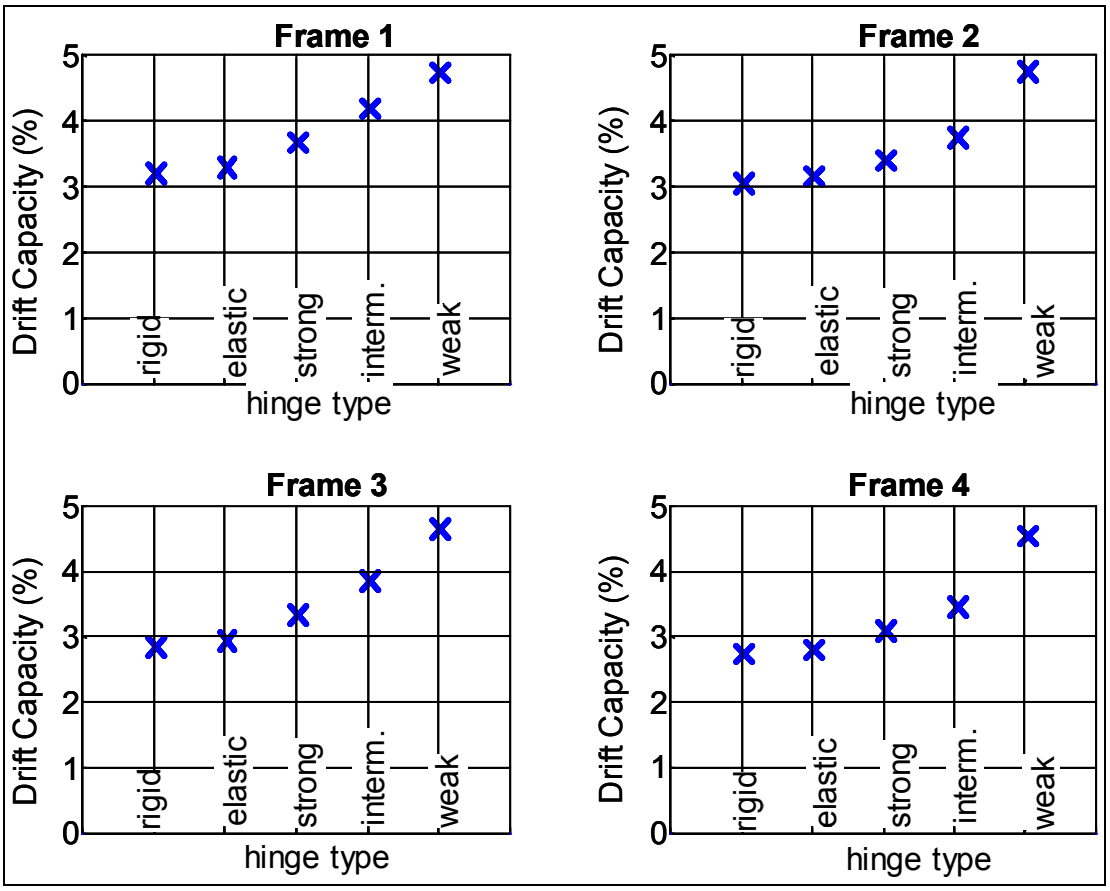

Figure 5-5: Effect of Hinge Flexibility on Maximum Drift Capacity (rigid joints)

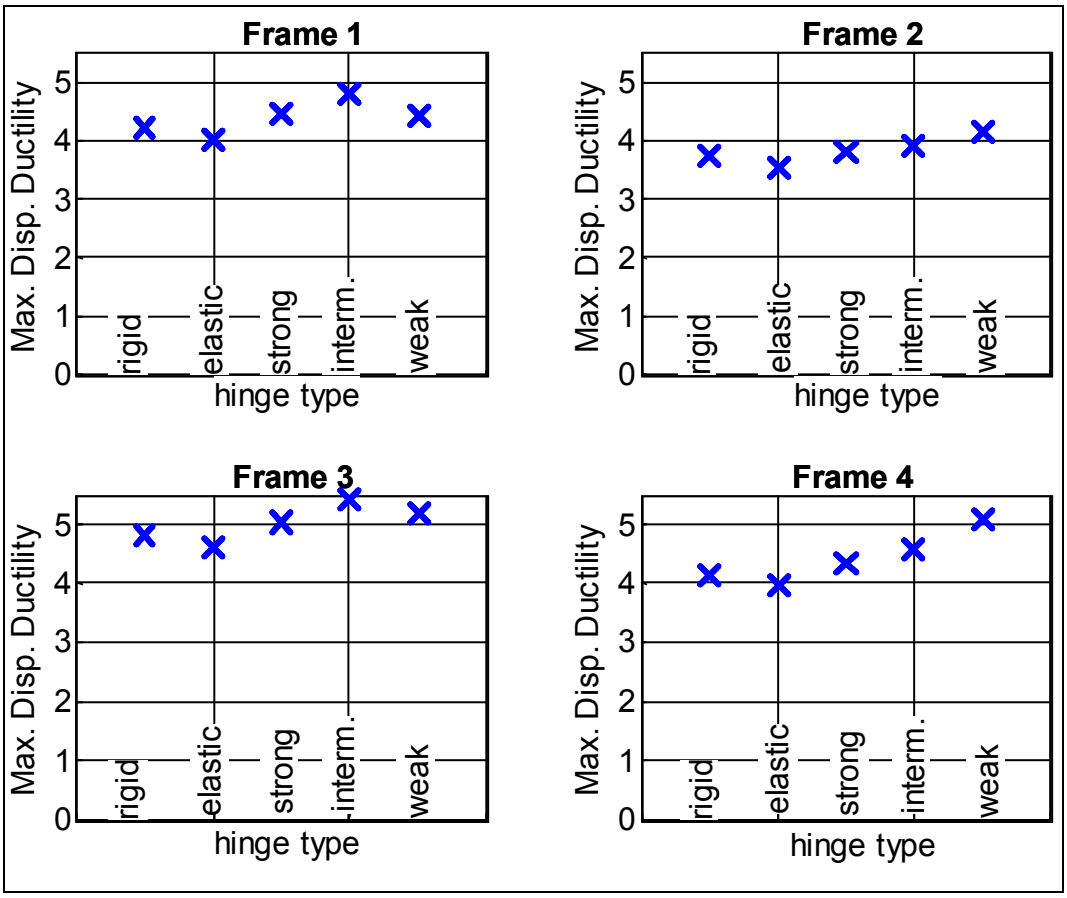

Figure 5-6: Effect of Hinge Flexibility on Maximum Displacement Ductility Capacity (rigid joints)

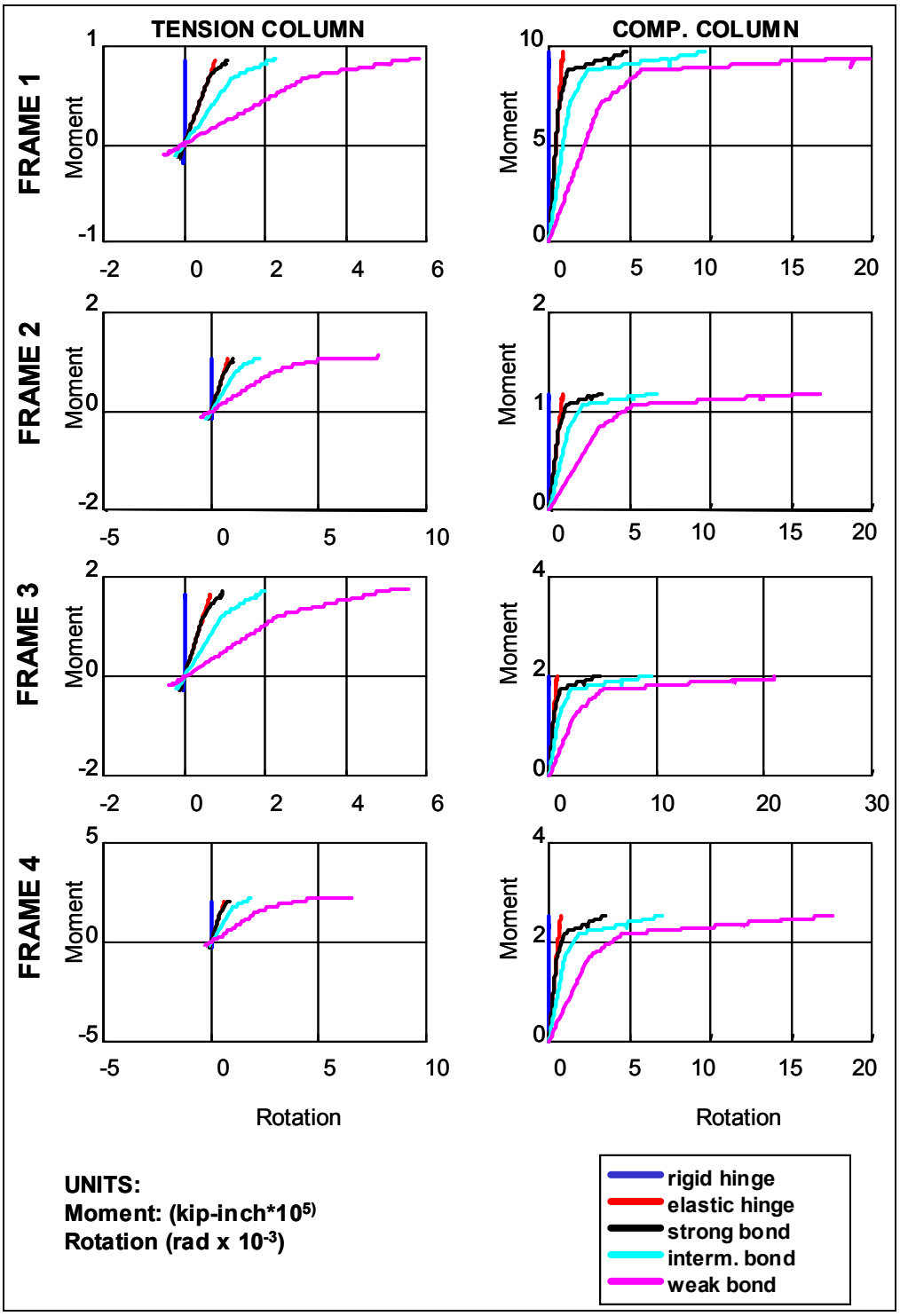

Figure 5-7: Flexible-Hinge Response during Pushover Analysis (rigid joints)

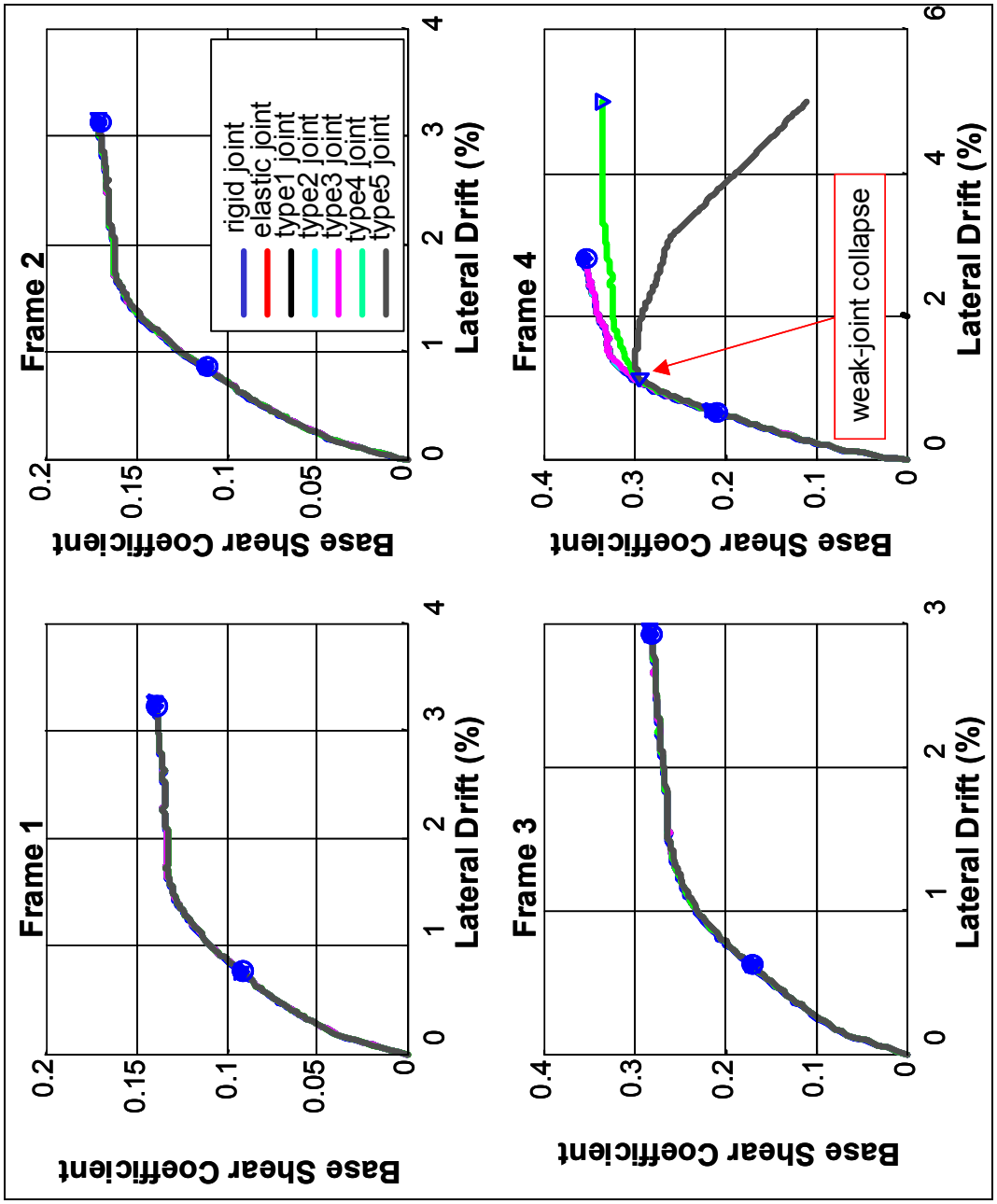

Figure 5-8: Effect of Joint Flexibility on Capacity Curve (rigid hinges)

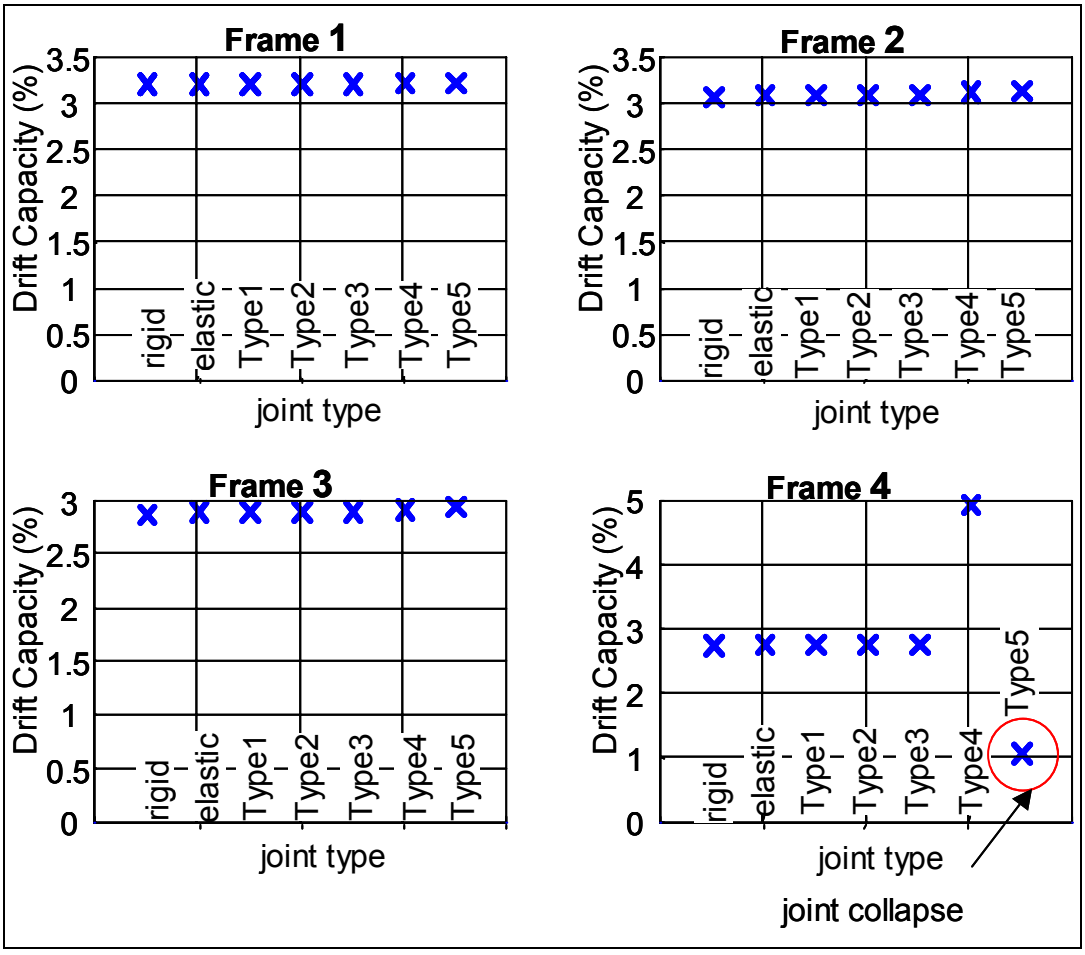

Figure 5-9: Effect of Joint Flexibility on Maximum Drift Capacity (rigid hinges)

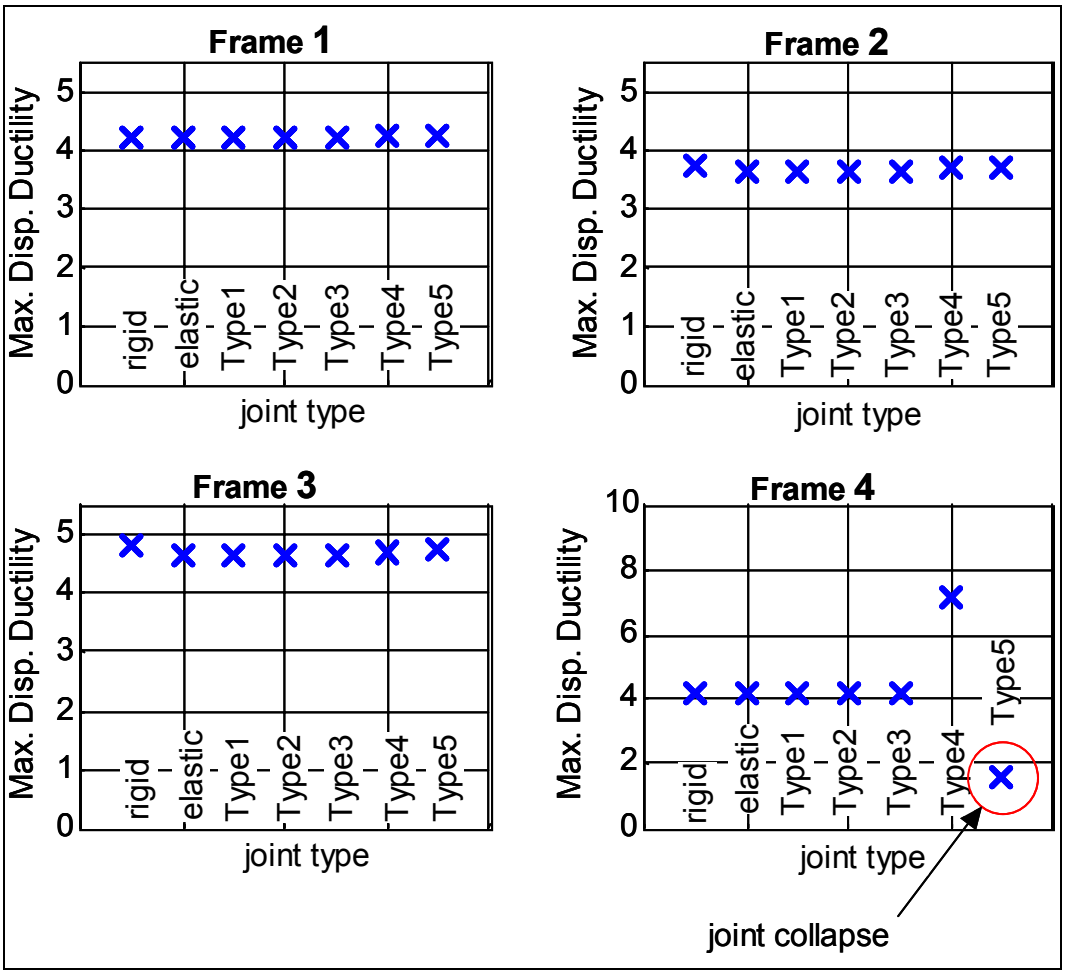

Figure 5-10: Effect of Joint Flexibility on Maximum Displacement Ductility Capacity (rigid hinges)

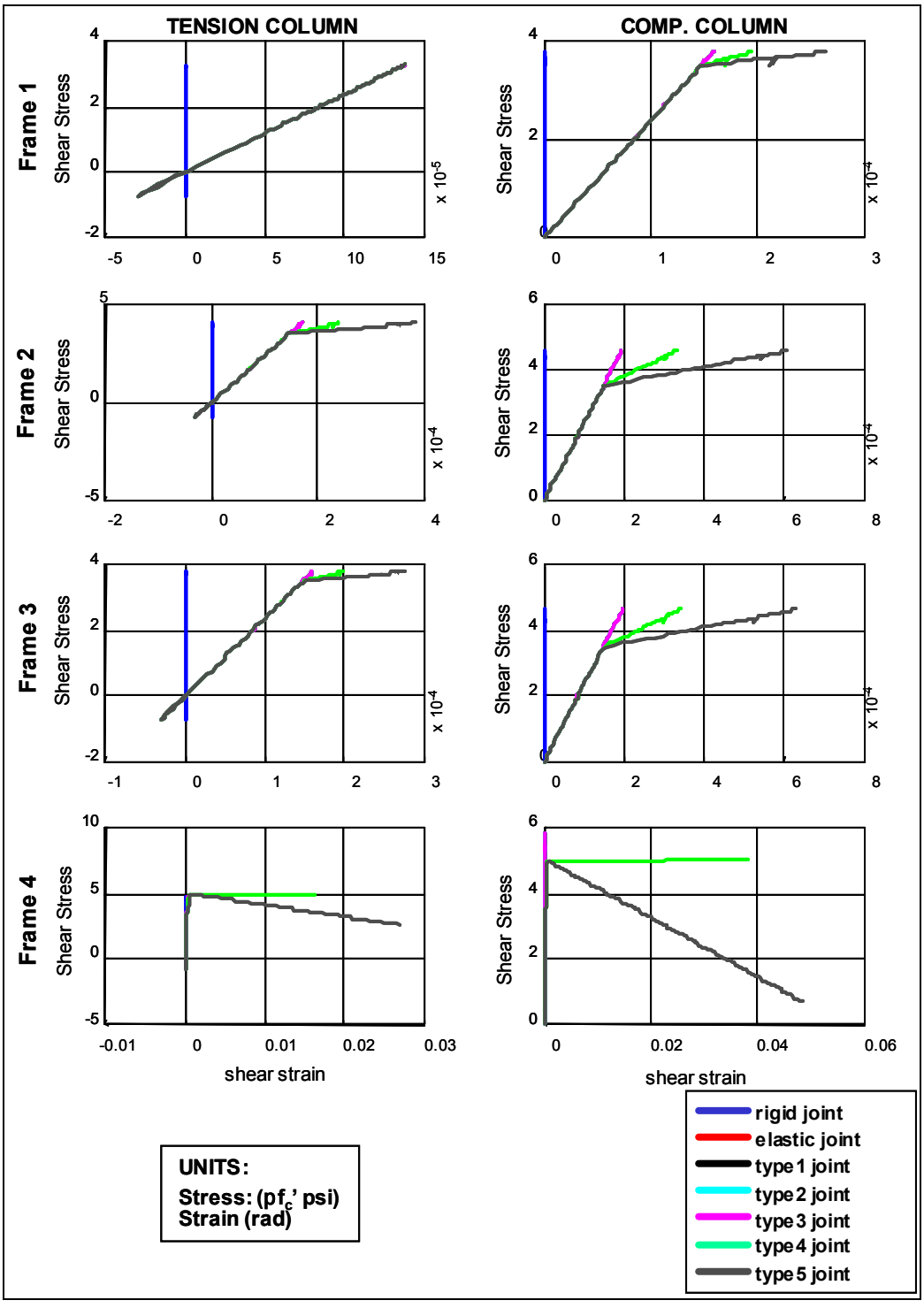

Figure 5-11: Flexible-Joint Response during Pushover Analysis (rigid hinges)

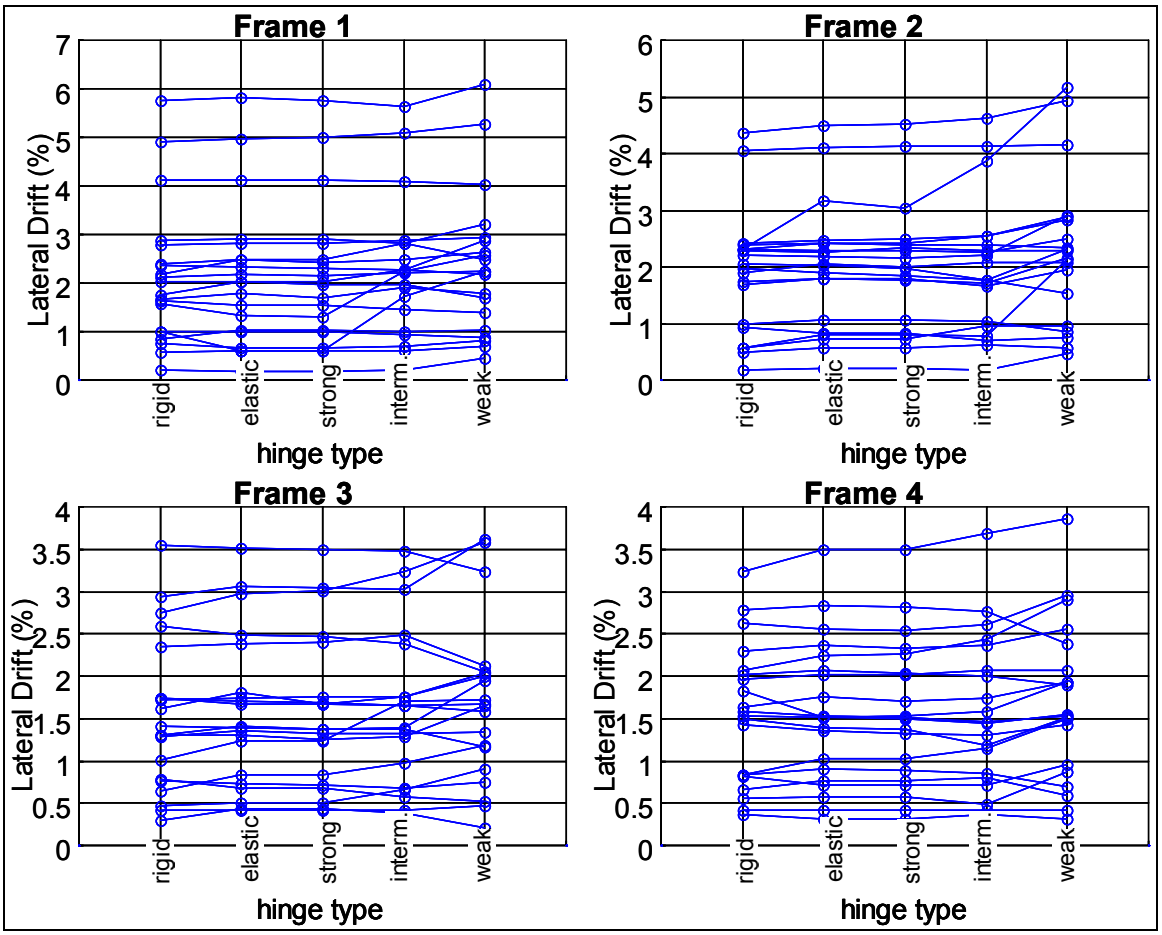

Figure 5-12: Effect of Hinge Flexibility on Max. Lateral Drift -- Near-Field Ground Motions

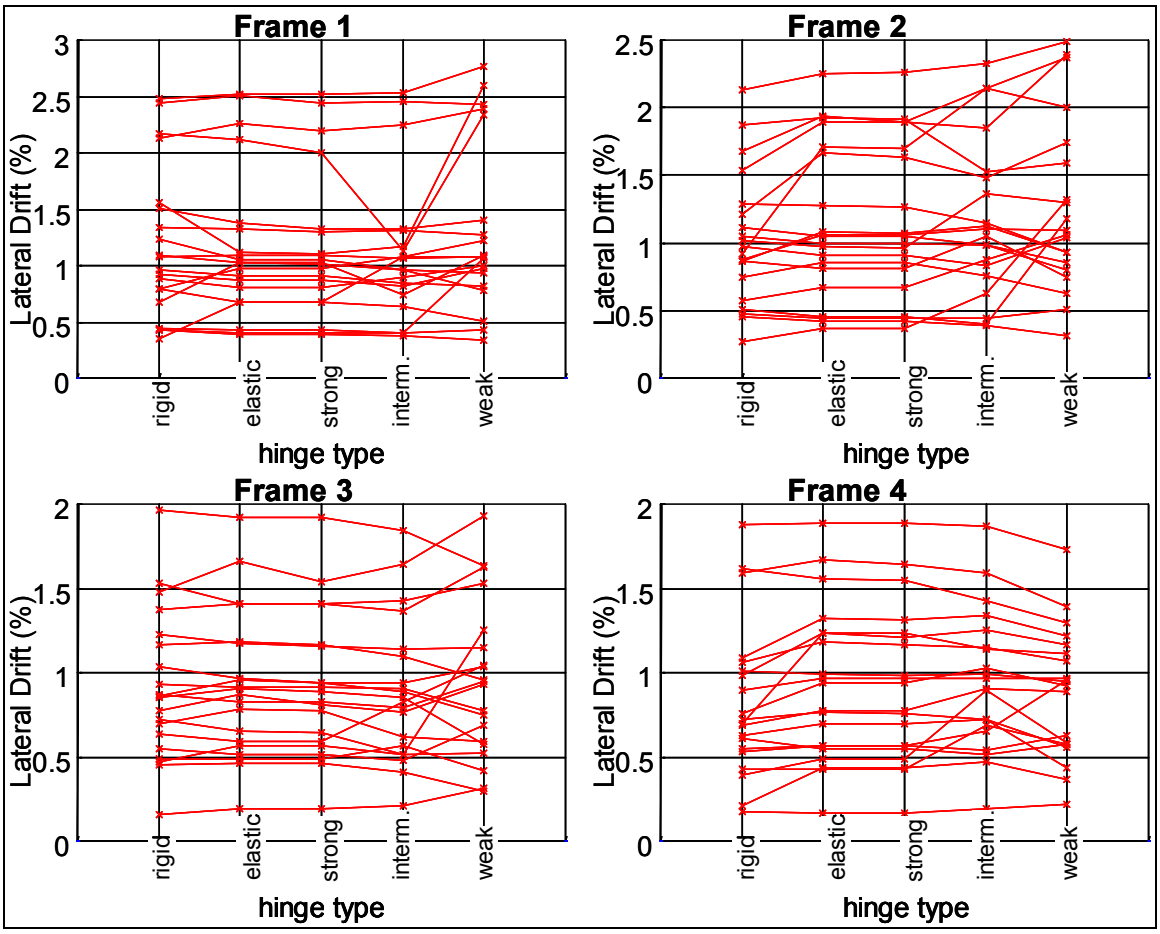

Figure 5-13: Effect of Hinge Flexibility on Max. Lateral Drift -- Far-Field Ground Motions

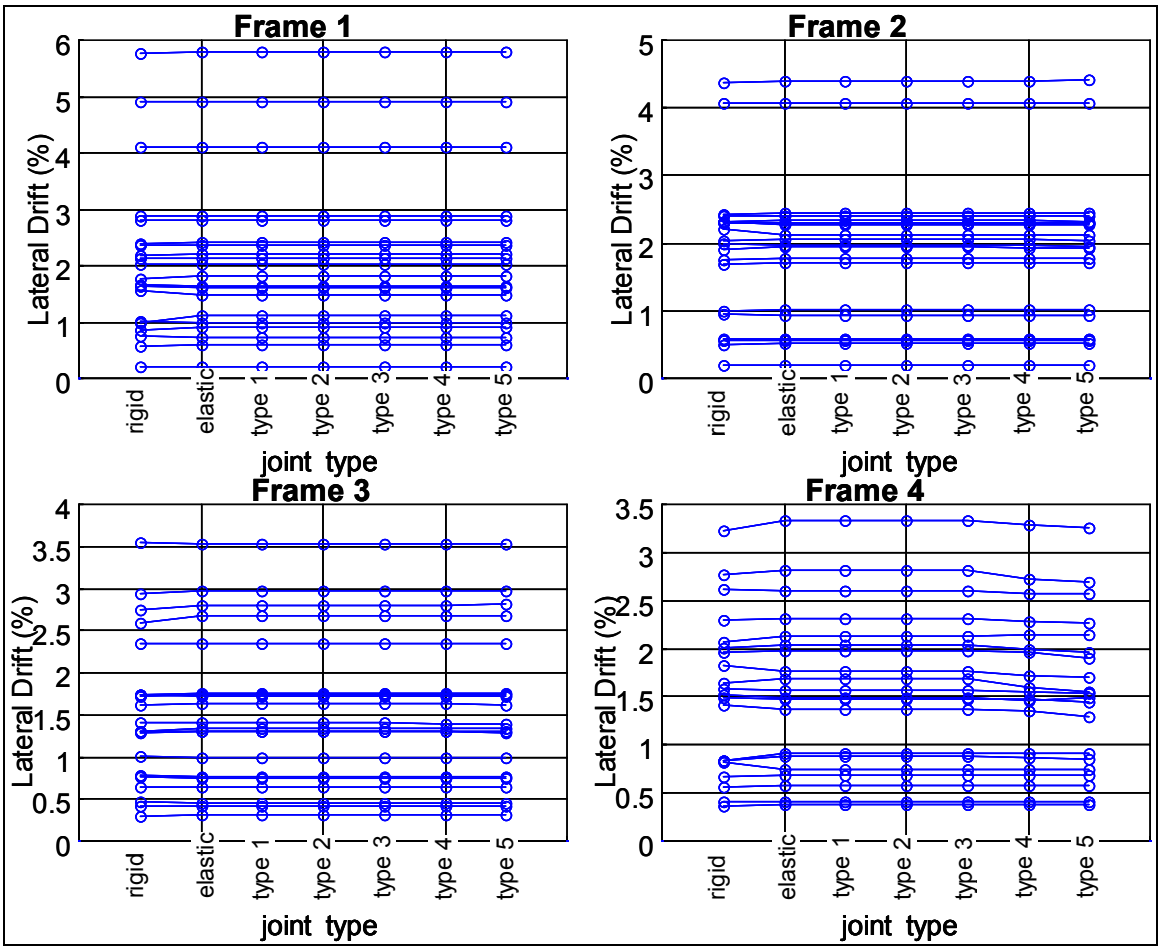

Figure 5-14: Effect of Joint Flexibility on Max. Lateral Drift -- Near-Field Ground Motions

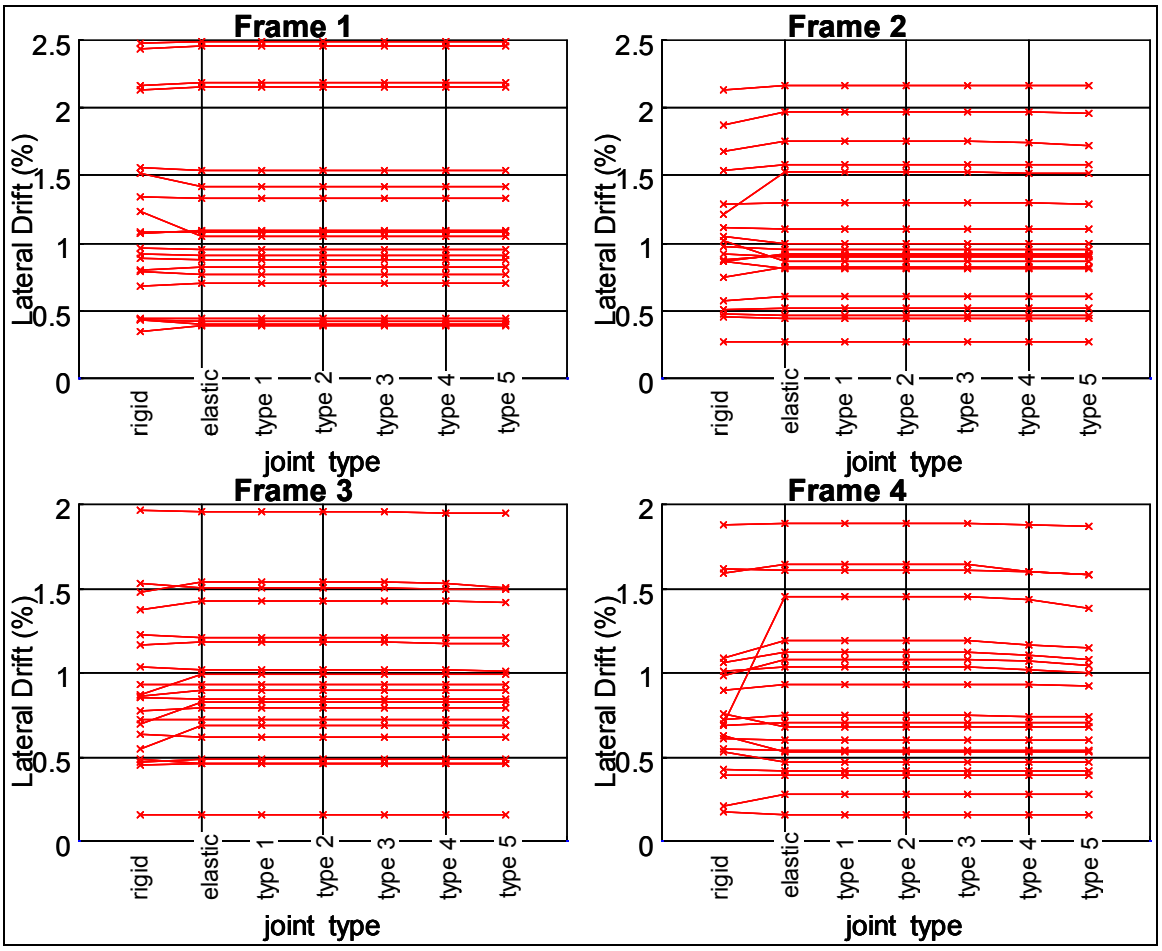

Figure 5-15: Effect of Joint Flexibility on Max. Lateral Drift -- Far-Field Ground Motions

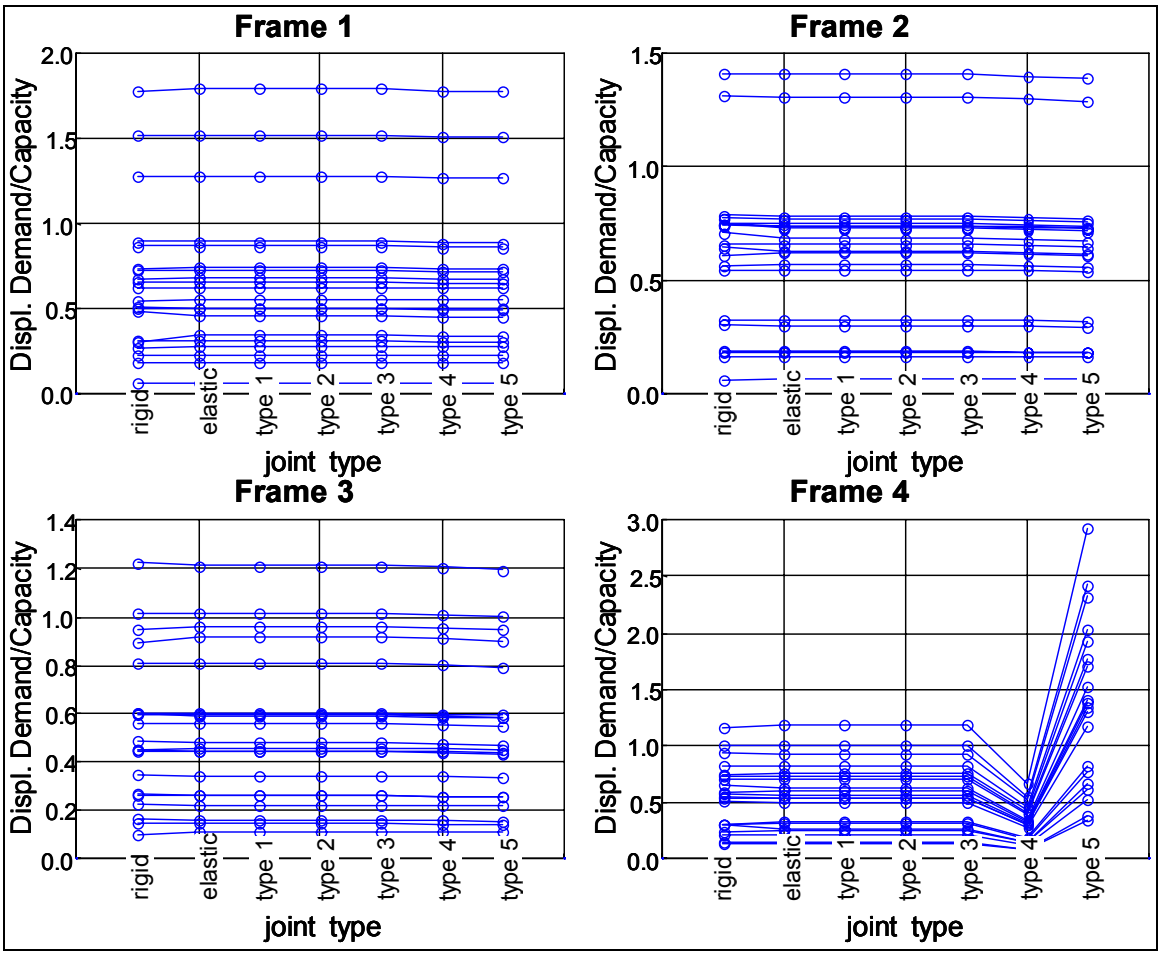

Figure 5-16: Effect of Joint Flexibility on Ratio of Max Displacement Demand to Capacity -- Near-Field Ground Motions

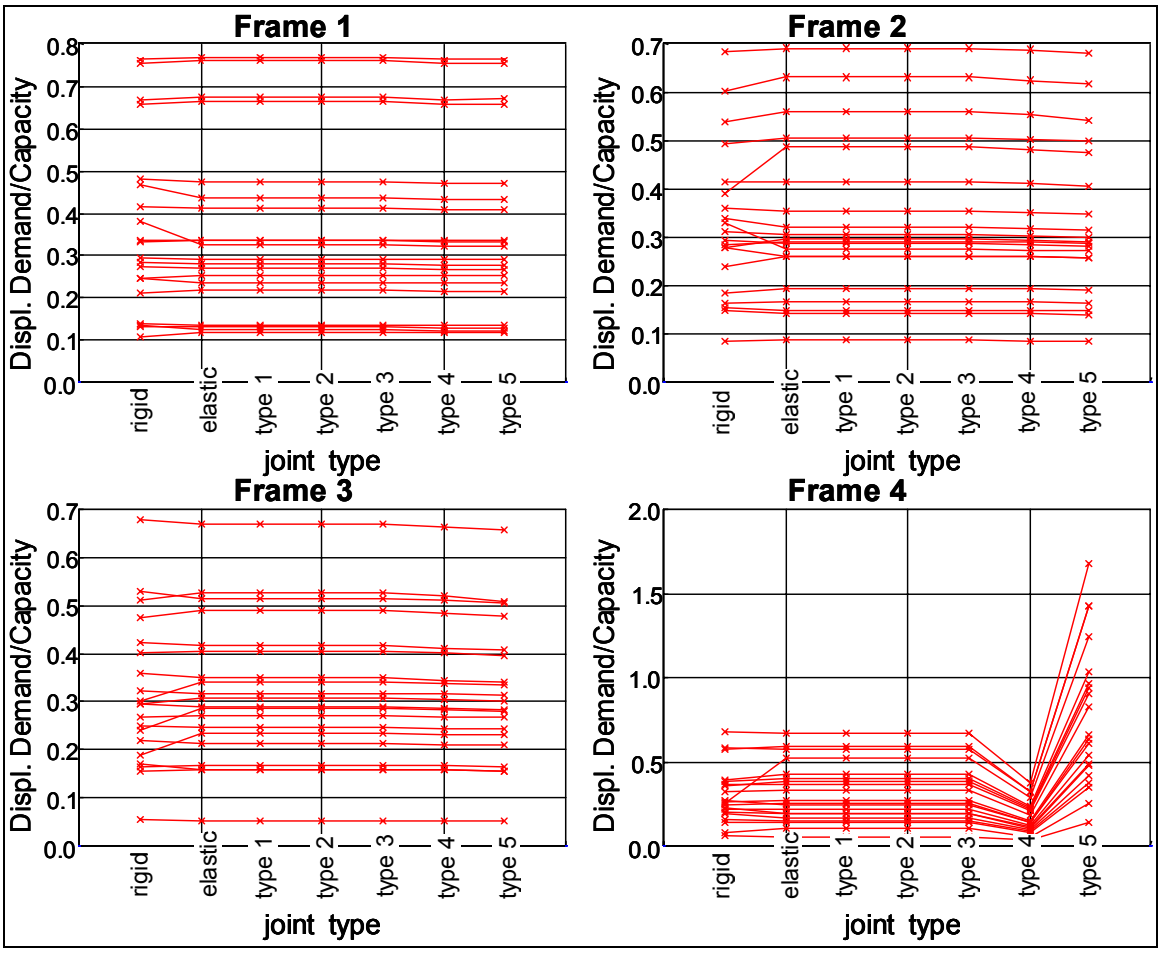

Figure 5-17: Effect of Joint Flexibility on Ratio of Max Displacement Demand to Capacity -- Far-Field Ground Motions

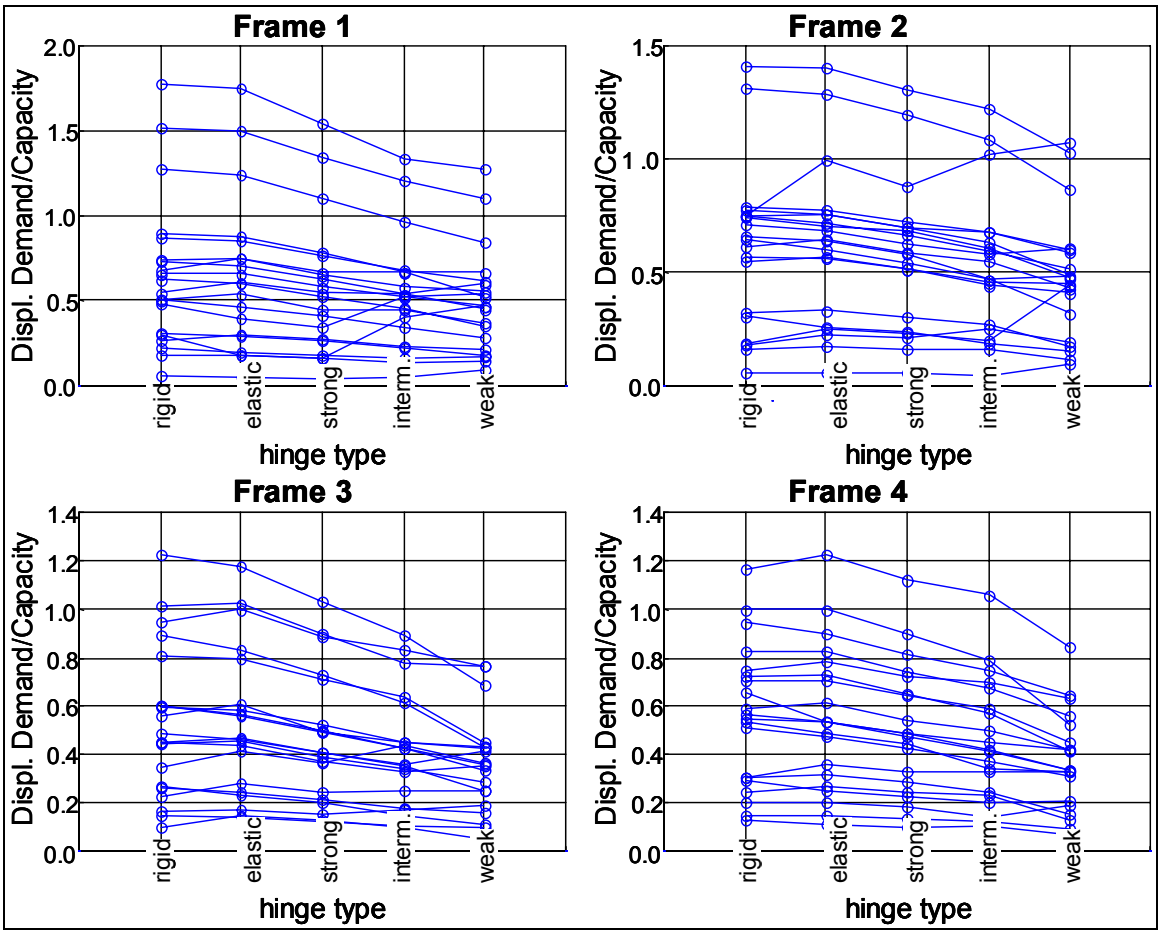

Figure 5-18: Effect of Hinge Flexibility on Ratio of Max Displacement Demand to Capacity -- Near-Field Ground Motions

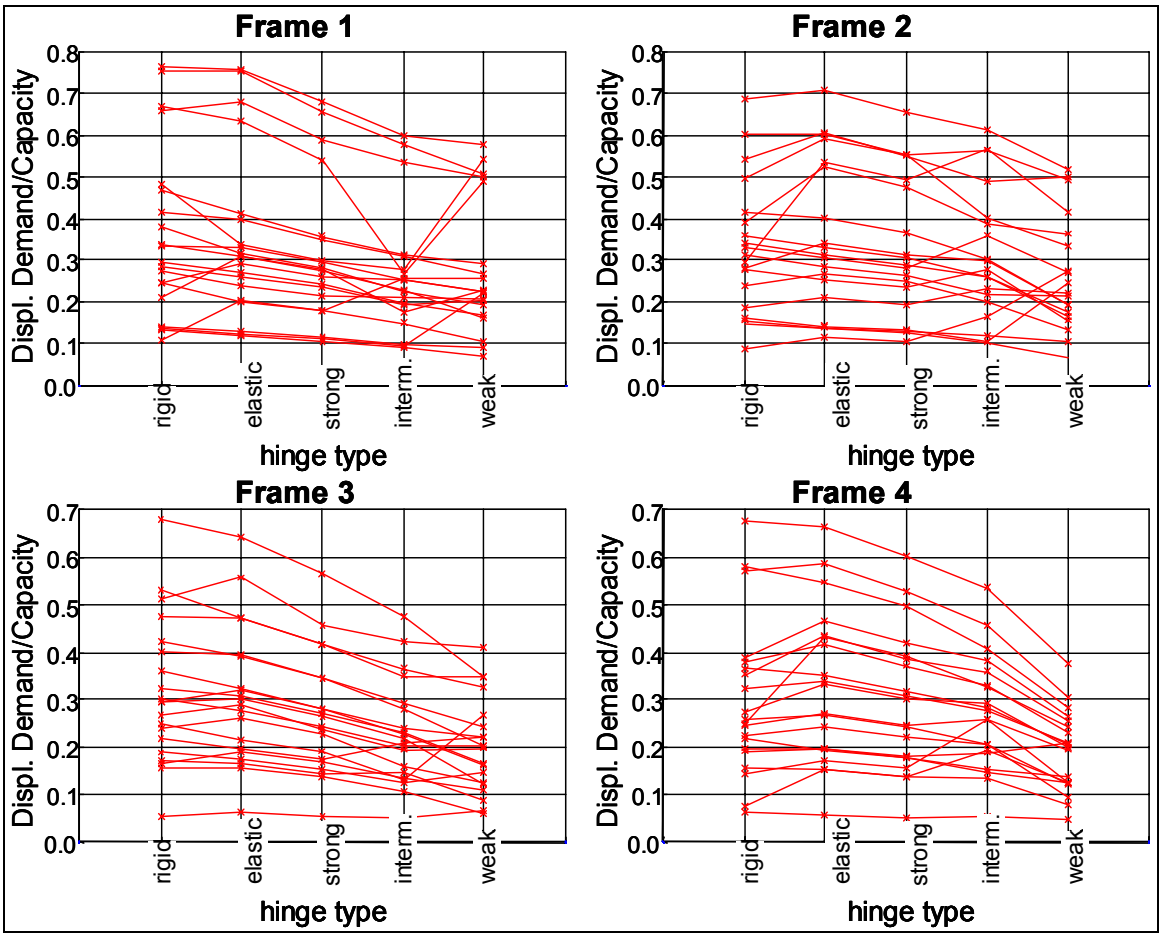

Figure 5-19: Effect of Hinge Flexibility on Ratio of Max Displacement Demand to Capacity -- Far-Field Ground Motions

Chapter 6. Consistent Linearization for Seismic Design

Trends in seismic structural engineering are heading toward performance-based design. The objective of this methodology is to design a structure that satisfies a specified performance criterion when subjected to a specified level of gravity and seismic input (design loads). Generally, there are three limit states defining performance criteria: serviceability limit state, reparability limit state, and ultimate limit state. To this end, an accurate assessment of the structural capacities and demands must be performed in the design procedure. For design purposes, a simplified methodology using static pushover analyses and elastic dynamic analyses is preferred.

Current procedures using pushover analysis are typically able to characterize the lateral-deformation capacities and lateral-load strengths of structural systems accurately. Available simplified analysis tools used to calculate the force and deformation demands, however, are limited in their ability to capture the dynamic characteristics of a nonlinear-inelastic prototype in a linear-elastic analysis model.

The proposed procedure is a consistent linearization methodology able to characterize the dynamic characteristics of the prototype structure at the prescribed limit state and give accurate demand estimates. Nonlinear stiffness reduction and hysteretic energy dissipation (damping) are the primary dynamic characteristics considered in the model. In the methodology, the linearized properties are localized to the structural elements. Hence, the methodology can be

applied to multiple-degree-of-freedom systems, even though it is herein implemented for a SDOF system.

Because local strains and deformations are considered to be the best indicators of damage, displacement-based design, where member deformation demands and capacities are the primary design parameters, was used as the framework for the proposed procedure. Here, the deformation capacities calculated from a nonlinear static pushover analysis are compared to the deformation demands calculated from a linear-elastic dynamic analysis.

The Capacity-Spectrum Method (CSM), developed by Freeman, has recently been recognized as a useful graphical tool in the interpretation of design results for SDOF systems [Freeman, 1994]. In this method, the capacity and demand are compared graphically. The static pushover curve, lateral-load coefficient versus deformation, represents the capacity curve. The demand curve, acceleration coefficient versus displacement, is obtained from an elastic spectral analysis at the prescribed damping level. When these two curves are plotted on the same graph (CSM), their intersection represents the maximum demand for the design of the structure, termed *performance point.* The relative location of the performance point along the capacity curve with respect to the limit-state point, termed *design point*, determines the effectiveness of the design. This method of interpreting results graphically, however, may be limited to single-degree-of-freedom systems.

6.1. Research Significance

The proposed methodology represents an improvement in simplified-analysis procedures so that more accurate demand estimates may be obtained in design. What is unique to the proposed methodology is the linearization procedure. In this procedure, the stiffness characteristics of the linearized structure are determined from the characteristics of the nonlinear

prototype structure at the prescribed limit state, calculated directly from the pushover analysis. No assumption is necessary for the distribution of damage among and within the structural elements at the limit state since it is determined in the pushover analysis.

While other methodologies reduce the structural model into a single-degree-of-freedom system, the linearized structure in the proposed procedure maintains the same structural elements as the prototype, with the nonlinearities localized to regions of the structural components. This procedure enables the determination of local element demands and capacities. Hence structural elements can be designed locally from the calculated element demands once the global deformation criteria are met.

6.2. Proposed Procedure

In the proposed procedure the lateral-deformation capacity, defined by a prescribed limit state, and the lateral-deformation demand of a structure subjected to the design gravity and seismic loads are calculated and compared. The procedure consists of four phases: the capacity phase, the linearization phase, the demand phase, and the evaluation phase. In the capacity phase the structure is subjected to a nonlinear static pushover analysis that includes the gravity loads. The limit-state lateral force and deflection, together with the local element loads and deformations, are obtained from this analysis. In the linearization phase, a linear-elastic model of the prototype structure is developed from the results of the pushover analysis. The linearized stiffness and damping characteristics are determined in this phase. In the demand phase the linearized model is subjected to the design loads and the lateral-deflection demand is calculated from a linear-elastic dynamic analysis. The capacity and demand are compared in the evaluation phase. This phase leads to an iterative design procedure that converges to the desired design

point. For a single-degree-of-freedom system, the Capacity-Spectrum Method can be used in the graphical evaluation of capacity and demand.

6.2.1. Capacity Phase

The nonlinear static pushover analysis is performed on the structure to determine its internal load and deformation characteristics and resulting lateral-load resistance at incremental lateral-deformation levels. The calculated lateral-deformation capacity at the prescribed limit state is ultimately compared to the demand calculated in the analysis phase to evaluate the design.

In the static pushover analysis, the structure is subjected to simultaneous gravity loads and an incremental displacement at the lateral degree of freedom. The lateral resisting force at the base is determined from state determination, compatibility, and equilibrium at each deflection increment. The analysis is terminated when the prescribed limit state is reached. The limit state can be defined as the point at which a critical section reaches a prescribed curvature. The prescribed curvature can correspond to a certain strain level in the material.

At the limit state, the internal loads and deformations of each structural component are determined. These element loads and deformations are used to calculate the linearization parameters and to determine local demands once the global-response criteria have been satisfied.

6.2.1.a. Bilinear Representation of Push-Over Curve

The nonlinear load-deformation curve of the structure can be represented by a bilinear approximation, as shown in Figure 6-1. This bilinear approximation is used to define the ductility capacity of the structure. The bilinear approximation has four defining characteristics: the

effective initial stiffness, the yield point deflection, the post-yield stiffness, and the limit-state point.

The initial stiffness, K_1, represents the elastic stiffness. In a system where gradual yielding occurs, this stiffness is taken as the secant in the pushover curve, passing through the lateral displacement and load when first yielding occurs. Gravity moments have a measurable effect on this stiffness.

The maximum load and deformation at the limit state, F_u and Δ_u respectively, in the bilinear approximation are equal to those of the nonlinear curve. The post-yield stiffness, K_2, is calculated by equating the monotonic strain energy in the nonlinear curve to that in the bilinear approximation to the limit state. The nonlinear strain energy, W_o, is calculated by integrating numerically the force-deformation response to the maximum displacement, as shown in Figure 6-2(a). The strain energy corresponding to the bilinear approximation is also equal to the area within the bilinear force-deformation relationship, as shown in Figure 6-2(b). By equating the strain energies, the post-yield stiffness, K_2, is calculated from:

$$K_2 = \frac{2 \cdot F_u \cdot \Delta_u - 2 \cdot K_1 \cdot W_o - F_u^2}{\Delta_u^2 \cdot K_1 - 2 \cdot W_o} \qquad (6-1)$$

This stiffness is typically represented as a fraction, α, of the initial stiffness K_1:

$$\alpha = \frac{K_2}{K_1} \qquad (6-2)$$

6.2.2. Yield Point & Displacement Ductility

The effective yield lateral load, F_y, and deformation, Δ_y, are defined by the intersection of the two segments in the bilinear approximation to the pushover curve shown in Figure 6-1:

$$F_y = \frac{F_u - K_2 \cdot \Delta_u}{1 - \alpha} \qquad (6-3)$$

$$\Delta_y = \frac{F_y}{K_1} \qquad (6-4)$$

The yield and limit-state deformations are used to defined the limit-state displacement ductility, μ_Δ:

$$\mu_\Delta = \frac{\Delta_u}{\Delta_y} \qquad (6-5)$$

6.2.3. Linearization Phase

In the linearization phase a linear-elastic model whose dynamic characteristics are representative of those of the nonlinear structure at the limit state is formulated. The linearized dynamic characteristics are defined to yield the same maximum load and deformation demands as the nonlinear-inelastic structure when subjected to the same design loads, gravity and seismic.

The stiffness reduction and hysteretic energy dissipation characterizing the dynamic response of the nonlinear structure are represented in the elastic model through a linearized-stiffness model and an equivalent viscous-damping model. While the damping linearization is performed at the global level, the stiffness linearization is performed at the element level.

6.2.3.a. Linearized Stiffness

To simplify the analysis procedure, elements that are designed to remain elastic during the response are assumed to remain elastic. Because their stiffness remains constant for all levels of deformation and is defined *a priori*, the selection of this stiffness is left to the choice of the designer. These elements are not considered in the linearization procedure.

The development of the proposed procedure is based on the assumption that flexural deformations control the structural response. The flexural stiffness, *EI*, is typically characterized in terms of the slope of the bending-moment versus curvature response at the section level, shown in Figure 6-3. Modeling difficulties arise in a yielding system where the nonlinear response of the structural materials results in a reduction in flexural stiffness with increasing deformation, as shown in the figure. The modeling of this stiffness reduction as the structure reaches the prescribed limit state is the basis of the proposed linearization procedure.

Typically, a reduced effective stiffness is used to represent the nonlinear inelastic members at the limit state. This effective secant stiffness, EI_{eff}, shown in Figure 6-3, is defined in terms of the cracked stiffness, EI_{cr}, and the curvature *ductility ratio*, μ_ϕ:

$$EI_{eff} = \frac{EI_{cr}}{\mu_\Delta} \qquad (6-6)$$

The curvature ductility ratio is sometimes referred to as *damage ratio*. It is a characteristic that can be correlated to the displacement ductility ratio. Assigning a single reduced-stiffness value to each structural element, as is typically done, does not satisfy all compatibility and equilibrium conditions at the element boundaries and incorrect load distribution between structural members may result in statically indeterminate systems.

The proposed procedure takes into account the variation of damage in the different structural elements by performing a step-by-step static pushover analysis, with a state determination at the end of each step. This procedure allows monitoring of all element sections using calculated moment-curvature relationships at the element-section level and follows the sequence of hinge formation. Damage ratios for the individual structural elements are thus determined from the pushover analysis rather than assumed *a priori* and are particular to each structural element.

In addition, the procedure takes into account the distribution of softening along the nonlinear elements and is able to account for the damage localization by assigning different damage ratios to different regions of the structural elements. For the general case when a structural element is subjected to double bending plastic hinges are expected to localize damage at the two ends while the remainder of the member remains essentially elastic, as shown in Figure 6-4. Here three different linearized stiffnesses can be assigned to the three different regions of the element, as shown in Figure 6-5.

To calculate the linearized stiffness parameters from equilibrium and compatibility conditions, the element actions (bending moment, shear and axial forces) and nodal deformations (translations and rotations) are extracted from the results of the pushover analysis at the prescribed limit state. To maintain proper load and deformation distribution in the structural system, the nonlinear-element boundary conditions, equilibrium and compatibility at the nodes, must be reproduced identically in the linear-elastic analysis at the limit state. Each element is considered individually.

The forces and deformations in the nonlinear and linearized elements at the limit state are shown in Figure 6-4 and Figure 6-5, respectively. The difference between the two models lays in the distribution of stiffness, hence curvature, along the elements. In the nonlinear element, the curvature distribution obeys a nonlinear moment-curvature relationship. In the linearized element, this distribution is simplified to three segmentally uniform elastic stiffnesses, with a corresponding linear curvature.

Compatibility of the relative nodal rotations and translations impose the two equations necessary to calculate the two end-stiffness parameters, EI_a and EI_b, of each element, as shown in Figure 6-5. The linearized stiffness of the central element, EI_o, is assumed constant and equal to the cracked stiffness and is calculated *a priori*.

The curvature distribution along the linearized element is calculated from the bending moment diagram and a linear moment-curvature relationship at the local level. The nodal translation, Δ_b, and rotation, Θ_a, are obtained using the principle of virtual work and are used to determine the stiffness parameters for each column:

$$\Delta_b - \Delta_a - \Theta_a \cdot L = \frac{1}{6}\cdot\frac{b_b^2}{L}\cdot\frac{\left(3\cdot L - 2\cdot b_b\right)\cdot M_b + 2\cdot b_b\cdot M_a}{EI_b} + \frac{1}{6}\cdot\frac{b_a}{L}\cdot\frac{\left(-2\cdot b_a^2 + 3\cdot L\cdot b_a\right)\cdot M_b + \left(6\cdot L^2 - 6\cdot L\cdot b_a + 2\cdot b_a^2\right)\cdot M_a}{EI_a} \ldots + \frac{1}{6}\cdot\frac{1}{L}\cdot\frac{\left(-3\cdot L\cdot b_b^2 + 2\cdot b_a^3 + 2\cdot b_b^3 + L^3 - 3\cdot L\cdot b_a^2\right)\cdot M_b + \left(-2\cdot b_b^3 + 2\cdot L^3 + 6\cdot L\cdot b_a^2 - 2\cdot b_a^3 - 6\cdot L^2\cdot b_a\right)\cdot M_a}{EI_o} \tag{6-7}$$

$$\Theta_b - \Theta_a = \frac{1}{2}\cdot\frac{b_b}{L}\cdot\frac{\left(2\cdot L - b_b\right)\cdot M_b + b_b\cdot M_a}{EI_b} + \frac{1}{2}\cdot\frac{b_a}{L}\cdot\frac{a\cdot M_b + \left(2\cdot L - b_a\right)\cdot M_a}{EI_a} \ldots + \frac{1}{2}\cdot\frac{1}{L}\cdot\frac{\left(L - b_b - b_a\right)\cdot\left[\left(L - b_b - b_a\right)\cdot M_b + \left(L + b_b - b_a\right)\cdot M_a\right]}{EI_o} \tag{6-8}$$

Where *L* is the length of the element and M_a and M_b are the end moments, as shown in the figure. Solving for the stiffness parameters:

$$EI_a = \frac{A1\cdot B2 - A2\cdot B1}{-B3\cdot A1 + \Theta_b\cdot A1 - \Delta_b\cdot B1 + B1\cdot A3} \tag{6-9}$$

$$EI_a = \frac{A1\cdot B2 - A2\cdot B1}{B3\cdot A2 - \Theta_b\cdot A2 + \Delta_b\cdot B2 - B2\cdot A3} \tag{6-10}$$

Where

$$A1 = \frac{1}{6}\cdot\frac{b_b^2}{L}\cdot\left[\left(3\cdot L - 2\cdot b_b\right)\cdot M_b + 2\cdot b_b\cdot M_a\right]$$

$$A2 = \frac{1}{6}\cdot\frac{b_a}{L}\cdot\left[\left(6\cdot L^2 - 6\cdot L\cdot b_a + 2\cdot b_a^2\right)\cdot M_a + \left(-2\cdot b_a^2 + 3\cdot L\cdot b_a\right)\cdot M_b\right] \tag{6-11}$$

$$A3 = \left(\Delta_a - \Theta_a\cdot L\right) + \frac{1}{6\cdot L}\cdot\frac{\left(-3\cdot L\cdot b_b^2 + 2\cdot b_a^3 + 2\cdot b_b^2 + L^3 - 3\cdot L\cdot b_a^2\right)\cdot M_b + \left(-2\cdot b_b^3 + 2\cdot L^3 + 6\cdot L\cdot b_a^2 - 2\cdot b_a^3 - 6\cdot L^2\cdot b_a\right)\cdot M_a}{EI_o}$$

And

$$B1 = \frac{1}{2}\cdot\frac{b_b}{L}\cdot\left[\left(2\cdot L - b_b\right)\cdot M_b + b_b\cdot M_a\right]$$

$$B2 = \frac{1}{2}\cdot\frac{b_a}{L}\cdot\left[\left(2\cdot L - b_a\right)\cdot M_a + b_a\cdot M_b\right] \tag{6-12}$$

$$B3 = \Theta_a + \frac{1}{2\cdot L}\cdot\frac{\left(L - b_b - b_a\right)\cdot\left[\left(L - b_b + b_a\right)\cdot M_b + \left(L + b_b - b_a\right)\cdot M_a\right]}{EI_o}$$

The intermediate-stiffness parameter, EI_o, can be calculated from the yield moment and curvature of the section:

$$EI_o = \frac{M_y}{\Phi_y} \qquad (6-13)$$

The lengths of the end segments, b_b and b_b, are additional parameters calculated from the bending-moment diagram. The length of these segments is equal to the length over which the bending moment exceeds the yield moment. From the bending-moment diagram, the lengths of the end segments are:

$$b_a = \frac{M_a - M_y}{M_a + M_b} \cdot L \qquad (6-14)$$

And

$$b_b = \frac{M_b - M_y}{M_a + M_b} \cdot L \qquad (6-15)$$

The yield moment, M_y, is calculated at the dead-load axial force. The sign convention used in the above expressions is consistent with Figure 6-4 and Figure 6-5.

6.2.3.b. Viscous-Damping Models

The linearized-damping model was formulated from an investigation of the energy-dissipation characteristics of the inelastic and linear-elastic systems. The non-conservative viscous-damping and hysteretic restoring forces in the inelastic system are modeled by the equivalent viscous-damping force in the linear-elastic system. The inertial forces are conservative in both systems, while the restoring force is conservative only in the elastic system.

The viscous-damping energy dissipated by a linear-elastic system having the following properties: mass M, natural frequency ω_n, and damping ratio ξ, subjected to a cycle of sinusoidal force with a rotational frequency of ω_E is defined as the work of the viscous-damping force over

the elastic displacement and is expressed in terms of the maximum displacement response, ξ_{max}:

$$E_{elastic} = \xi \cdot 2 \cdot \pi \cdot \omega_n \cdot \omega_E \cdot M \cdot x_{max}^2 \qquad (6-16)$$

To achieve the maximum deformation response, the frequency of the forcing function is taken equal to the natural frequency of the structure. Using the known relationship between natural frequency, mass and stiffness, *K*, the elastic energy is simplified to:

$$E_{elastic} = \xi \cdot 2 \cdot \pi \cdot K \cdot x_{max}^2 \qquad (6-17)$$

This energy is represented graphically in Figure 6-6.

To calculate the equivalent damping ratio, this dissipated energy is equated to the total energy dissipated by the inelastic system in one cycle. This energy is equal to the work done by the restoring and viscous-damping forces on the nonlinear deformation. To simplify the formulation, it is assumed that the viscous-damping ratio of the inelastic system, ξ_o, is carried over to the elastic system. Thus, the equivalent damping ratio has two components: that representing the hysteretic energy dissipation, E_{hyst}, and that representing the viscous-damping ratio ξ_o. The equivalent damping ratio corresponding to the linearized system, ξ_{eqv}, is thus calculated from the energy balance:

$$\xi_{eqv} = \frac{E_{hyst}}{2 \cdot \pi \cdot K \cdot x_{max}^2} + \xi_o \qquad (6-18)$$

The hysteretic energy, equal to the work done by the restoring force on the inelastic deformation can be calculated from the area within the nonlinear force-deformation response. Different analytical and empirical force-deformation models have been used in the literature, resulting in different expressions for the equivalent damping ratio.

One such expression was proposed by Gulkan [Gulkan, 1974]. It estimates the equivalent damping ratio from the displacement ductility ratio, μ_Δ, measured for a set of experimental frames:

$$\xi_{Gulkan} = 0.2 \cdot \left(1 - \frac{1}{\sqrt{\mu_\Delta}}\right) + 0.02 \qquad (6-19)$$

This expression was developed empirically from an experimental study of one-story, one-bay frames. Using measured quantities, the above expression represents the observed trend in the equivalent damping ratio resulting from the energy balance versus the measured displacement ductility. The definition of displacement ductility in the Gulkan model differs from that of the proposed model.

Another expression, proposed by Kowalsky, also estimates the equivalent damping ratio from the displacement ductility ratio [Kowalsky, 1994]:

$$\xi_{Kowalsky} = \frac{1}{\pi} \cdot \left(1 - \frac{0.95}{\sqrt{\mu_\Delta}} - 0.05 \cdot \sqrt{\mu_\Delta}\right) + 0.05 \qquad (6-20)$$

This procedure is based on equating the strain energy of a single cycle of hysteretic response to that of a single cycle of the viscously damped linearized system. A Takeda-type model was used to define the hysteretic loop, shown in Figure 6-7. [Takeda, 1970].

The procedure of equating the strain and viscous energies of a single cycle of response is also used in the procedure proposed by ATC-40 [Comartin, 1996]. The expression for the equivalent damping ratio is based on the yield and ultimate forces and deflections, defined in Figure 6-8:

$$\xi_{ATC40} = \frac{2}{\pi} \cdot \frac{F_y \cdot \Delta_u - F_u \cdot \Delta_y}{F_u \cdot \Delta_u} \qquad (6-21)$$

For equivalent-damping ratios greater than 16.25%, this factor is reduced to:

$$\xi_{ATC40mod} = 1.13 - 0.51 \cdot \frac{F_y \cdot \Delta_u - F_u \cdot \Delta_y}{F_u \cdot \Delta_u} \qquad (6-22)$$

This model may overestimate damping because its unloading model does not account for the reduction in stiffness during unloading, as shown in the figure.

6.2.3.c. Proposed Equivalent Viscous Damping Ratio

The equivalent damping ratio proposed in this procedure was developed using the same energy-balance procedure and using the Takeda hysteresis model shown in Figure 6-7. In the model used in this procedure, the unloading stiffness is proportional to the initial stiffness. Adapted from Timoshenko, the proportionality factor, β, was set equal to $\mu_\Delta^{-0.5}$

The total hysteretic energy for a single cycle of nonlinear response, as shown in the figure, is equal to:

$$E_{hyster} = 2 \cdot \left(\Delta_u + \frac{F_y}{K_1} \cdot \sqrt{\mu_\Delta} \right) \cdot F_u \qquad (6-23)$$

Substituting the hysteretic-energy expression into the equivalent-damping-ratio expression and manipulating the terms give the proposed expression for the equivalent damping ratio for the linear-elastic analysis given by:

$$\xi_{eqv} = \frac{1}{\pi} \cdot \left(1 - \frac{1-\alpha}{\sqrt{\mu_\Delta}} - \alpha \cdot \sqrt{\mu_\Delta} \right) + \xi_o \qquad (6-24)$$

Even though this expression is similar to that proposed by Kowalsky, the definitions of displacement ductility differ in the two models. The definition proposed in this methodology is consistent with the observed results.

In the proposed expression, the stiffness of the linear-elastic system was set equal to the one corresponding to the secant stiffness to the limit state, as would result from the proposed procedure, shown in Figure 6-1. This expression indicates that the equivalent damping ratio is dependent on the displacement ductility level and the ratio of the post-yield stiffness to the initial stiffness. For the case of μ_Δ=1, α also equals one, and ξ_{eqv} is equal to ξ_o, the viscous-damping ratio of the nonlinear system.

6.2.4. Demand Phase

In the demand-analysis phase, the linearized system, with an effective stiffnesses and an equivalent damping ratio is subjected to the design loads – seismic and gravity. A series of linear-elastic time-history analyses can be performed on the structure to obtain an average value for the maximum demand. These analyses are performed on the linearized structure as a multi-degree-of-freedom system. Otherwise, design spectra can also be used estimating demands. The secant stiffness to the limit state is used to calculate the equivalent elastic period.

Because the damping ratio is a function of the deformation-ductility level, the initial estimate of damping must be corrected on the basis of the actual deformation-demand level. The iteration on the damping ratio converges rapidly and the maximum deformation demand is thus obtained.

6.2.5. Evaluation Phase

In this phase, the calculated capacity and demand are compared to evaluate the design. If the two quantities are equal, the design procedure has converged to the desired performance point. This point corresponds to the design limit state. If the deformation demand exceeds the deformation capacity, or vice versa, the design of the structural system needs to be modified.

Typically, the design variables available for modification are few so that convergence of the design to the prescribed limit state can be reached rapidly.

6.2.5.a. Capacity-Spectrum Method

An alternative method for the evaluation phase, applicable for SDOF systems, is the Capacity Spectrum Method (CSM) [Freeman, 1994]. In this method, the normalized pushover curve and elastic demand spectrum are compared graphically (Figure 6-9). The lateral load is normalized into the lateral-load coefficient by dividing it by the superstructure weight. The spectral acceleration in normalized to the spectral coefficient by dividing it by g, the gravitational acceleration. In this figure, as an example, a set of representative pushover curves is compared to an UBC-type design spectrum. Using this method for the evaluation phase leads to an iteration scheme slightly different from the one described above. Both methods, however, will converge to the same limit state.

6.3. Implementation

The proposed procedure was implemented in the design of a two-column reinforced-concrete bridge bent subjected to gravity and horizontal seismic loads in the plane of the frame. This type of structural system was chosen because it is a simple structure that maintains the characteristics of statically indeterminate structures in a single-degree-of-freedom system. The bent is shown in Figure 6-10, the loading is shown in Figure 6-11.

The objectives of the design process in the proposed methodology are: to calculate the limit-state lateral-deformation capacity of the structural system, compare it to the maximum lateral-deformation demand of the linearized structure subjected to the design loads, and select a design which meets the prescribed performance criteria. This design procedure is presented herein. For validation, a set of ground motions whose mean elastic spectrum is representative of

the design spectrum used in the design was selected. The final structure was thus subjected to the selected ground motions. The resulting mean displacement demand was compared to the demand calculated for the linearized model.

The performance level chosen for the implementation procedure was the ultimate limit state. This limit state was defined as the maximum deformation capacity of the structure. It corresponds to the limiting curvature at the critical section when the extreme compression fiber in the concrete core reaches a strain equal to the maximum strain capacity of confined concrete.

What is particular to the seismic response of bridge structures is that the structural members are designed to have plastic hinges forming at the column ends rather than in the beams, as is typical in building design. The primary consequence of this design method is that the interaction between the column axial load and flexural strength and stiffness becomes important in the design process. The proposed procedure was thus developed to address three primary considerations which arise in the implementation of simplified design and analysis procedures for such statically-indeterminate system: the overturning-moment effects, the effect of beam flexibility on joint restraint, and the additional bending moments due to gravity loads.

6.3.1. Overturning-Moment

The presence of the overturning moment due to the lateral load leads to different axial forces in the two columns, as shown in the support reactions of Figure 6-11. A moment-curvature analysis indicates that the difference in axial load leads to a difference in flexural stiffness, flexural strength, and curvature capacity, between the two columns, as shown in Figure 6-12. Because of the relatively low axial load in bridge columns, well below the balanced point, and because hinges are designed to form in the columns, the additional compression force increases the flexural strength of the “compression column,” while the additional tension force decreases the flexural strength of the “tension column,” with respect to the case of zero

overturning moment. The resulting lack of symmetry between the two columns leads to difficulties in estimating element stiffnesses in the nonlinear range. It is worth noting at this point that the “compression column,” in addition to having limited curvature capacity; it is the stiffer element and thus attracts higher shear forces and corresponding bending moments. Thus, this column controls the response of the structure, even though it has a higher strength.

6.3.2. Beam Flexibility

The relative magnitude-to-column flexural stiffness determines the amount of restraint at the beam-column connection, hence the magnitude of the column bending moment due to the lateral loads at this location. This beam flexibility is due to the first moment of inertia of the beam section and to the length of the beam element. In bridge-design practice the beam is typically assumed to be rigid. The beam-flexibility effect becomes evident when the two limiting cases shown in Figure 6-13 are considered. If the beam is “infinitely flexible,” i.e. significantly more slender than the columns, the portal frame acts as two cantilever columns with the same lateral deflection. The resultant lack of rotational restraint at the beam-column connection induces zero bending moments at the beam end of the columns and zero bending moments and shears in the beam. In this case hinges form only at the base of the columns If the beam is “infinitely rigid,” i.e. significantly more squat than the columns, rotation at the joint is restrained to zero and the system acts as two rigidly-connected columns subjected to double bending. The bending moments at the ends of each column are equal. In this case plastic hinges form at both column ends simultaneously. While the point of inflection of the “infinitely-flexible” beam system was located at the connection, the point of inflection in this case is located at the column mid-height. The behavior of a “real” portal frame with typical member proportions – “flexible beam” – lies between the two limiting cases, depending on the relative stiffness of the beam. Hence, hinges form at the column ends at different times with only one hinge reaching its maximum

deformation capacity, defining the limit state. The magnitude of inelastic demand on the other hinges at the limit state cannot be estimated without a pushover analysis.

6.3.3. Gravity Moments

Consideration of the beam flexibility also leads to consideration of the gravity bending-moments at the joint, which are often neglected. These additional moments amplify the effects of the lateral loads on the column flexural demands near the joints and deamplify these effects at the supports. The symmetric bending moment diagram for the distributed gravity load is compared to the anti-symmetric one for the lateral load in Figure 6-14. It has already been shown that the compression-column bending moments due to the lateral load are higher than those in the tension column because of the higher stiffness. As shown in the figure, the gravity load, uniformly distributed along the beam length, further increases the bending moments in the compression column and reduces those in the tension column. Therefore, accounting for gravity moments at the joints, which is not commonly done, further reduces the lateral-load strength and lateral-deformation capacity of the structural system.

Because the gravity bending moment is higher at the joint than at the support, this load may relocate the plastic hinge from the base of the column to the beam end. The gravity moments have a significant effect on initiation of yield and the corresponding deformation, forcing the formation of the first hinge at the column-joint interface rather than at the support. Hence, when ductility factors are considered, gravity bending moments are important in the calculation of the yield deflection and at low-ductility limit states.

6.3.4. Results

The design characteristics of the test frame are within the typical values currently used in Caltrans design, but are not identical to any particular frame. A set of eight different time

histories was used in the analysis and 5% viscous damping was included in the nonlinear system. The frame had the following characteristics:

- Circular-column diameter: 6ft
- Column height: 30ft
- Rectangular-Beam length: 30ft
- Ratio of beam to column moment of inertia: 1.25
- Column longitudinal-steel ratio: 2.5%
- Ratio of dead-load axial force to nominal axial strength of column: 6%

A pushover analysis of the portal frame was performed to determine (a) the lateral load and deformation response characteristics and (b) the internal loads and deformations necessary to determine the linearized stiffness characteristics. The pushover curve is shown in Figure 6-15. The limit-state load and deformation, F_u and Δ_u, for the portal frame were calculated to be 1218 kips and 15.7 inches, respectively. The initial and secondary stiffnesses, K_1 and K_2, were calculated to be 138.3 and 41.5 kip/inch, respectively. The corresponding yield force and deformation, F_y and Δ_y, were calculated to be 810 kip and 5.9 inches, respectively, with a displacement-ductility capacity of 2.7.

The natural period of the linearized structure was calculated to be 1.8 seconds. The damping ratio of the linearized structure, including the 5% viscous damping, was calculated to be 10.1%. The mass of the system, corresponding to a column axial load of 6% of its gross capacity, was $2.7*10^6$ lb-mass. Using these properties, the linearized system was subjected to eight ground motions, scaled to correspond to the prescribed limit state.

To assess the validity of the methodology, the response of the linearized system was compared to the response of the nonlinear prototype subjected to the same input ground motion. The ratio of maximum elastic-deformation demand to maximum nonlinear-deformation demand was calculated for each time history. The mean and standard deviation for all eight time histories

were calculated to be 1.06 and 12.7%, respectively. An example of this comparison is shown in Figure 6-16. This figure corresponds to the response to the Tabas ground motions in the X direction, scaled by a factor of 1.25.

6.4. Figures

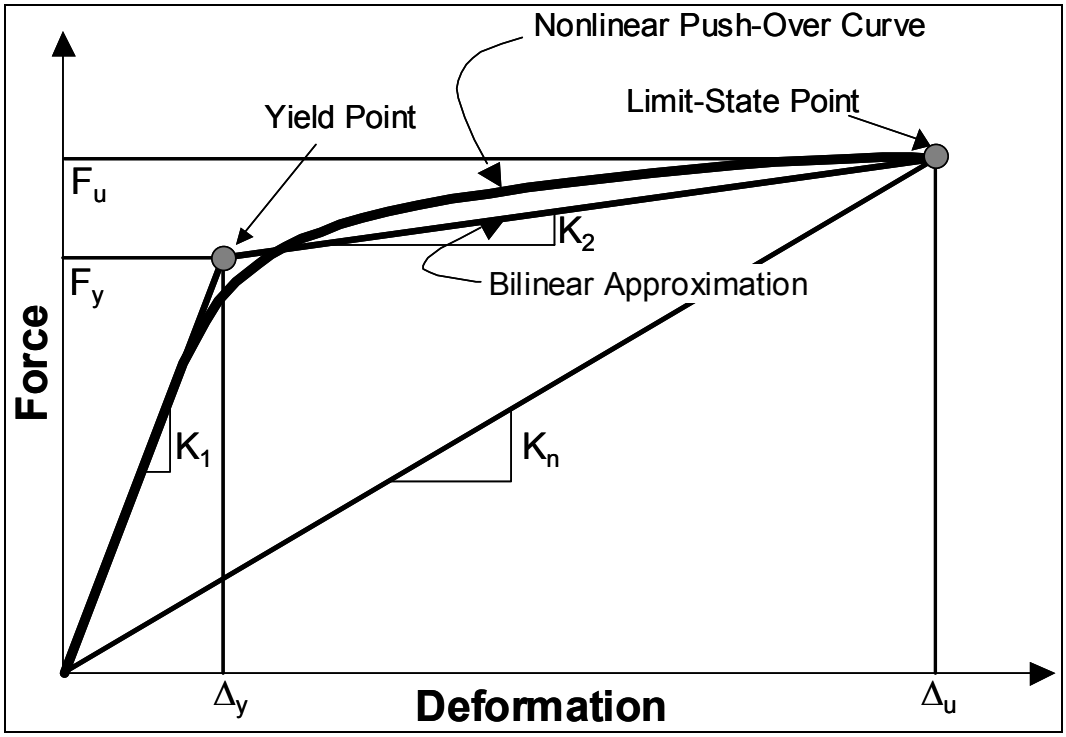

Figure 6-1: Bilinear representation of nonlinear load-deformation curve

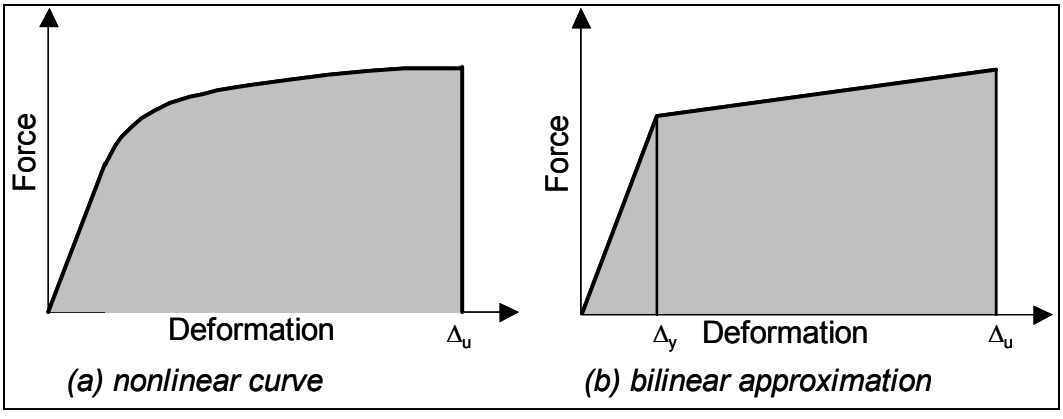

Figure 6-2: Strain energy and pushover curves

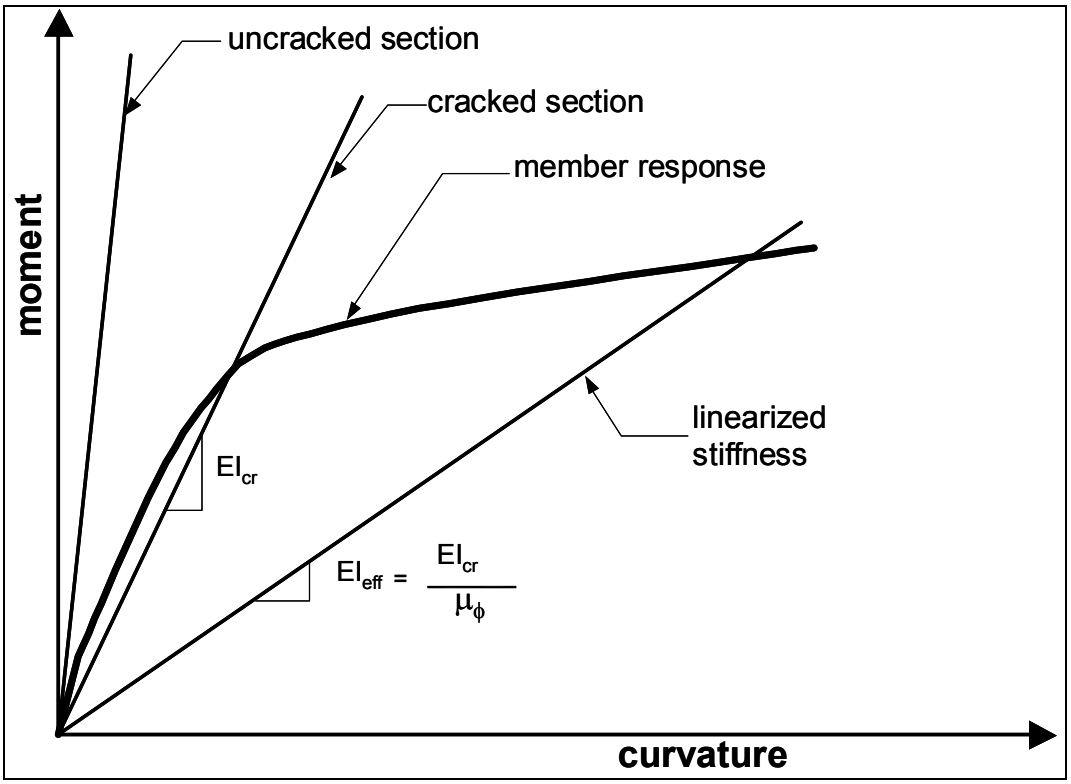

Figure 6-3: Moment-curvature response of section

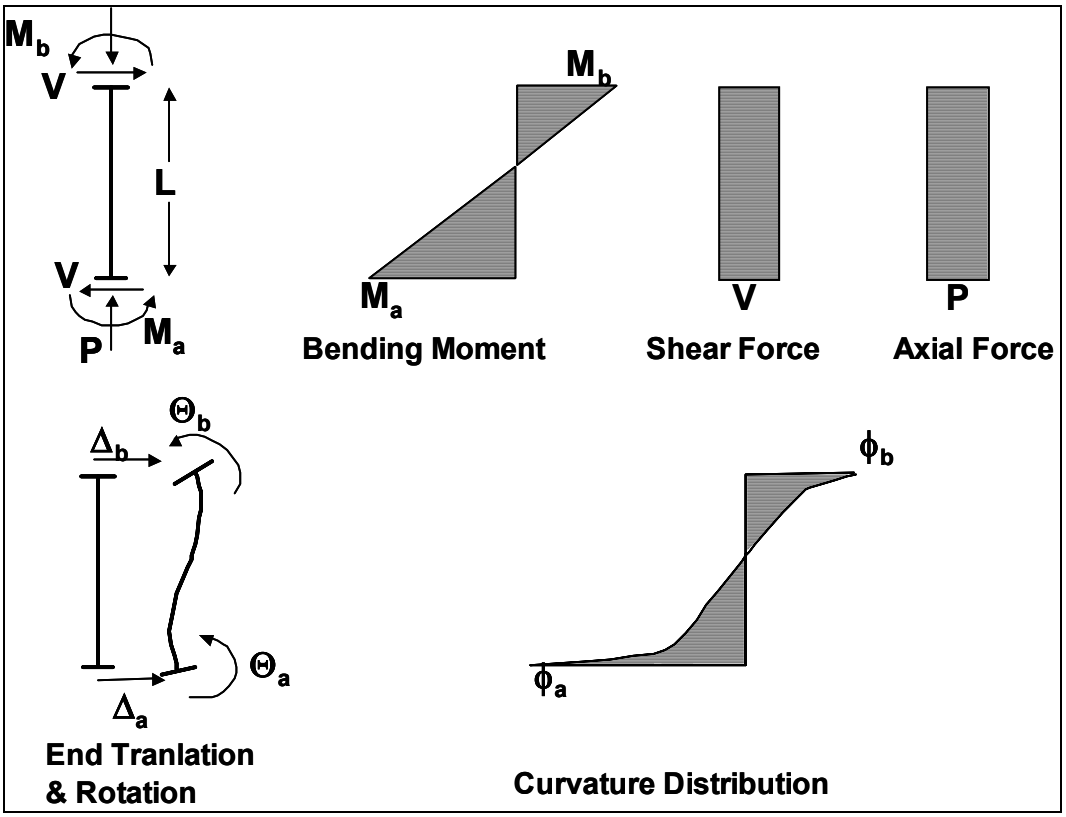

Figure 6-4: Element actions and deformations – nonlinear model

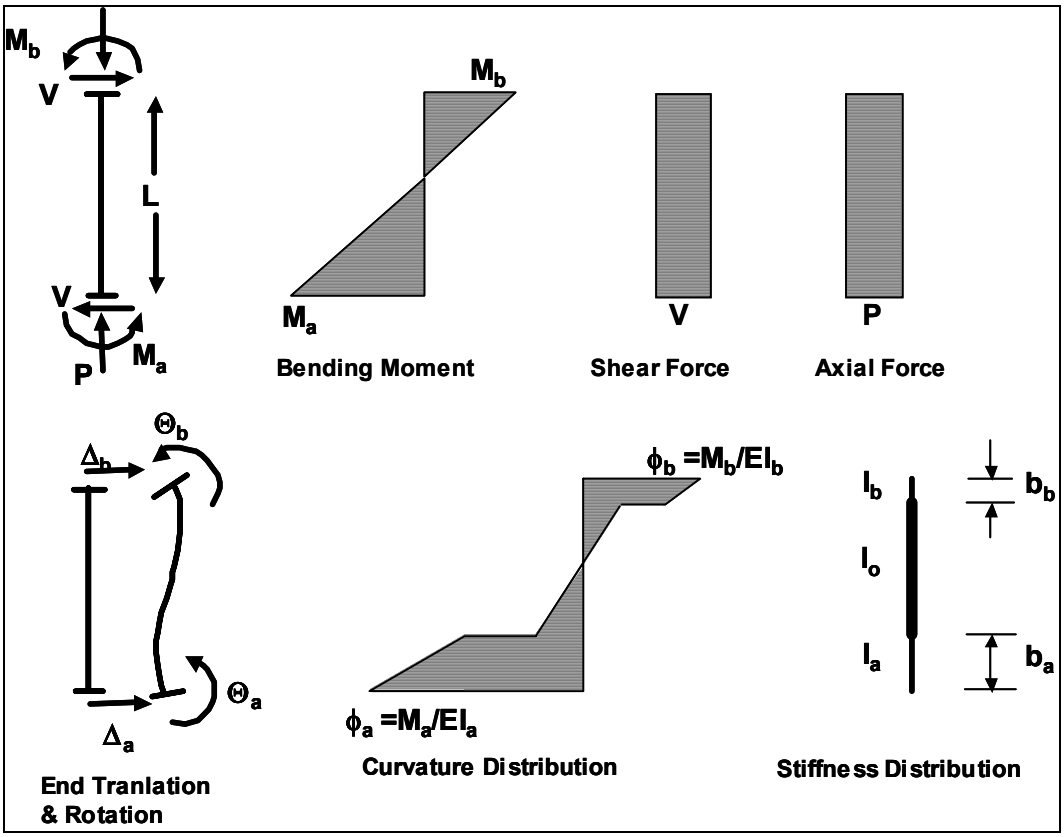

Figure 6-5: Element actions and deformations – linearized model

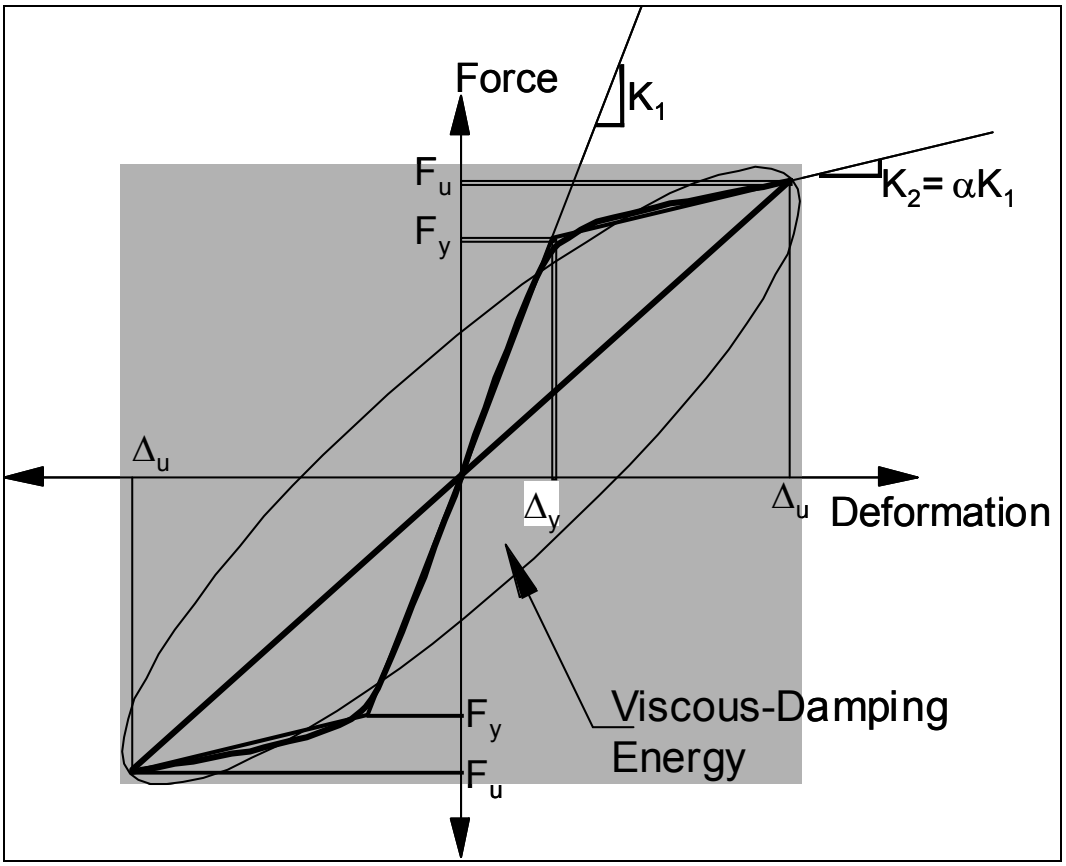

Figure 6-6: Viscous-damping energy in linear-elastic response

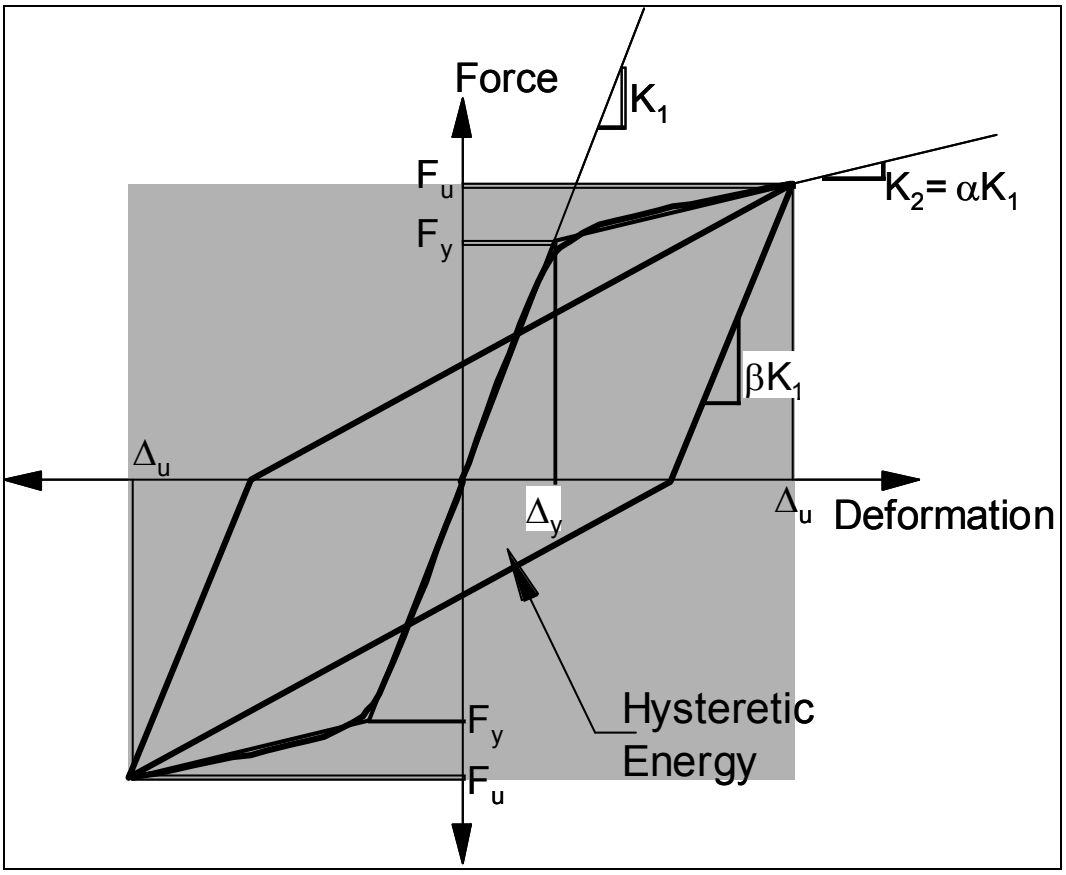

Figure 6-7: Takeda model used in calculating hysteretic energy

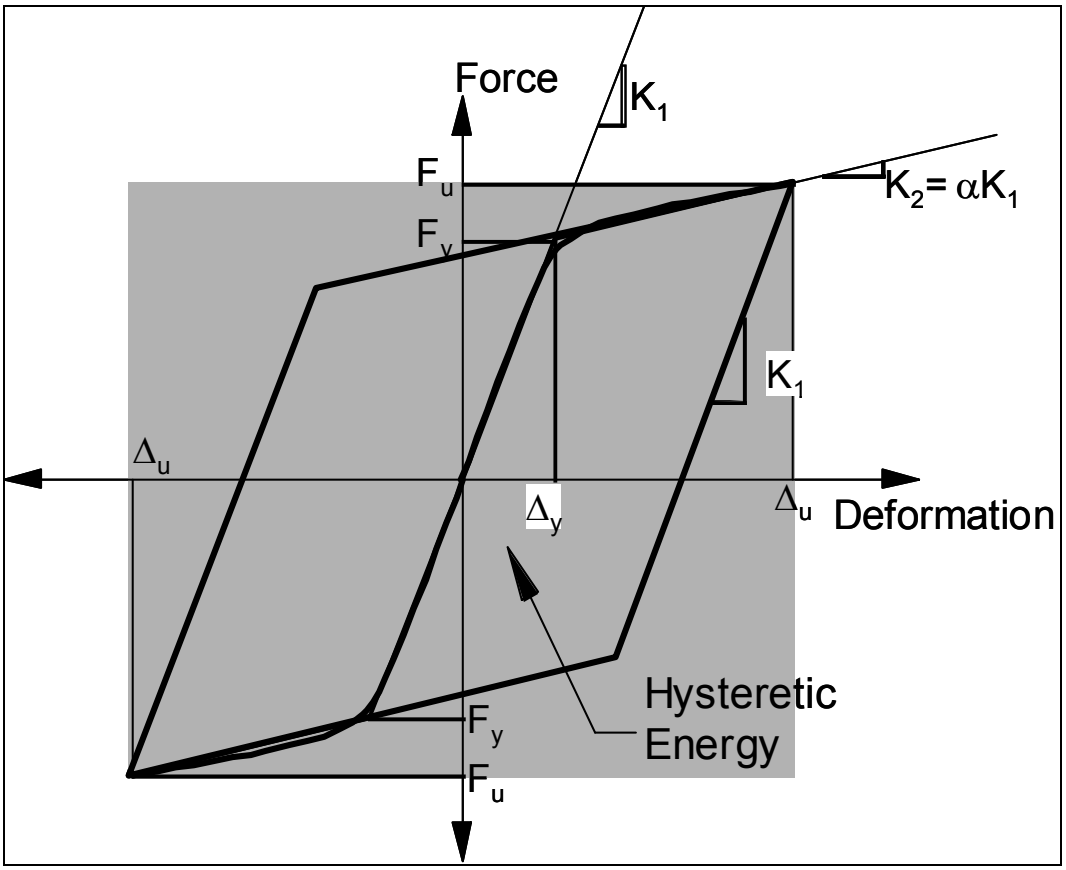

Figure 6-8: Hysteretic model used by ATC-40 [Comartin, 1996]

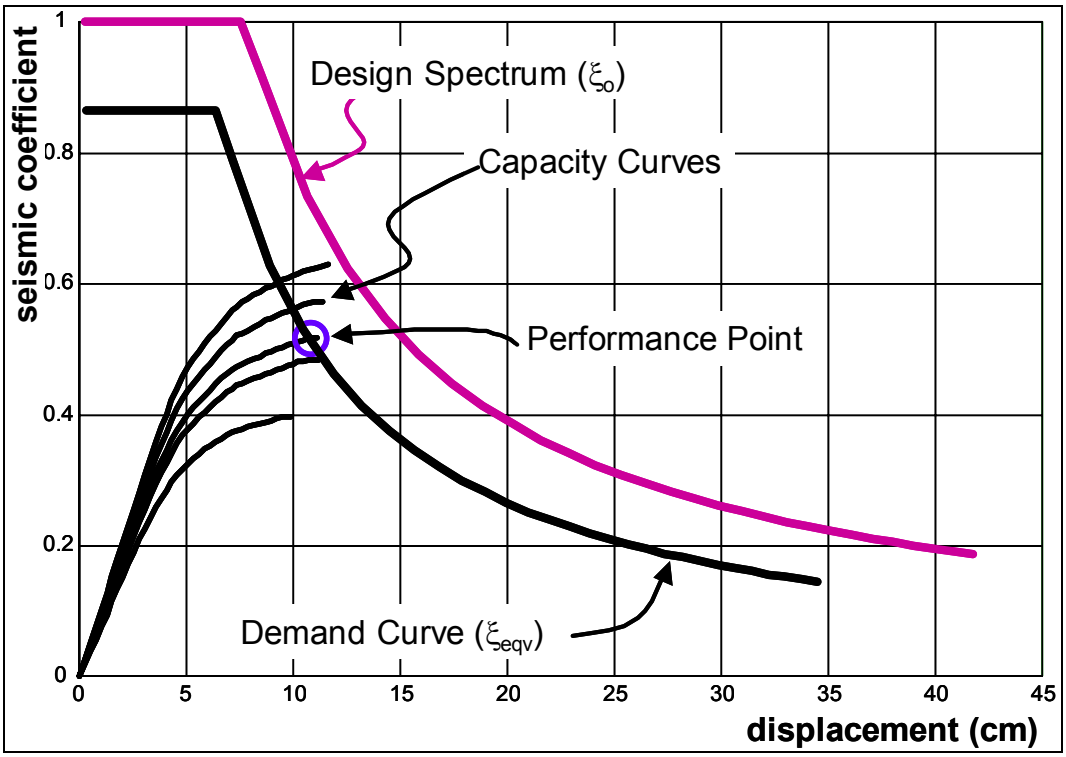

Figure 6-9: Graphical representation of Capacity-Spectrum Method

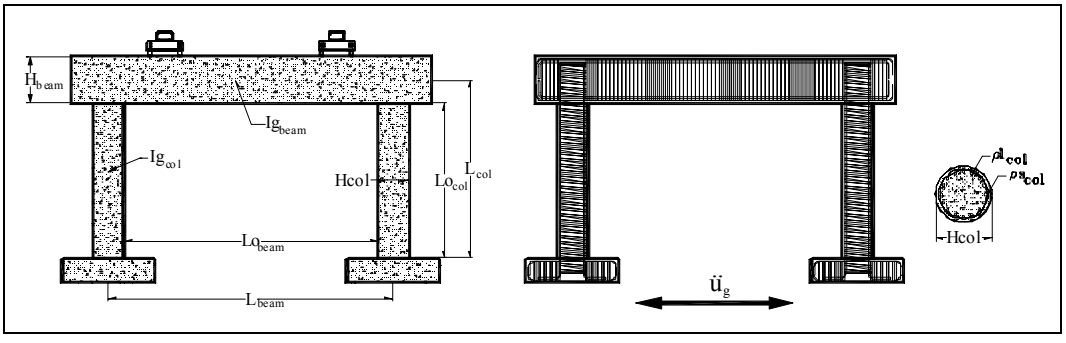

Figure 6-10: Two-column reinforced-concrete bridge bent

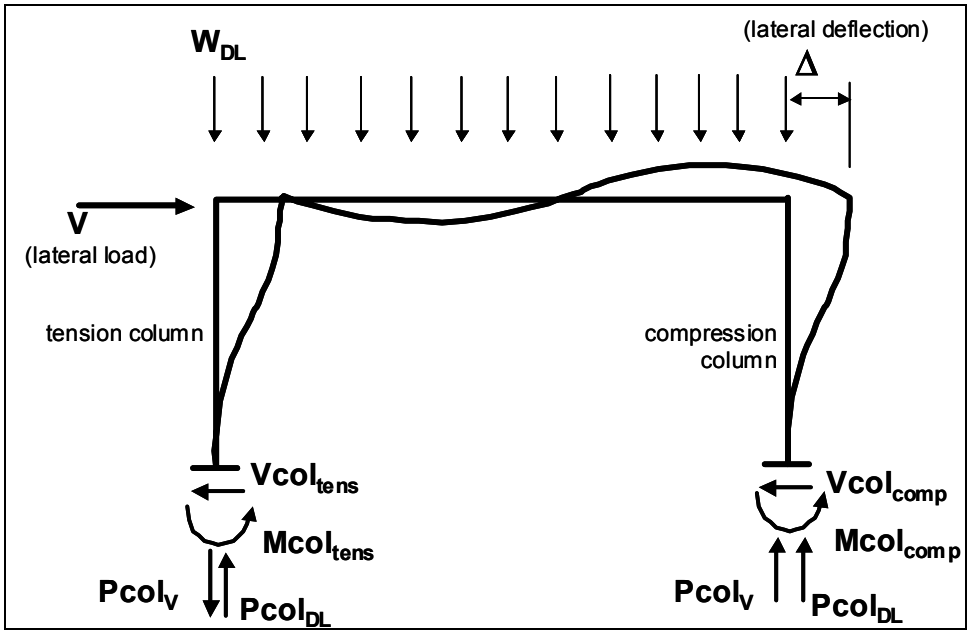

Figure 6-11: Lateral and gravity loads, support reactions, and lateral deflection of portal frame

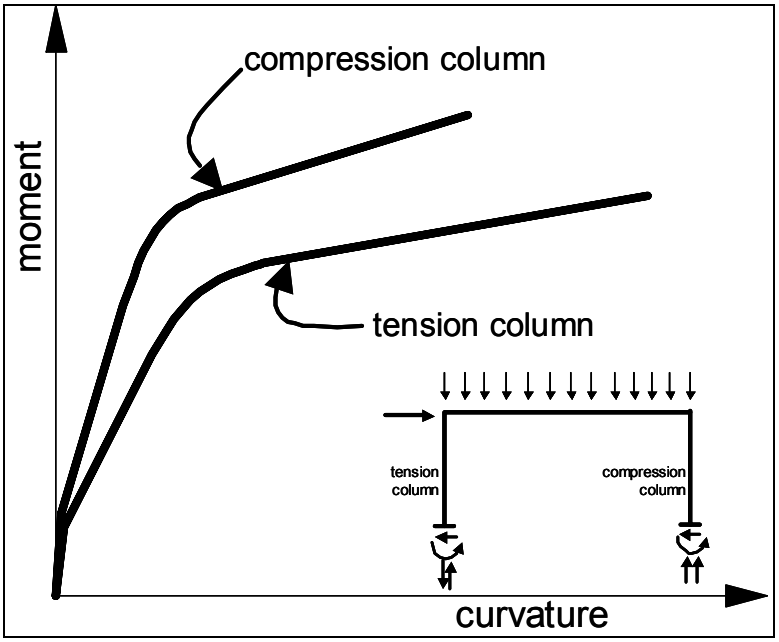

Figure 6-12: Effect of axial force on moment-curvature

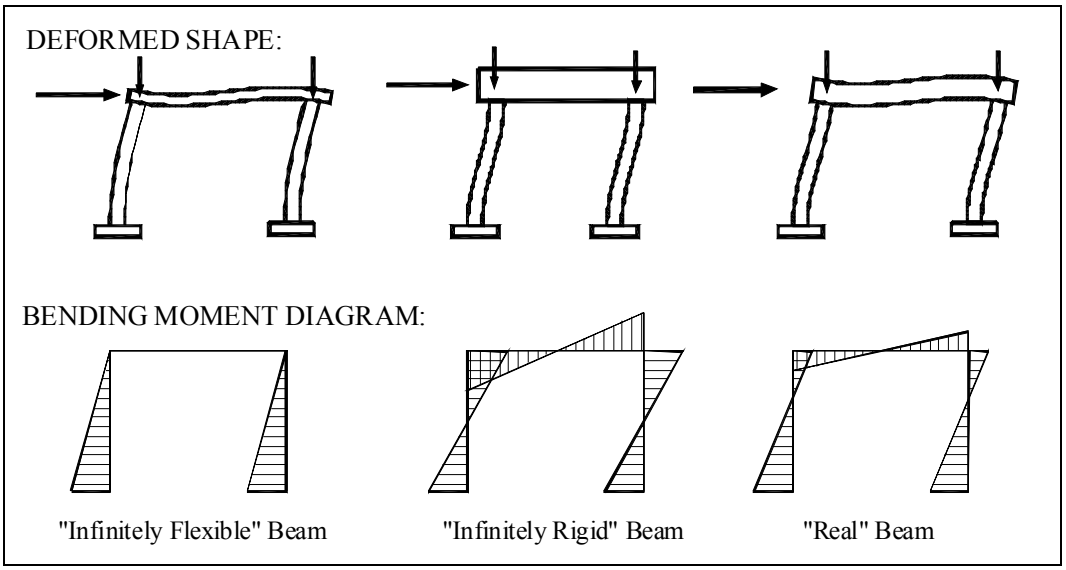

Figure 6-13: Effect of beam flexibility on lateral response

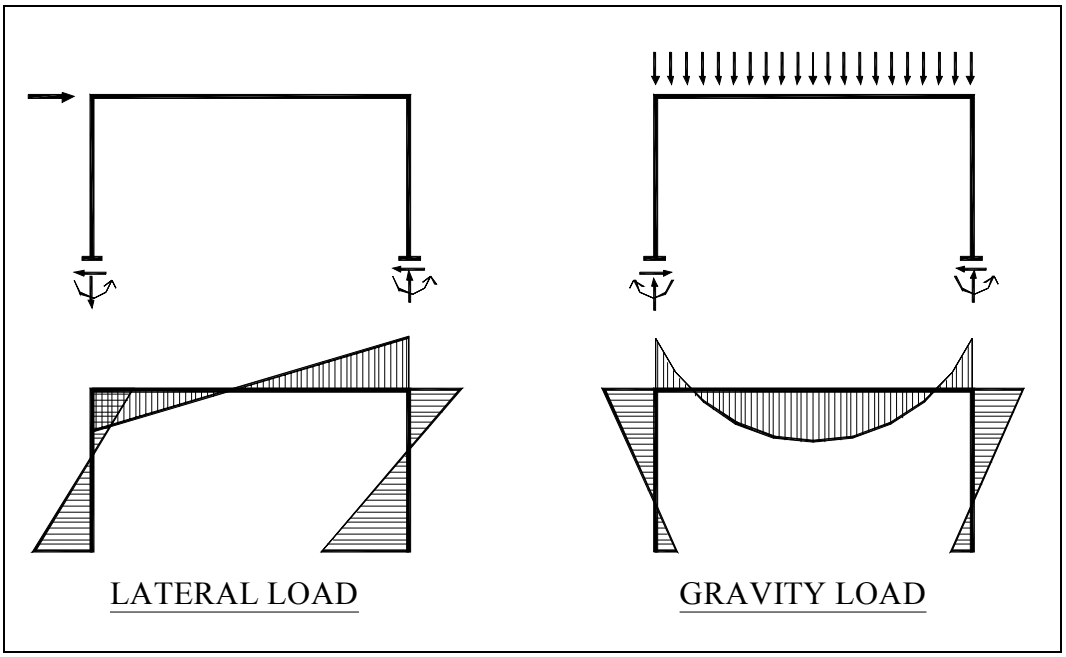

Figure 6-14: Comparison of lateral-load and gravity-load bending moment diagrams

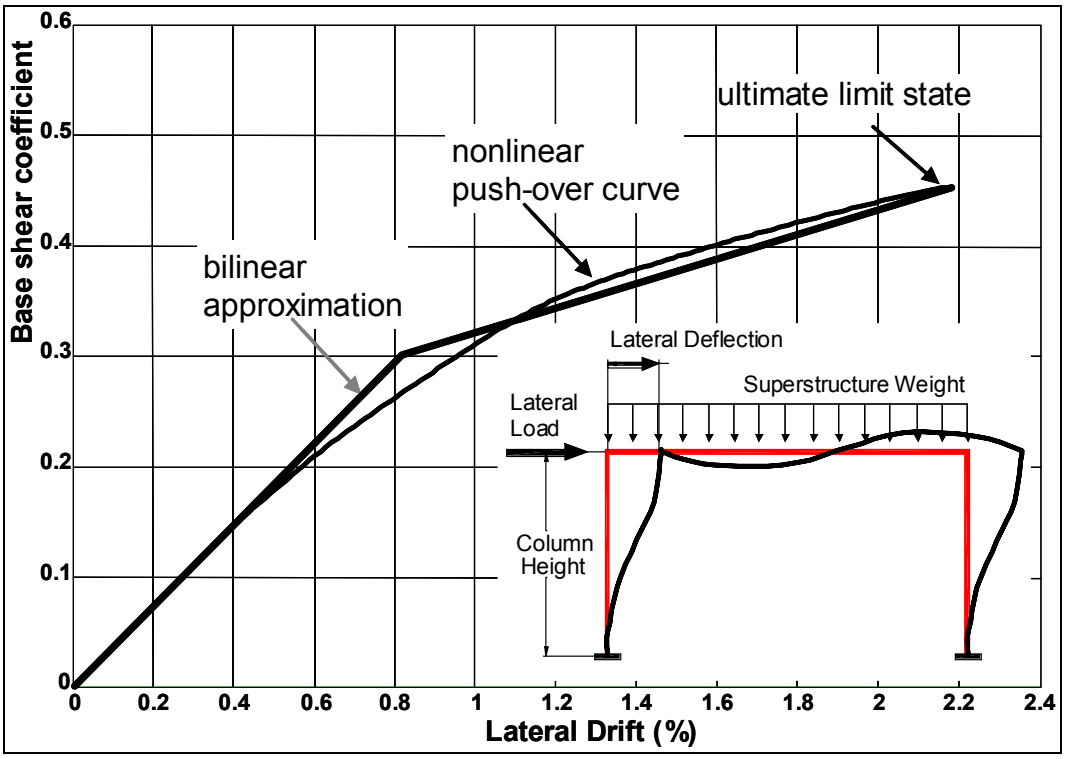

Figure 6-15: Pushover curve of test frame

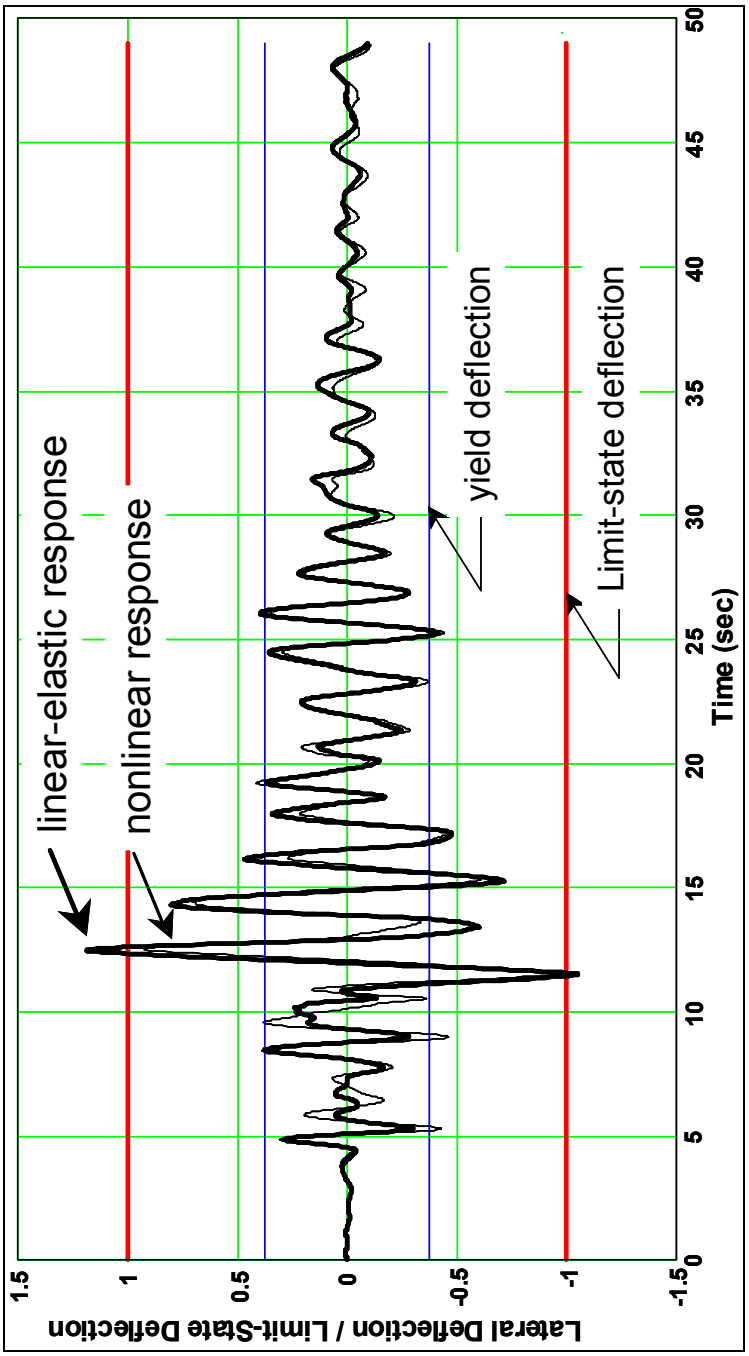

Figure 6-16: Time-history response of nonlinear and linearized test structure. Tabas X-Direction.

Chapter 7. Summary of Findings and Recommendations

7.1. Summary

A comprehensive study of beam-column joints and plastic hinge zones in reinforced-concrete bridge frames has been presented in this report. The objectives of the research were to characterize the behavior of the beam-column joints and plastic hinge zones and to develop simplified design and analysis models. In summary, the behavior of the beam-column joint is controlled by the shear strength and deformation characteristics of the joint panel. The behavior of the plastic hinge zone is controlled by the flexural response of the column section, as well as the relative elongation of the column longitudinal reinforcement within the anchorage zone, leading to rigid-body rotations at the column-joint interface. These behavior characteristics were evaluated by comparing their effects on the nonlinear lateral-deformation capacity of the structural systems to their effects on the lateral-deformation demands during seismic-excitation excursions into the nonlinear range. Based on this evaluation, models for these deformation characteristics were developed within the framework of a simplified design and analysis procedure.

The joint model consists of a nonlinear rotational spring that simulates the shear deformation of the joint panel. The strength and deformation characteristics of this spring are based on a transformation of the shear stress and strain characteristics into moment and rotation characteristics. Similarly, the hinge model consists of a flexural element, consistent with currently implemented modeling methodologies, and a nonlinear rotational spring. The strength and deformation characteristics of the hinge spring are based on the flexural strength of the

column section and the elongation characteristics of the column-longitudinal reinforcement. These elongation characteristics are dependent on the material properties and the assumed bond-stress distribution along the anchorage length.

7.2. Research Findings

7.2.1. Effects on static behavior

The study has shown that the hinge deformations have a significant contribution to the lateral response of a bridge frame subjected to a monotonic load. It was found that a decrease in anchorage strength leads to an increase in hinge flexibility. While it does increase the lateral-deformation capacity of the bridge frame at the ultimate limit state, this additional flexibility has no effect on the lateral-load strength of the bridge frame and does not compromise its structural integrity, unless large deformations lead to additional considerations such as P-delta effects. Because the additional flexibility also tends to increase the drift level at first yield, the overall ductility capacity of the bridge bent is not affected significantly.

On the other hand, the study has shown that the behavior of the beam-column joint can have a detrimental effect on the static behavior of a bridge frame by limiting its lateral-load strength. This effect is manifested when the shear strength of the connection is significantly lower than the shear stress demands at the design loads of the framing flexural members. Because the large size of joint panels in bridge bents maintains the joint shear stresses relatively low, joint failure was only found for the cases of moderately-reinforced and weak joints. It was also found that joint failure occurred without warning, as the joint flexibility does not have a measurable effect on the lateral flexibility of the bridge bent.

7.2.2. Effects on dynamic behavior

Even though it leads to a slight change in natural period of the bridge frame, the hinge flexibility does not have a measurable effect on the deformation demands during seismic excitation. By increasing the deformation capacity and not the demand, therefore, an increase in hinge flexibility leads to a decrease in the demand-to-capacity ratio.

Because the joint behavior affects the strength rather than stiffness of the bridge bent, it was found that the different types of joint do not affect the drift demands calculated for seismic excitation. When these demands are compared to capacities, however, it was found that a bridge bent with moderately reinforced and weak joints would not be able to sustain a seismic event without collapse.

7.3. Recommendations for Design of Bridge Frames

It is not possible to affect bar-anchorage and joint-shear strengths and demands in an existing structural system. It is possible, however, in the design of a new bridge structure, where the designer should attempt to minimize both hinge and joint effects to ensure the development of the design strength of the bridge frame.

7.3.1. Plastic hinge area

Yield penetration of the column longitudinal reinforcement into the joint cannot be prevented when the plastic hinge forms at the column-joint interface. However, improving the anchorage strength of the development length can reduce its effects. This may be done in one of the following ways:

- Use standard hooks or certified headed reinforcement for bars terminating in the joint. Whenever possible, terminate these bars on the outside of the beam longitudinal reinforcement at the opposite face of the joint;

- Increase ratio of joint-depth to column-reinforcement diameter;
- Provide adequately detailed horizontal and vertical transverse reinforcement in the joint region to enable bond transfer;
- Provide adequate confinement in the plastic hinge zone by reducing the spacing of the column spiral to a distance of at least one column diameter away from the joint face.

7.3.2. Beam-column joint area

Similarly, beam-column joint shear strength and demands may be affected by implementing one or more of the following:

- Increase joint size by increasing beam depth;
- Provide adequately detailed horizontal and vertical transverse reinforcement in the joint region to enable force transfer and core confinement;
- Decrease joint demands by decreasing flexural strength of framing members. This can be achieved by reducing the longitudinal-reinforcement ratio of the columns framing into the joint.

These recommendations show that improving beam-column joint and anchorage conditions are complementary effects. The Caltrans Seismic Design Criteria and the ACI-ASCE Committee 352 recommendations for Beam-Column Connections can also be used as guidelines in implementing these recommendations.

7.3.3. Caltrans Seismic Design Criteria (SDC)

The Caltrans Seismic Design Criteria provide minima on the amount of transverse reinforcement in the joint. Section 7.4.4.2 of the criteria prescribes a minimum joint shear reinforcement in the form of column transverse steel continued into the bent cap, with a minimum volumetric ratio of transverse column reinforcement, ρ_s, of:

$$\rho_{s,\min} = \frac{3.5\sqrt{f'_c}}{f_{yh}}(psi)$$

Additional horizontal and vertical stirrups, horizontal side reinforcement, J dowels, and transverse reinforcement are recommended for joints where the principal tension stress exceeds $3.5\sqrt{f'_c}$.

7.3.4. ACI-ASCE 352 Recommendations for Beam-Column Connections

While these recommendations are prescribed for building frames where hinging is expected in the beams rather than the columns, they can be used as guidelines for detailing the beam-column joint area to supplement the SDC recommendations. Limits for both development length and amount of transverse reinforcement in the joint are prescribed. A minimum development length for hooked bars is given by:

$$l_{dh} = \frac{\alpha f_y d_b}{75\sqrt{f'_c}}(psi)$$

Where α is the stress multiplier for longitudinal reinforcement at joint/member interface for joints in seismic regions, taken to be equal to 1.25. f_y, d_b, and f'_c are the nominal yield strength of the reinforcement, the bar diameter, and the nominal compressive strength of the concrete, respectively. This length can be reduced by 20% if spacing of the transverse reinforcement in the joint is less than or equal to three times the diameter of the bar being developed.

A minimum value for the beam-depth to column bar diameter for bars passing through the joint is also prescribed:

$$\frac{h_{beam}}{db_{column}} \geq 20\frac{f_y(psi)}{60000} \geq 20$$

Detailing requirements for bars terminating with a standard head are also recommended.

The ACI-ASCE Committee 352 publication also prescribes two values for the minimum amount of transverse reinforcement recommended within the joint. When spiral reinforcement is used, the volumetric steel ratio, ρ_s, should not be less than:

$$\rho_s = 0.12\frac{f_c'}{f_{yh}}$$

But should not be less than:

$$\rho_s = 0.45\left(\frac{A_g}{A_c} - 1\right)\frac{f_c'}{f_{yh}}$$

Where A_g is the gross are of column section, A_c is the area of column core, f_c' is the nominal compressive strength of the concrete and f_{yh} is the specified yield strength of the spiral reinforcement.

7.4. Recommendations on Joint Model

Based on the study presented in this report, the beam-column joint should be considered in the calculation of structural deformations when the joint shear stress corresponding to the maximum moment strength of the columns framing into the joint exceeds one-half of the factored nominal shear strength of the joint. The one-half factor was chosen as it likely represents a value near the cracking strength of the joint. In such cases the joint strength and flexibility are expected to have a significant contribution to the overall strength and deformation of the bridge frame.

As the first step, one must estimate the nominal joint shear strength. Joint geometry and size, reinforcement detailing and loading conditions are a few of the characteristics to be considered. Based on a review of joint detailing and behavior, the following classification is recommended, a variation of it may be used:

- **Weak joint** -- nominal joint shear strength $v_n = 5\sqrt{f_c'}$ (psi). This classification applies to joints that were designed prior to the 1970's. Typically, these joints have minimal amounts, if any, of transverse reinforcement in the joint. Once the cracking strength is reached the joint fails in shear.

- **Moderate joint** – nominal joint shear strength $v_n = 5\sqrt{f_c'}$ (psi). This classification applies to joints that were designed between 1970 and 1990. Joints falling into this classification have a nominal amount of transverse reinforcement (satisfying minimum requirements of the time, but not satisfying current design requirements), adequately detailed to sustain concrete cracking without collapse. A study of the particular joint and further research are necessary to assess the post-cracking behavior of the joint. It can be assumed, however, to be able to sustain the nominal strength.

- **Intermediate joint** – nominal joint shear strength $v_n = 7.5\sqrt{f_c'}$ (psi). This classification applies to joints that have a nominal amount of transverse reinforcement (satisfying minimum requirements of the time, but not necessarily satisfying current design requirements), enough to maintain integrity of the joint past cracking, but not enough to sustain large deformations near yielding of the framing members. Beam-column joints where bars are unable to develop their yield strength fall under this category. Bar development may be precluded by the lack of standard hooks, or by insufficient anchorage length for column bars passing through the joint. The designer may consider increasing the nominal joint shear strength on the basis of an evaluation of the amount and layout of the transverse reinforcement in the joint region.

- **Strong joint** -- nominal joint shear strength to be calculated from the Caltrans Seismic Design Criteria limits on tensile ($p_t \le 12\cdot\sqrt{f_c \cdot psi}$) and compressive ($p_c \le 0.25 f_c$) principal stresses. This classification applies to beam-column joints designed after the 1990's. These joints typically contain significant amounts of horizontal and vertical reinforcement in the joint to enable proper confinement of the joint core and provide the necessary mechanisms for force transfer and bar anchorage. These joints are expected to be able to sustain large inelastic deformations of the framing members without significant loss in joint panel strength or stiffness.

The next step is to develop a shear stress-strain relationship for the joint panel based on the joint classification. The recommended models are shown in Figure 7-1. The model developed by Priestley should be used in modeling the weak joint [Priestley, 1993]. Further research is currently needed to determine how the moderate and intermediate joints are expected to sustain inelastic deformations/rotations beyond their nominal strength: with or

without strength loss. In the absence of data, the designer should determine this behavior on the basis of the whether the amount and layout of the reinforcement in the joint region is adequate for core confinement and force transfer. The amount of "strain-hardening" in the post-nominal-strength portion of the strong joint should also be based on the characteristics of the amount and layout of the transverse and longitudinal reinforcement in the joint region.

Once the shear stress and strain characteristics of the joint have been determined, they can be transformed to moment-rotation characteristics my multiplying the shear stress values by the volume of the joint to obtain the moment, and maintaining the shear strain and spring rotation as equivalent. For simplicity, the volume of the joint may be calculated from the smallest effective depth of the members framing into the joint in the three spatial dimensions independently. This procedure is shown in the example in the following chapter.

The procedure recommended for developing the joint strength and demand is summarized in the following outline and shown in the example, and shown graphically in Figure 7-2:

- **Calculating strength:**
  1. Categorize joint, see above.

  2. Calculate factored nominal joint shear strength (ϕv_n), using a strength-reduction factor of 0.7.

Nominal Shear Strength	Weak Joint	Moderate Joint	Intermediate Joint	Strong Joint
v_n	$v_n = 5\sqrt{f'_c}$	$v_n = 5\sqrt{f'_c}$	$v_n = 7.5\sqrt{f'_c}$	SDC limits

Note, since the SDC limits do not include a strength reduction factor, calculate v_n of the strong joint as the joint shear stress corresponding to the limiting tensile or compressive principal stress times the inverse of the strength reduction factor. The implementation of the SDC limits is shown in Figure 7-3.

3. Multiply joint shear stress by volume of joint to obtain characteristics moments in Moment-Rotation relationship. The shear strain and the rotation are equal.

4. Plot Moment-Rotation characteristics of joint spring

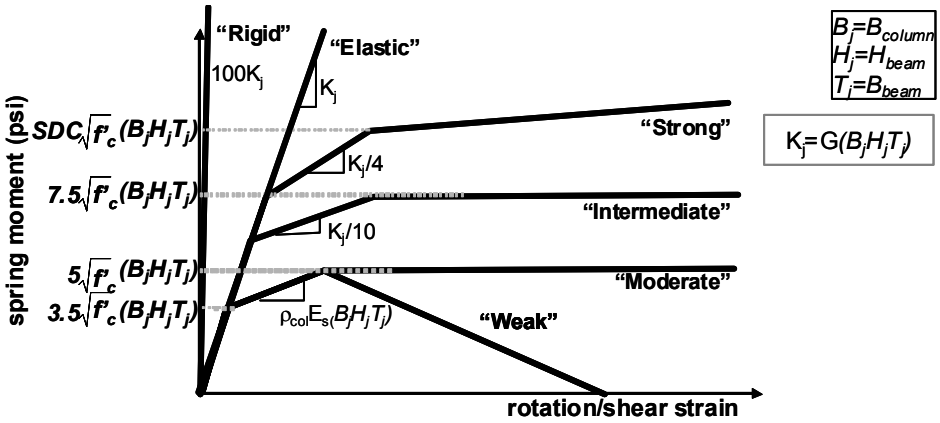

- **Calculating demand:**

1. Calculate member-end forces at joint boundary in equilibrium with maximum flexural strength of vertical members framing into joint:

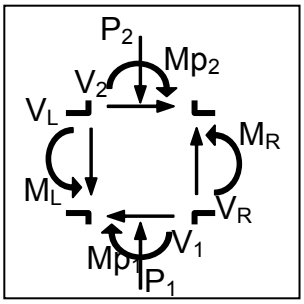

2. Convert vertical-member moment and axial force into tension-compression couple:

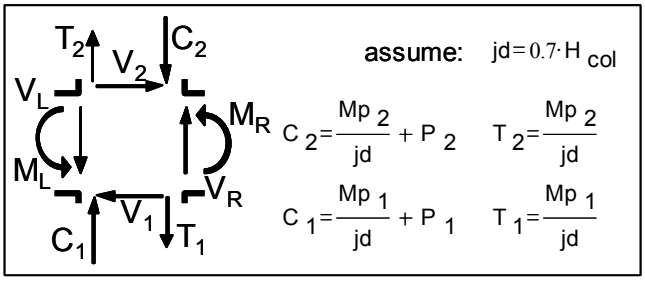

3. Calculate corresponding vertical joint shear stress at maximum flexural strength of vertical members framing into joint ($\mathbf{v_j}$):

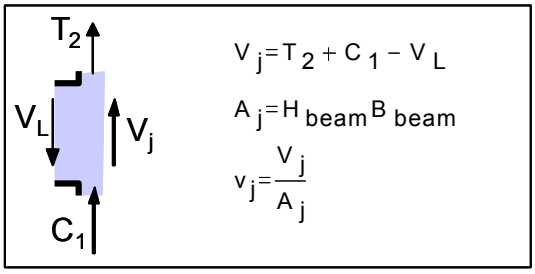

7.5. Recommendations on Hinge Model

The first component of the plastic-hinge model is a flexural element. The flexural behavior of bridge columns has been studied extensively and simplified models are already in use in design and analysis. The second component of the plastic-hinge model is a nonlinear spring representative of the rotation due to the elongation of the column longitudinal reinforcement. The deformation characteristics of this spring are based on the moment-curvature behavior of the column section and the assumed bond-stress distribution along the development length, determined by the anchorage conditions. The model presented herein assumes a two-value constant bond-stress distribution: constant bond stress along the elastic length of the bar (q_e) and constant bond stress along the post-yield length of the bar (q_p). In a manner similar to that developed for the beam-column joints, the bond-stress characteristics can be classified into three categories:

- **Weak bond** – elastic bond stress $q_e = 12pf_c'$ (psi), post-yield bond stress $q_p = 6pf_c'$ (psi). This condition applies to anchorage regions that are expected to undergo significant inelastic deformations that compromise the integrity of the concrete core into which the bars are anchored. This classification also applies to anchorage zones where the framing column are expected to yield on either side of the joint with a short development length available, such as

the lower-level beam-column joint of a double-deck bridge frame with relatively shallow beams. Cases where the column terminates into the joint may also fall under this category, such as T joints, if the bars are not well anchored or confined. Typically, a beam-column joint classified as weak is associated with weak bond characteristics.

- **Intermediate bond** – elastic bond stress $q_e = 30pf_c'$ (psi), post-yield bond stress $q_p = 15pf_c'$ (psi). It is recommended that this classification be used for anchorage zones that are not well known and do not qualify for the other classifications. It is recommended that intermediate bond conditions be used in conjunction with intermediate beam-column joints.

- **Strong bond** – elastic bond stress $q_e = 30pf_c'$ (psi), post-yield bond stress $q_p = 30pf_c'$ (psi). This classification applies to anchorage conditions where the column longitudinal reinforcement terminates in a deep footing expected to remain elastic. This classification can also be used in conjunction with strong deep beam-column joints that are expected to remain elastic.

The procedure recommended for developing the hinge model is summarized in the following outline, and shown graphically in Figure 7-4:

- Perform Moment-Curvature analysis of column section. Calculate moment-curvature data at yield, nominal and ultimate limit states: M_y, M_n, M_u, and corresponding steel strain (εs_y, εs_n, εs_u)

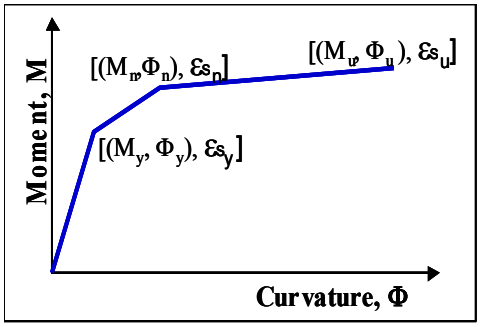

- Save section properties: column diameter (H_c), longitudinal-bar diameter (d_b)
- Select simplified steel and concrete material model, using the steel model

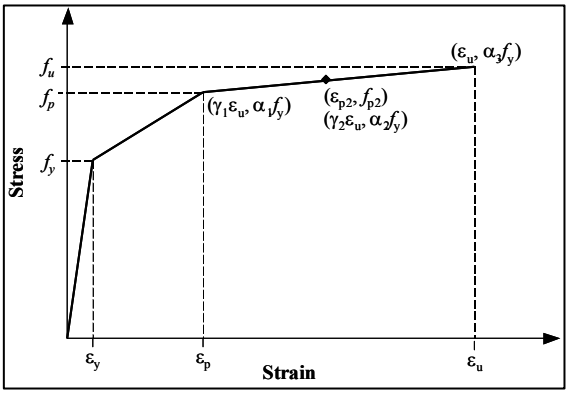

prescribed by the Caltrans Seismic Design Criteria. The following values correspond to this model: f_y=68ksi, ε_y=68ksi/29000ksi, ε_u=0.1, α_1=1.32, α_2=1.36, α_3=1.4, γ_1=0.5, γ_2=0.7;

- Classify anchorage characteristics and select bond-stress distribution

"Strong" bond model :	"Intermediate" bond model:	"Weak" bond model:	bar stress
$q_e=30\sqrt{f'_c}$	$q_e=30\sqrt{f'_c}$	$q_e=12\sqrt{f'_c}$	pre-yield
$q_e=30\sqrt{f'_c}$	$q_e=15\sqrt{f'_c}$	$q_e=6\sqrt{f'_c}$	post-yield

- Determine steel-strain vs. rotation relationship using the following equations:

$$\left[\varepsilon_y, \left(\theta_y = \frac{1}{4}\cdot\frac{d_b}{H_c}\cdot\varepsilon_y\cdot\frac{f_y}{u_e}\right)\right]$$

$$\left[\left(\gamma_1\cdot\varepsilon_u\right), \left[\theta_p = \theta_y + \frac{1}{4}\cdot\frac{d_b}{H_c}\cdot\left(\varepsilon_y + \gamma_1\cdot\varepsilon_u\right)\cdot\left(\alpha_1 - 1\right)\cdot\frac{f_y}{u_p}\right]\right]$$

$$\left[\left(\gamma_2\cdot\varepsilon_u\right), \left[\theta_{p1} = \theta_y + \frac{1}{4}\cdot\frac{d_b}{H_c}\cdot\left[\left(\varepsilon_y + \gamma_1\cdot\varepsilon_u\right)\cdot\left(\alpha_1 - 1\right) + \varepsilon_u\cdot\left(\gamma_1 + \gamma_2\right)\cdot\left(\alpha_2 - \alpha_1\right)\right]\cdot\frac{f_y}{u_p}\right]\right]$$

$$\left[\varepsilon_u, \left[\theta_u = \theta_y + \frac{1}{4}\cdot\frac{d_b}{H_c}\cdot\left[\left(\varepsilon_y + \gamma_1\cdot\varepsilon_u\right)\cdot\left(\alpha_1 - 1\right) + \varepsilon_u\cdot\left(1 + \gamma_1\right)\cdot\left(\alpha_3 - \alpha_1\right)\right]\cdot\frac{f_y}{u_p}\right]\right]$$

- Interpolate moment-curvature steel strains (εs_y, εs_n, εs_u) in steel-strain vs. rotation relationship to obtain (Θs_y, Θs_n, Θs_u)

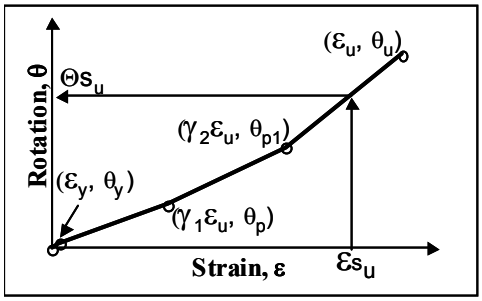

- Plot Moment-Rotation relationship for hinge spring element (Θs_y ,M_y) (Θs_n ,M_n) (Θs_u ,M_u)

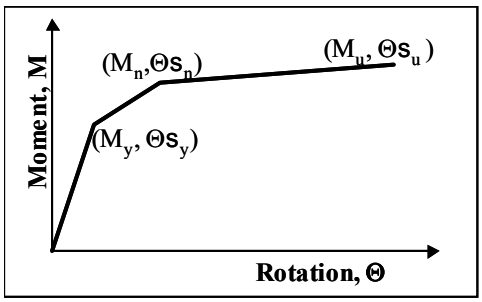

The moment-curvature relationship corresponding to the different bond classifications is shown in Figure 7-5.

7.6. Recommendations for analysis and design procedures

The following procedures are recommended for performance-based design and evaluation, respectively, and shown graphically in Figure 7-6 and Figure 7-7:

- **Recommended Performance-Based Design Procedure:**
  1. Design structural members framing into joint (columns and beams)
  2. Calculate joint-boundary forces based on equilibrium at maximum moment strength of framing column.
  3. Calculate joint shear stress demand ($\mathbf{v_j}$)
  4. Calculate factored nominal joint shear strength ($\phi\mathbf{v_n}$) on the basis of joint classification
  5. Compare joint shear stress demand to factored strength:
     a) If $\mathbf{v_j < 0.5}(\phi\mathbf{v_n})$: Beam-column joint can be assumed rigid
     b) If $\mathbf{0.5}(\phi\mathbf{v_n}) \# \mathbf{v_j}$: Reduce joint shear strength and/or decrease joint shear stress demand using the design recommendations given in this report. Return to step 2.
  6. Construct hinge model on the basis of hinge classification (Figure 7-4)
  7. Proceed to calculating structural displacement capacities and demands by incorporating hinge model into structural model of bridge frame.
- **Recommended Performance-Based Evaluation Procedure:**
  2. Design structural members framing into joint (columns and beams)
  3. Calculate joint-boundary forces based on equilibrium at maximum moment strength of framing column.
  4. Calculate joint shear stress demand ($\mathbf{v_j}$)
  5. Calculate factored nominal joint shear strength ($\phi\mathbf{v_n}$) on the basis of joint classification
  6. Compare joint shear stress demand to factored strength:
     a) If $\mathbf{v_j < 0.5}(\phi\mathbf{v_n})$: Beam-column joint can be assumed rigid
     b) If $\mathbf{0.5}(\phi\mathbf{v_n}) \# \mathbf{v_j} \# (\phi\mathbf{v_n})$: Beam-column joint can be modeled as an elastic member. Yielding of bam-column joint will occur without measurable

strength loss. Construct joint model recommended in this report (Figure 7-2)

c) If (ϕv_n) **<** v_j: Strength and stiffness degradation can be expected. Construct joint model recommended in this report (Figure 7-2)

7. Construct hinge model on the basis of hinge classification (Figure 7-4)
8. Proceed to calculating structural displacement capacities and demands by incorporating joint and hinge models into structural model of bridge frame.

7.7. Figures

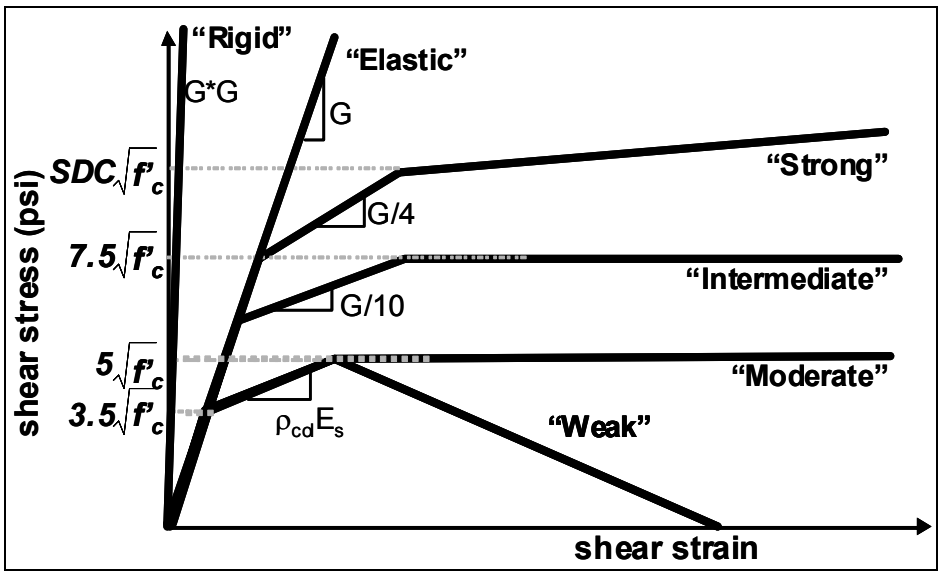

Figure 7-1: Models of Joint Shear Strength

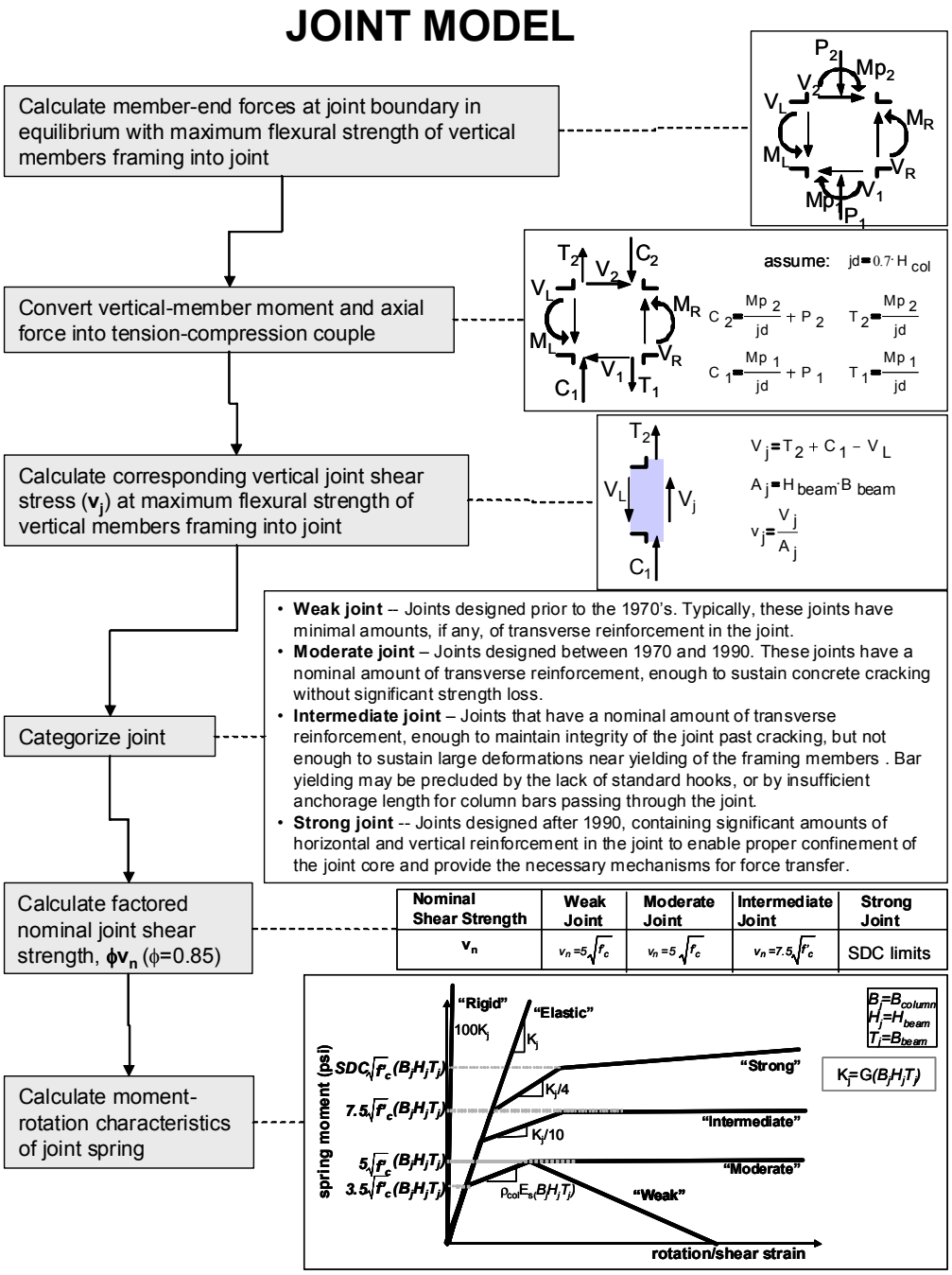

Figure 7-2: Recommended Procedure for Joint Model

Seismic Design Criteria – JOINT PRINCIPAL-STRESS LIMITS

December 2001 version 1.2

7.4 Superstructure Joint Design

….

7.4.2 Joint Proportioning

All superstructure/column moment resisting joints shall be proportioned so the principal stresses satisfy equations 7.8 and 7.9. See section 7.4.4.1 for the numberical definition of principal stress

(7.8) Principal compression $p_c \le 0.25 \cdot f_c$

(7.9) Principal tension $p_t \le 12 \cdot \sqrt{f_c \cdot psi}$

7.4.4 T Joint Shear Design

7.4.4.1 Principal Stress Definition

The principapl tension and compression stresses in a joint are defined as follows:

(7.11) $$p_t = \frac{f_h + f_v}{2} - \sqrt{\left(\frac{f_h - f_v}{2}\right)^2 + v_{jv}^2}$$

(7.12) $$p_c = \frac{f_h + f_v}{2} + \sqrt{\left(\frac{f_h - f_v}{2}\right)^2 + v_{jv}^2}$$

(7.13) $$v_{jv} = \frac{T_c}{A_{jv}}$$

(7.14) $$A_{jv} = l_{ac} \cdot B_{cap}$$

(7.15) $$f_v = \frac{P_c}{A_{jh}}$$

(7.16) $$A_{jh} = \left(D_c + D_s\right) \cdot B_{cap}$$

(7.17) $$f_h = \frac{P_b}{B_{cap} \cdot D_s}$$

Where:

A_{jh} = The effective horizontal joint area
A_{jv} = The effective vertical joint area
B_{cap} = Bent cap width
D_c = Cross-sectional dimension of column in the direction of bending
D_s = Depth of superstructre at the bent cap
l_{ac} = Length of column reinforcement embedded into the bent cap
P_c = The column axial force including the effects of overturning
P_b = The beam axial force at the center of the joint including prestressing
T_c = The column tensile force defined as M_o^{col}/h, where h is the distance from c.g. of tensile force to c.g. of compressive force on the section, or alternatively T_c may be obtained from moment-curvature analysis of the cross section.

Limiting joint shear stress on the basis of principal stresses:

SDC limit on principapal tensile stress: $$v_{jT} \le \frac{1}{2} \cdot \sqrt{\left| -f_h^2 + 2 \cdot f_h \cdot f_v - f_v^2 + \left(f_h + f_v - 2 \cdot p_t\right)^2 \right|}$$

SDC limit on principal compressive stress: $$v_{jC} \le \frac{1}{2} \cdot \sqrt{\left| -f_h^2 + 2 \cdot f_h \cdot f_v - f_v^2 + \left(2 \cdot p_c - f_h - f_v\right)^2 \right|}$$

Figure 7-3: Joint Principal Stress Limits per Caltrans Seismic Design Criteria

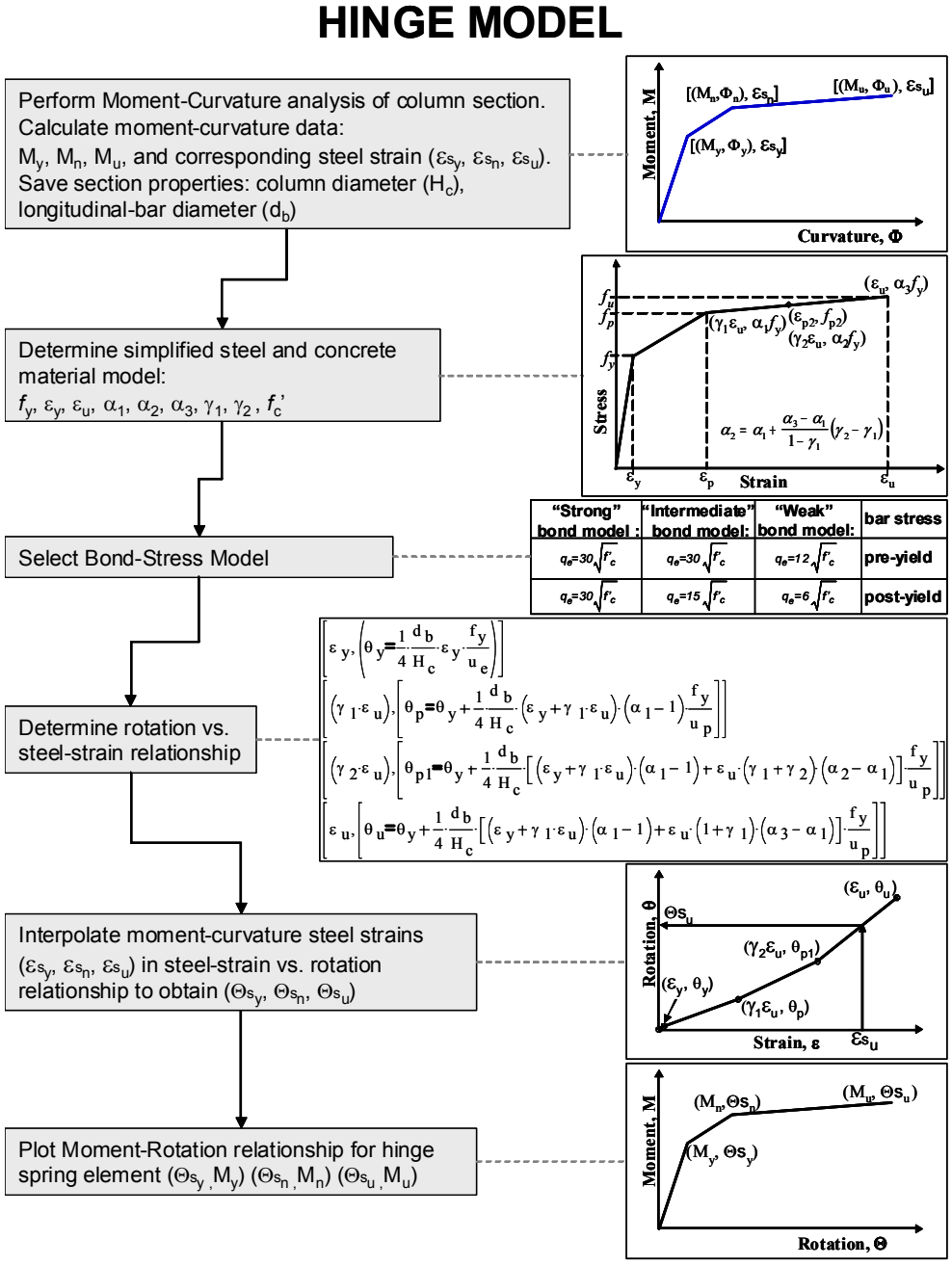

Figure 7-4: Recommended Procedure for Hinge Model

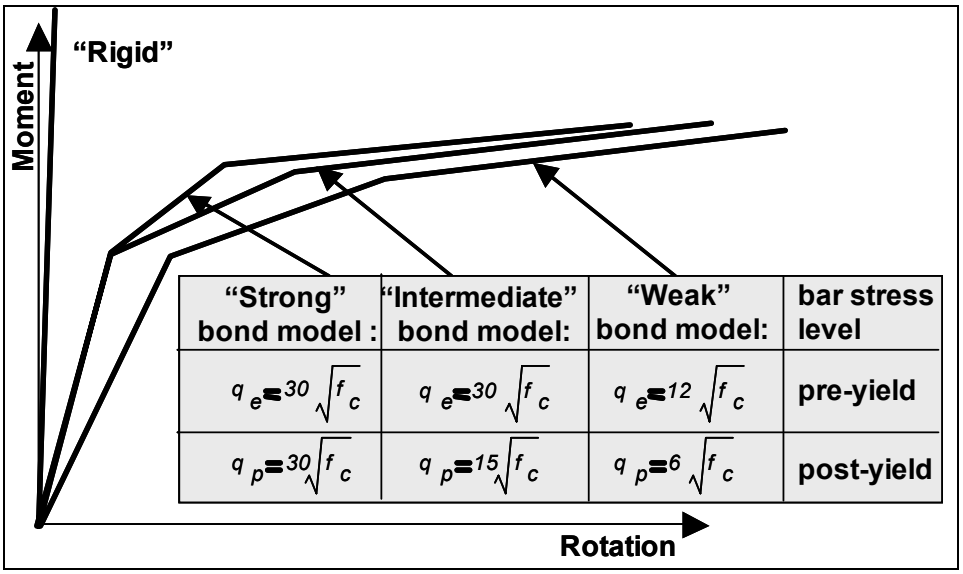

Figure 7-5: Moment-Rotation Response of Hinge based on Bond Strength of Anchorage

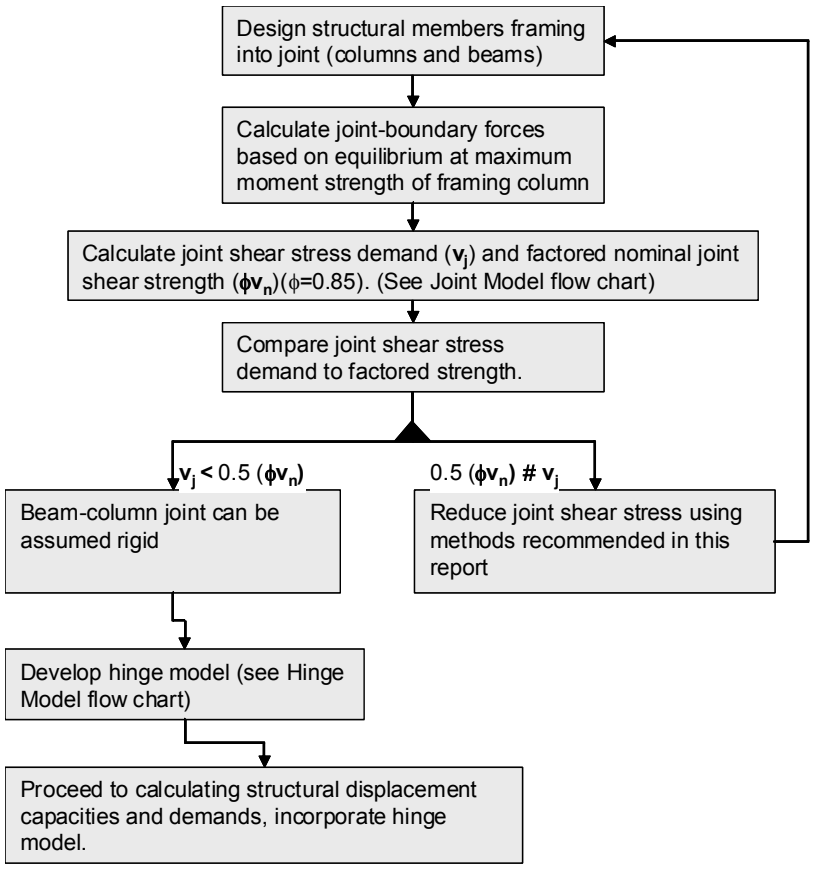

Figure 7-6: Recommended performance-based design procedure – joint and hinge considerations

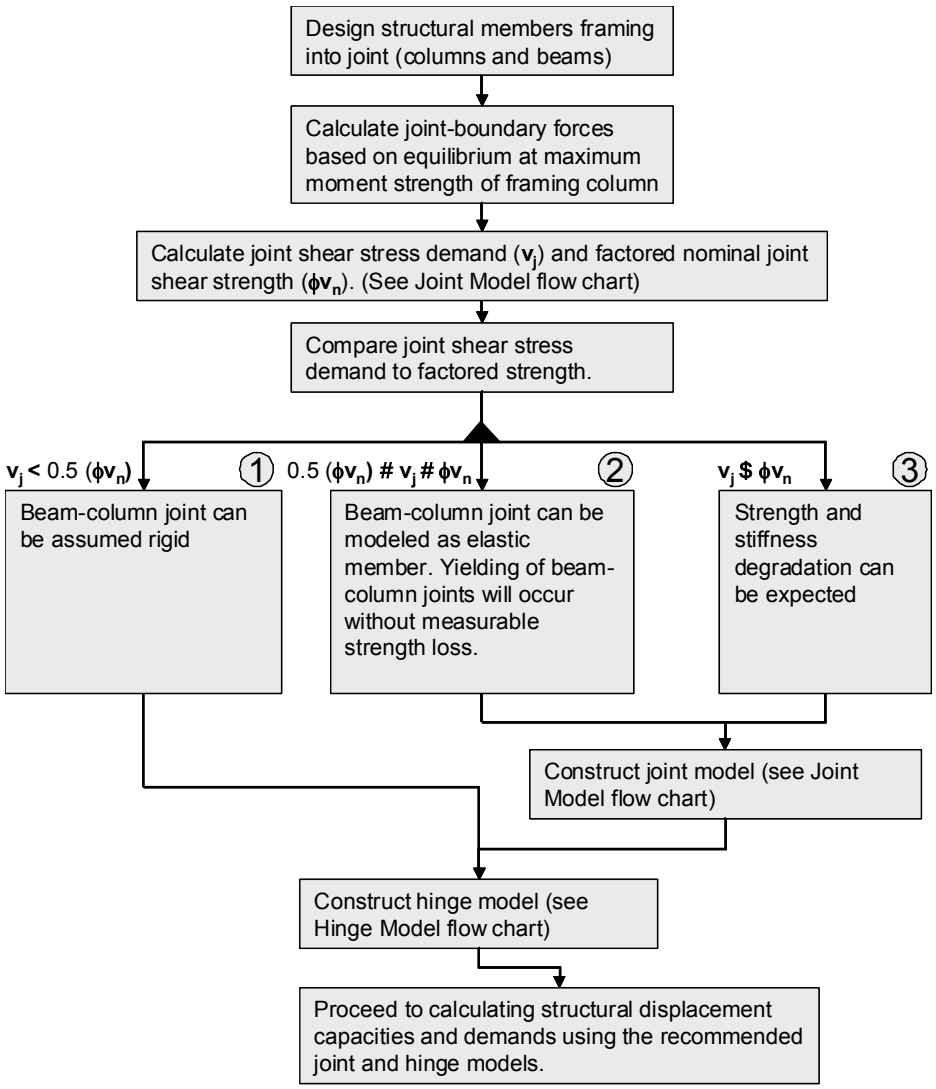

Figure 7-7: Recommended performance-based evaluation procedure – joint and hinge considerations

References

ACI-ASCE Committee 352. Recommendations for Design of Beam-Column Joints in Monolithic Reinforced Concrete Structures (ACI 352R-91). ACI Manual of Concrete Practice. American Concrete Institute. 1991.

ACI Committee 318. Building Code Requirements for Structural Concrete (ACI 318-95) and Commentary (ACI 318R-95). American Concrete Institute. 1995.

ACI Committee 408. State of the Art Report: Bond Under Cyclic Loads (ACI 408.2R-92). American Concrete Institute.1992.

Comartin, Craig D.; Niewiarowski, Richard W.; Rojahn, Christopher. Seismic evaluation and retrofit of concrete buildings. SSC 96-01; Report (California. Seismic Safety Commission) no. SSC 96-01; ATC (Series) 40, Seismic Safety Commission, State of California, Sacramento, CA 1996, 2 v.

Eligehausen, Rolf, Egor P. Popov, Vitelmo V. Bertero. Local Bond Stress-Slip Relationships of Deformed Bars Under Generalized Excitations. Earthquake Engineering Research Center Report No. UCB/EERC-83/23. October 1983.

Filippou, F.C. A Simple Model for Reinforcing Bar Anchorages Under Cyclic Excitations. Earthquake Engineering Research Center Report No. UCB/EERC-85/05. 1985.

Filippou, F.C., E.P. Popov, V.V. Bertero. Effects of Bond Deterioration on Hysteretic Behavior of Reinforced Concrete Joints. Earthquake Engineering Research Center Report No. UCB/EERC-83/19. 1983.

Freeman, S. A. The capacity spectrum method for determining the demand displacement. ACI 1994 Spring Convention, March 23, 1994.

Gulkan, P., M. Sozen. Inelastic Responses of Reinforced Concrete Structures to Earthquake Motions. Proceedings, Journal of the American Concrete Institute. No. 12, Vol. 71December 1974. pp. 604-610.

Ingham, Jason M., M.J. Nigel Priestley, Frieder Seible. Seismic Performance of Bridge Knee Joints - Volume I: Rectangular Column/Cap Beam Experimental Results. UCSD Structural Systems Research Project Report No. SSRP - 94/12. June 1994.

Ingham, Jason M., M.J. Nigel Priestley, Frieder Seible. Seismic Performance of Bridge Knee Joints - Volume II: Circular Column/Cap Beam Experimental Results. UCSD Structural Systems Research Project Report No. SSRP - 94/17. October 1994.

Ingham, Jason M., M.J. Nigel Priestley, Frieder Seible. Seismic Performance of a Bridge Knee Joint with Headed Reinforcement. UCSD Structural Systems Research Project Report No. SSRP - 96/06. September 1996.

Kowalsky, M. J.; Priestley, M. J. N.; MacRae, G. A. Displacement-based design: A methodology for seismic design applied to single degree of freedom reinforced concrete structures. SSRP-94/16, Structural Systems Research, University of California, San Diego, La Jolla, Calif., Oct. 1994

Lehman, Dawn Ellen. Seismic Performance of Well-Confined Concrete Bridge Columns. Ph.D. Dissertation, University of California, Berkeley. 1998.

Lowes, Laura N., Jack P. Moehle. Seismic Behavior and Retrofit of Older Reinforced Concrete T-Joints. Earthquake Engineering Research Center Report No. UCB/EERC-95/09. September 1995.

Mander, J.B., M.J.N. Priestley, R. Park Theoretical Stress-Strain Model for Confined Concrete. Journal of Structural Engineering, ASCE,114(8), 1804-1826. August 1988.

Mazzoni, Silvia. Design and Response of Lower-Level Beam-Column Joints in Ductile Reinforced-Concrete Double-Deck Bridge Frames. Ph.D. Dissertation, University of California Berkeley. 1997.

Moehle, Jack P., Claudia Soyer. Behavior and Retrofit of Exterior RC Connections. Proceedings of the Second Annual Seismic Research Workshop. California Department of Transportation. Sacramento, CA. March 16-18, 1993.

Monti, Giorgio, Enrico Spacone, Filip C. Filippou. Model for Anchored Reinforcing Bars Under Seismic Excitations. Earthquake Engineering Research Center Report No. UCB/EERC-93/08. 1993.

Morita, Shiro, Tetsuzo Kaku. Local Bond Stress-Slip Relationship Under Repeated Loading. Symposium on the Resistance and Ultimate Deformability of Structures Acted on by Well Defined Repeated Loads. International Association for Bridge and Structural Engineering. 1973.

Morita, S., T. Kaku. Slippage of Reinforcement in Beam-Column Joint of Reinforced Concrete Frame. Proceedings of the Eighth. World Conference on Earthquake Engineering, Vol. VI, 477-484. 1984.

Naito, Clay J., Khalid M. Mosalam, Jack P. Moehle. Evaluation of Reinforced Concrete Bridge Joints. Proceedings of the 12th World Conference on Earthquake Engineering. Computer file: Paper #1903. 2000.

Priestley, M.J.N. Assessment and Design of Joints for Single-Level Bridges with Circular Columns. UCSD Structural Systems Research Project Report No. SSRP 93/02. February 1993.

SEQAD Consulting Engineers. Seismic Performance of a Bridge Column/Cap Beam Knee Joint Designed with Headed Reinforcement. Report for Headed Reinforcement Corporation, Canada, Report No. 95/12. SEQAD Consulting Engineers, P.O. Box 61, Solana Beach, CA 92705. August, 1995.

Sritharan, Sri, M.J. Nigel Priestley, Frieder Seible. Seismic Design and Performance of Concrete Multi-Column Bents for Bridges. UCSD Structural Systems Research Project Report No. SSRP - 97/03. June 1997.

Sritharan, Sri, M.J. Nigel Priestley, Frieder Seible. Seismic Response of Column/Cap Beam Connections with Cap Beam Prestressing. UCSD Structural Systems Research Project Report No. SSRP - 96/09. 1996.

Stojadinovic, Bozidar, Christopher R. Thewalt. Upgrading Bridge Outrigger Knee Joint Systems. Earthquake Engineering Research Center Report No. UCB/EERC-95/03. June 1995.

Takeda, T., M. A. Sozen, NN Nielsen. Reinforced Concrete Response to Simulated Earthquakes. Proceedings, ASCE, V. 96, ST12, Dec 1970. pp. 2557-2573.

Viwathanatepa, S., E.P. Popov, V.V. Bertero. Effects of Generalized Loadings on Bond of Reinforcing Bars Embedded in Confined Concrete Blocks. Earthquake Engineering Research Center Report No. UCB/EERC-79/22. August 1979.

Yankelevsky, David Z., Moshe A. Adin, Daniel N. Farhey. Mathematical Model for Bond-Slip Behavior under Cyclic Loading. ACI Structural Journal, ACI, 89(6), 692-698. December 1992.

Appendix A: Beam-Column Joint Database

(see attached file)

Appendix B: Example

B.1 The following is an example of calculations for Frame 4 presented in Chapter 5.

(see attached file)

Sample Input File

The following is a sample input file for generating the structural model of Frame 4, presented in Chapter 5. The script is to be used as input for OpenSees, the Open System for Earthquake Engineering Simulation, a software framework for simulating the seismic response of structural and geotechnical systems (http://opensees.berkeley.edu/).

```
# OPENSEES INPUT FILE FOR CREATING BRIDGE-BENT MODEL

# Create modelbuilder
model basic -ndm 3 -ndf 6;   # basic: modelbuilder type, ndm= # dimensions, ndf= # dof/node

# Define Units
set in    1.;                           # define basic units
set sec 1.;
set kip  1.;
set ksi  [expr $kip/pow($in,2)];        # define engineering units
set psi  [expr $ksi/1000.];
set ft    [expr 12.*$in];
set PI   [expr 2*asin(1.0)];            # define constants
set U    1.e10;                         # a really large number
set u    $U;                            # another really large number
set g    [expr 32.2*$ft/pow($sec,2)];  # gravitational acceleration

# define GEOMETRY parameters
set Hcol       [expr 6.5*$ft];                  # column diameter
set Lcol       [expr 36*$ft];                   # column length
set Hbeam   [expr 8.*$ft];                   # column diameter
set Lbeam   [expr 36.*$ft];                  # beam length
set GrhoCol  0.0175;                          # column longitudinal-steel ratio
set Weight   [expr 3000.*$kip];              # superstructure weight
set GMfact   1.5;                             # ground-motion scaling facto
set Bbeam   $Hcol;
set Rcol       [expr $Hcol/2];                  # column radius
set Acol       [expr $PI*pow($Rcol,2)];         # column cross-sectional area
set cover      [expr $Hcol/15];                 # column cover width
set IgCol      [expr $PI*pow($Rcol,4)/4];       # column gross moment of inertia, uncracked
set IyCol      $IgCol;                          # elastic-column properties
set IzCol      $IgCol;                          # elastic-column properties
set GcolAsp  [expr $Lcol/$Hcol*2.];           # column aspect ratio
set IzBeam   [expr $Bbeam*pow($Hbeam,3)/12];     # beam moment of inertia, horizontal Z-axis
set IyBeam   [expr $Hbeam*pow($Bbeam,3)/12];     # beam moment of inertia, vertical Y-axis
set Abeam    [expr $Hbeam*$Bbeam*10000];         # beam cross-sectional area
set GLbLc    [expr $Lbeam/$Lcol];                # beam length to column ratio

# define MATERIAL parameters
set fc         [expr -5.5*$ksi];                # CONCRETE Compressive Strength, ksi   (+T, -C)
set Ec         [expr 57*$ksi*sqrt(-$fc/$psi)]; # Concrete Elastic Modulus
set fc1C       [expr 1.26394*$fc];              # CONFINED concrete (mander model), max stress
```

```
set eps1C     [expr 2.*$fc1C/$Ec];              # strain at maximum stress
set fc2C      $fc;                              # ultimate stress
set eps2C     [expr 5*$eps1C];                  # strain at ultimate stress # set eps2C -0.013667
set fc1U      $fc;                              # UNCONFINED concrete maximum stress
set eps1U     -0.003;                           # strain at maximum stress
set fc2U      [expr 0.1*$fc];                   # ultimate stress
set eps2U     -0.006;                           # strain at ultimate stress
set Fy        [expr 68.*$ksi];                  # STEEL yield stress
set Es        [expr 29000.*$ksi];               # modulus of steel
set epsY      [expr $Fy/$Es];                   # steel yield strain
set Fy1       [expr 89.8*$ksi];                 # steel stress post-yield
set epsY1     0.06;                             # steel strain post-yield
set Fu        [expr 95.2*$ksi];                 # ultimate stress of steel
set epsU      0.1;                              # ultimate strain of steel
set Bs        [expr ($Fu-$Fy)/($epsU-$epsY)/$Es];   # post-yield stiffness ratio of steel
set pinchX      1.0;                            # pinching parameter for hysteretic model
set pinchY      1.0;                            # pinching parameter for hysteretic model
set damage1   0.0;                            # damage parameter for hysteretic model
set damage2   0.0;                            # damage parameter for hysteretic model
set betaMUsteel    0.0;       # degraded unloading stiffness for hysteretic material MU^(-beta)
set betaMUjoint    0.0;       #          -- timoshenko value of 0.5
set betaMUph 0.0;
set G       $U;                               # Torsional stiffness Modulus
set J       1.;                               # Torsional stiffness of section
set GJ      [expr $G*$J];                     # Torsional stiffness

# define COLUMN REINFORCEMENT paramters
set NbCol     20;                             # number of column longitudinal-reinforcement bars
set AsCol     [expr $GrhoCol*$Acol];          # total steel area in column section
set AbCol     [expr $AsCol/$NbCol];           # bar area of column longitudinal reinforcement

# set up parameters for column section and element definition
set np          5;          # Number of integration points
set riCol       0.0;        # inner radius of column section
set roCol       $Rcol;      # outer radius of column section
set IDcore      1;          # ID tag for core concrete
set IDcover     2;          # ID tag for cover concrete
set IDsteel     3;          # ID tag for steel
set IDjointMat  4;          # ID tag for joint material properties
set IDphtMat    5;          # ID tag for plastic hinge material properties
set IDphbMat    6;          # ID tag for base plastic hinge material properties
set nfCoreR     8;          # number of radial fibers in core
set nfCoreT     16;         # number of tangential fibers in core
set nfCoverR    2;          # number of radial fibers in cover
set nfCoverT    16;         # number of tangential fibers in cover
set IDcolFlex   2;          # ID tag for column section in flexure, before aggragating torsion
set IDcolTors   10;         # ID tag for column section in torsion
set IDcolSec    1;          # ID tag for column section
set IdcolTrans  1;          # ID tag for column transformation, defining element normal
set IDbeamTrans  2;         # ID tag for beam transformation, defining element normal

# define GRAVITY paramters
set Pdl       [expr $Weight/2];                 # gravity axial load per column
set GPcol     [expr -$Pdl/$Acol/$fc];           # ….. as a fraction of compressive strength
set Wbeam     [expr $Weight/$Lbeam];            # gravity dl distributed along beam length
set Mdl       [expr $Wbeam*pow($Lbeam,2)/12];   # nodal moment due to distributed dl
```

```
set Mass      [expr $Weight/$g];                    # mass of superstructure
set Mnode     [expr $Mass/2];                       # nodal mass for each column joint

# define DAMPING
set xDamp      0.02;          # modal damping ratio

# define JOINT material parameters
set nu      0.2;                                  # poisson's ratio for concrete
set Gc      [expr $Ec/2/(1+$nu)];                 # shear modulus of concrete
set Bjoint $Hcol;                                 # joint width
set Hjoint $Hbeam;                                # joint depth
set Tjoint $Bbeam;                                # joint dimension into plane
set Kjoint [expr $Gc*$Bjoint*$Hjoint*$Tjoint];

# JOINT shear stress-strain characteristics
set vv1 7.5
set vv2 10
set vv3 1.01
set rrG 0.25
set v1   [expr $vv1*pow(-$fc/$psi,0.5)*$psi];  # yield stress of STRONG JOINT
set v2   [expr $vv2* pow(-$fc/$psi,0.5)*$psi]; # ultimate stress of strong joint
set v3   [expr $vv3*$v2];
set rG   [expr $rrG];                             # from Jamison's data
set G1   [expr $Gc];                              # initial shear modulus
set G2   [expr $G1*$rG];                          # post-cracking modulus
set G3   [expr ($v3-$v2)/(0.05)];                 # post-yield modulus
set q1   [expr $v1/$G1];                          # cracking strain of weak joint
set q2   [expr ($v2-$v1)/$G2+$q1];                # yield strain of weak joint
set q3   [expr ($v3-$v2)/$G3+$q2];                # ultimate strain of weak joint
# calculate properties of rotational spring representing the joint model
set Mv1 [expr $Bjoint*$Hjoint*$Tjoint*$v1];   # moment at yield stress (secant past cracking)
set Mv2 [expr $Bjoint*$Hjoint*$Tjoint*$v2];   # Ultimate moment, point 2 in M-Theta of rot. spring
set Mv3 [expr $Bjoint*$Hjoint*$Tjoint*$v3];   # Residual moment, point 3
set Qv1 $q1;                                      # yield rotation
set Qv2 $q2;                                      # ultimate rotation
set Qv3 $q3;                                      # residual rotation

# Define PLASTIC-HINGE parameters, rotation due to relative elongation and slip of long. reinf.
set ecn 0.003;                                    # concrete strain at nominal
set rhos 0.008
set alpha1 1.32
set alpha2 1.4
set gamma1 0.5
set gamma2 0.75
set dblong [expr 1.693*$in];                      # diameter of longitudinal reinforcement #14
set eu 0.1

#read moment-curvature relationship from matlab output unit:  phi: 1/in   mom: kip*
source data/iphiYNU.tcl
source data/imomYNU.tcl
set phiYo $iphiY;
set phiNo $iphiN;
set phiUo $iphiU;
set momYo $imomY;
set momNo $imomN;
set momUo $imomU;
```

```
set phiY [expr $phiYo/$in];
set phiN [expr $phiNo/$in];
set phiU [expr $phiUo/$in];
set momY [expr $momYo*$kip*$in];
set momN [expr $momNo*$kip*$in];
set momU [expr $momUo*$kip*$in];
set hcore [expr $Hcol-2*$cover];                                    # core diameter
set fy $Fy;
set fyh $Fy;
set fcc $fc1C;
set ey $epsY
set fp [expr $alpha1*$fy];
set fu [expr $alpha2*$fy];
set ep [expr $gamma1*$eu];
set ep2 [expr $gamma2*$eu];
set alpha3 [expr $alpha1+($alpha2-$alpha1)*($gamma2-$gamma1)/(1-$gamma1)];
set fp2 [expr $alpha3*$fy];
set esy $ey;
set fsy $fy;
set esn [expr $phiN*$hcore-$ecn]
if {$esn<=$eu}  {set fsn [expr $fp+($fu-$fp)*($esn-$ep)/($eu-$ep)]};   # less than ultimate
if {$esn<=$ep}  {set fsn [expr $fy+($fp-$fy)*($esn-$ey)/($ep-$ey)]};   # and less than plastic
set ecu [expr 0.004+1.4*$rhos*$fyh*$eu/(-$fc)];
if {$ecu>0.02} {set ecu 0.02};
set esu [expr $phiU*$hcore-$ecu];
if {$esu<=$eu}  {set fsu [expr $fp+($fu-$fp)*($esu-$ep)/($eu-$ep)]};
if {$esu<=$ep}  {set fsu [expr $fy+($fp-$fy)*($esu-$ey)/($ep-$ey)]};
set Mph1 $momY;   # MOMENT values for rotational spring
set Mph2 $momN;
set Mph3 $momU;

# Define ROTATION values for rotational spring --  STRONG HINGE
set Ue [expr 30.*pow(-$fc/$psi,0.5)*$psi];     # bond stress in pre-yield portion of bar (fc is -)
set Up [expr 30.*pow(-$fc/$psi,0.5)*$psi];     # bond stress in post-yield portion of bar (fc is -)
set DslipY [expr 1/8.*$dblong*$ey*$fy/$Ue];
set DslipP [expr $DslipY +1/8.*$dblong*($ey+$gamma1*$eu)*($alpha1-1)*($fy/$Up)];
set DslipP2 [expr $DslipY +1/8.*$dblong*(($ey+$gamma1*$eu)*($alpha1-
    1)+$eu*($gamma1+$gamma2)*($alpha3-$alpha1))*($fy/$Up)];
set DslipU [expr $DslipY +1/8.*$dblong*(($ey+$gamma1*$eu)*($alpha1-
    1)+$eu*(1+$gamma1)*($alpha2-$alpha1))*($fy/$Up)];
set QslipY [expr $DslipY/($hcore/2)];
set QslipP [expr $DslipP/($hcore/2)];
set QslipP2 [expr $DslipP2/($hcore/2)];
set QslipU [expr $DslipU/($hcore/2)];
set Qy $QslipY
if {$ep2<$esn} {set Qn [expr $QslipP2+($QslipU-$QslipP2)*($esn-$ep2)/($eu-$ep2)]}
if {$esn<=$ep2} {set Qn [expr $QslipP + ($QslipP2-$QslipP)*($esn-$ep)/($ep2-$ep)]}
if {$esn<=$ep}   {set Qn [expr $QslipY + ($QslipP-$QslipY)*($esn-$ey)/($ep-$ey)]}
if {$ep2<$esu} {set Qu [expr $QslipP2+($QslipU-$QslipP2)*($esu-$ep2)/($eu-$ep2)]}
if {$esu<=$ep2} {set Qu [expr $QslipP + ($QslipP2-$QslipP)*($esu-$ep)/($ep2-$ep)]}
if {$esu<=$ep}   {set Qu [expr $QslipY + ($QslipP-$QslipY)*($esu-$ey)/($ep-$ey)]}
set Qph1S $Qy;
set Qph2S $Qn;
set Qph3S $Qu;
set Kph [expr $Mph1/$Qph1S];        # elastic stiffness of rotational spring
```

```
# Define nodes  ------ frame is in X-Y plane (X-horizontal, Y-vertical)
    #                          3------------------------4
    #                          |                        |
    #                          |                        |
    #                          |                        |
    #                          |                        |
    #                          |                        |
    #                         --1--                    --2--
set      IDctrlNode 3
node    1       0.0             0.0       0.0       # base
node    2       $Lbeam          0.0       0.0
node    11      0.0             0.0       0.0       # connects base to column via strong hinge element
node    12      $Lbeam          0.0       0.0       #       to control boundary conditions
node    3       0.0             $Lcol     0.0       -mass $Mnode 0.0 0.0 0.0 0.0 0.0
node    4       $Lbeam          $Lcol     0.0       -mass $Mnode 0.0 0.0 0.0 0.0 0.0
node    13      0.0             $Lcol     0.0;      # connects column to joint via hinge element
node    14      $Lbeam          $Lcol     0.0
node    23      0.0             $Lcol     0.0;      # connects joint to beam via joint element
node    24      $Lbeam          $Lcol     0.0

# Boundary conditions
fix   11   1  1  1  1  1  1;       # 1: fixed, 0: released
fix   12   1  1  1  1  1  1
fix    1   0  0  1  1  1  0
fix    2   0  0  1  1  1  0
fix    3   0  0  1  1  1  0
fix    4   0  0  1  1  1  0
fix   13   0  0  1  1  1  0
fix   14   0  0  1  1  1  0
fix   23   0  0  1  1  1  0
fix   24   0  0  1  1  1  0

# define MATERIALS
# uniaxial Kent-Scott-Park concrete model with linear unloading/reloading, no tensile strength   (-
    ve compression)
uniaxialMaterial Concrete01 $IDcore $fc1C    $eps1C $fc2C    $eps2C;              # confined
uniaxialMaterial Concrete01 $IDcover         $fc1U    $eps1U $fc2U    $eps2U;   # unconfined
# Reinforcing steel, uniaxial hysteretic steel model with isotropic hardening.
uniaxialMaterial Hysteretic $IDsteel $Fy $epsY $Fy1 $epsY1 $Fu $epsU -$Fy -$epsY -$Fy1 -
    $epsY1 -$Fu -$epsU $pinchX $pinchY $damage1 $damage2 $betaMUsteel
# Hysteretic response of joint
uniaxialMaterial Hysteretic $IDjointMat $Mv1 $Qv1 $Mv2 $Qv2 $Mv3 $Qv3 -$Mv1 -$Qv1 -$Mv2 -
    $Qv2 -$Mv3 -$Qv3 $pinchX $pinchY $damage1 $damage2  $betaMUjoint
# PLASTIC-HINGE "ROTATIONAL" spring -- TOP HINGE
# Hysteretic response of plastic hinge
uniaxialMaterial Hysteretic $IDphtMat $Mph1 $Qph1S $Mph2 $Qph2S $Mph3 $Qph3S -$Mph1 -
    $Qph1S -$Mph2 -$Qph2S -$Mph3 -$Qph3S $pinchX $pinchY $damage1 $damage2
    $betaMUph
# PLASTIC-HINGE "ROTATIONAL" spring -- BASE HINGE, controls boundary conditions
uniaxialMaterial Elastic $IDphbMat [expr 1/$Kph] ;    # super-flexible hinge for case of pin base

# Define COLUMNS
# procedure to define circular fiber section for flexural characteristics
proc RCcircSection {id ri ro cover coreID coverID steelID numBars barArea nfCoreR nfCoreT
    nfCoverR nfCoverT} {
# Define the fiber section
  section fiberSec $id {
```

```
    # Core radius
    set rc [expr $ro-$cover]
    # Define the core patch
    patch circ $coreID $nfCoreT $nfCoreR 0 0 $ri $rc 0 360
    # Define the cover patch
    patch circ $coverID $nfCoverT $nfCoverR 0 0 $rc $ro 0 360
    if {$numBars <= 0} {
     return
    }
    # Determine angle increment between bars
    set theta [expr 360.0/$numBars]
    # Define the reinforcing layer
    layer circ $steelID $numBars $barArea 0 0 $rc $theta 360
  }
}
RCcircSection $IDcolFlex  $riCol $roCol $cover $IDcore $IDcover $IDsteel $NbCol  $AbCol
     $nfCoreR $nfCoreT $nfCoverR $nfCoverT
uniaxialMaterial Elastic $IDcolTors $GJ;                  # Define torsional stiffness
section Aggregator $IDcolSec   $IDcolTors     T   -section   $IDcolFlex;      # attach torsion to
     flexure and create a new section IDtag
geomTransf Linear     $IDcolTrans          0 0 1;                # Linear: no second-order effects
     # element element type  ID, node I, node J, no. int pts, section ID, transf. ID
     element nonlinearBeamColumn  1    1   3    $np  $IDcolSec        $IDcolTrans
     element nonlinearBeamColumn  2    2   4    $np  $IDcolSec        $IDcolTrans
# Define JOINTS
# connect beams and columns at joint node with a rotational spring.
#    the rotational spring represents the joint and a hysteretic material is used to represent
#    the joint behavior.  The rotational spring has a moment-rotation relationship, which is
#    determined from the shear stress versus strain relationship for the joint.
# read procedure file which generates assigns the rotational spring about the z-axis
#      between the two nodes and constrains translations.
proc rotSpringDOF6 {eleID nodeR nodeC matID nodeQ} {
    # Create the zero length element
    element zeroLength $eleID $nodeR $nodeC -mat $matID -dir 6
    # Constrain the translational DOF with a multi-point constraint
    #         retained constrained DOF_1 DOF_2 ... DOF_n
    equalDOF $nodeQ $nodeC 1 2
}
#IDphtMat  has been defined in parameters.tcl and materials.tcl  -- TOP PLASTIC HINGE,
     connects column to joint
#            eleID    nodeR    nodeC  matID     nodeQ
rotSpringDOF6     101        3          13        $IDphtMat    3
rotSpringDOF6     102        4          14        $IDphtMat    4
#IDjointMat  has been defined in parameters.tcl and materials.tcl -- JOINT, connects hinge to
     beam
#            eleID    nodeR    nodeC  matID              nodeQ
rotSpringDOF6     201        13         23        $IDjointMat       3
rotSpringDOF6     202        14         24        $IDjointMat       4
#IDphbMat  has been defined in parameters.tcl and materials.tcl  -- BASE PLASTIC HINGE,
     connects base to columns
#            eleID    nodeR    nodeC  matID     nodeQ
rotSpringDOF6     301        11         1         $IDphbMat    11
rotSpringDOF6     302        12         2         $IDphbMat    12
# Define BEAM
geomTransf Linear    $IDbeamTrans       0 0 1;          # vector in element X-Z plane in global
     coords
```

```
element elasticBeamColumn   3  23 24   $Abeam    $Ec   $G $J   $IyBeam    $IzBeam
    $IDbeamTrans; # Iz  for in-plane analysis
```